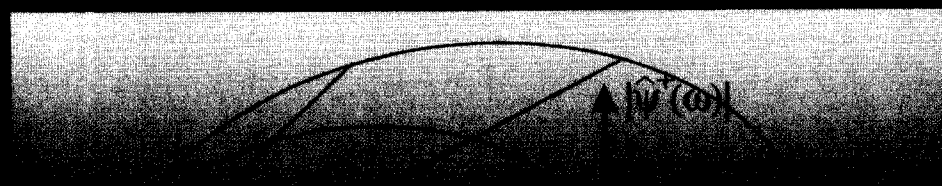


Seismic Applications of Complex Wavelet Transforms



Rutger van Spaendonck



TR
3881-51

Stellingen

Behorende bij het proefschrift

Seismic Applications of Complex Wavelet Transforms

Door

R.L.C. van Spaendonck

i

Naar analogie van de relatie tussen de discrete cosinus transformatie en de Fourier transformatie, kan men concluderen dat de uitbreiding van de discrete wavelet transformatie naar de complexe variant, een bredere toepassing heeft. (*Hoofdstuk 5 van dit proefschrift*).

ii

De Hilbert transformatie resulteert vaak vanwege haar globale karakter in een door artefacten overheerst analytisch signaal. De wavelet-gebaseerde Hilbert transformatie biedt de mogelijkheid lokaal te snijden zonder deze artefacten te introduceren. (*Hoofdstukken 4 en 6 van dit proefschrift*).

iii

De pseudo-horizon in combinatie met een attribuut dat het signaal karakteriseert, zoals bijvoorbeeld lokale schaal, leent zich uitstekend voor het door geologen veel toegepaste principe van stereoscopische interpretatie. (*Hoofdstuk 7 van dit proefschrift*).

iv

In 4-D seismiek wordt in essentie gekeken naar zeer lokale veranderingen van de geologische toestand over een tijdspanne veel groter dan die van de seismische meting. De attributen in dit proefschrift zijn ontworpen om lokale veranderingen in tijd en ruimte te karakteriseren en zijn dus bij uitstek geschikt voor 4-D interpretatie. (*Hoofdstuk 7 van dit proefschrift*).

Bij coherente systemen, zoals bijvoorbeeld communicatie systemen of beeldvorming aan de hand van synthetische apertuur radar, staat de fase van het signaal centraal. De conventionele discrete wavelet transformatie is door gebrek aan faseinformatie niet geschikt voor dit soort toepassingen. De complexe wavelet transformatie is in dit opzicht niet gehandicapt en kan in deze toepassing een relevante rol gaan spelen.

Het opgeven van de strikte translatie-invariantie eigenschap van een filter, kan in veel gevallen een beter resultaat van de gefilterde uitkomst leveren dan verkregen wordt met een translatie-invariant filter.

De leek wordt overspoeld met namen van bouwstenen van signalen, zoals bijvoorbeeld wavelets, curvelets, symmlets, ridgelets, coiflets, beamlets, wedgelets, edgelets, binlets, vaguelets, stantlets, morlets en contourlets. Ten onrechte suggereert deze wildgroei in benaming dat de naam de functionaliteit bepaalt, terwijl deze uitsluitend wordt bepaald door de wiskundige definitie van het wavelet.

Het Nederlands AiO-systeem, waarin de AiO een project uitvoert dat door een ander zeer gedetailleerd is opgezet, fnuikt de wetenschappelijke inventiviteit en bevordert wetenschappelijk conformisme.

Zoals de term reeds aangeeft is reizen met het *openbaar* vervoer een *apocalyptische* ervaring.

Door de overstelpende hoeveelheid informatie die door de ICT over allerlei gremia wordt uitgestort geldt voor de besluitvorming: het is een mail op zeven.

Propositions

Accompanying the PhD-thesis

Seismic Applications of Complex Wavelet Transforms

By

R.L.C. van Spaendonck

i

In analogy to the relationship between discrete cosine transform and the Fourier transform, it can be concluded that the extension of the discrete wavelet transform to a complex equivalent has a larger range of applications. (*Chapter 5 in this thesis*).

ii

The Hilbert transform generally results in an analytic signal that is dominated by artefacts due to its global character. The wavelet-based Hilbert transform provides the opportunity to act locally on the signal without introducing these artefacts. (*Chapters 4 and 6 in this thesis*).

iii

The pseudo-horizon in combination with a signal characterization attribute, such as local scale for example, provides us with an excellent platform for the principle of stereoscopic interpretation, which is frequently employed by geologists. (*Chapter 7 in this thesis*).

iv

4-D seismic imaging studies local changes in the geological state over a time span much larger than that of the seismic measurement. The attributes in this thesis are designed to characterize local changes in time and space and are hence suitable for 4-D interpretation. (*Chapter 7 in this thesis*).

Phase plays a crucial role in coherent systems, such as communication systems and synthetic aperture radar imaging for example. The conventional discrete wavelet transform cannot handle this type of data, due to the absence of phase information in the transform. The complex wavelet transform on the other hand is not handicapped in this respect, and may play an important role in the future for this type of application.

When we abandon the strict property of shift-invariance of a filter, we can often obtain a better filtering result than can be obtained with shift-invariant filter.

For an outsider the variety of names of the building blocks for signals can be confusing, e.g. wavelets, curvelets, bandelets, brushlets, symmlets, ridgelets, coiflets, beamlets, wedgelets, edgelets, binlets, vaguelets, stantlets, morlets, and contourlets. This proliferation in denomination suggests that the name determines its functionality, whereas the functionality is purely determined by the mathematical definition of the wavelet.

In the Dutch PhD-system, where a student carries out a project that has been set up in detail by somebody else, the scientific inventiveness is suppressed and scientific conformism encouraged.

Traveling by Dutch public transport is an apocalyptic experience.

Due to the overwhelming amount of information that is poured out by the ICT (Information and Communication Technology) over boards, applies for decision processes: it is one mail to Sevenum.

3881
776434
5

SEISMIC APPLICATIONS TR 3881
OF
COMPLEX WAVELET TRANSFORMS



**SEISMIC APPLICATIONS
OF
COMPLEX WAVELET TRANSFORMS**

PROEFSCHRIFT

ter verkrijging van de graad van doctor
aan de Technische Universiteit Delft,
op gezag van de Rector Magnificus prof. dr. ir. J. T. Fokkema,
in het openbaar te verdedigen ten overstaan van een commissie,
door het College voor Promoties aangewezen,
op woensdag 5 juni 2002 te 16:00 uur

door

Rutger Lucas Cyril VAN SPAENDONCK

mijnbouwkundig ingenieur
geboren te Nijmegen



Dit proefschrift is goedgekeurd door de promotoren:

Prof. dr. ir. J. T. Fokkema

Prof. dr. R. G. Baraniuk

Samenstelling promotiecommissie:

| | |
|----------------------------------|---|
| Rector Magnificus, | voorzitter |
| Prof. dr. ir. J. T. Fokkema, | Technische Universiteit Delft, promotor |
| Prof. dr. R. G. Baraniuk, | Rice University, Houston, promotor |
| Prof. dr. S. M. Luthi, | Technische Universiteit Delft |
| Prof. dr. ir. L. J. van Vliet, | Technische Universiteit Delft |
| Prof. dr. S. A. P. L. Cloetingh, | Vrije Universiteit Amsterdam |
| Prof. dr. R. van der Hilst, | Massachusetts Institute of Technology, Boston |
| Dr. T. P. H. Steeghs, | TNO Fysisch Electronisch Laboratorium |

Dr. ir. G. G. Drijkoningen heeft als begeleider in belangrijke mate aan de totstandkoming van dit proefschrift bijgedragen

ISBN 90-9015810-3

Copyright © 2002 by R.L.C. van Spaendonck, Section of Applied Geophysics,
Faculty of Applied Earth Sciences, Delft University of Technology.

All rights reserved. No parts of this publication may be reproduced, stored in a retrieval system or transmitted, in any form or by any means, electronic, mechanical, photocopying, recording, or otherwise, without the prior written permission of the author.

*Aan Karin
en
mijn ouders*

Support

The research reported in this thesis has been financially supported by the Dutch Science Foundation (NWO) NEESDI program and the Rice Consortium for Computational Seismic Interpretation (CCSI).

Contents

| | |
|---|-----------|
| Abstract | v |
| 1 Introduction | 1 |
| 1.1 The seismic interpretation problem | 1 |
| 1.2 Approach taken in this thesis | 3 |
| 1.3 Outline of the thesis | 5 |
| 2 Representations and Operators | 7 |
| 2.1 Notations and conventions | 8 |
| 2.2 Fourier transformation | 9 |
| 2.3 Relatives of the Fourier transformation | 10 |
| 2.3.1 Z-transform | 10 |
| 2.3.2 Hilbert transform and the analytic signal | 12 |
| 2.3.3 Radon transform | 14 |
| 3 Wavelets and Filter Banks | 19 |
| 3.1 Wavelets and wavelet expansions | 21 |
| 3.1.1 Scale and scaling functions | 21 |
| 3.1.2 Wavelets from scaling functions | 28 |
| 3.1.3 Wavelet transformation | 29 |
| 3.1.4 Inverse wavelet transformation | 32 |
| 3.2 Filter banks and multiresolution | 33 |
| 3.2.1 Discrete orthogonal filters | 33 |
| 3.2.2 Filter banks | 34 |

| | | |
|----------|--|------------|
| 3.2.3 | Daubechies wavelets | 37 |
| 3.3 | Cascading filter banks. | 39 |
| 3.3.1 | Average with $H(\Omega)$ | 39 |
| 3.3.2 | Detail with $G(\Omega)$ | 42 |
| 3.3.3 | Reconstruction wavelet tree | 43 |
| 3.4 | Tiling and Fourier partitioning. | 44 |
| 3.5 | Multi-dimensional wavelet transform | 45 |
| 3.5.1 | Two-dimensional separable wavelet transform | 45 |
| 3.5.2 | Three-dimensional separable wavelet transform | 51 |
| 4 | Local Hilbert transformation | 53 |
| 4.1 | Discrete Hilbert transform | 54 |
| 4.1.1 | Analytic signal and Hardy space | 55 |
| 4.1.2 | Wavelet-based Hardy-space projection. | 56 |
| 4.2 | Performance | 60 |
| 4.2.1 | Energy density. | 60 |
| 4.2.2 | Instantaneous phase and frequency | 62 |
| 4.3 | Conclusions on local and global Hilbert transformation | 64 |
| 4.4 | Seismic attributes | 65 |
| 4.4.1 | Conventional seismic attributes | 65 |
| 4.4.2 | Geometric seismic attributes | 73 |
| 4.4.3 | Seismic volume attributes | 80 |
| 5 | Pre-projection complex wavelet transform | 89 |
| 5.1 | Complex wavelet transforms: How and why? | 90 |
| 5.1.1 | Ideal analytic scaling functions and wavelets | 93 |
| 5.1.2 | Spanning the spaces: Multiresolution or Hardy space? | 97 |
| 5.2 | Pre-projection complex wavelet transform | 99 |
| 5.2.1 | Wavelet transformation in Softy space | 100 |
| 5.2.2 | Discrete filter bank implementation | 104 |
| 5.2.3 | Amplitude and phase | 107 |
| 5.2.4 | Shift-invariance | 112 |
| 5.3 | Geometric multi-dimensional complex wavelet transforms | 114 |
| 5.3.1 | Two-dimensional pre-projection complex wavelet transform | 116 |
| 5.3.2 | Three- or more dimensional pre-projection transform | 122 |
| 5.3.3 | Volume attributes of the complex wavelet transform | 126 |
| 6 | Iterated complex wavelet transform | 131 |

| | | |
|----------|---|------------|
| 6.1 | Construction of complex scaling functions and wavelets . . . | 132 |
| 6.1.1 | Revisiting the ideal analytic scaling functions | 134 |
| 6.1.2 | Wavelets and scaling functions of the complex wavelet transform | 134 |
| 6.1.3 | Convergence to Hardy space | 137 |
| 6.2 | Discrete filter bank implementation | 141 |
| 6.2.1 | Amplitude and phase | 143 |
| 6.2.2 | Shift-invariance | 146 |
| 6.3 | Wavelet-based discrete Hardy-space projection | 147 |
| 6.3.1 | Discrete Hardy-space projection with complex wavelet packets | 148 |
| 6.3.2 | Building the boxcar filter with finite functions | 152 |
| 6.3.3 | Instantaneous frequency by wavelet-packet Hardy projection | 154 |
| 6.4 | Multi-dimensional iterated complex wavelet transforms | 155 |
| 6.4.1 | Two dimensional iterated complex wavelet transform | 157 |
| 6.4.2 | Three and higher dimensional iterated complex wavelet transform | 165 |
| 7 | Quantitative seismic volume attributes | 167 |
| 7.1 | Synthetic reflection model | 169 |
| 7.1.1 | Shape of single reflector | 169 |
| 7.1.2 | Synthetic migrated seismic data | 170 |
| 7.2 | Attributes based on local Hardy projection | 171 |
| 7.2.1 | Radial frequency | 172 |
| 7.2.2 | Dip and azimuth | 174 |
| 7.3 | Pre-projection complex wavelet transform based attributes | 174 |
| 7.3.1 | Scale | 175 |
| 7.3.2 | Dip and azimuth | 176 |
| 7.3.3 | Towards volume segmentation of seismic data | 176 |
| 7.4 | The Pseudo-horizon for visualization | 178 |
| 7.4.1 | From amplitude to virtual topography | 178 |
| 7.4.2 | Combined attribute representations | 180 |
| 7.5 | Seismic Field data | 182 |
| 7.5.1 | Gulf of Mexico, South Marsh Island | 183 |
| 7.5.2 | North Sea, Block L05 | 187 |
| 8 | Conclusions | 213 |

| | |
|-------------------------|------------|
| Bibliography | 219 |
| Samenvatting | 227 |
| Dankwoord | 231 |
| Curriculum Vitae | 233 |

Abstract

This dissertation develops new multi-resolution signal processing techniques for analyzing the seismic reflection environment.

Seismic attributes play a pivotal role in three-dimensional seismic interpretation. After migration and stacking of the raw reflection data, the seismic image corresponds to an amplitude map of the stratification and structure of the subsurface. In order to identify geological features in this image, we must quantify seismic signal parameters with attributes which ideally are related to the subsurface stratigraphy. Especially for opaque three-dimensional seismic data, attributes are indispensable for visualizing and characterizing reflection properties. In recent years sophisticated three-dimensional techniques have been developed that localize faults and lateral variations in a multi-trace fashion. Our philosophy concerning seismic volume analysis is that a complete description of the reflection environment in terms of meaningful structural and physical parameters helps to obtain a better understanding of the subsurface geology.

The massive amount of data we deal with in seismic imaging presses the need for computationally efficient signal analysis algorithms. Therefore, the traditional attributes have been based mostly on single trace characterizations or relatively simple multi-trace operations. Partially for this reason, the currently used volume attributes, such as instantaneous frequency, instantaneous phase, and lateral coherence are not well-suited to describe the signal in terms of relevant geological or physical parameters, but are often chosen because efficient algorithms exist.

Apart from the geological meaning of some of the conventional attributes,

the computational efficiency also comes at the cost of the accuracy of attributes. The complex-trace attributes that are derived from the analytic signal are a perfect example of this. The complex-trace attributes are computed using sample-based operations combined with finite Fourier transforms. Although relatively fast, the algorithm illustrates that the discrepancy between local and global operations results in attributes that are disturbed by ringing artifacts and spikes.

In our approach to seismic volume analysis we use the discrete wavelet transform (DWT). The DWT uses basis functions that are local in time and local in frequency and hence are natural for multiresolution analysis. This implies that we can perform frequency analysis locally in time and thus describe the signal completely. Besides the elegance of the transform for analysis purposes, the motivation for its use is also found in its computational efficiency. The wavelet transformation is one of the most successful new tools in signal processing since years, and has had great impact in the field. It has been successfully applied for image compression, denoising, segmentation, data modeling and many other signal processing applications.

We use the multiresolution concept of the DWT for computation of volume attributes such as scale, direction of inclination, and orientation of reflection patterns. However, the DWT has several drawbacks. Since seismic images originate from a measured wave field, amplitude and phase are key properties as in any wave-propagation system. In a seismic image, amplitude is a measure for the contrast in rock parameters and phase determines the timing of reflections. For this reason phase information is indispensable for a complete description of seismic data. However, the phase is absent in the DWT. Another disadvantage of the DWT is that it is not invariant under translation and it shows poor directional information for higher dimensions.

The existing discrete wavelet transforms that include phase information either involve complicated design criteria, or their real and imaginary parts do not form an locally analytic pair, which means that they are not in approximate quadrature. Without the latter property the phase is is not very useful for our purpose.

One of the main contributions made in this thesis is the extension of the DWT to two new complex wavelet transforms. The two transforms can be constructed using any real wavelet. Both preserve the desirable DWT qualities, but include phase information. In addition, both complex transforms show improved translation-invariance and directional discrimination. The algorithms are relatively simple to design and are extremely efficient with their

linear computational complexity. The first transformation involves a projection before the discrete wavelet transformation. The second transformation embeds the projection in the wavelet-tree structure.

The projection we use to create the imaginary part of the complex wavelet transforms is based on a local form of the Hilbert transform. This new implementation of the Hilbert transform is an important contribution in this thesis. By itself it can be used for local analysis and for the computation of local complex-trace volume attributes.

In our quest for a complete description of the reflection environment, we compute local geometry, local scale and reflection strength. For the computation of these attributes we use our new three-dimensional complex wavelet transform. We decompose local geometry into angle of inclination and orientation. The attributes have been validated using a synthetic reflector model with moderately varying geometry and constant frequency. The resulting attribute images show that the complex wavelet transform is an excellent tool for the quantification of the geometric shape of a reflector and its three-dimensional scale character.

Application of the attributes on field data shows that they visualize signal characteristics that remain hidden in the amplitude data. The attributes are robust against minor variations and noise in the field data. For the visualization of the attributes we introduce the new concept of time-slice topography. The combination of geometric information in a lateral slice results in a virtual horizon that corresponds to the local geometry in the neighborhood of this slice. In this way we can capture the two geometry attributes in a single image. With the time-slice topography concept we have created new opportunities for attribute visualization and seismic structural interpretation; we can capture the entire description of the significant local reflection properties in a single image.

Introduction

This dissertation presents a new approach to the analysis of three-dimensional seismic data volumes. A novel implementation of the Complex Discrete Wavelet Transformation is proposed and its application to seismic attribute extraction is demonstrated. The purpose of this introductory chapter is 1) to introduce the problem of three-dimensional seismic interpretation and to summarize the current approach to this problem, 2) to provide a concise description of the approach that is taken and 3) give an outline of the thesis.

1.1 The seismic interpretation problem

Seismic imagery of the Earth's subsurface plays a critical role in all aspects of oil and gas exploration and production — from the location of reserves to their appraisal and subsequent monitoring. In oil and gas exploration, seismic cross-sections are scrutinized by interpreters who search for features that indicate possible hydrocarbon reservoirs. Seismic images are a representation of the acoustic impedance contrast in the subsurface. Seismic interpretation starts from the premise that the acoustic impedance contrasts find their origin in changes in the composition of the rocks. By tracking and identification of these changes in seismic sections the image can be interpreted in terms of the subsurface geology.

With the introduction of three-dimensional seismic profiling in the 1980s a major revolution started in seismic imaging. Being the last step in the seismic processing sequence, the development of new seismic interpretation methods lagged behind the tremendous advancements that were made in seismic data acquisition and processing. This lasted until the mid-1990s, when also the approach towards seismic interpretation radically changed. Previously, seismic interpreters largely depended on techniques that were developed for relatively small numbers of 2-D seismic cross sections for the interpretation of huge three-dimensional data volumes. Nowadays, the paper and pencils of the first decades of seismic interpretation have been replaced by powerful computers and advanced computer programs that are able to visualize the seismic data through sections, slices and reflection interfaces, which are being tracked through the volume (Brown, 1999). For the seismic interpreter, the extra dimension meant a radical change in the nature of his work. The interpretation of three-dimensional seismic data made structural interpretation relatively easy. However, at present the seismic data is expected to yield detailed information that goes far beyond global structural interpretation. In this quest for detail, the interpreter is confronted with opaque seismic data volumes and enormous amounts of data.

The tremendous increase in the size of seismic data volumes has created the need for methods that automatically extract the relevant features from the data. Presently, the detail and quantity of seismic data cannot be used to its full potential, due to limitations of the analysis and visualization tools.

Towards the end of the 1970s novel interpretation tools were introduced to study the characteristics of seismic signals. Local changes of the frequency of the seismic signal provide information on the stratification of the geological formations. The complex-trace analysis that was introduced by Taner *et al.* (1979), reveals extra information in the seismic trace to help the interpreter. Complex-trace analysis decomposes the signal into two basic parameters: amplitude and phase. From these parameters seismic *attributes* can be derived that may provide indicators of the lithological and structural origins of the seismic reflection character.

Three-dimensional seismic data acquisition required a change of the approach towards seismic interpretation. The previously unavailable horizon and time-slice views show the spatial extent of features from above. The realization of the relevance of the time-slice view has had a huge impact on seismic interpretation. The first technique for analyzing lateral variations along horizontal volume slices was introduced by Bahorich and Farmer (1995a).

This technique studied the lateral coherence of data. The so-called *coherence cube* approach demonstrated that by analyzing changes in the three-dimensional reflection character, information is revealed that can be hard to recognize in the standard image display (Bahorich *et al.*, 1995; Bahorich and Farmer, 1995b; Gersztenkorn and Marfurt, 1996; Marfurt *et al.*, 1998). At almost the same time several researchers came up with technologies that gave similar results. Steeghs (1997) proposes three-dimensional local power spectra to estimate local geometry (dip and azimuth). Dessing (1997) used the continuous wavelet transform for edge-detection and hence localization of the lateral incoherencies in reflection interfaces. This approach has been further extended by Verhelst (2000), who demonstrates the use of the continuous wavelet transform for the extraction of seismic attributes. In this dissertation we further extend and enhance the wavelet-transform approach to seismic attribute extraction. The approach that is taken and the underlying assumptions are the subject of the next section.

1.2 Approach taken in this thesis

The data processing sequence that precedes seismic interpretation results in a projection of the seismic reflections onto the contrasts in the Earth's subsurface that caused those particular reflections. This entails that all the wave propagation effects are removed from the seismic data. The process that is responsible for this de-propagation is called *migration*.

The resulting seismic image after migration shows reflections at the correct time or depth with the true amplitude of the band-limited reflection coefficients. We assume that either the structures in the Earth correspond to the seismic image or that there is a linear mapping of the structures in the Earth onto our seismic image. For the latter, the structures can be mapped to depth through the propagation velocities in the layers.

The reflections from the Earth's subsurface that we use for interpretation merely give an indication of the contrasts in the Earth. Classification of the reflection patterns on the basis of the character of the seismic signal is the first step towards a geological interpretation of the seismic data. For this purpose, we decompose the seismic data into several elemental seismic image features. Some of these features can be directly associated with structures in the Earth, others reveal patterns that may be associated with a certain depositional environment or lithology. The transformation we have developed for the analysis are decompositions of a seismic data volume in terms of scale,

orientation and reflection strength.

The reason for choosing a scale transform is threefold. Scale transforms change the size of the analysis window, as the frequency permits. The lower the frequency, the larger the window size. In this way the drawback of local Fourier analysis — dependence of the results on the size and shape of the analysis window — can be avoided. The second reason is that reflection events show-up at different scales. High amplitude and low-frequency information attract the attention. Small scale events in the seismic data such as the seismic expression of channels are hardly visible with the bare eye, but can be enhanced by scale decomposition. Signal jump-discontinuities, such as faults, are expected to show up through all scales in the wavelet transform. The third reason originates in the physics of the problem: the wavelet transform and the wave-equation are of a similar form. Both dilate and translate a short-duration function. This behaviour becomes visible especially in the case of time-lapse seismic profiling, where the differences in the seismic data sets appear as a phase-shift and a dilation of the waveform (Dillen, 2001).

The scale decomposition which we developed for the analysis of seismic data, is a modified wavelet transform. The transform operates in the space/time domain. The wavelet transform is modified in such a way that each of the subbands consists of an imaginary and real part in quadrature together with the ability to discriminate different angles.

For the interpretation of the scale decompositions, the transforms are characterized through attributes. The attributes are basic statistical measures, such as the mean of mode of the scale distributions. For complex wavelet transform, we use three attributes: local geometry, local scale and local reflection strength. It will be demonstrated that these three parameters are very suitable for characterization of a three-dimensional signal.

Like the coherence type attributes, the local geometric quantities enrich the horizontal slice or time-slice interpretation. Conventional amplitude-slices can be seen as faint contour maps. The direction of inclination gives a much better impression of the geological structure than these contours. With a single glimpse the interpreter gets an impression of the structure at a certain depth. The scale and reflection strength attributes are more closely related to the complex-trace or instantaneous frequency attributes (Taner *et al.*, 1979; Steeghs and Drijkoningen, 2002). They serve as lithology indicators. The added value is that the local scale is independent from the geometry.

1.3 Outline of the thesis

The notation, basic operators, mathematical representations, and transformations are introduced in Chapter 2.

In Chapter 3 we discuss the concept of wavelets and wavelet transforms. The theory for the discrete wavelet transformation in terms of wavelets and scaling functions — the basis functions for the transform — is discussed in this chapter. The discrete wavelet transformation can be represented as a cascade of filters in frequency. This representation results in an approximate wavelet transform that is called the *fast wavelet transform*, because of its computational efficiency. We show that the filter bank is a very useful representation for wavelet design, because of its simple structure. In the construction of wavelets, the filter design plays a crucial part. Finally, the multi-dimensional extension of the discrete wavelet transform is briefly addressed.

In Chapter 4 we introduce a new discrete implementation of the Hilbert transformation. When we consider the short-duration functions in the wavelet transformation, the computation of an analytic equivalent of these functions by the Fourier transformation does not seem appropriate. In this chapter we introduce a *local* form of the Hilbert transformation that uses local-support heavily constrained filters for the computation of Hilbert transform. We address the design of the filters and their properties. We compare several signal attributes and compare those with the conventional Hilbert transform attributes. In this chapter we also introduce the Hardy space — the space containing strictly positive frequencies. In addition, *local* Hardy space is introduced — a space in which negative frequencies are suppressed with local-support filters.

In Chapter 5 we introduce a novel complex wavelet transformation. The discrete wavelet transformation has some major drawbacks for attribute extraction. One of those is that the transform is not invariant under shifts in the input signal. Another drawback arises when extending the transform to more dimensions. These transforms carry almost no directional information in its subbands, which makes the transform inadequate for attribute extraction. In this chapter we will introduce a wavelet transform that has reduced shift-variance and superior directional selectivity. The transform uses a projection onto local Hardy space, before the scale decomposition. The projection filters are closely related to the local Hilbert transformation filters, discussed in Chapter 4. In the last section of this chapter we will define the attributes that can be extracted from the complex discrete wavelet transform.

In Chapter 6 another type of complex wavelet transformation is dis-

cussed. From the motivation of the ideal filter approximation, we found a second approach for the design of complex wavelet transforms. This particular transform embeds the projection within the stages of the transformation. As a consequence the transform has renewed quadrature at every scale. This implies that the spaces do not satisfy the nesting property, one of the basic motivations for wavelet transforms. We will address the design of the transform and the properties. We will show that transform spans Hardy space in the limit. For the discrete-time Hardy projection we introduce a wavelet-packet approach that enables us to construct the brick-wall with local-support filters and sampling operators. The multi-dimensional extension of the transform is briefly considered and its directional selectivity compared to that of the transform introduced in Chapter 5.

We will show in Chapter 7 how the various transforms perform for the computation of seismic volume attributes. The transforms that are addressed for this purpose are the local Hardy projection operator and the pre-projection complex wavelet transform. First, the algorithms will be validated on a simple seismic reflection model. Furthermore, we show how we can compute a structure map of a depth- or time-slice on the basis of the geometric attributes. This virtual topography map combines the two geometry attributes in a single image. In addition we can imprint the radial frequency on the topographical map and create a platform for a bird's eye view geological interpretation. In the second part of this chapter we demonstrate the proposed method on two seismic field data volumes. The first data volume is from the Gulf of Mexico. The pre-projection complex wavelet transform attributes are compared to the analytic filter attributes. A second data volume from the North Sea has been analyzed with the robust pre-projection algorithm. We present the results as virtual topography images of time-slices.

Representations and Operators

With seismic imaging, we try to compose an image of the structures and the layering in the subsurface using sound waves. The sound waves penetrate into the Earth, propagate through the layers and partly reflect on the acoustic and elastic contrasts in the Earth. We measure the reflected waves upon returning at the surface. A single measurement of the reflected wave field is not enough for a geophysicist to come to an image, but a collection of measurements and sources provides us enough information to estimate propagation velocities of seismic formations in the Earth. These velocities can be used subsequently to de-propagate the reflected wave field from the surface, where it was measured, back to the contrast, where the reflected wave originated. This whole procedure from the measurement to the final image of the contrasts in the Earth is called *migration*. With migration the wave-propagation effects are removed from the measurements so that the data converge towards an image of the contrasts in the subsurface.

The image of the Earth after migration is the starting point for seismic interpretation, because it is literally a representation of the Earth. Since the image represents the contrasts and does not reveal rock parameters directly, it is the interpreter's task to classify the seismic formations with his expert eyes. To this end, the interpreter studies the reflection *environment*, i.e. the amplitude, the geometry and the continuity of reflectors. The characteriza-

tion of the reflection on the basis of its environment is the red line of this thesis, starting with this chapter.

First we classify the types of images we use, so that the meaning of the parameters is unambiguous. Two classes of migration are commonly known, depth-migration and time-migration. In both types of migration the wave-propagation is removed from the data, however in the first case the contrasts are portrayed according to depth, in the second case these are portrayed in terms of time. Depending on the type of migration we have used, we end up either with a volume in three-dimensional space (depth-migration), or with a spatio-temporal volume with two spatial axes in horizontal directions and with time along the vertical axis (time-migration). With the knowledge on the type of seismic image we are working with, the local reflection parameters can be interpreted accordingly. The processing history of the seismic image reveals the mapping of the Earth onto the seismic image and onto the attributes.

In this chapter we discuss the transformations and representations that are used throughout the thesis. Basic relationships between time, position and frequency are discussed, such as the Fourier and the Radon transformation. These relations bridge the gap between the geometry in a spatial volume and the geometry in a spatio-temporal volume as they are obtained after the different types of migration. These are fundamental issues for the understanding of the attributes, since these can be computed either from depth-migrated or from time-migrated seismic data and have to be interpreted accordingly.

2.1 Notations and conventions

To specify position in a configuration, we employ the coordinates $\{x_1, x_2, x_3\}$ with respect to a Cartesian reference frame with origin \mathcal{O} and three mutually perpendicular base vectors $\{\hat{i}_1, \hat{i}_2, \hat{i}_3\}$ of unit length each. In the indicated order, the base vectors form a right-handed system. The time coordinate is denoted by t . The subscript notation for Cartesian vectors and tensors is used, except when explicitly specified otherwise. We use the Einstein convention which means that summation is indicated by repeated subscripts. The subscript notation applies to repeated lower-case Latin subscripts that range over the values 1, 2 and 3. The third dimension is used to indicate depth. Whenever appropriate, the position is also specified by the vector $\mathbf{x} = x_m \hat{i}_m$. To denote the horizontal coordinates only, Greek subscripts are used to which the values 1 and 2 are to be assigned. We use the vector

$\mathbf{x}_T = x_1\mathbf{i}_1 + x_2\mathbf{i}_2$ to specify the transverse components only, and employ $\mathbf{x}_D = x_1\mathbf{i}_1 + x_3\mathbf{i}_3$ to indicate the components in a two-dimensional seismic image with a single horizontal component and the preferential depth direction. The symbol \cup is used to denote the union of sets, while $\mathcal{D}^{(1)} \subset \mathcal{D}^{(2)}$ denotes that $\mathcal{D}^{(1)}$ is a proper subset of $\mathcal{D}^{(2)}$ and $\bar{\mathcal{D}}$ denotes the complement of the domain \mathcal{D} in \mathbb{R}^3 . The symbol i is used to indicate the imaginary unit $i = \sqrt{-1}$. We employ the symbol \oplus to indicate the direct sum of two vector spaces.

2.2 Fourier transformation

The temporal Fourier coordinate or *frequency* is denoted by ω . Time and frequency are related through the temporal Fourier transformation

$$\mathcal{F}\{g(t)\}(\omega) = \hat{g}(\omega) = \int_{t \in \mathbb{R}} g(t) \exp(-i\omega t) dt, \quad (2.1)$$

in which the Fourier operator is denoted by \mathcal{F} . The inverse temporal Fourier transform is given by

$$\mathcal{F}^{-1}\{\hat{g}(\omega)\}(t) = g(t) = \frac{1}{2\pi} \int_{\omega \in \mathbb{R}} \hat{g}(\omega) \exp(+i\omega t) d\omega. \quad (2.2)$$

The spatial Fourier coordinates or *wavenumbers* are denoted by $\{\mathbf{k}_1, \mathbf{k}_2, \mathbf{k}_3\}$. Position and wavenumber are related through a similar Fourier transform pair as above, but with opposite signs. For a volume function $u(\mathbf{x})$, we obtain

$$\tilde{u}(\mathbf{k}) = \int_{\mathbf{x} \in \mathbb{R}^3} u(\mathbf{x}) \exp(+i\mathbf{k}_l x_l) d\mathbf{x}, \quad (2.3)$$

and the inverse

$$u(\mathbf{x}) = \frac{1}{(2\pi)^3} \int_{\mathbf{k} \in \mathbb{R}^3} \tilde{u}(\mathbf{k}) \exp(-i\mathbf{k}_l x_l) d\mathbf{k}. \quad (2.4)$$

The Fourier transformation of functions $u(\mathbf{x}, t)$ that are dependent on both time and space, such as wave functions, can be described as a sequential operation of Eq. 2.1 and 2.3.

The Fourier transformation is a global operator which uses basis functions of infinite extend to describe the signal. This means that in the Fourier domain, no spatial or temporal information is found in the amplitude, and vice versa. This particular property has been the drive behind the time-frequency representations and wavelet transformations that operate with *local* basis functions to describe a signal. The latter transformation is extensively discussed in Chapter 3.

2.3 Relatives of the Fourier transformation

The Fourier transformation is a widely used mathematical tool with many different applications. Some of these applications use modified Fourier transforms or closely related transformations. In this section we discuss three important relatives of the Fourier transformation that are frequently used in other chapters. The first transformation we consider, is the discrete variant of the Fourier transformation and its relative, the z -transformation. This transformation provides us with an efficient and transparent platform for the design and understanding of discrete systems. The temporal convolution becomes an inner product in frequency and vice versa (Bracewell, 1978). The second transform, we will discuss, is the Hilbert transformation. The Hilbert transform plays a key role in the definition of the complex wavelet transformations discussed in the Chapters 5 and 6. The transform is indispensable for the definition of the *analytic* signal. The analytic signal is used for the conventional complex trace attributes, such as instantaneous frequency and phase and for the comparison of signals on basis of their energy content. The third transformation we will introduce, is the Radon transformation. This transformation is especially important for the interpretation of geometry of time-migrated images, because the transform relates the angle between time and space in a spatio-temporal system.

■ 2.3.1 Z-transform

In practice, transformations and operators are implemented to operate on *discretely* measured signals. Especially in the discussion on wavelets and wavelet transforms, the discrete character of the signal is important. The discrete wavelet transformation is based on temporal convolutions with finite functions or filters.

In this section we will address the z -transformation. This transformation is a discrete operator and is close family of the discrete-time Fourier transformation. The z -transformation is discussed for one-dimensional as well as for multi-dimensional signals.

Let us change the continuous time variable t to a discrete variable n sampled at Δt interval, and with a signal length of $N\Delta t$. A signal $g(t)$ then changes to $g(n\Delta t)$. When we normalize the sampling interval $\Delta t = 1$, the definition of the Fourier transform in Eq. (2.1) of the signal $g(t)$ changes into

a *discrete-time Fourier transform* $\hat{g}(\Omega)$ of the discrete signal $g(n)$

$$\hat{g}(\Omega) = \sum_{n=-\infty}^{\infty} g(n) \exp(-i\Omega n), \quad \text{for } \Omega \in [0, 2\pi), \quad (2.5)$$

in which Ω denotes the frequency variable which is periodic with a period of 2π . Now the *inverse discrete-time Fourier transform* is given by

$$g(n) = \frac{1}{2\pi} \int_0^{2\pi} \hat{g}(\Omega) \exp(i\Omega n) d\Omega. \quad (2.6)$$

We can use a conversion from the frequency variable Ω to the complex variable z . Upon rewriting definition Eq. 2.5 with the variable $z = r \exp(i\Omega)$, we obtain the z -transform

$$\hat{g}(z) = \sum_{n=-\infty}^{\infty} g(n) z^{-n}. \quad (2.7)$$

We employ the *hat*-symbol to indicate the Fourier transforms as well as the z -transform, because the transforms are closely related. The variable in between parentheses determines which type of transform is considered.

The conversion from Ω to z is commonly used in discrete signal processing. Due to its shape, the z -transform simplifies the formulation of discrete-time shifting and convolution. Filter design criteria for wavelets are often expressed in the z -domain, because they are easier to apprehend in this domain.

Since we work with seismic images that consist of more than one dimension, we also define a three-dimensional z -transform. To this end we introduce the discrete-space volume function $u(\mathbf{m}) = u(m_1 \Delta x_1, m_2 \Delta x_2, m_3 \Delta x_3)$ with the discrete-space vector $\mathbf{m} = \{m_1, m_2, m_3\}$ sampled at $\{\Delta x_1, \Delta x_2, \Delta x_3\}$ intervals with $\{M_1, M_2, M_3\}$ number of samples in the appropriate direction. the spatial Fourier variable vector \mathcal{K} is defined in the subspace Λ_3 of \mathbb{R}_3 according to

$$\Lambda_3 = \{\mathcal{K} \in \mathbb{R}^3; 0 \leq \mathcal{K}_1 \leq 2\pi, 0 \leq \mathcal{K}_2 \leq 2\pi, 0 \leq \mathcal{K}_3 \leq 2\pi\}. \quad (2.8)$$

The definition of the spatial Fourier transform in Eq. (2.3) changes after normalization of the sampling distance $\{\Delta x_1 = 1, \Delta x_2 = 1, \Delta x_3 = 1\}$ into the three-dimensional *discrete-space Fourier transform* $\tilde{u}(\mathcal{K})$ of the volume function $u(\mathbf{m})$, viz.

$$\tilde{u}(\mathcal{K}) = \sum_{m_1, m_2, m_3 = -\infty}^{\infty} u(\mathbf{m}) \exp[i(\mathcal{K}_1 m_1 + \mathcal{K}_2 m_2 + \mathcal{K}_3 m_3)], \quad \text{for } \mathcal{K} \in \Lambda_3, \quad (2.9)$$

The *inverse discrete-space Fourier transform* is then given by

$$u(\mathbf{m}) = \frac{1}{(2\pi)^3} \int_{\mathcal{K} \in \Lambda_3} \tilde{u}(\mathcal{K}) \exp[-i(\mathcal{K}_1 m_1 + \mathcal{K}_2 m_2 + \mathcal{K}_3 m_3)] d\mathcal{K}. \quad (2.10)$$

We can use a conversion from the spatial Fourier variable vector \mathcal{K} to the complex variable vector $\mathbf{z} = \{z_1, z_2, z_3\}$. Upon rewriting definition Eq. (2.9) with the variables $z_1 = r_1 \exp(i\mathcal{K}_1)$, $z_2 = r_2 \exp(i\mathcal{K}_2)$ and $z_3 = r_3 \exp(i\mathcal{K}_3)$, we obtain the three-dimensional spatial z -transform,

$$\tilde{u}(\mathbf{z}) = \sum_{m_1, m_2, m_3 = -\infty}^{\infty} u(\mathbf{m}) z_1^{m_1} z_2^{m_2} z_3^{m_3}. \quad (2.11)$$

We employ the *tilde*-symbol to indicate the 3-D Fourier transforms as well as the 3-D z -transform, because these are closely related. The variables in between parentheses specify the type of transform that is used.

Due to its shape, the three-dimensional z -transform simplifies the formulation of discrete-space shifts and convolution. We will use this representation to formulate filter design criteria for three-dimensional wavelet transforms.

■ 2.3.2 Hilbert transform and the analytic signal

Measured signals, such as seismic signals, and modulated signals are real-valued signals. For signal analysis or processing, it is often advantageous to describe a signal in terms of an amplitude and a phase. Therefore we can use the analytic signal, which is a complex signal that is uniquely related to the real-valued signal.

The relation in the analytic signal between the real-valued input signal and its imaginary counterpart is described by the Hilbert transformation. The resulting Hilbert transform represents the imaginary part, which is in quadrature with the input signal.

Since decades the Hilbert transform plays a prominent role in seismic interpretation, after the introduction of the complex-trace attributes by Taner and Sheriff (1977). The smooth envelope and the phase properties of the analytic signal have proven to be helpful for lithological interpretation and for energy comparison.

The operator for computation of the analytic signal consists of two parts, one resulting in the real part, and the other in the imaginary counterpart, which is in quadrature with the real part. The analytic signal $\mathcal{A}(u(t))$ of a

real-valued signal $u(t) \in \mathbb{R}$, can be decomposed in terms of a real and an imaginary part

$$\begin{aligned} \mathcal{A}\{u(t)\} = u^A(t) &= u^R(t) + iu^I(t) \\ &= |A(t)| \exp[i\varphi(t)], \end{aligned} \quad (2.12)$$

in which u^A represents the analytic signal, u^R the real part, and u^I the imaginary part. $|A(t)|$ is the envelope, and φ is the phase. The real part is represented by the signal itself. In an integral formulation the real part of an analytic signal can be written as a convolution of the input signal with a Dirac-function,

$$u^R(t) = \int_{-\infty}^{+\infty} \delta(t - \tau)u(\tau)d\tau = u(t). \quad (2.13)$$

The imaginary part of the analytic signal is equal to i times the Hilbert transform of the signal. The Hilbert operator is defined in the time-domain as (Bracewell, 1978)

$$u^I(t) = \mathcal{H}\{u(t)\} = \int \frac{1}{\pi(t - \tau)}u(\tau)d\tau, \quad (2.14)$$

in which \mathcal{H} represents the Hilbert operator and \int is defined as the Cauchy-principal value integral. This integral has a pole at $t = \tau$ and is odd symmetric. In the limits the function asymptotically approaches zero. The most straightforward way to calculate the Hilbert transform of a signal is by Fourier transformation of the signal, subsequent multiplication of the amplitude spectrum with the signum function $\text{sign}(\omega)$, followed by inverse Fourier transformation, *viz.*

$$u^I(t) = -i \mathcal{F}^{-1}\{\text{sign}(\omega)\mathcal{F}\{u(t)\}\}, \quad (2.15)$$

in which

$$\text{sign}(\omega) = \{-1, 0, 1\} \quad \text{for } \omega \in \{-\infty, 0, +\infty\}. \quad (2.16)$$

The resulting function $u^I(t)$ is a ninety degrees phase-shifted version of the original signal, which means that it is in quadrature with the real-valued signal $u^R(t)$.

When we write the equation for the analytic signal given in Eq. (2.12) as the modulus and the argument or phase, the derivative of the instantaneous phase is the *instantaneous frequency*

$$\langle f(t) \rangle = \frac{1}{2\pi} \frac{d\varphi(t)}{dt}. \quad (2.17)$$

In Chapter 4, we deal with the discrete implementations of the Hilbert transform, and in particular a novel convolution-based implementation for non-stationary signals.

■ 2.3.3 Radon transform

Geological interpretation is the final step in seismic imaging of the subsurface. For an adequate interpretation of a seismic image, we need to know what type of processing is done to come to the final seismic image. The two classes of migration lead to different representations of the subsurface;

Depth-migration depicts a one-to-one map of the structures in the Earth, whereas time-migration portrays the structures in time instead of depth. Each image demands its own interpretation of reflection geometry and frequency. In this section we will explain in what way the geometry in a spatial volume is related to the geometry in a spatio-temporal volume through the Radon transformation.

With migration the wave-propagation effects are removed from the seismic data. Depending on the type of migration, time- or depth-migration, the resulting image is a representation of the subsurface in terms of reflection amplitudes positioned at the correct depth or the correct time in the subsurface. Depth-migration results in one-to-one mapping of the geological structures in the subsurface onto the reflection amplitudes. Time-migration results in a spatio-temporal representation of the subsurface, in which the time-axis is linearly related to depth through the propagation velocities of the layers. Laterally the structures are in the correct position, but depth still has to be recovered from time. Time-migration needs an additional step before the reflection geometries are mapped one-to-one with the correct interfaces in the subsurface. This procedure is called time-to-depth conversion. The wave-propagation velocities in the different geological strata or layers are needed to obtain one-to-one mapping of the Earth onto the seismic image.

The algorithms presented in this thesis can be used on time- as well as depth-migrated seismic images. However, because the algorithms and their resulting images are geometry and frequency related, these need a different interpretation for each type of migration. From a structural point of view, when the migration is performed in a proper way, the information is adequate in both time- and depth migration, however, the quantitative angles in a seismic section are not exact in the case of time-migration.

One of the features we extract from seismic images, is the local geometry of a reflector. In three-dimensional space, orientation can be decomposed

into the angle of inclination, or *dip* and the direction in which the object inclines, or *azimuth*. For depth-migrated seismic images these quantities have a geological significance. In this case we work on an image $I(x_1, x_2, x_3)$, that is totally space-dependent and the angle of inclination and the azimuth are well-defined and directly reflect the actual angles of the geological structures in the Earth. For a time-migrated seismic image, the angles are less straightforwardly associated with the subsurface structures. The image or volume is then a function of area and time $I(x_1, x_2, t)$. What is the meaning of an angle between time and space?

The answer to this question is hidden in the Radon transformation as used in geophysics (Chapman, 1981; Deans, 1983; Fokkema and van den Berg, 1993). The Radon transformation relates time to position. An image obtained from time-migration lives in a frame that is spanned laterally by position and vertically by time. For the following discussion we refer to Fig. 2.1 in which we show the three-dimensional frame for a time-migrated

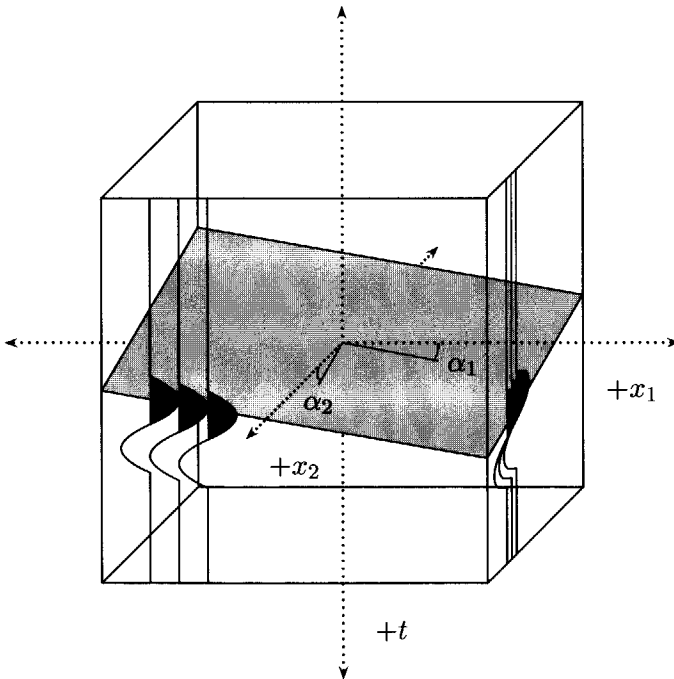


Figure 2.1: Geometry depends on $\{x_1, x_2, t\}$ after seismic time-migration; angle α_1 and α_2 indicate spatio-temporal angles.

volume. In this spatio-temporal frame the horizontal components are denoted by the position vector $\mathbf{x}_T = x_1\mathbf{i}_1 + x_2\mathbf{i}_2$, the wavenumbers by $\mathbf{k}_T = k_1\mathbf{i}_1 + k_2\mathbf{i}_2$. Time t is indicated along the vertical axis instead of the depth x_3 . The horizontal slowness vector is denoted by $\mathbf{p}_T = p_1\mathbf{i}_1 + p_2\mathbf{i}_2$ and relates time and lateral position through the slope and intercept time,

$$t = \mathbf{p}_T \cdot \mathbf{x}_T + \tau. \quad (2.18)$$

The lines with angles $\alpha_T = \{\alpha_1, \alpha_2\}$ intersect with the time-axis at intercept time τ . The relation between the angles α_1 and α_2 and the slowness vector are given by

$$\mathbf{p}_T = \begin{pmatrix} p_1 \\ p_2 \end{pmatrix} = \begin{pmatrix} \frac{dt}{dx_1} \\ \frac{dt}{dx_2} \end{pmatrix} = \begin{pmatrix} \tan(\alpha_1) \\ \tan(\alpha_2) \end{pmatrix}. \quad (2.19)$$

The angles α_1 and α_2 represent the angle of inclination in $\{x_1, t\}$ and $\{x_2, t\}$, respectively, when we are working with time-migrated seismic data. The tangent of this angle vector α_T yields the horizontal slownesses that have a geometrical meaning in (\mathbf{x}_T, t) .

The Radon transform or *slant stack* is defined as

$$\check{u}(\mathbf{p}_T, \tau) = \int_{\mathbf{x}_T \in \mathbb{R}^2} u(\mathbf{x}_T, \tau + \mathbf{p}_T \cdot \mathbf{x}_T) d\mathbf{x}_T. \quad (2.20)$$

When we take the Fourier transformation with respect to the intercept time τ , Eq. (2.20), changes into

$$\widehat{\check{u}}(\mathbf{p}_T, \omega) = \int_{\tau \in \mathbb{R}} \exp(-i\omega\tau) \check{u}(\mathbf{p}_T, \tau) d\tau. \quad (2.21)$$

When we substitute the integral in Eq. (2.20) into Eq. (2.21), we can rewrite the Fourier transform to

$$\widehat{\check{u}}(\mathbf{p}_T, \omega) = \int_{\mathbf{x}_T \in \mathbb{R}^2} \exp(i\omega\mathbf{p}_T \cdot \mathbf{x}_T) \widehat{u}(\mathbf{x}_T, \omega) d\mathbf{x}_T. \quad (2.22)$$

in which we changed the order of integration and used the fact that the time-delay in Eq. (2.20) can be written as the exponential $\exp(i\omega\mathbf{p}_T \cdot \mathbf{x}_T)$ in the Fourier domain. Equation (2.22) is a Fourier transformation of the function $u(\mathbf{x}_T, \omega)$ over the spatial coordinates $\{x_1, x_2\}$. The relation between the wavenumber vector \mathbf{k}_T and the slowness vector \mathbf{p}_T is given by

$$\mathbf{k}_T = \omega\mathbf{p}_T. \quad (2.23)$$

The relation between angle vector α_T and the wavenumber vector k_T is given by

$$\tan(\alpha_T) = \frac{k_T}{\omega}. \quad (2.24)$$

The above relation describes an important relation in the context of the geometry information in time-migrated seismic images. The algorithms in this thesis make use of the relations between geometry in space and in the Fourier domain. The algorithms are designed as if operating in space, however they are also applicable on spatio-temporal images. Equation (2.24) illustrates the difference of geometric interpretation. In a three-dimensional spatial volume, ω in the right term of the expression in Eq. (2.24), would be replaced by k_3 . For interpretation of time-migrated seismic images it might be useful to illustrate the geometry in terms of the slowness instead of the angle. This can be implemented by simply computing the tangent of the angle vector.

Wavelets and Filter Banks

From the previous chapter we have seen that we can transform seismic data to different domains. The Fourier transformation and the Radon transformation together hand us an accurate combination to characterize seismic images in terms of geometry and frequency. However, due to the nature of the basis functions, these operators act globally on the signal and will not provide us local information.

The Fourier transformation gives us the opportunity to work on the frequencies in the signal and thus to filter the signal on the basis of its frequency characteristics. The Fourier transformation does not enable us to see what frequency information is localized at which location in time. To overcome this problem, scientists have come up with different time-frequency techniques such as the short-time Fourier transform and the Wigner distribution (Baraniuk and Jones, 1993; Cohen, 1995; Steeghs, 1997). Most of these techniques are well-suited for analysis, but are not fit for processing, because of their redundancy and their computational inefficiency.

The wavelet transformation is a relatively new transformation that localizes information in time as well as in frequency and that gives us the opportunity for analysis *and* processing. The wavelet transformation quickly gained popularity since its invention in the mid 1980s by the geophysicist Morlet (1983). In his search for finer resolution of seismic images, he ex-

explored the space between time and frequency. Morlet stated that due the Heisenberg uncertainty principle, a signal cannot be represented in exact time and exact frequency together. However one can find a certain time-interval at which a certain band of frequencies exist. He discussed this issue with Grossmann and they were the first to define (complex) wavelets and used these for geophysical purposes (Grossman and Morlet, 1984). The idea was further explored by Meyer (1985-1986) and Daubechies (1988). The idea of wavelets was linked to the concept of multiresolution and filter banks by Mallat (1989). Daubechies (1992), Meyer (1990) and Vetterli (1992) have had considerable contributions to the development and polishing of the wavelet transforms and filterbanks to what they currently are. The wavelet transform has many different areas of applications varying from digital signal analysis and processing to image processing, Magnetic Resonance Imaging (MRI), optics, speech and data modeling. Today wavelets have gained renewed interest for seismic processing applications.

Because the wavelet transformation uses short-duration basis functions or *wavelets* to span the signal, the wavelet transform is very suitable for local operations on signals. The choice of the wavelet influences the coefficients of the transform and their localization in time and frequency.

Wavelet transformations can be classified in three categories, the continuous wavelet transformation for continuous signals and with continuous scale, the discrete wavelet transformation for continuous signals with discrete scale and the fast discrete wavelet transformation for discrete signals and discrete scale. The latter two transforms can be related to the concept of *multiresolution* (Burrus *et al.*, 1998; Mallat, 1998). Although the continuous wavelet transform has shown to be a valuable tool especially for log analysis and small-scale seismic applications (Herrmann and Stark, 1999; Verhelst, 2000; Goudswaard, 2001), the transform has several disadvantages which make it less attractive for large-scale applications: computational inefficiency, extensive data increase and no perfect reconstruction properties. The discrete wavelet transform (DWT) has most of the beneficial properties of the continuous wavelet transform, but is much better suited to handle large amounts of data. For this reason, the wavelet theory discussed in this thesis pertains to the *discrete* wavelet transformation, since the seismic signal is discretely sampled during measurement.

The wavelet coefficients at different scales of the transform are related to each other through filters. Each class of wavelets uniquely corresponds to a finite-impulse response filter (FIR). The coefficients of the wavelet transform

can be simply computed by consecutive convolution with these filters. The filters which link the different subbands in a wavelet transform consist of an analysis and a synthesis part linked by sampling operators. Such a set of filters is called a *filter bank* (Vetterli, 1986; Vaidyanathan, 1993; Strang and Nguyen, 1996).

Filter banks provide us with a solid basis for the design of wavelets and wavelet transforms. One of the most important constraints for data processing is the perfect reconstruction condition. We show that a wavelet transform can be obtained by the recursive convolution with filter banks. The recursion can be applied in many different ways, called wavelet packets. The most generally known way of recursion however results in the so-called *dyadic* discrete wavelet transform (DWT) that satisfies the natural scaling condition.

3.1 Wavelets and wavelet expansions

As we have mentioned, the discrete wavelet transform can be categorized according to three different transformations. We only address the discrete wavelet transformation, because of the discrete character of the seismic signal and the massive amounts of data we analyze. We will discuss the discrete wavelet transform for continuous signals in this section, which will be subsequently linked to the fast discrete wavelet transform and filter banks in the next section. We start with the introduction of the notion scale and the scaling functions that can be used to describe scale. We show that the different scale spaces are inter-related by filters. The wavelets are introduced as the functions that span the space between two scales. These spaces are also related to the scale spaces through filters. In the last section we show how we can write a signal in terms of a linear combination of a scaling function and a set of wavelets. When we put strong conditions on the design of wavelets and scaling function, the signal can be reconstructed perfectly.

■ 3.1.1 Scale and scaling functions

For the derivation of the discrete wavelet transform, we first introduce the notion scale in continuous time. The scale of a signal is related to the resolution at which we study a signal. The finest scale of a signal is equal to the original signal, the coarsest scale is a constant value over the whole range of the signal. Knowledge on the consistency of signals over scale provides us additional information in a local sense. This knowledge of the signal connects to our seismic message and leads to the understanding of the geological

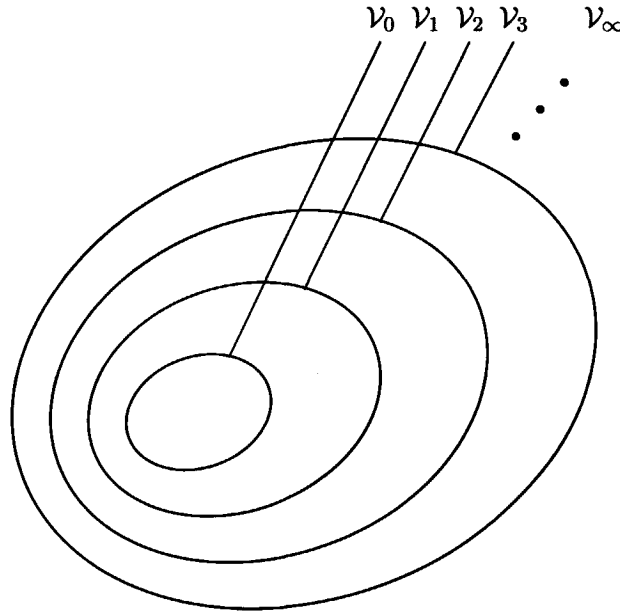


Figure 3.1: Domains $\mathcal{V}_0 - \mathcal{V}_3$ are spanned by the scaling functions

complexity. We use local operators for the definition of scale, because the scale is locally related to the signal.

We follow Heijmans (1993) in this section for the derivation of the discrete wavelet transform. First we introduce the scale within a multiresolution concept in Fig. 3.1. Suppose we can span a function $u_0(t) \in \mathcal{V}_0$ by a set of translations of a function $\varphi(t)$, according to

$$u_0(t) = \sum_{k=-\infty}^{\infty} a_k \varphi_k(t), \quad (3.1)$$

in which $\varphi_k(t)$ is given by

$$\varphi_k(t) = \varphi(t - k), \quad (3.2)$$

in which $k = k\Delta t$ and Δt is 1 unit of time. Note that two worlds melt together, continuous t and discrete k . Let us look at the Fourier transform of Eq. (3.1)

$$\hat{u}_0(\omega) = \hat{\varphi}(\omega) \sum_{k=-\infty}^{\infty} a_k \exp(-i\omega k). \quad (3.3)$$

When we notice that the second term resembles the discrete Fourier transform of a_k (Eq.2.5), this equation can be rewritten to,

$$\hat{u}_0(\omega) = \hat{\varphi}(\omega)A(\omega), \quad (3.4)$$

in which the term $A(\omega)$ is of the same form as the *discrete* Fourier transform of a_k

$$A(\omega) = \sum_{k=-\infty}^{\infty} a_k \exp(-i\omega k). \quad (3.5)$$

Now consider the deconvolution form

$$\frac{\hat{u}_0(\omega)}{\hat{\varphi}(\omega)} = A(\omega). \quad (3.6)$$

The Fourier transform of the original signal $u_0(t)$ deconvolved with the scaling function $\varphi(t)$ is decomposed into a discrete Fourier spectrum. This is possible for the regular functions we consider.

When we generalize Eq. (3.1) for basis functions $\varphi_{j,k}(t)$ spanning different \mathcal{V}_j , we obtain the following relation

$$u_j(t) = \sum_{k=-\infty}^{\infty} a_{j,k} \varphi_{j,k}(t), \quad (3.7)$$

in which the basis functions $\varphi_{j,k}(t)$ are given by

$$\varphi_{j,k}(t) = 2^{j/2} \varphi(2^j t - k). \quad (3.8)$$

The Fourier transform $\hat{u}_j(\omega)$ then becomes

$$\hat{u}_j(\omega) = \hat{\varphi}_j(\omega) \sum_{k=-\infty}^{\infty} a_{j,k} \exp\left(-i\frac{\omega}{2^j} k\right). \quad (3.9)$$

in which we have used the following definition of $\hat{\varphi}_j(\omega)$

$$\hat{\varphi}_j(\omega) = 2^{-j/2} \hat{\varphi}\left(\frac{\omega}{2^j}\right) \quad (3.10)$$

After deconvolution of $\hat{u}_j(\omega)$ with $\hat{\varphi}_j(\omega)$, we obtain the following relation

$$2^{-j/2} \frac{\hat{u}_j(\omega)}{\hat{\varphi}_j(\omega)} = A\left(\frac{\omega}{2^j}\right), \quad (3.11)$$

with

$$A\left(\frac{\omega}{2^j}\right) = \sum_{k=-\infty}^{\infty} a_{j,k} \exp\left(-i\frac{\omega}{2^j}k\right). \quad (3.12)$$

From this equation we can conclude that we have the function $\hat{u}_j(\omega) \in \mathcal{V}_j$ deconvolved with the basis function $\hat{\varphi}_j(\omega)$ spanning the subspace \mathcal{V}_j which has to be decomposed into a discrete Fourier spectrum.

When we consider the signal in its finest resolution and hence suppose $j \rightarrow \infty$, we see that the function $\hat{u}_j(\omega)$ converges to the signal provided that the basis function $\hat{\varphi}_j(\omega)$ converges to 1 for $j \rightarrow \infty$. This implies that the coefficients $A(\omega)$ are equal to the original signal $\hat{f}(\omega)$ at infinite resolution

$$\hat{u}_{j \rightarrow \infty}(\omega) = \hat{u}(\omega) \rightarrow A(\omega). \quad (3.13)$$

From Eq. (3.13) we can see that for infinite fine scale, the scaling function converges to 1. Since in reality we will never have a continuous signal, the function $\hat{\varphi}_{j,k}(\omega)$ will not converge to identity, but to an approximation. For the implementation of the wavelet transform with filter banks, however, the scaling function at the finest scale is often assumed to be equal to identity. This assumption is called the *wavelet crime* by Strang and Nguyen (1996). In their book they propose several ways to handle this problem correctly. The applications discussed in this thesis do not account for the wavelet crime.

The notion $\varphi(t)$ is complex in general. To decompose easier, we can choose the functions $\varphi(t)$ to be orthogonal so that the following constraint has to be met

$$\int_{-\infty}^{\infty} \varphi(t-k)\varphi^*(t-p)dt = \delta_{kp}. \quad (3.14)$$

Where the asterisk denotes complex conjugation. When we perform the Fourier transformation and apply Plancherel's theorem (Heijmans, 1993), this equation alters to

$$\int_{-\infty}^{\infty} \hat{\varphi}^*(\omega)\hat{\varphi}(\omega) \exp(i\omega(k-p))d\omega = \delta_{kp}. \quad (3.15)$$

We can rewrite this equation into the following integral

$$\int_{-\infty}^{\infty} |\hat{\varphi}(\omega)|^2 \exp(i\omega(k-p))d\omega = \delta_{kp}. \quad (3.16)$$

We can split the integral into a summation over integers and an integral with adjusted boundaries

$$\sum_{m=-\infty}^{\infty} \int_{-\pi+2m\pi}^{\pi+2m\pi} |\hat{\varphi}(\omega)|^2 \exp(i\omega(k-p))d\omega = \delta_{kp}, \quad (3.17)$$

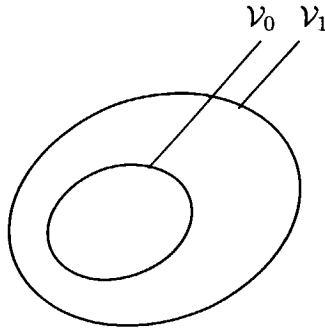


Figure 3.2: Domains \mathcal{V}_0 and \mathcal{V}_1 are spanned by scaling functions

into a periodic integral and a summation over k integers

$$\int_{-\pi}^{\pi} \exp(i\omega(k-p)) \sum_m |\hat{\varphi}(\omega + 2m\pi)|^2 d\omega = \delta_{kp}, \quad (3.18)$$

in which the summation adds to unity

$$\sum_m |\hat{\varphi}(\omega + 2m\pi)|^2 = 1. \quad (3.19)$$

This shows that orthogonal functions are very well fit for the decomposition and the subsequent reconstruction of a function that lives in a certain space. When we study the function at different resolutions according to Fig. 3.1, the basis function can be dilated to fit in the same space. The dilated version of the scaling function is directly related to its higher resolution equivalent. This is where filter banks come into play.

Let us consider the two spaces \mathcal{V}_0 and \mathcal{V}_1 in Fig. 3.2. These spaces are spanned by the scaling functions $\varphi_{0,k}(t)$ and $\varphi_{1,k}(t)$, respectively, in which $\varphi_{j,k}(t)$ is defined by Eq. (3.8). Functions in \mathcal{V}_0 can be written in terms of expansions of functions in \mathcal{V}_1 since $\mathcal{V}_0 \subset \mathcal{V}_1$. This means that the basis functions at different scales can be written as linear combinations of dilated versions of itself

$$\varphi(t) = \sum_{n=-\infty}^{\infty} h(n) \sqrt{2} \varphi(2t - n). \quad (3.20)$$

This expansion is known as the *dilation* equation. We take the Fourier transformation of Eq. (3.20),

$$\widehat{\varphi}(\omega) = \frac{1}{\sqrt{2}} \widehat{\varphi}\left(\frac{\omega}{2}\right) \sum_n h_n \exp\left(-i\frac{\omega}{2}n\right). \quad (3.21)$$

Note that the summation resembles the structure of the *discrete Fourier transform* of h_n . We can rewrite Eq. (3.21) as

$$\widehat{\varphi}(\omega) = H\left(\frac{\omega}{2}\right) \widehat{\varphi}\left(\frac{\omega}{2}\right), \quad (3.22)$$

with

$$H\left(\frac{\omega}{2}\right) = \frac{1}{\sqrt{2}} \sum_n h_n \exp\left(-i\frac{\omega}{2}n\right). \quad (3.23)$$

In which it is specifically noted that $H(\omega)$ is not the Fourier transform of h_n , but is equal to the filter defined above. When $\widehat{\varphi}(\omega)$ has a value at $\omega = 0$, we find the following restriction for $H(\omega)$

$$\widehat{\varphi}(0) \neq 0 \implies H(0) = 1. \quad (3.24)$$

For $\omega = 0$, the exponential in Eq. (3.23) equals unity, hence the sum over h_n needs to satisfy

$$\frac{1}{\sqrt{2}} \sum_n h_n = 1. \quad (3.25)$$

According to Eq. (3.23), $H(\omega)$ is given by

$$H(\omega) = \frac{1}{\sqrt{2}} \sum_n h_n \exp(-i\omega n). \quad (3.26)$$

To prove that $H(\omega)$ is 2π -periodic, we derive the expression for $H(\omega + 2\pi)$

$$\begin{aligned} H(\omega + 2\pi) &= \frac{1}{\sqrt{2}} \sum_n h_n \exp(-i(\omega + 2\pi)n), \\ &= \frac{1}{\sqrt{2}} \sum_n h_n \exp(-i(\omega)n), \\ &= H(\omega), \end{aligned} \quad (3.27)$$

which means that $H(\omega)$ is periodic with a periodicity of 2π . We refer to Eq. (3.19),

$$\sum_k |\widehat{\varphi}(\omega + k2\pi)|^2 = 1, \quad (3.28)$$

According to Heijmans (1993) we can use the property that $\hat{\varphi}(\omega)$ is orthonormal and write

$$\sum_k |\hat{\varphi}(2\omega + k2\pi)|^2 = 1. \quad (3.29)$$

When we combine this information with Eq. (3.22), we find the following derivation

$$1 = \sum_k |\hat{\varphi}(2\omega + k2\pi)|^2 = \sum_k |H(\omega + k\pi)|^2 |\hat{\varphi}(\omega + k\pi)|^2. \quad (3.30)$$

Since we have found in Eq. (3.27) that the filter $H(\omega)$ is 2π -periodic, we can rewrite Eq. (3.30) to

$$1 = |H(\omega)|^2 \sum_k |\hat{\varphi}(\omega + 2k\pi)|^2 + |H(\omega + \pi)|^2 \sum_k |\hat{\varphi}(\omega + \pi + 2k\pi)|^2. \quad (3.31)$$

This leads to the basic representation for the orthonormality of the filter, which is the basis of the filter bank approach of orthonormal wavelets treated in the next section,

$$|H(\omega)|^2 + |H(\omega + \pi)|^2 = 1, \quad (3.32)$$

which leads to the spectral factorization of $|H(\omega)|^2$ for the orthogonal analysis and reconstruction filters. For the next coarser resolution space we find the following relation

$$\hat{\varphi}(\omega) = H\left(\frac{\omega}{2}\right) H\left(\frac{\omega}{4}\right) \hat{\varphi}\left(\frac{\omega}{4}\right), \quad (3.33)$$

hence we obtain for K resolution the cumulative product of filter coefficients and the scaling function spanning the finest scale

$$\hat{\varphi}(\omega) = \prod_{k=1}^K H\left(\frac{\omega}{2^k}\right) \hat{\varphi}\left(\frac{\omega}{2^K}\right). \quad (3.34)$$

When taking $K \rightarrow \infty$

$$\hat{\varphi}(\omega) = \prod_{k=1}^{\infty} H\left(\frac{\omega}{2^k}\right) \hat{\varphi}(0), \quad (3.35)$$

in which the scaling function for an infinite fine scale converges to unity (remember wavelet crime), or

$$\hat{\varphi}(0) = 1. \quad (3.36)$$

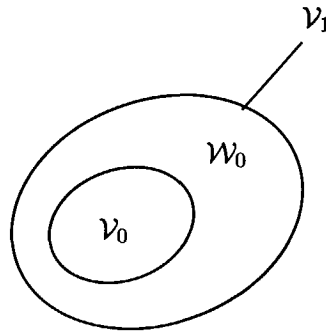


Figure 3.3: Domain \mathcal{W}_0 is spanned by a wavelet.

So far we have seen that we can decompose a function that lives in a domain \mathcal{V}_j by a set of orthogonal scaling functions. By choosing the right constraints on these scaling functions, we can design a filter with which we can adjust the basis function to span the space of a coarser scale. In the discrete wavelet transform we are able to invert for the latter by spanning the spaces *in between* two scales. The basis functions used for that purpose are called the *wavelets*.

■ 3.1.2 Wavelets from scaling functions

The scaling functions described in the previous section are useful for the description of functions at different levels of resolution. When we want to be able to go from one level to another we have to be able to span the space between these two. For that purpose we can use wavelets.

For the derivation of wavelets we make use of the fact that they span the difference space between two adjacent scales. First we consider the spaces $\mathcal{V}_0, \mathcal{V}_1$ and \mathcal{W}_0 in Fig. 3.3. In a mathematical formulation the spaces are related through

$$\mathcal{V}_1 = \mathcal{V}_0 \oplus \mathcal{W}_0, \quad (3.37)$$

in which \oplus means direct sum. Both 0-spaces are embedded in \mathcal{V}_1 , or $\mathcal{V}_0 \subset \mathcal{V}_1$ and $\mathcal{W}_0 \subset \mathcal{V}_1$. In the same way as for the scaling function in Eq. (3.1) we can span a function $f_0(t) \in \mathcal{W}_0$ as a set of translations of a wavelet $\psi(t)$,

according to

$$f_0(t) = \sum_{k=-\infty}^{\infty} b_k \psi_k(t) \quad (3.38)$$

and when we consider the function $f_j(t) \in \mathcal{W}_j$ which lives in an arbitrary detail space, we come to a more general formulation

$$f_j(t) = \sum_{k=-\infty}^{\infty} b_{j,k} \psi_{j,k}(t) \quad (3.39)$$

Since the general expression of wavelets $\psi_{j,k}(t)$ lives in the space \mathcal{V}_{j+1} they satisfy Eq. (3.8), and are hence given by

$$\psi_{j,k}(t) = 2^{j/2} \psi(2^j t - k). \quad (3.40)$$

When we consider Fig. 3.3, it also means that the wavelet $\psi(t)$ spanning \mathcal{W}_0 can be written in terms of expansions of the scaling functions spanning \mathcal{V}_1 , so

$$\begin{aligned} \psi(t) &= \sqrt{2} \sum_{n=-\infty}^{\infty} g_n \varphi(2t - n) \\ &= \sqrt{2} \sum_{n=-\infty}^{\infty} g_n \varphi_{1,n}(t). \end{aligned} \quad (3.41)$$

Wavelets are related to scaling functions through filters. This means that we are able to go step by step from a coarser to a finer scale by just adding a detail-space that is spanned by wavelets. This brings us to the wavelet transform that describes a function in terms of a coarse approximation with a summation of linear combinations of wavelets up to infinitely fine resolution.

■ 3.1.3 Wavelet transformation

The scaling function and the wavelets discussed in the previous sections provide us with an excellent way to decompose a signal into resolution subspaces. Because of the orthogonality of the wavelets and the scaling functions, the signal can be perfectly reconstructed with an inverse transform.

Let us write a function $u(t) \in \mathcal{V}_\infty$ as a summation of translations of the scaling function $\varphi(t)$ spanning the coarsest scale \mathcal{V}_0 and the wavelets spanning each additional detail space

$$u(t) = \sum_k a_k \varphi(t - k) + \sum_{j=0}^{\infty} \sum_k b_{j,k} 2^{j/2} \psi(2^j t - k). \quad (3.42)$$

When we assume that $\mathcal{V}_\infty \approx L^2$, this expression is the general expression for the *discrete wavelet transformation*. The coefficients a_k and $b_{j,k}$ in this wavelet expansion are called the discrete wavelet transform (DWT) of the signal. For orthogonal systems of wavelets, this means that these coefficients can be calculated by the inner products

$$a_k = \langle u(t), \varphi_k(t) \rangle = \int_{t \in \mathbb{R}} u(t) \varphi_k(t) dt, \quad (3.43)$$

and

$$b_{j,k} = \langle u(t), \psi_{j,k}(t) \rangle = \int_{t \in \mathbb{R}} u(t) \psi_{j,k}(t) dt. \quad (3.44)$$

In practice, the wavelet coefficients are not calculated through the wavelets and scaling functions, but with their corresponding filter coefficients h_n and g_n , which relate the scaling coefficients and wavelets at different scales according to Eqs. (3.20) and (3.41), respectively. This implementation is called the *filter bank* approach and will get more attention in the next section. For now we will derive the relationship between the filter coefficients themselves.

In the same way as for the scaling function in Eq. (3.22), we find the following relation for the Fourier transform of the wavelet $\widehat{\psi}(\omega)$ (Heijmans, 1993),

$$\begin{aligned} \widehat{\psi}(\omega) &= \frac{1}{\sqrt{2}} \widehat{\varphi}\left(\frac{\omega}{2}\right) \sum_n g_n \exp\left(-i\frac{\omega}{2}n\right), \\ &= G\left(\frac{\omega}{2}\right) \widehat{\varphi}\left(\frac{\omega}{2}\right), \end{aligned} \quad (3.45)$$

in which

$$G\left(\frac{\omega}{2}\right) = \frac{1}{\sqrt{2}} \sum_n g_n \exp\left(-i\frac{\omega}{2}n\right). \quad (3.46)$$

When we replace the scaling function $\widehat{\varphi}(\omega/2)$ using Eq. (3.35), we can write Eq. (3.45) as

$$\widehat{\psi}(\omega) = G\left(\frac{\omega}{2}\right) \prod_{k=2}^{\infty} H\left(\frac{\omega}{2^k}\right), \quad (3.47)$$

in terms of a cumulative product of consecutive filtering operations.

The term $G(\omega)$ can be expressed in terms of $H(\omega)$ by

$$G(\omega) = \exp(-i(\omega + \pi)) H^*(\omega + \pi). \quad (3.48)$$

In order to find an expression for g_k in terms of h_k we use the following derivation to find the expression for $H^*(\omega + \pi)$,

$$\begin{aligned} H(\omega) &= \frac{1}{\sqrt{2}} \sum_k h_k \exp(-ik\omega), \\ H(\omega + \pi) &= \frac{1}{\sqrt{2}} \sum_k h_k \exp(-ik(\omega + \pi)), \\ H^*(\omega + \pi) &= \frac{1}{\sqrt{2}} \sum_k h_k^* \exp(+ik(\omega + \pi)). \end{aligned} \quad (3.49)$$

Subsequently we multiply with the exponential in Eq. (3.48)

$$\exp(-i(\omega + \pi))H^*(\omega + \pi) = \frac{1}{\sqrt{2}} \sum_k h_k^* \exp(+i(k-1)(\omega + \pi)). \quad (3.50)$$

Now that we have found this expression we can change the variable k into a new variable n , with

$$k - 1 = -n, \quad (3.51)$$

and write $G(\omega)$ in terms of the coefficients of h_n

$$\begin{aligned} G(\omega) &= \frac{1}{\sqrt{2}} \sum_{n=-\infty}^{\infty} h_{-n+1}^* \exp(-in(\omega + \pi)), \\ &= \frac{1}{\sqrt{2}} \sum_{n=-\infty}^{\infty} h_{-n+1}^* (-1)^n \exp(-in\omega), \end{aligned} \quad (3.52)$$

which leads to the relation between h_n and g_n , viz.

$$g_n = (-1)^n h_{1-n}^*. \quad (3.53)$$

The wavelet transformation as discussed in Eq. (3.42) hands us an algorithm to decompose a signal into different scales using simple finite impulse response filters. Since we want to be able to reconstruct our original signal, we still have to find an inverse transformation. This quest has become straightforward since we have chosen to use orthogonal wavelets for the forward transformation.

■ 3.1.4 Inverse wavelet transformation

Because we imposed orthogonality conditions on the scaling functions and wavelets, the inverse wavelet transform can be found fairly straightforward.

Knowing the coefficients of the projections onto the subspaces \mathcal{V}_0 and \mathcal{W}_0 to be given by the Eqs. (3.43) and (3.44), respectively

$$a_{0,k} = \langle u, \varphi_{0,k} \rangle, \quad (3.54)$$

and

$$b_{0,k} = \langle u, \psi_{0,k} \rangle. \quad (3.55)$$

we can show that we can form the signal at a finer scale in \mathcal{V}_1 . A signal that lives in this particular space can be written as the linear combination

$$u_1(t) = \sum_k a_{1,k} \sqrt{2} \varphi_1(2t - k), \quad (3.56)$$

or in terms of the signal at a coarser scale and the signal in the detail space \mathcal{V}_0

$$u_1(t) = \sum_k a_{0,k} \varphi(t - k) + \sum_k b_{0,k} \psi(t - k). \quad (3.57)$$

We rewrite this equation using Eqs. (3.20) and (3.41) to

$$\begin{aligned} u_1(t) &= \sum_k a_{0,k} \sum_n h_n \sqrt{2} \varphi(2t - 2k - n) \\ &+ \sum_k b_{0,k} \sum_n g_n \sqrt{2} \varphi(2t - 2k - n). \end{aligned} \quad (3.58)$$

Because all of these functions are orthogonal, multiplying Eqs. (3.56) and (3.58) with the scaling function $\varphi(2^{j+1}t - k')$ and integrating, evaluates the coefficient as

$$a_{1,k} = \sum_m a_{0,m} h_{k-2m} + \sum_m b_{0,m} g_{k-2m}. \quad (3.59)$$

From this equation we can see that the reconstruction filters are the adjoints of the analysis filters. We can reconstruct each level of resolution up to the finest level, which returns the original signal at the finest resolution. So far we have discussed the discrete wavelet transform for continuous functions. In the next section we will introduce filter banks. Concatenation of these filter banks in a smart way leads to an approximation of the wavelet transform. Because of its computational efficiency this approximation is called the *fast* discrete wavelet transform.

3.2 Filter banks and multiresolution

In this section we will show that we can efficiently implement the discrete wavelet transformation using orthogonal filter banks. This approximation is known as the fast discrete wavelet transform. We will first introduce the concept of filter banks and show how they are related to the filters that we have seen to relate the different scales. Perfect reconstruction plays a critical role in the design of filter banks, because it allows for processing. In the second paragraph we will discuss a special kind of filter banks which leads to the Daubechies wavelets. Further on we will show how we can influence the amount of aliasing in the fast wavelet transform by the choice of filter.

■ 3.2.1 Discrete orthogonal filters

For the comparison of the filter banks with the discrete wavelet transformation, we will study the filters derived in the previous section more closely and show what alterations have to be made to obtain locally supported FIR filters.

In general the same relations apply for the filters introduced in the previous section when the wavelets have finite support. In the discussion, a finite set of filter coefficients c_0, \dots, c_N will be found when $\phi(t)$ is supported on the interval $[0, N]$ as opposed to the infinite extent discussed in the previous section. Due to this discretization, the relationship between the low- and highpass filter h_n and g_n changes to the following relation

$$g_n = (-1)^k h(N - n). \quad (3.60)$$

This solution is known as the alternating flip solution (Strang and Nguyen, 1996) that immediately follows from the orthogonality conditions on wavelets and filters. In z -domain, Eq. (3.60) becomes

$$G(z) = z^{-N} H(-z^{-1}). \quad (3.61)$$

In this section we consider real-valued coefficients and real-valued wavelets and scaling functions. In frequency, the orthogonality condition is given by Eq. (3.32), which changes for discretized frequency to

$$|H(\Omega)|^2 + |H(\Omega + \pi)|^2 = 1, \quad (3.62)$$

with the components $|H(\Omega)|^2$ and $|H(\Omega + \pi)|^2$. We will show how the same constraint can be derived for orthogonal filterbanks with perfect reconstruction. The quadratic filter $|H(\Omega)|^2$ in Eq. (3.62) is called a *halfband* filter (Strang and Nguyen, 1996).

■ 3.2.2 Filter banks

Filter banks are sets of filters connected through sampling operators. The first filter bank dates back to the beginning of the 20th century (Haar, 1910). Not until the 1980s, the Haar functions turned out to be the shortest orthogonal wavelets. One of the important aspects of filter banks is the perfect reconstruction property. The design of perfect reconstruction filter banks has had a tremendous amount of attention in the middle 1980s (Smith and Barnwell, 1986; Vaidyanathan, 1987; Vetterli, 1986).

Because filter banks split a signal into a set of signal components, they are very well fit for signal analysis. In the case that a filter bank simply splits the signal into a highpass and a lowpass version of the signal, iteration on the lowpass branch leads to a multiresolution representation of the signal. The concept of multiresolution is based on a chain of filter banks that iteratively filter the signal. The filters that are used, produce subspaces of L^2 , either containing smooth trend information on the signal or certain detail information of the signal. When we think of it in terms of resolution, we could say that a highpass filter keeps mainly detail information, whereas the smoothness is kept by the lowpass filter. Mallat (1989) showed that the multiresolution concept was related to the discrete wavelet transform and he came up with the *fast* discrete wavelet transform.

Down-sampling in time shows up as stretching in frequency. Suppose we have a filter h_n with its Fourier equivalent $H(\Omega)$. When we remove every other sample of the original function h_n , the frequency response becomes $|H(\Omega/2)|$. The problem however is that another term is introduced by down-sampling,

$$\mathcal{F}\{(\downarrow 2)h_n\} = \frac{1}{2} \left[H\left(\frac{\Omega}{2}\right) + H\left(\frac{\Omega}{2} + \pi\right) \right], \quad (3.63)$$

in which the first term on the right reproduces the desired original function at a lower scale, and the second term introduces an undesirable side effect called aliasing. Subsequent up-sampling by putting zeros in between the signal values returns the correct frequency range and leads to the following representation of the filter in frequency

$$\mathcal{F}\{(\uparrow 2)(\downarrow 2)h_n\} = \frac{1}{2} [H(\Omega) + H(\Omega + \pi)]. \quad (3.64)$$

This structure looks similar to Eq. (3.62), except for the squares.

Now consider the structure as given in Fig. 3.4. First we discuss the figure without the sampling operators. Perfect reconstruction of the signal allowing

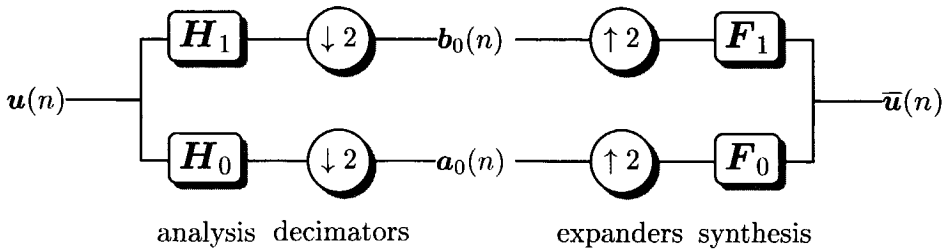


Figure 3.4: Analysis and synthesis filter banks

for a shift of l samples, would mean in the z -domain

$$F_0(z)H_0(z) + F_1(z)H_1(z) = z^{-l}. \quad (3.65)$$

Orthogonal filterbanks include sampling operators. The downsampling step stretches the frequency and introduces aliasing, subsequent upsampling brings back the former scale. Now suppose we downsample after the analysis operation and upsample before the synthesis filter, are we still able to extract the information that we want, canceling the induced aliasing, but remaining the summation of the halfbands? The relation after downsampling and upsampling according to the scheme in Fig. 3.4 becomes,

$$F_0(z)H_0(z)U(z) + F_0(z)H_0(-z)U(-z) + F_1(z)H_1(z)U(z) + F_1(z)H_1(-z)U(-z) = 2z^{-l}U(z), \quad (3.66)$$

or

$$[H_0(z) + H_0(-z)]F_0(z) + [H_1(z) + H_1(-z)]F_1(z) = 2z^{-l}, \quad (3.67)$$

in which $-z$ indicates a frequency-shift by π due to aliasing. This relation can be split into two fundamental equations,

$$H_0(z)F_0(z) + H_1(z)F_1(z) = 2z^{-l}, \quad (3.68)$$

which is *constructive*, and

$$H_0(-z)F_0(z) + H_1(-z)F_0(z) = 0, \quad (3.69)$$

which is *destructive*, because Eq. (3.69) represents the handling of the aliasing terms. Note that in Eq. (3.68), a factor of 2 appears due to the downsampling and up-sampling operations. To compensate for losing half of the

components due to the down-sampling operation, we can normalize the signal after the operation by $\sqrt{2}$. This normalization can be included in the filters and therefore we introduce the following set of analysis filters

$$H(z) = \sqrt{2}H_0(z), \quad (3.70)$$

and

$$G(z) = \sqrt{2}H_1(z). \quad (3.71)$$

For the special case that $H(z)$ is chosen to be a lowpass subband filter and $G(z)$ is chosen to be its complementary highpass, these are the filter coefficients of the wavelet transform, that connect the different multiresolution spaces (Eqs. (3.22) and (3.45))!

The Eqs. (3.68) and (3.69) are the fundamental equations behind the two-channel filter banks, which invoke perfect reconstruction. They are also used for wavelet design. An obvious solution can be found by determining some of the filters from others for instance by choosing

$$F_0(z) = H_1(-z), \quad (3.72)$$

and

$$F_1(z) = -H_0(-z). \quad (3.73)$$

The choice for orthogonality of the filters, restrains the system strongly and only few solutions are possible. The most widely used solution under orthonormality conditions and that allows for *FIR* filters is the alternating flip solution as mentioned in Eq. (3.60) in which we choose for $H_1(z)$ the following representation,

$$H_1(z) = z^{-N}H_0(-z^{-1}). \quad (3.74)$$

The synthesis filter $F_0(z)$ becomes in terms of $H_0(z)$

$$F_0(z) = z^{-N}H_0(z^{-1}). \quad (3.75)$$

The filter $F_1(z)$ is immediately determined by Eq. (3.73)

Now we define the product filter $P_0(z)$ by

$$P_0(z) = F_0(z)H_0(z) = z^{-N}H_0(z^{-1})H_0(z), \quad (3.76)$$

and $P_1(z)$ by

$$P_1(z) = F_1(z)H_1(z) = -z^{-N}H_0(-z^{-1})H_0(-z) = -P_0(-z). \quad (3.77)$$

The reconstruction in Eq. (3.66) in terms of $P_0(z)$ becomes

$$P_0(z) - P_0(-z) = 2z^{-l}. \quad (3.78)$$

Multiplying both sides with $z^l = z^N$ to center the filters, and choosing a normalized product filter $P(z)$, changes Eq. (3.78) to

$$P(z) + P(-z) = 2, \quad (3.79)$$

with

$$P(z) = H_0(z^{-1})H_0(z). \quad (3.80)$$

The analysis and reconstruction filters are the spectral factors of the halfband filter $P(z)$. After the normalization of the filters according to Eqs. (3.70) and (3.71), the sum adds to unity

$$H(z^{-1})H(z) + G(-z^{-1})G(-z) = 1. \quad (3.81)$$

Now we come to finalize what we intended to do. When we compare the relation in Eq. (3.32) with the relation in Eq. (3.81), we can observe that the filter coefficients in the wavelet transform are identical to those found through the orthogonal filter banks with perfect reconstruction.

■ 3.2.3 Daubechies wavelets

An outstanding family of orthogonal filters are the Daubechies filters. The respective wavelets can be designed on the basis of the properties of the FIR filters. These filters are known as maxflat filters, which means that their frequency responses have maximum flatness at $\Omega = \pi$. The resulting FIR filters are the shortest possible polynomial approximations of ideal brick-wall filters, given the filterlength.

Maximum flatness is implemented by the number of zeros of the filter $P(\Omega)$ in Eq. (3.80) at $\Omega = \pi$. This number of vanishing moments or derivatives at $\Omega = \pi$ gives the number of polynomials contributing to the filter. They are a measure for the flatness or the smoothness of the filter in the Fourier domain. For extensive reading on the design and theory behind Daubechies wavelets we refer to Daubechies (1992).

In Fig. 3.5 (a) we show the Fourier response of the Daubechies-4 filters. the number 4 is related to the length of the filter and inherently to the number of vanishing moments, which is 2 for the Daubechies-4 filter. In the figure, the Fourier response of the lowpass filter is indicated with $|H(\omega)|^2$, and

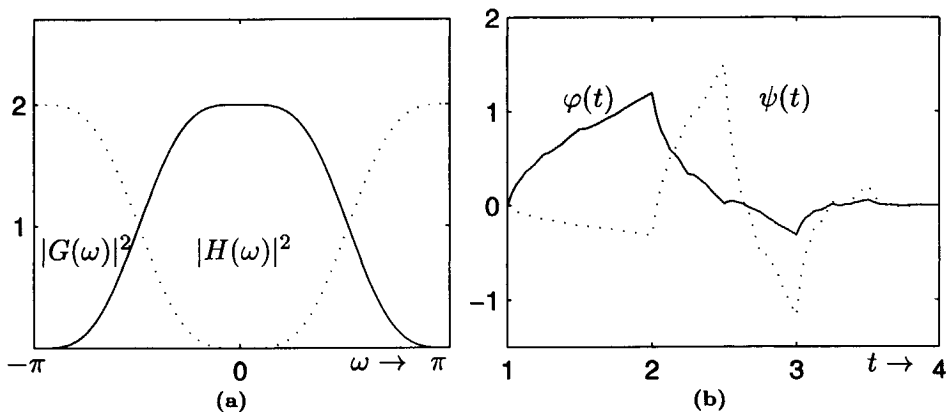


Figure 3.5: (a) The Fourier of the response of the Daubechies-4 lowpass $|H(\omega)|^2$ and highpass filters $|G(\omega)|^2$. (b) The amplitude responses of the scaling function $\varphi(t)$ and the wavelet $\psi(t)$.

the response of the highpass filter by $|G(\omega)|^2$. The wavelet and the scaling function that are related to the Fourier responses are depicted in Fig. 3.5 (b).

As we have seen, the analysis filters h_n and g_n form the linkage between the coefficients in the different scales. The lowpass filter or *average* filter h_n is used for the iteration, and the highpass filter g_n gives the *detail*. When the filters h_n and g_n are part of an orthonormal system, the system is heavily constrained (Strang and Nguyen, 1996). Once h_n is chosen, the other three filters are automatically determined for orthonormal filter banks. The filter h_n is the spectral factor of a halfband filter $p(n)$, with the z-domain equivalent given by Eq. (3.80). We can choose the desired properties of the filter h_n by putting constraints on the design of the halfband filter $P(z)$. In the case of the Daubechies filter, the halfband filter is designed in such a way that the flatness of the frequency response is maximal for the length of the filter. The product filter $P(z)$ in Eq. (3.80) is given for the Daubechies case by the following relation (Daubechies, 1988)

$$\begin{aligned}
 P(z) &= 2 \left(\frac{1+z}{2} \right)^p \left(\frac{1+z^{-1}}{2} \right) \\
 &\times \sum_{k=0}^{p-1} \binom{p+k-1}{k} \left(\frac{1-z}{2} \right)^k \left(\frac{1-z^{-1}}{2} \right)^k.
 \end{aligned} \tag{3.82}$$

with $z = \exp(i\omega)$ and p is the number which determines the zeros at $\omega = \pi$. From this equation we can see that we can choose the number of roots at $z = 1$ and $z = -1$. By choosing this number we can determine the steepness of the descent of the function. The more roots at $\omega = \pi$ we choose, the flatter the frequency response of the filter and the smoother the filters look in time. These filters have been described extensively in literature (Daubechies, 1992; Strang and Nguyen, 1996; Vetterli and Kovačević, 1995; Burrus *et al.*, 1998).

The filter $H(z)$ is a spectral factor of $P(z)$, $H(z^{-1})$ being its adjoint for reconstruction. Their time-domain equivalents each contain half the number of polynomials present in $P(z)$. This means that a Daubechies-4 filter is length 4 and has 2 vanishing moments, which is equal to quadratic approximation.

3.3 Cascading filter banks.

We have seen in the previous sections that the filters of the perfect reconstruction two-channel filter banks are identical to those in the discrete wavelet transform. Mallat (1989) showed that these filters can be used for the fast implementation of discrete the wavelet transform. In this section we address the subject of cascading the filter banks very briefly.

■ 3.3.1 Average with $H(\Omega)$.

The scale spaces V_j that are spanned by the scaling functions $\phi_{j,k}(t)$ are directly related by filters as we have seen in the dilation equation, Eq. (3.34). In order to move between the spaces we can simply apply the right filters to go to finer or coarser scales. This concept fits very well in a tree structure; From Eq. (3.63) we know that the frequency stretches when we down-sample a signal. The so-obtained signal can be used as an input for the next iteration. In a mathematical formulation in frequency these consecutive steps mean for a discrete input signal $u(n)$,

$$\mathcal{F}\{h(n) * u_0(n)\} = H(\Omega) U_0(\Omega), \quad (3.83)$$

which results in a smooth approximation of the signal $u(n)$. Subsequently the signal is down-sampled by two,

$$\begin{aligned} \mathcal{F}\{(\downarrow 2)h(n) * u_0(n)\} &= U_1(\Omega) \\ &= \frac{1}{2} \left[H\left(\frac{\Omega}{2}\right) U_0\left(\frac{\Omega}{2}\right) + H\left(\frac{\Omega}{2} + \pi\right) U_0\left(\frac{\Omega}{2} + \pi\right) \right]. \end{aligned} \quad (3.84)$$

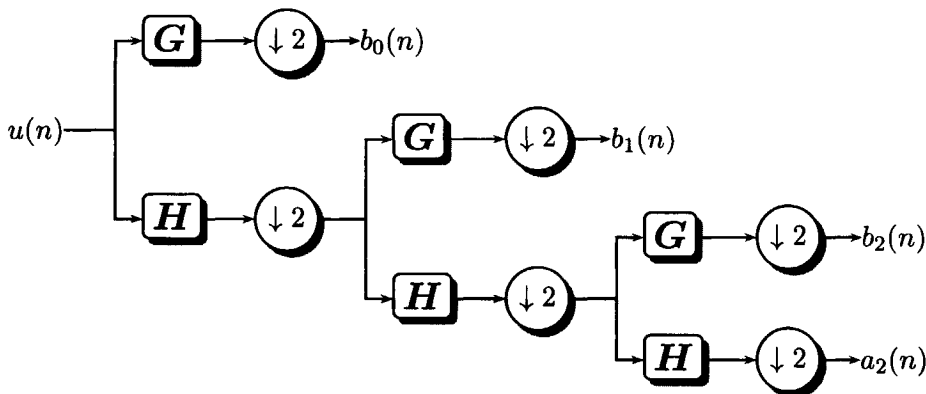


Figure 3.6: Analysis filter bank tree of $u(n)$ obtained by cascading low- and highpass filters. The outputs $b_0 - b_2$ are the wavelet- and a_2 the scaling coefficients.

Note that in this step, aliasing terms are introduced due to the lower sampling rate in $u_1(n)$. We do not care for these terms, since we know from the previous section in Eq. (3.69) that in the reconstruction only the *constructive* terms are taken into account whereas the *destructive* aliasing terms are cancelling out. However it is important to keep in mind that these terms are included in each iteration step and are thus present in the transform. The number of vanishing moments influences the amplitude of these general low energetic aliasing terms. Especially for reconstruction of isolated subbands, the aliasing terms play an important role.

The signal $u_1(n)$, resulting from the first iteration, is used as the input for the next filtering iteration, resulting in

$$\mathcal{F}\{h(n) * (\downarrow 2)h(n) * u_0(n)\} = U_2(\Omega) = H(\Omega)U_1(\Omega), \quad (3.85)$$

which can be repeatedly implemented. When we look at Eq. (3.85) we see that repeated application can be written as a cumulative inner product of the filters including the low amplitude "folding" terms (which are suppressed in the inverse transform),

$$U_K(\Omega) = \prod_{j=1}^K H\left(\frac{\Omega}{2^j}\right) U_0\left(\frac{\Omega}{2^K}\right) + \text{folding terms}. \quad (3.86)$$

When we compare the structure in Eq. (3.86) and compare this with the structure in Eq. (3.34), we immediately see a large coherence between the two equations.

When we assume that $u_K(n)$ is spanned by the scaling function $\phi_K(t)$, which is true for any $u(n) \in L^2$ when $K \rightarrow \infty$ $u_K(n)$ converges to $u(n)$ according to Eq. (3.36). This means that the K^{th} consecutive iteration on the lowpass branch of the filter bank results in a fully downsampled representation a_K of $u(n)$ at scale K and low energetic *folding terms*.

From Eq. (3.86) it follows that the product $H(\Omega)H(2\Omega)H(4\Omega)$ plays an important role. Figure 3.7 shows what this product looks like for the Daubechies-4 filter and the Daubechies-16 filter and what the separate filters look like. It is clear from this picture that the vanishing moments play an important role in the leakage of the aliasing terms into the signal; the energy of the aliasing terms in the transform is much higher for the Daubechies-4

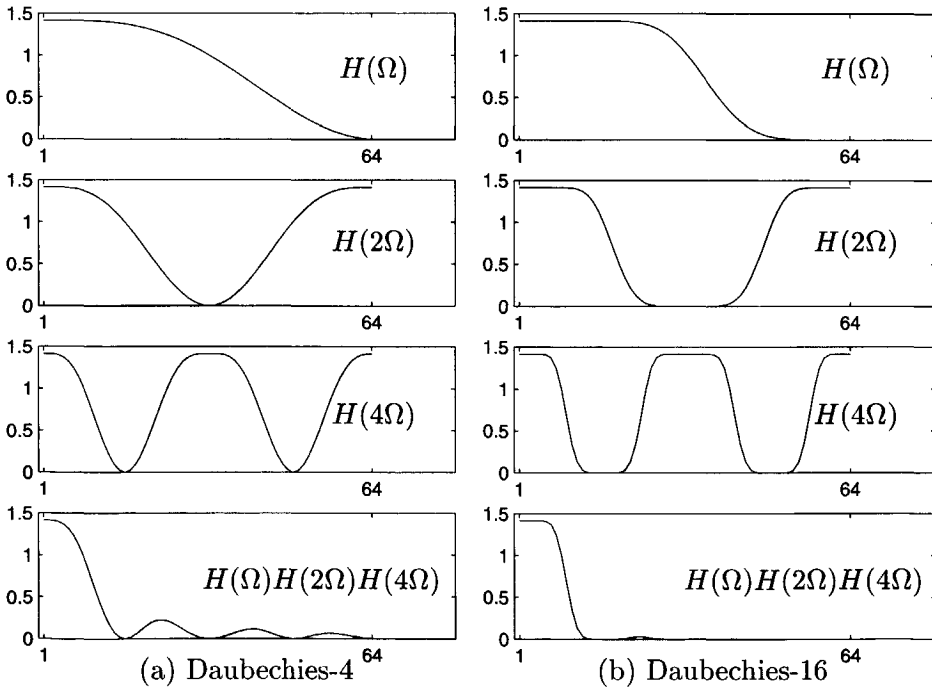


Figure 3.7: The Fourier magnitude responses of consecutive filtering for (a) Daubechies-4 and (b) Daubechies-16.

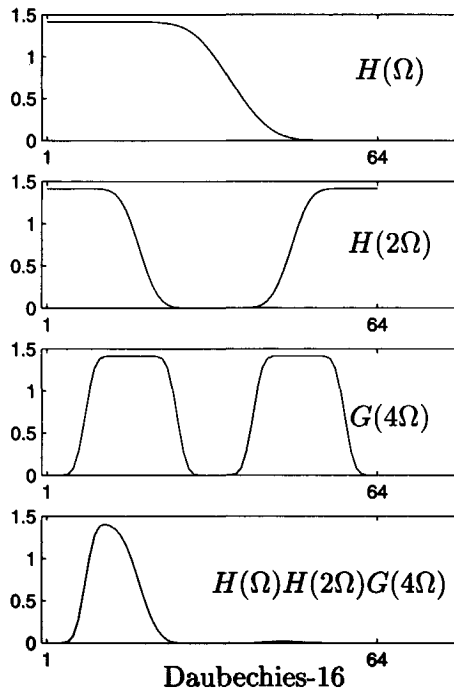


Figure 3.8: Magnitude response of consecutive filtering for the Daubechies-16 wavelet.

filter than for the Daubechies-16 filter. For reconstruction with orthogonal filter banks aliasing cancels.

■ 3.3.2 Detail with $G(\Omega)$.

The same reasoning as above can be followed for spaces spanned by the wavelets $\psi_{j,k}(t)$. These detail spaces can be calculated using the highpass filters $G(\Omega)$. These spaces, which give the detail at a certain scale, are also related to the scale spaces spanned by $H(\Omega)$ in the previous section.

From Eq. (3.45) we know that we can calculate the detail space spanned by a wavelet $\psi(\omega)$ at a certain scale by the inner product of the encompassing scaling function $\hat{\phi}(\omega/2)$ with the filter $G(\omega/2)$. For the discretized filters we combine this information with the formulation in Eq. (3.47), which leads to

the following representation for $U_{\Delta K}(\Omega)$

$$U_{\Delta K}(\Omega) = G\left(\frac{\Omega}{2}\right) \prod_{j=2}^{\infty} H\left(\frac{\Omega}{2^j}\right) U_0\left(\frac{\Omega}{2^K}\right) + \text{folding terms}. \quad (3.87)$$

Figure 3.8 shows the response of the filter $H(\Omega)H(2\Omega)G(4\Omega)$, the highpass counterpart of the Daubechies-16 variant in Fig. 3.7.

■ 3.3.3 Reconstruction wavelet tree

For the reconstruction of the wavelet transform, we can use the inverse wavelet tree as shown in Fig. 3.9. Each of the branches gives the inverse for its analysis counterpart in Fig. 3.6. The inverse of the down-sampling operation is performed by up-sampling, the inverse of the filtering operation is obtained by filtering with the adjoint filters. Due to the perfect reconstruction constraint in Eq. (3.68) we certify that the correct signal information constructively adds together to form the reconstructed input signal $\bar{u}(n)$. Equation (3.69) certifies that the aliasing terms or folding terms in Eqs. (3.86) and (3.87) cancel each other.

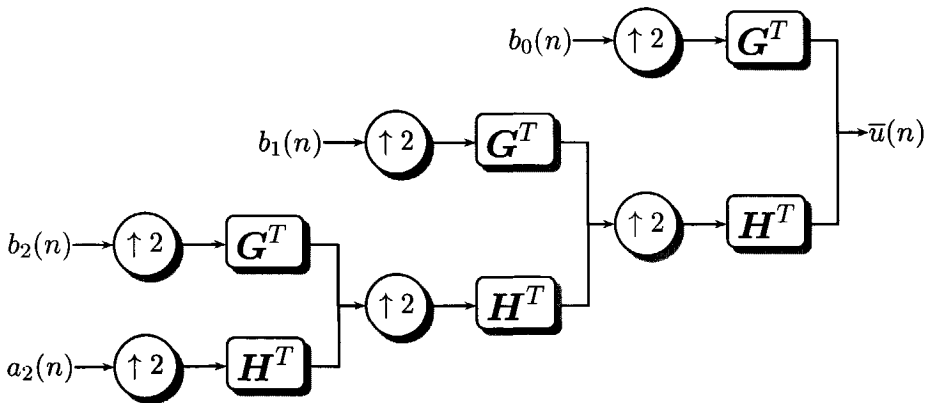


Figure 3.9: Reconstruction filter bank tree with coefficients as input and with output $\bar{u}(n)$.

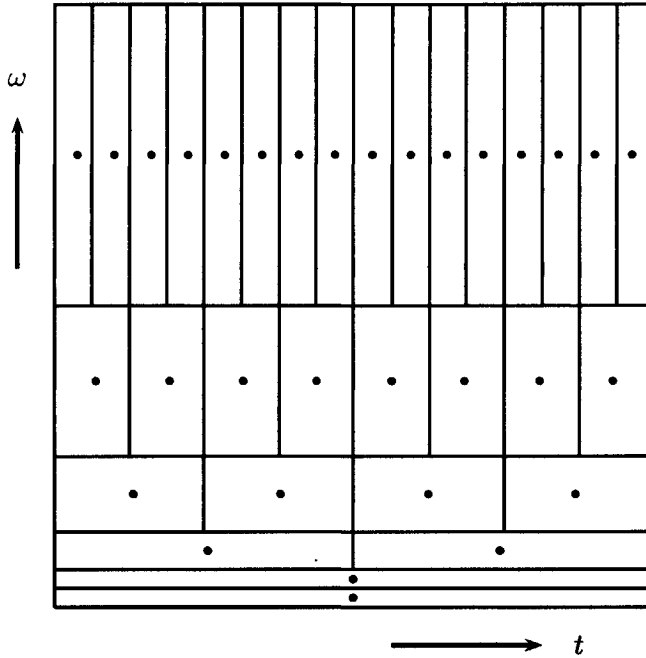


Figure 3.10: Tiling of dyadic wavelet transform coefficients

3.4 Tiling and Fourier partitioning.

As we have seen, within a critically sampled framework, the number of wavelet coefficients decreases for coarser scales (see Fig. 3.6). From the point of view of multiresolution, this makes sense. At finer scales more samples are needed to describe the fine-scale information than at coarser scales. Organizing the wavelet coefficients according to their scale is generally called the *tiling* of the wavelet transform. In Fig. 3.10 the tiling is shown of the discrete wavelet transform. The horizontal axis represents time-sampling, the vertical axis shows frequency sampling. From the Figure, we can conclude the following: A sample in the high frequency zone indicates a broad band of frequencies, but is very well localized along the time-axis. A sample at low frequencies has a very bad localization along the temporal axis, but only

covers a very small low frequency-band.

3.5 Multi-dimensional wavelet transform

Seismic data has a multi-dimensional character. In seismic interpretation we use images or volumes of data. For most seismic applications it is of vital importance to use a transformation that can be extended to more than one dimension without excessively increasing the amount of data. The wavelet transformation can be extended to more dimensions. There are however multiple ways to extend the wavelet transform to more dimensions. These can be classified in two basic categories, the *separable* transforms and the *non-separable* transforms. The first type of transformation is computationally very efficient and has a straightforward implementation. This type of transform will get ample attention in this chapter and is also used in combination with complex wavelets in Chapter 5. The separable transform refers to the separable application of one-dimensional filters (mostly FIR) in the horizontal and vertical directions. Transformations of the second kind, the non-separable transforms are the transformations that need the use of pure multi-dimensional filters applied in multi-dimensional convolutions. A transform that belongs to this category is the Steerable Pyramid representation (Freeman and Adelson, 1991; Simoncelli *et al.*, 1992; Karasarisidis and Simoncelli, 1996). In the past we have employed this representation for attribute analysis (van Spaendonck and Baraniuk, 1999; Hindriks *et al.*, 2000).

In this chapter we address the conventional separable two- and three-dimensional wavelet transforms and their important properties such as the tiling of the transform, the Fourier partitioning of the filters, and the directional information they carry.

■ 3.5.1 Two-dimensional separable wavelet transform

The conventional two-dimensional wavelet transformation is a separable wavelet transformation in which the filters are applied separately on the rows and on the columns at each scale. The resulting transform is very much like the one-dimensional wavelet transform in which each subband adds finer detail to the image. The two-dimensional scaling function $\Phi(x, y)$ is separable if

$$\Phi(x, y) = \varphi_1(x)\varphi_2(y). \quad (3.88)$$

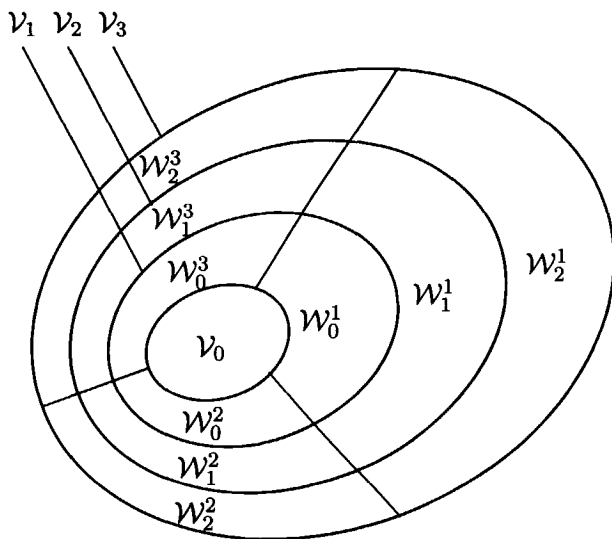


Figure 3.11: The resolution bands spanned by the 2-D wavelets are split into three sub regions.

The two-dimensional wavelet transformation can be written in the same kind of multi-resolution formulation as the one-dimensional transformation. The spaces spanned by the wavelets and the scaling functions are shown in Fig. 3.11. The spaces \mathcal{V}_j are the spaces spanned by the two-dimensional separable scaling function, the spaces \mathcal{W}_j^m are the spaces spanned by the wavelets. From the Figure we can see that the spaces spanned by the wavelets are split into three subspaces at each scale ($m = 1, 2, 3$).

The two-dimensional discrete wavelet transform of an image $U(x_1, x_2)$ is given by

$$\begin{aligned}
 U(x_1, x_2) &= \sum_l \sum_k e(k, l) \Phi(x_1, x_2, k, l) + \sum_l \sum_k \sum_{j=0}^{\infty} [f_j(k, l) \Psi_j^1(x_1, x_2, k, l) \\
 &\quad + g_j(k, l) \Psi_j^2(x_1, x_2, k, l) + h_j(k, l) \Psi_j^3(x_1, x_2, k, l)],
 \end{aligned} \tag{3.89}$$

in which the separable functions Φ and Ψ_j^m span the spaces \mathcal{V}_0 and \mathcal{W}_j^m ,

respectively in Fig. 3.11. They are given by the inner products of their one-dimensional equivalents

$$\Phi(x_1, x_2, k, l) = \varphi(x_1, k)\varphi(x_2, l), \tag{3.90}$$

$$\Psi_j^1(x_1, x_2, k, l) = \psi_j(x_1, k)\varphi_{j+1}(x_2, l), \tag{3.91}$$

$$\Psi_j^2(x_1, x_2, k, l) = \varphi_{j+1}(x_1, k)\psi_j(x_2, l), \tag{3.92}$$

$$\Psi_j^3(x_1, x_2, k, l) = \psi_j(x_1, k)\psi_j(x_2, l). \tag{3.93}$$

In the expansion in Eq. (3.89), the first summation gives a function that is a low resolution or smoothed version of $U(x_1, x_2)$; For each increasing index k in the following summations, a finer resolution is added, which contains increasing detail. The coefficients e, f_j, g_j and h_j are called the two-dimensional discrete wavelet transform. If the wavelet system is orthogonal, these coefficients can be computed in the same way as for the one-dimensional

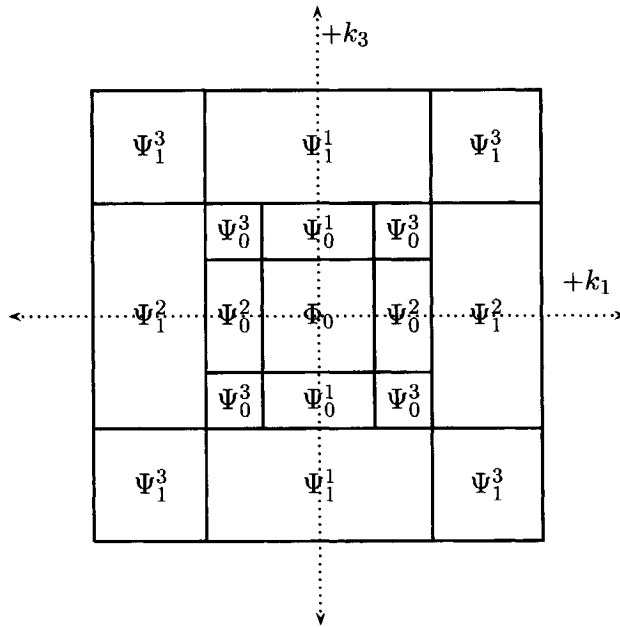


Figure 3.12: Frequency-domain energy localization of tensor wavelets in a two-level 2-D DWT.

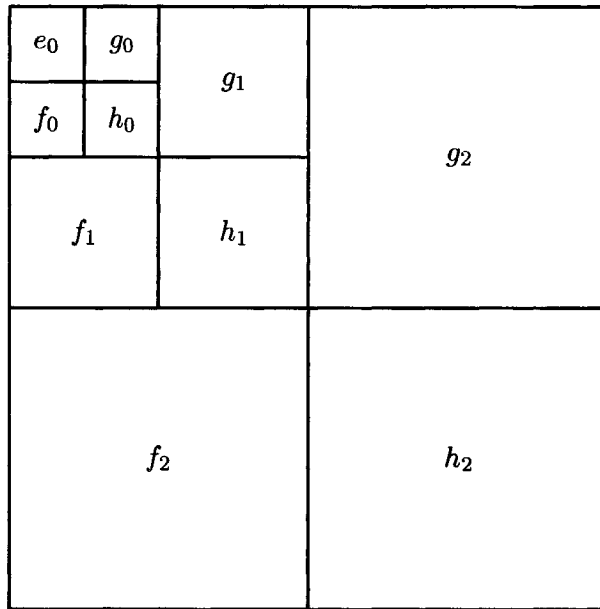


Figure 3.13: Tiling of the wavelet transform coefficients of the two-dimensional DWT.

wavelet transform, by calculating the inner products

$$e(k, l) = \langle U, \Phi(\cdot, \cdot, k, l) \rangle, \quad (3.94)$$

$$f_j(k, l) = \langle U, \Psi_j^1(\cdot, \cdot, k, l) \rangle, \quad (3.95)$$

$$g_j(k, l) = \langle U, \Psi_j^2(\cdot, \cdot, k, l) \rangle, \quad (3.96)$$

$$h_j(k, l) = \langle U, \Psi_j^3(\cdot, \cdot, k, l) \rangle. \quad (3.97)$$

Because the two-dimensional wavelets can be decomposed into one-dimensional wavelets, also the filters relating the wavelets at different scales are applicable for the two-dimensional case. The filter response of the ideal filters that are associated with the wavelets and scaling functions are shown in Fig. 3.12. The wavelets are used to indicate what frequencies their filters span.

From the Fourier domain, we observe that the coefficients have a poor directional support. The conventional wavelet transform has a poor *directional selectivity*, which means that it provides us hardly any directional information. In the Fourier domain, directional information is found in the angle around the zero-frequency. From the support in the Fourier domain of the different wavelets in Fig. 3.12, we can see that it is selective for horizontal, vertical and diagonal information. The coefficients related to the different quadrants in Fig. 3.12 can be organized in an efficient way, which immediately tells us which information is in which coefficient. The two-dimensional tiling that we use for that purpose is shown in Fig. 3.13.

The basis functions contributing to the different angles are shown in Fig. 3.14 for Daubechies-4 filters in each direction. In Fig. 3.15, we can see an example of the wavelet transform of a seismic image. In the left

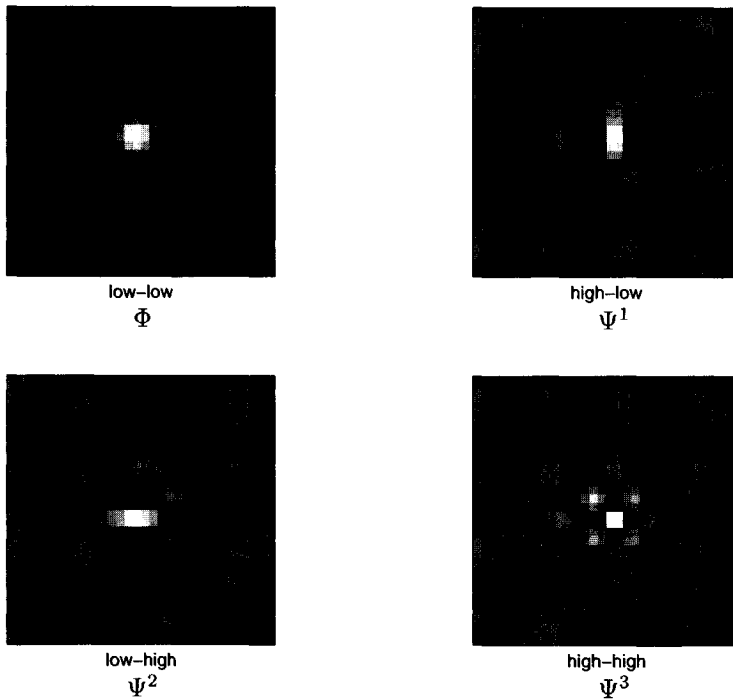


Figure 3.14: The basis functions spanning four different spaces. Low-low is the scaling function Φ , low-high, high-low and high-high are the wavelets, respectively Ψ^1 , Ψ^2 and Ψ^3 .

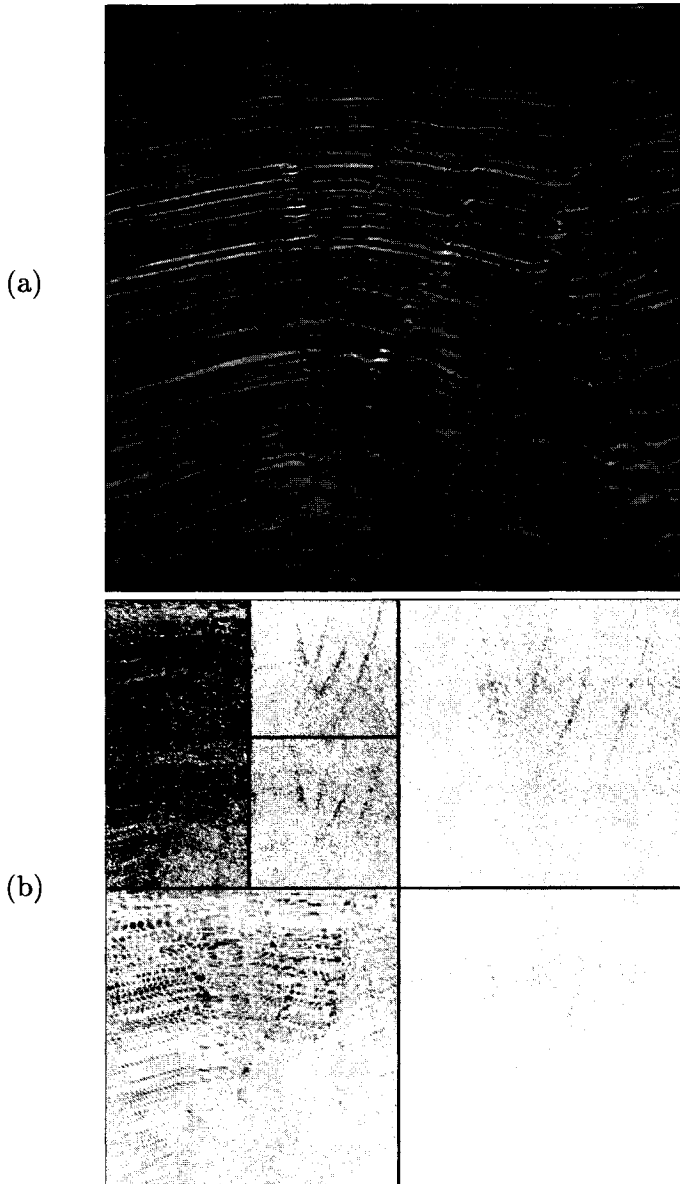


Figure 3.15: (a) Seismic section with faults, (b) Modulus of 2-D DWT with tiling shown in Fig. 3.13; Solely horizontal, vertical and diagonal information.

Figure, we show a part of a seismic section which contains several faults embedded in nearly horizontal reflectors. The right figure shows the envelope of the two-dimensional wavelet transform of the section. The close-to-vertical faults become visible in the upper two subbands that contain the coefficients g_1 and g_2 in Fig. 3.13. The horizontal reflections show up mainly in the left two subbands which are associated to f_1 and f_2 in the tiling figure (Fig. 3.13). No difference is made between the positive and negative angles. The faults which show up in both positive and negative direction show up in the same subbands.

■ 3.5.2 Three-dimensional separable wavelet transform

The extension from two to three dimensions is quite straightforward for separable wavelet transforms. For that reason we concisely discuss the subject. The most important issue is the frequency response of the filters.

It is important to know how the three-dimensional Fourier domain is split by the filters. In three dimensions, the separable wavelet transform separates the outer frequencies which are spanned by the wavelets into seven different subspaces as seen in Fig. 3.16 (opposed to three in the two-dimensional case). The Fourier domain is split in the same way as for the two-dimensional wavelet transform with one extra dimension. Only very little directional information is kept in each of the subbands. Later on, with the introduction of *complex* wavelets, we obtain a tremendous improvement of directional selectivity because we are then able to separate positive from negative frequencies and wavenumbers.

In the next chapter we will introduce the first step towards complex wavelet transforms, the local Hilbert transform. This transform uses local-support filters for the Hilbert transformation. In Chapter 5 and 6 the combination of this transform with the wavelet transformation yield the complex wavelet transforms which are directional selective and thus fit for attribute extraction.

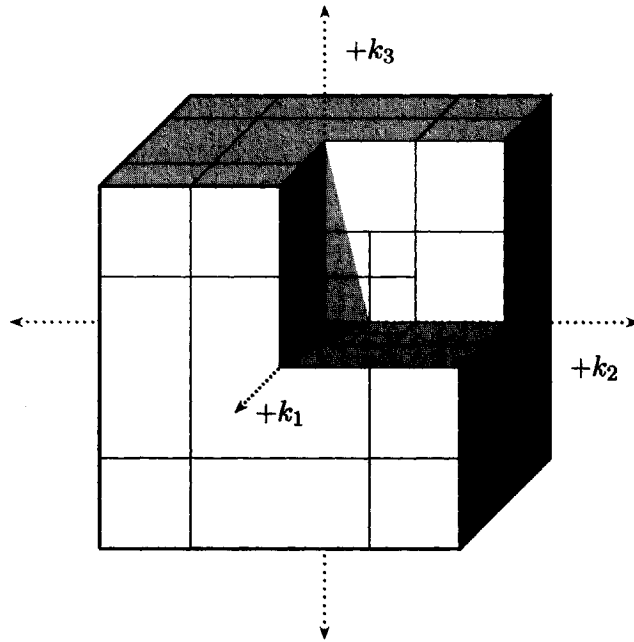


Figure 3.16: *Fourier-domain energy localization of tensor wavelets in a two-level 3-D DWT.*

Local Hilbert transformation

The analytic signal plays an important role in the characterization of signals (Bracewell, 1978; Cohen, 1995; Steeghs, 1997). For the computation of maxima, energies, envelopes, mean frequencies and other derivatives from the signal, the quadrature relationship between the real and imaginary part is an indispensable property.

Signal analysis and processing often requires complex signals consisting of an amplitude and a phase. In Chapter 2, we have introduced the Hilbert transformation, which uniquely calculates an imaginary signal from a real-valued signal. The analytic signal that can be obtained from the sum of the Hilbert transform with the real-valued signal, suppresses the negative frequencies and consists of an amplitude and a phase expression. From these quantities we can derive several important signal parameters such as instantaneous frequency and instantaneous bandwidth. The real part of the analytic signal is equal to the input signal. The additional imaginary part is in quadrature with the real-valued input signal. The analytic signal lives in a space called the Hardy space of functions that solely contains positive frequencies.

The traditional numerical implementation of the Hilbert transformation uses the fast Fourier transform (FFT). Zeroing out the negative Fourier coefficients and subsequently inverting the transform delivers a discrete approx-

imation of the analytic signal in which the imaginary part is equal to the Hilbert transform. The Fast Fourier transform has several draw-backs for this application. First, the Fourier transformation introduces artifacts due to its global character. The jump from negative to positive frequencies introduces ringing, as well as do the edges of the time-signal. These artifacts automatically extend to the quantities that can be derived from the analytic signal, such as instantaneous frequency. Second, the complete signal is needed for the operation, which makes the transform less attractive for *real-time* applications. In this chapter we introduce a new type of numerical implementation that is based on the principles of the wavelet transform. The short finite impulse response (FIR) filters which are used to relate the different scale spaces in the wavelet transform, can be modified in such a way that they relate a space of real-valued functions to a space of analytic functions. Because of the limited length of the filters, the operation becomes computationally extremely efficient and only has a local influence. Therefore it is fit for real-time performance and for non-stationary signals. The so-called *local* Hilbert transformation is very well-suited for combination with wavelets and wavelet transforms, due to their corresponding filter characters. These will be discussed in Chapter 5 and 6. In this chapter we will show that apart from the efficiency of the method, the accuracy of the calculated signal parameters, such as instantaneous phase and instantaneous frequency outperforms those calculated through the state-of-the-art existing methods. For seismic applications, these attributes are compared to the conventional complex seismic trace attributes. Furthermore we will show that also geometry related (volume) attributes can be calculated from this advanced transform, merited by the computational efficiency.

4.1 Discrete Hilbert transform

The analytic signal can be calculated in a simple way in the frequency domain, where the redundant information in the Fourier domain is eliminated from the transform. Suppression of the negative frequencies yields the analytic signal.

Since we work with finite length discrete signals, the Fourier transformation is commonly implemented as the Fast Fourier Transformation (FFT), which uses periodic basis functions—complex exponentials. Due to the choice of basis functions, the transformation is not very well-suited for short-duration signals, such as impulses and non-stationary signals. These features

affect the whole signal and interfere with information that is present in the rest of the signal. Common problems that arise are wrap-around and ringing due to the Gibbs phenomena. These effects become clearly visible when we calculate the analytic signal of a short duration or non-stationary function straightforward with the FFT. In order to suppress the side-effects, windowing functions can be used to taper the operator before any other processing steps are performed. These windowing functions that operate on the imaginary part are usually large length IIR or FIR filters. When using these windowing functions for shorter signals, one has to be careful not to look at the characteristics of the windowing function instead of the signal.

As we have seen in Chapter 3, the wavelet transformation is designed to handle non-stationary signals. Since it uses short-duration basis-functions to build the transform, the transform is less bugged by side-effects. Depending on the type of implementation, periodic extension or symmetric extension, artifacts due to wrap-around can be suppressed even more. The wavelet transformation operates in the time-domain and uses convolutions with short signals, which makes the transform computationally fast. It is for those reasons that we have developed a *local* Hilbert transformation van Spaendonck *et al.* (2002b). The discrete implementation of this transformation is a simple convolution with FIR filters. Basically the filter-coefficients of *any* real wavelet can be modified and used for this transformation. The filters are easily designed and can be designed for different lengths and with varying slopes in frequency.

In this section we show the relationship between the filters of the local Hilbert transform and those of the wavelet transform. Its performance in the field of signal characterization is compared to the results of the traditional FFT-based Hilbert transform and to the state-of-the-art time-frequency transforms. We show that for a large range of signals, the local Hilbert transform results in much smoother and more accurate representations, due to a smoother envelope and phase. We show in later chapters how the local Hilbert projection filters elegantly combine with the wavelet transform to form a complex wavelet transform which combines the beneficial properties of both transforms.

■ 4.1.1 Analytic signal and Hardy space

As we have seen in Chapter 2, the analytic signal $u^A(t)$ derived from a real-valued signal $u(t) \in \mathcal{R}$, can be interpreted as the convolution of this real-

valued function with an operator,

$$\mathcal{A}\{u(t)\} = u^A(t) = u^R(t) + iu^I(t) \quad (4.1)$$

$$= |A(t)| \exp(i\varphi(t)) \quad (4.2)$$

in which u^A represents the analytic signal, u^R the real part, and u^I the imaginary part. $|A(t)|$ is the modulus or amplitude, and φ is the phase expression. The imaginary part can be calculated with the Hilbert transform which is given in the Fourier domain by Eq. (2.14)

$$u^I(t) = -i \mathcal{F}^{-1} \{ \text{sign}(\omega) \mathcal{F} \{ u(t) \} \} \quad (4.3)$$

in which

$$\text{sign}(\omega) = \{-1, 0, 1\} \quad \text{for } \omega \in \{-\infty, 0, +\infty\}. \quad (4.4)$$

Problems arise however when we want to discretize the transformation. The time-domain Hilbert operator is a convolution operator with a pole at $t = \tau$. It is difficult to describe such a function with infinite (periodic) functions as is done by the FFT. Fourier series at a jump result in undesirable oscillation. This phenomenon brought forward the need for locally operating functions or FIR filters. Scientists have developed different algorithms to mitigate the problem. IIR filters and widely expanding FIR filters are designed to approximate the Hilbert operator as close as possible. The problem still remains however that local information is spread over the data to a large extent. For this reason we have developed a *local* Hilbert transformation which uses a band-limited approximation of the sign function $\text{sign}(\omega)$ in the Fourier domain, and operates as an FIR convolution filter in time. The particular filter that we use is a shifted halfband filter that is commonly used in wavelet transforms. The accuracy of the filter depends on the length of the filter. This approximation of the Hilbert transform is often a more desirable approximation of the continuous Hilbert transform than is the FFT-based Hilbert transform.

■ 4.1.2 Wavelet-based Hardy-space projection.

The operator for the analytic signal has the shape of a brick-wall in frequency. Hence it seemed logical to use a phase-shifted halfband filter for that operation. The accuracy of the projection is then dependent on the differentiability of the filter.

For the projection onto positive frequencies, the roots of $P(z)$ in Eq. (3.80) have to be chosen at $z = i$ and $z = -i$ or $\omega = \pi/2$ and $\omega = -\pi/2$. We can

$$u(n) \longrightarrow \boxed{P_+} \longrightarrow u(n) + i\mathcal{H}\{u(n)\}$$

Figure 4.1: Hardy space projection filter P_+ .

achieve this by simply shifting of the halfband filter $P(z)$ in Eq. (3.82) by $\omega = \pi/2$, the halfband filter then projects onto positive frequencies, *viz.*

$$P^+(z) = P(iz). \quad (4.5)$$

The halfband filter, together with its negative equivalent $P_-(z)$ yield perfect reconstruction just as in Eq. (3.79), when

$$P^+(z) + P^-(z) = 2 \quad (4.6)$$

In the same way as for the relation between the highpass and the lowpass halfband filters, the halfband filter in Eq. 4.5 that projects the energy on positive frequencies, the projection onto negative frequencies, that is obtained by convolution with $p_-(n)$ can be written in terms of $p_+(n)$ according to Eq. (3.77)

$$P^-(z) = -P^+(-z) \quad (4.7)$$

The negative frequency projection filter is equal to the positive frequency projection filter shifted by $\omega = \pi$. This is exactly the filter that is mirrored in the zero-frequency axis, which means that

$$P_-(z) = P_+^*(z^{-1}) \quad (4.8)$$

Combining Eq. (4.6) with Eq. (4.8) shows that the real part of each of the projection filters $p^-(n)$ and $p_+(n)$ actually has a flat system response. Because the negative counterpart is the complex conjugate of the positive filter, the filter can be neglected for perfect reconstruction. This means that we have a halfband filter that alone gives perfect reconstruction! The imaginary part of the product filter $p^+(n)$ can be interpreted as the *local Hilbert transform* operator as we can see in Fig. 4.1. Given the filterlength the maximally flat approximation of the ideal filter is given by $P_+(z)$.

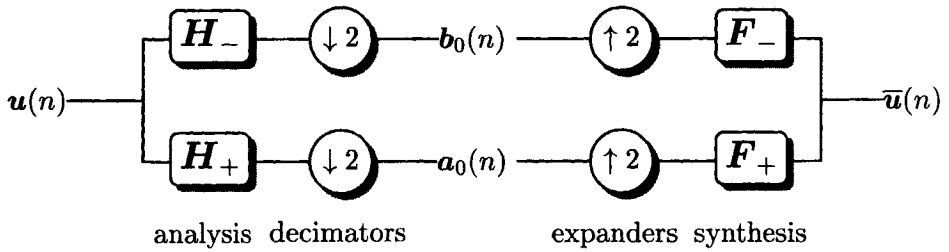


Figure 4.2: Analysis and synthesis filter banks

In the same way as we have seen in Eq. (3.80) for the halfband filter $P(z)$ of the wavelet transformation we can optionally factor the halfband filter $P^+(z)$ into its spectral components $H_+(z)$ and $F_+(z)$ (see Fig. 4.2), according to

$$P^+(z) = H^+(z)H^-(z^{-1}), \quad (4.9)$$

in which we have substituted

$$F^+(z) = z^{-N}H^+(z^{-1}) \quad (4.10)$$

and multiplied by z^N . The spectral factorization gives us the opportunity to down-sample the system without losing the perfect reconstruction property.

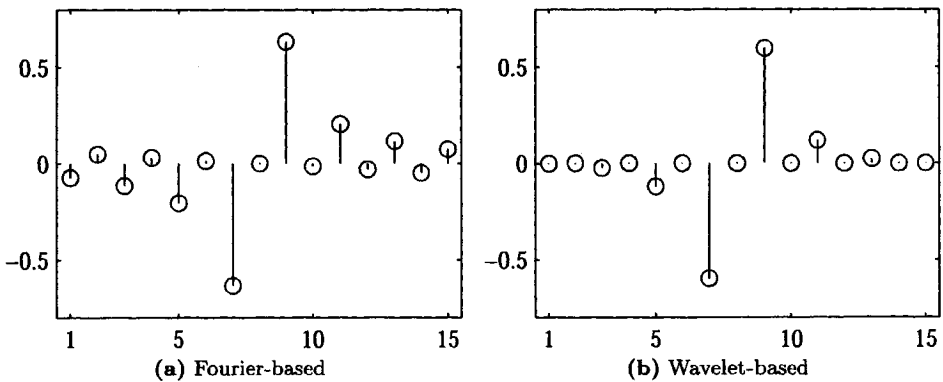


Figure 4.3: Hilbert operator filters: (a) 15-point based on FFT, (b) 15-point Maxflat FIR filter (Daubechies-8).

Each of the spectral factors contains half of the roots in P_+ . In Fig 4.3 we show an example of two different discrete length-15 Hilbert convolution operators. Each of the filters operates as an approximate sign function in frequency. Fig 4.3 (a) shows the filter obtained by inverse Fourier transform of a length-15 sign function. The resulting time-domain convolution filter

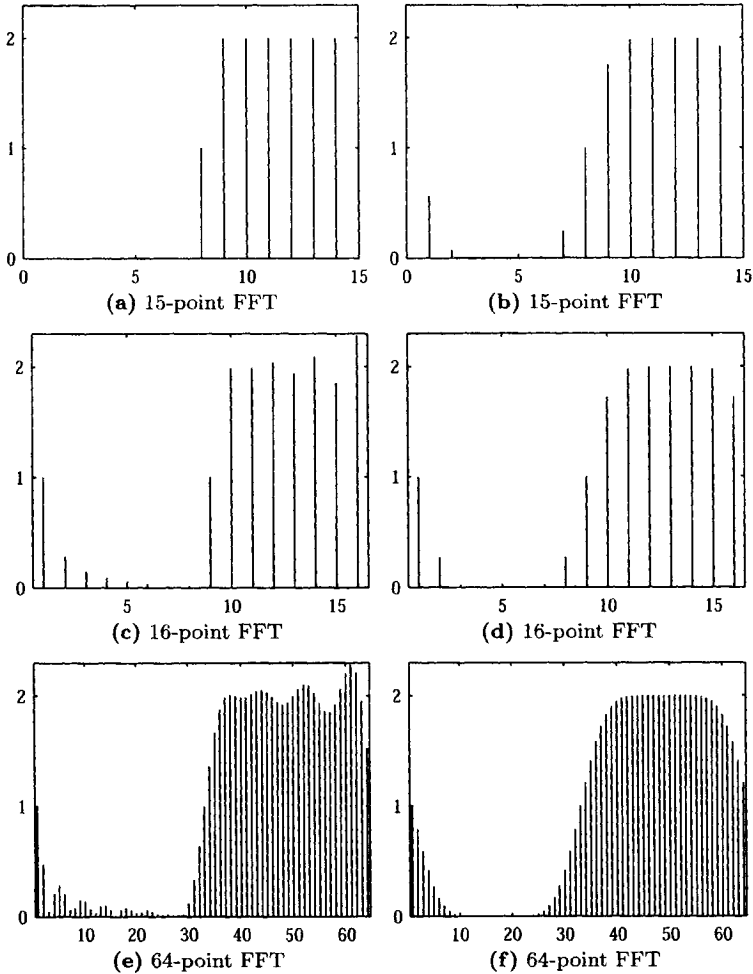


Figure 4.4: The Fourier responses of the length-15 analytic Fourier- and local operators, using variable length FFT's going from length-15 in (a) and (b), to length-64 in (e) and (f).

resembles the odd-counterpart of a truncated sinc function. In Fig. 4.3 (b) we show the length-15 maxflat FIR filter. The filter strongly resembles the figure on the left, but the energy is suppressed towards the boundaries which results in a smooth approximation of the sign function in frequency.

In Fig. 4.4 we show the Fourier responses of the equivalent analytic filters that use the Hilbert operators in Fig. 4.3. On top in Fig 4.4 (a) and (b) we show the length-15 FFT of the respective filters in Fig. 4.3 (a) and (b). As we could expect, the FFT-based analytic operator suppresses all the negative frequencies in a signal of 15 samples length. The maxflat FIR filter has a less firm suppression of negative frequencies. The figures (c),(d), (e) and (f) show the results of zero-padded FFT's. The lower two left figures show the responses of the conventional length-15 Hilbert transform for a length-16 and a length-64 FFT. From (c) and (d) we can see that as soon as a longer signal is convolved with the operator, the step function changes into the shape of a less attractive window function which contains a considerable amount of energy in the negative frequency range. The Figs. 4.4 (d) and (e) show that the maxflat filter is not susceptible to interference of energy in the negative frequency range. The window preserves its shape.

4.2 Performance

The performance of the Hilbert transform consists of several critical properties. One of the most important properties of the analytic signal is that it provides us with a good measure for instantaneous energy. Instantaneous energy is a stable quantity for signal comparison and analysis. The phase of the analytic signal is the other important property. As we have seen in Section 4.1.1, the derivative of the phase of the analytic signal yields the instantaneous frequency. However in most discrete implementations of the Hilbert transform, the phase is not very stable and is often contaminated by negative frequencies, which by definition should not be present. For real-time applications it is of course of crucial importance to use efficient and fast algorithms.

■ 4.2.1 Energy density.

Energy density is an important quantity in signal and image processing. On the basis of this quantity we can compare signals with each other and discriminate information within the signal, not only on its amplitude, but also on the basis of its energy content.

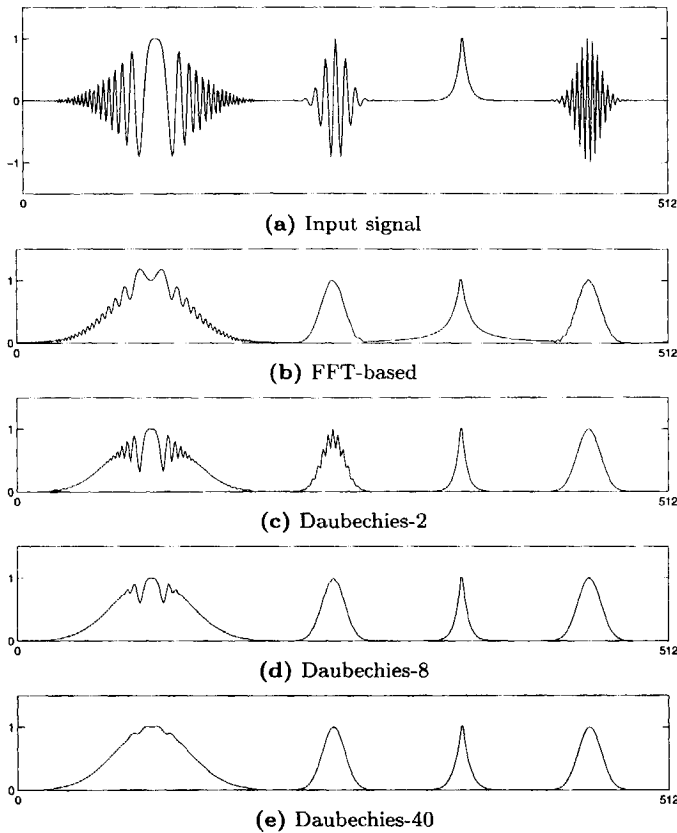


Figure 4.5: The envelopes of a non-stationary discrete analytic signal; (a) the signal, (b) its FFT-based envelope, (c)-(e) envelopes of local analytic signals.

In Fig (4.5) (a) we show an example of a non-stationary signal containing in the following order, a Gaussian modulated chirp (chirplet), a Gaussian modulated sinusoid, followed by a scaling delta-pulse and another modulated sinusoid at a higher frequency than the first. We know exactly what the envelope should look like. In the case of the Gaussian modulated signals, the envelope should look like the particular Gaussian bell-shape.

We have calculated the Hilbert transform of the signal with the Fourier transform and with different length maxflat FIR filters. The envelopes of the analytic signals using the respective Hilbert transforms are shown in Fig. 4.5 (b)-(d). Fig. 4.5 (b) shows the envelope obtained with the FFT-based Hilbert

transform. This transform is obtained from a global transformation, which uses periodic functions to build the signal. The Fourier window used is a brick-wall filter, which in the time-domain operates as a convolution with a truncated odd sinc function. The result is interfered with Gibbs phenomena.

The third figure(c) shows the envelope obtained by convolution with a length-3 Daubechies-2 maxflat halfband FIR filter. Although some parts in the envelope appear smoother than in the FFT-based transform, the length of the filter limits its influence. Specifically the lower frequencies cause trouble, because the filter cannot reach far enough to span the period between the pulses.

As soon as we increase the order of the maxflat projection filter and implicitly the number of samples used for the convolution, we see that the gaps in the lower frequency parts of the chirplet and the lower frequent sine are filled in. In (d), the Daubechies-8 filter has established sufficient range for a smooth envelope of the first sine, although the low frequency information in the chirplet is not yet fully resolved.

In Fig. 4.5 (e) we have used a length-79 maxflat FIR filter which is related to the Daubechies-40 filter. The envelope of all the signal segments evidence that the quadrature is established for all the frequencies present in the signal.

■ 4.2.2 Instantaneous phase and frequency

The analytic signal can be written in terms of a modulus and a phase. In the previous paragraph we have addressed the performance of the local Hilbert transform for the estimation of energy in the signal, which is directly related to the modulus of the analytic signal. In this paragraph we will address the accuracy of the phase and phase related features. These features are not only compared to those of the global Hilbert transform, but also to state-of-the-art techniques such as the short-time Fourier transform.

Although the conventional time-frequency representations can lead to very accurate average frequency estimators, they depend on the window shape, size and the overlap. Tuning of the parameters of the short-time Fourier transform leads to very accurate instantaneous frequency estimators. The drawback is that these estimators are limited to frequency content within the window and that they can change due to the shape of the window. Besides the window-dependency, the computational efficiency is lower than that of the Fourier transform and the transform results in a redundant two-dimensional representation.

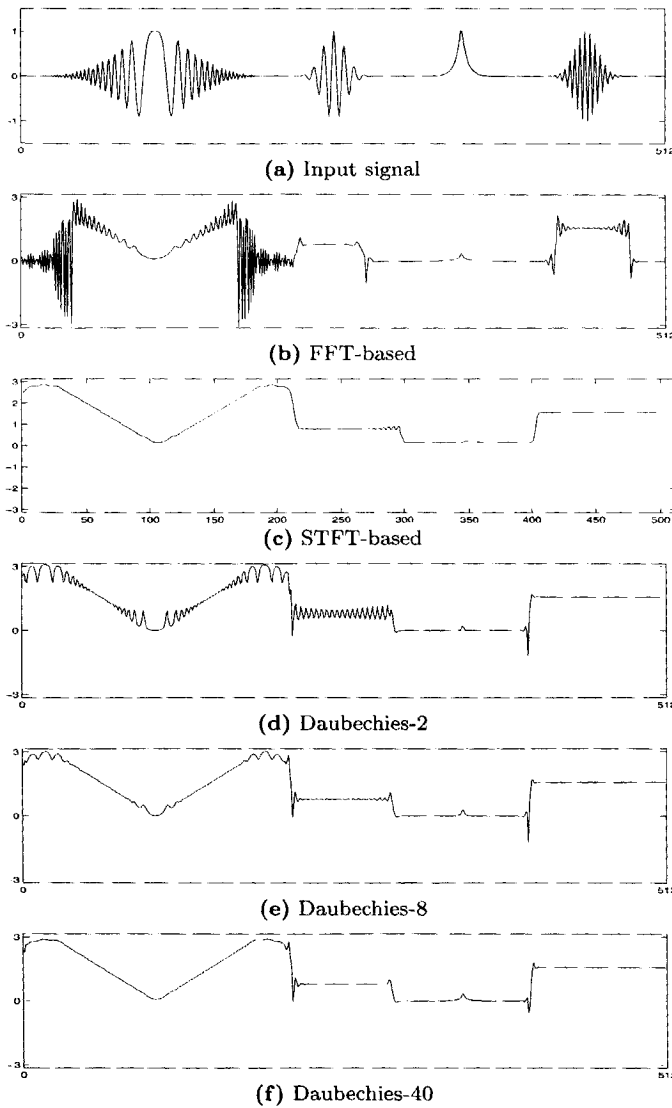


Figure 4.6: The instantaneous frequency of a non-stationary discrete analytic signal; (a) the signal, (b) instantaneous frequency calculated through FFT-based Hilbert transform, (c) instantaneous frequency calculated through STFT, (d)-(f) instantaneous frequency through different maxflat FIR filters.

For signal characterization, the phase of the analytic signal plays a key role. The derivatives of the phase are measures for instantaneous frequency and instantaneous bandwidth. The instantaneous phase is a sensitive quantity which is hard to analyze. In the first place the phase varies between $-\pi$ and π . Because the phase often wraps around the bounds, the phase is unwrapped before its derivatives are calculated.

We study the accuracy of the phase by means of the instantaneous frequency, which is the first derivative of the unwrapped phase. A smooth phase will result in an accurate first derivative. For comparison and validation of the results we have calculated the instantaneous frequency of a spectrogram.

In Fig. 4.6 we show the instantaneous frequencies of our test signal. We have used different algorithms for the determination. In (a), the input signal is shown. In (b), the instantaneous frequency calculated through the conventional FFT-based Hilbert transform is shown. The estimate is noisy and disturbed by negative frequencies, that by definition should not exist. In Fig. 4.6 (c) the result of the instantaneous frequency calculated through the spectrogram is shown. The spectrogram uses a length-64 FFT of a length-20 Hamming window and a length-19 overlap. The estimate is smooth over the whole signal, although the resolution at the scaling delta-pulse is quite low. Near the edge of the first modulated sine, we can observe some small artifacts. Fig. 4.6 (d)-(f) shows the instantaneous frequency estimates calculated through the phase expression of different length local Hilbert operators. The estimate in (d) shows the result using a very short-duration Daubechies-2 maxflat filter for the Hilbert transform. Although the result is contaminated by noise, the trends are clearly visible and in the intermediate frequency zone, the frequency seems to be resolved quite accurately, judging by the response of the second modulated sine and the center frequencies in the chirplet. By increasing of the filter-length and the number of vanishing moments in (e) and (f), we see that the estimate of the instantaneous frequency converges to a response that looks very similar to the response in Fig. 4.6 (c) of the spectrogram. The lack of negative frequencies is plausible and the limited amount of negative energy can be explained by the shape of the filter, which allows for some negative frequency information.

4.3 Conclusions on local and global Hilbert transformation

From the examples in the previous section and from the theoretical background on the transforms we can state the following conclusions.

For short duration signals or signals with strong frequency variations over time, a local Hilbert transform achieves a more accurate quadrature relationship between the real and the imaginary parts than the conventional FFT-based Hilbert transform. The side effects from a periodic transform, such as wrap-around and ringing, are suppressed due to the local character and the smoothness of the filter in frequency.

The local Hilbert transform is a band-limited version of the global Hilbert transform. Consequently, this may result in unwanted side-effects for high and low frequencies. These effects can be largely suppressed by choosing a higher order projection filter with a different length. For efficient implementation, a better way to tackle this problem is combining the local Hilbert transformation with the discrete wavelet transformation (see Chapter 6).

Because of its local support, the local Hilbert transform does not experience global effects due to spikes or step-functions in the signal. As a consequence the phase is smoother, resulting in more accurate phase-related signal attributes, such as the derivatives of phase, which compete with the state-of-the-art short-time Fourier transform derived features.

The local Hilbert transform is computationally fast, which makes it suitable for real-time applications. It uses an order $O(N)$ operations whereas the FFT-based Hilbert transform needs $O(N \log(N))$ operations.

4.4 Seismic attributes

The local Hilbert transform can be directly implemented for the computation of seismic attributes. We can straightforwardly implement the conventional complex trace attributes for the maxflat analytic signal as well as for the FFT-based analytic signal. In this way we are able to compare the performance of the attributes computed through the local Hilbert transform to those computed through the conventional Hilbert transform.

In this section we also show that we can extract geometric attributes with these techniques. By combining the frequency information in each direction we can extract instantaneous reflection angle and instantaneous polar frequency. The computational efficiency even allows for application on 3-D seismic data.

■ 4.4.1 Conventional seismic attributes

The conventional complex trace attributes are the reflection strength, the instantaneous phase and its derivative, the instantaneous frequency of a seismic

image. These will be the subject of the following paragraphs.

For that purpose we will first define the analytic image in the preferential direction x_3 . We can directly extend the one-dimensional formulation of the analytic signal in Eq. (2.12) to a two-dimensional analytic image by simply calculating the analytic signal along one dimension of the real-valued image $u(\mathbf{x}_D) \in \mathbb{R}^2$

$$\mathcal{A}_3 \{u(\mathbf{x}_D)\} = u_3^A(\mathbf{x}_D) = u_3^R(\mathbf{x}_D) + i u_3^I(\mathbf{x}_D) \quad (4.11)$$

$$= |A_3(\mathbf{x}_D)| \exp(i\varphi_3(\mathbf{x}_D)) \quad (4.12)$$

in which $\mathbf{x}_D = \{x_1, x_3\}$, u_3^A represents the analytic signal of an image in the specified direction x_3 , $u_3^R(\mathbf{x}_D)$, the real part, and $u_3^I(\mathbf{x}_D)$ the imaginary part. $|A_3(\mathbf{x}_D)|$ is the envelope, and $\varphi_3(\mathbf{x}_D)$ is the phase in x_3 . The real part of the analytic image represents the signal itself, or

$$u_3^R(\mathbf{x}_D) = u(\mathbf{x}_D), \quad (4.13)$$

the imaginary part can be calculated with the Hilbert transform in the vertical direction which is given in the Fourier domain by Eq. (2.14)

$$u_3^I(\mathbf{x}_D) = \mathcal{H}_3 \{u(\mathbf{x}_D)\} = -i \mathcal{F}_3^{-1} \{\text{sign}(k_3) \mathcal{F}_3 \{u(\mathbf{x}_D)\}\} \quad (4.14)$$

in which

$$\text{sign}(x) = \{-1, 0, 1\} \quad \text{for } x \in \{-\infty, 0, +\infty\}. \quad (4.15)$$

and \mathcal{F}_3 represents the spatial Fourier operator in the x_3 -direction.

From the analytic image we can extract the various signal characterization parameters that we have studied in the previous sections. We compare the attributes obtained with the novel local Hilbert transform with those obtained through the conventional Hilbert transform.

Reflection strength and instantaneous phase. According to Eq. (4.12), the analytic image can be decomposed into its envelope and phase. In this section we will compare the two signal attributes computed through the local Hilbert transformation and the conventional Hilbert transformation.

In Fig. 4.7, we compare the envelopes ($|A(\mathbf{x}_D)|$ in Eq. (4.12)) and the instantaneous phase ($\varphi(\mathbf{x}_D)$ in Eq. (4.12)) of the two methods.

The image we use for the example, is the 128×128 zoneplate image (Simoncelli, 2002) in Fig. 4.7 (a). The image consists of concentric circles that have a chirp-like behaviour in the polar direction. The image contains all

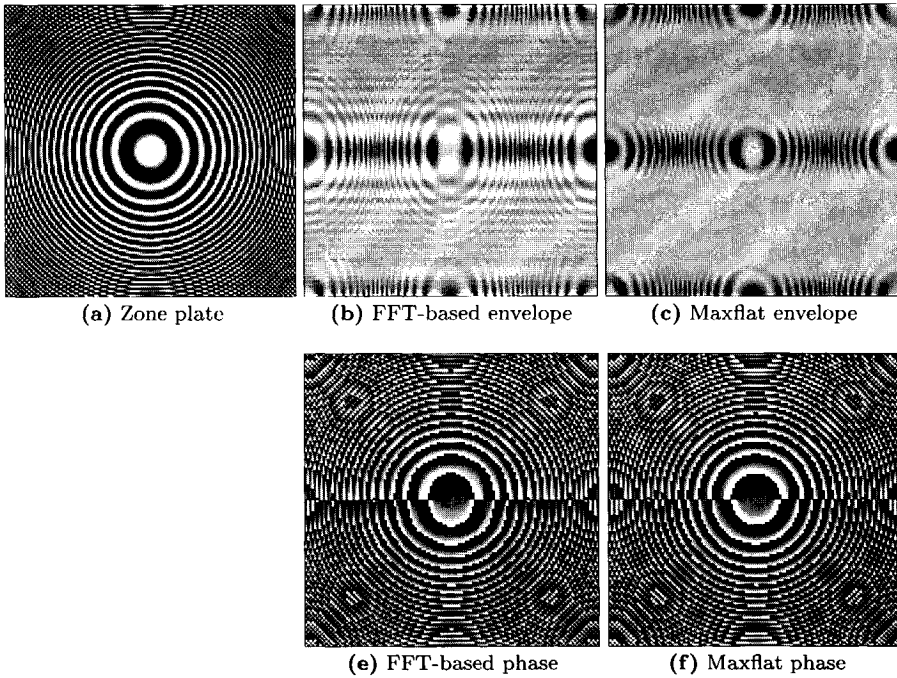


Figure 4.7: (a) The zoneplate, (b) FFT-based envelope, and (c) the Daubechies-16 maxflat-based envelope. (e) FFT-based instantaneous phase, and (f) Daubechies-16 maxflat filter instantaneous phase.

angles, and shows a large range of frequencies, varying from very low (polar) frequencies in the center towards very high frequencies at the periphery. In the upper right two figures we show the envelopes, (b) is the envelope computed through the Fourier transform, (c) is the envelope after convolution with a complex maxflat Daubechies-16 filter. Both energy representations have trouble with the very high and very low vertical frequencies. As for the intermediate parts, the envelope in Fig. 4.7 (c) has a much smoother response than the conventional envelope in (b) has. The envelope in (b) is contaminated by interference patterns.

In the lower right two figures we show the phase responses of the analytic images. Fig. 4.7 (e) is the instantaneous phase computed through the FFT, (f) is the instantaneous phase of the zoneplate computed through the complex maxflat Daubechies-16 filter. The results are very much alike, however the shape of the concentric circles in (e) seems to be slightly compressed in

horizontal direction. This phenomenon will certainly affect the instantaneous frequency computation, which is the vertical derivative of the phase.

In Fig. 4.8- 4.9, we show a seismic example of a time-migrated seismic section. In Fig. 4.8 (a), part of the seismic section (512×512 , $dt = 0.004s$, $dx = 25m$) is shown. The data emanates from the L5-block in the North Sea near the Netherlands. Due to a salt dome on the left of the image, the seismic section contains a variety of angles and small scale faults. The envelope in Fig. 4.9 (a) is computed on the basis of the FFT, the envelope in Fig. 4.9 (b) on the basis of the complex maxflat Daubechies-16 filter. With the bare eyes, we discern hardly any difference between the two figures. However, when we look at the difference between both envelopes in Fig. 4.8 (b), we observe that there is a considerable difference in the instantaneous envelopes. On the basis from what we have seen in the zoneplate, we state that most of the energy in the difference image is to be ascribed to the inaccurate values of the envelope of the conventional analytic signal.

Instantaneous frequency is the first derivative of the phase of the analytic signal as we have seen in Eq. (2.17). For seismic applications the instantaneous frequency shows additional information which can be helpful for lithological interpretation.

We define the instantaneous frequency of an image $u(\mathbf{x}_D)$ along the preferential direction x_3 as follows. We isolate the phase of the analytic image $u_3^a(\mathbf{x}_D)$ as given by Eq. (4.12), and take its vertical derivative according to

$$\langle f_3(\mathbf{x}_D) \rangle = \frac{1}{2\pi} \frac{d\varphi(\mathbf{x}_D)}{dx_3}. \quad (4.16)$$

in which $\langle f_3(\mathbf{x}_D) \rangle$ is the instantaneous frequency in the x_3 -direction.

The numerical implementation for the computation of the instantaneous frequency commonly uses the FFT-based Hilbert transform to compute the analytic image. The instantaneous frequency computed in this way is however often contaminated by negative frequency information, which cannot be interpreted. Due to the nature of the maxflat filter, the frequency response of the maxflat analytic signal does not necessarily need to contain strictly positive frequencies. This filter suppresses negative frequencies, but does not set all negative frequencies to zero. The smooth shape of the filter allows for some negative frequency content in the highest frequency range and near DC (direct current). The amount of energy located in that frequency range depends on the order of the Daubechies filter.

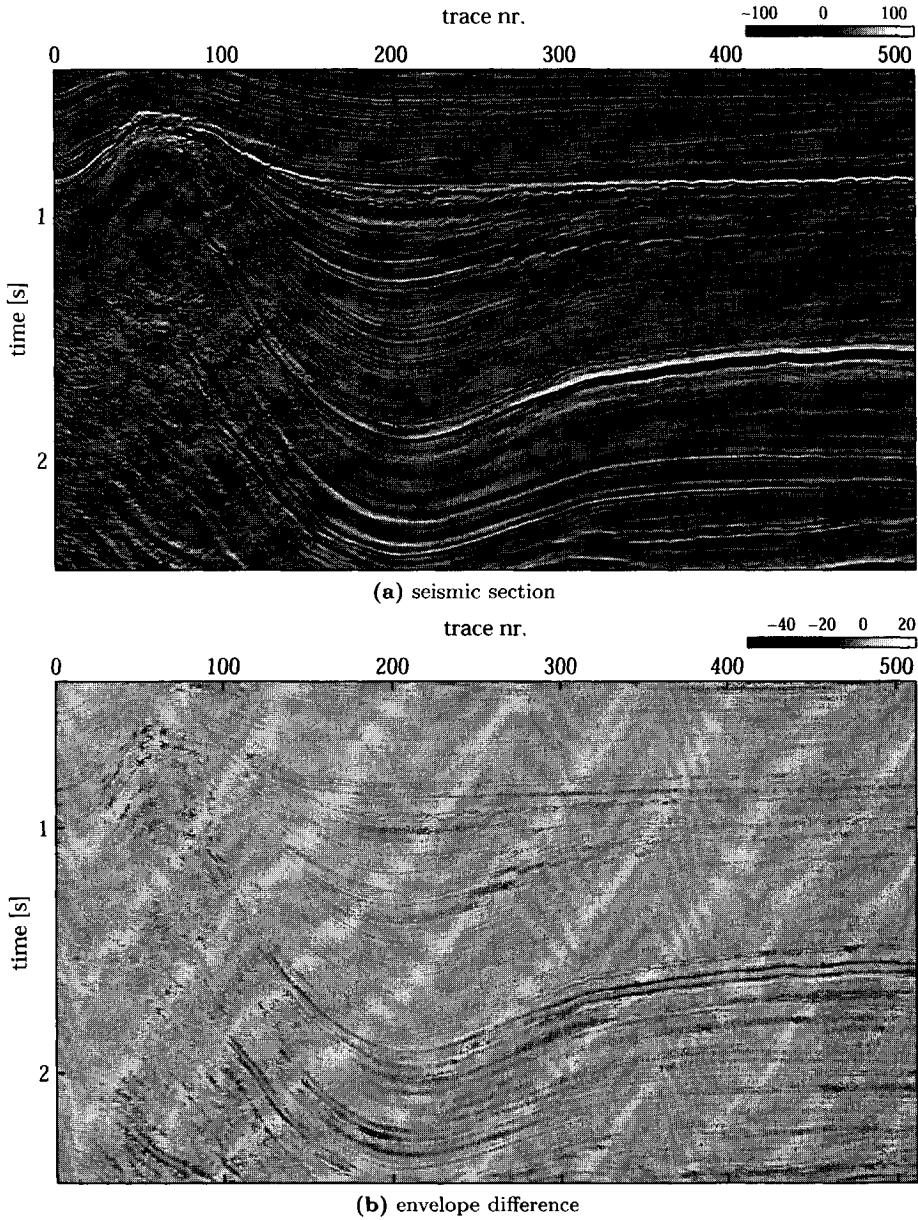
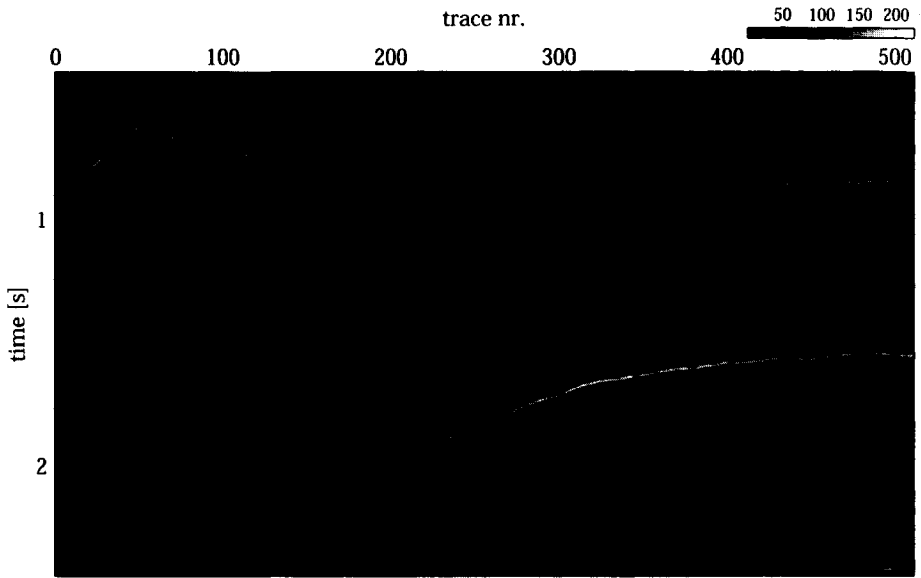
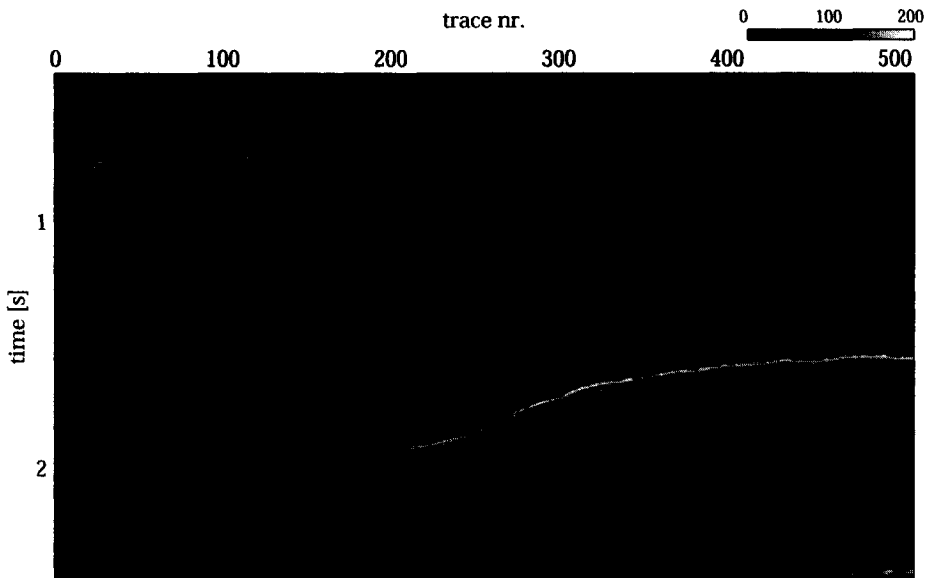


Figure 4.8: Seismic section ($dt=.004$ [s], $dx=25$ [m]) (a), Difference between envelopes in Fig. 4.9.



(a) FFT-based envelope



(b) maxflat envelope

Figure 4.9: (a) FFT-based envelope, (b) Daubechies-16 maxflat envelope of section in Fig. 4.8 (a).

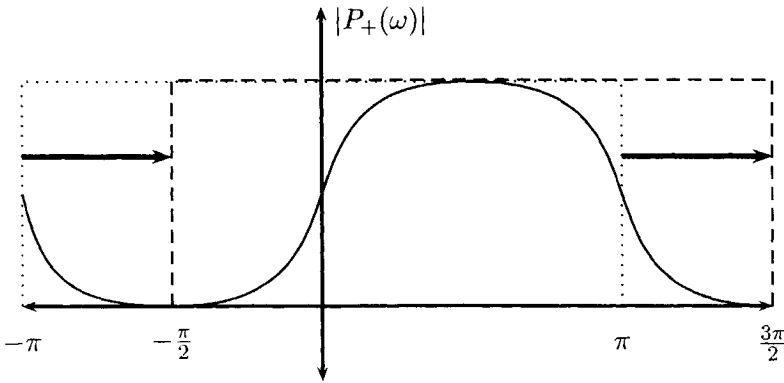
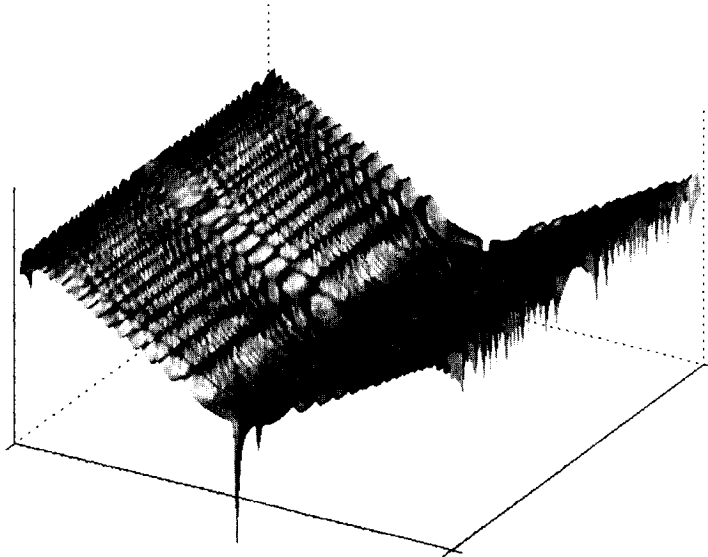


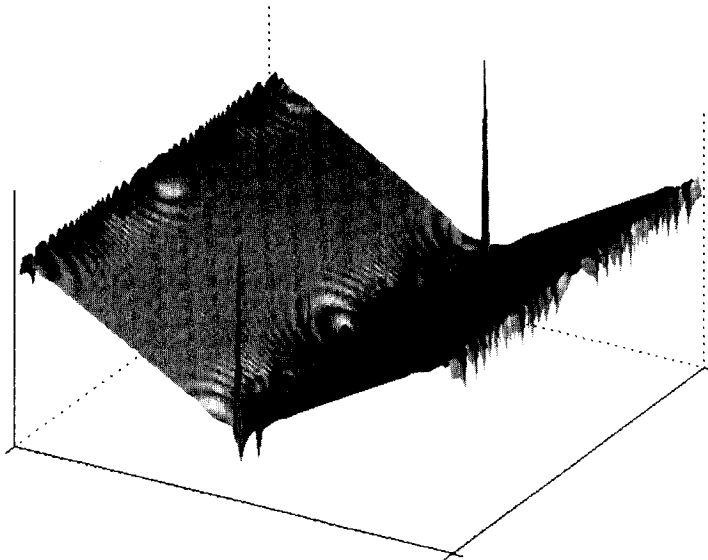
Figure 4.10: Window the instantaneous frequency from $-\frac{\pi}{2}$ to $\frac{3\pi}{2}$.

In order to obtain a smooth course of frequencies we can even well take the period of the maxflat filter into account, and window the frequency between $-\pi/2$ to $3\pi/2$ instead of $-\pi$ to $+\pi$. This procedure prevents us from introducing wrap around effects with highly negative frequencies, see Fig. 4.10. The operation can simply be done after the computation of the instantaneous frequency, by adding 2π to the instantaneous frequencies that have values of $-\pi/2$ and lower. For seismic applications, this operation is not necessarily performed, depending on the type of maxflat filter, due to the band limitation of the frequency range.

In order to illustrate the difference in performance of the FFT-based analytic signal with the maxflat filter response, we revisit the zoneplate. We have computed the vertical instantaneous frequencies, which can be considered to be along the temporal axis. The responses are shown in Fig. 4.11. The response of the FFT-based instantaneous frequency is shown in the upper figure, (a). The lower figure, in (b) shows the results of the instantaneous frequency calculated through the complex maxflat Daubechies-16 filter. The orientation of both figures is twisted such that the top of the zoneplate is located on the left, the bottom on the right. The vertical axis represents the spectral amplitude, the horizontal axes, the 2-D plane of the zoneplate. In accordance to what we expect to see, the chirp-like behaviour along the vertical axis clearly shows up in both responses: the frequencies decrease towards the centre and increase after passing through the center. The maxflat filter response is considerably smoother than the rippled surface of the FFT-based instantaneous frequency.



(a) FFT-based IF



(b) Maxflat IF

Figure 4.11: FFT-based instantaneous frequency (a) of the zoneplate in Fig. 4.7, and the Daubechies-16 maxflat instantaneous frequency.

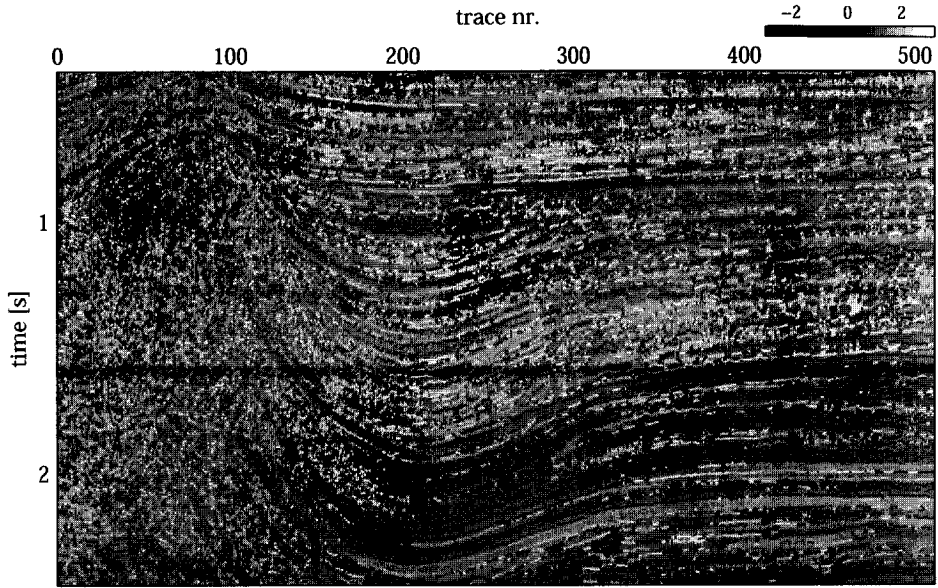
In Fig. 4.12 we compare the performance of both methods on seismic data. The instantaneous frequencies of the seismic section in Fig. 4.9 show a large resemblance. In Fig. 4.12 (a) we show the FFT-based instantaneous frequency, in (b) the maxflat instantaneous frequency is shown. Both sections show a large amount of negative frequencies. The Fourier based method is by definition not allowed to show any negative frequencies, the maxflat instantaneous frequency response only *suppresses* negative frequencies. When negative frequencies are present in the FFT-based method, we do not know how to handle or interpret these. The maxflat instantaneous frequency is allowed to contain a small amount of negative frequency information. Remember that the filter ranges from $-\frac{\pi}{2}$ to $\frac{3\pi}{2}$, so should the instantaneous frequency. The colorbars illustrate the difference. In the left figure the values reach from $-\pi$ to π , and a substantial amount of energy is located in the negative frequency range, contaminating the constructive positive frequency information by noise. The values in the right figure, reach from $-\frac{\pi}{2}$ to $\frac{3\pi}{2}$ in accordance with the filter response and have a smoother decay. There is some negative information.

■ 4.4.2 Geometric seismic attributes

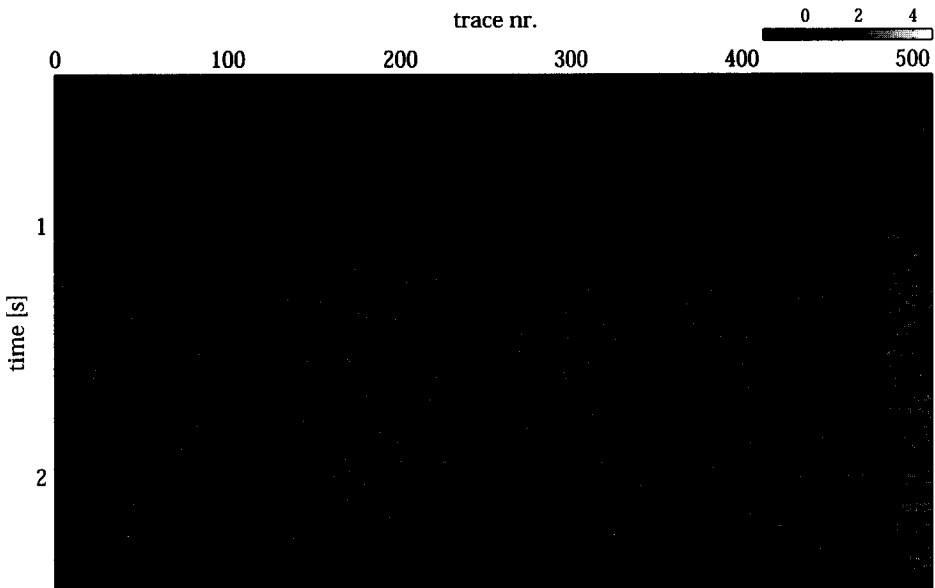
In the previous Section we have seen that we can determine the instantaneous frequency of a seismic image. However, a seismic section consists of multiple dimensions. As we have seen in Chapter 2, the angles in the Fourier domain and in the spatio-temporal domain are directly related to each other. We can use this information to combine the local Fourier information we have with the location in space and time (van Spaendonck *et al.*, 2002a). By doing so, we can describe our seismic data in terms of geometric attributes (Steeghs *et al.*, 2001). In the following paragraphs we discuss two different attributes, the innovative local polar frequency, and the local angle.

Local polar frequency The instantaneous frequency as discussed above, contains information on the vertical or temporal frequency only. Although there certainly is correlation to a large extent between adjacent traces and thus between their instantaneous frequencies, inclusion of the second dimension for the calculation of the instantaneous frequency seems logical. From the combined frequencies we can extract *local polar frequency* information. In that way we can manage to track reflectors on the basis of their polar frequency content, instead of just on the basis of their vertical frequency.

We can determine the local polar frequency using a straightforward ex-



(a)



(b)

Figure 4.12: (a) *FFT-based instantaneous frequency of seismic section in Fig. 4.9;*
(b) *its Daubechies-16 maxflat instantaneous frequency.*

tension of the instantaneous frequency of an image as defined in Eq. (4.16). When we consider this definition, we can apply the local Hilbert operator in the horizontal as well as in the vertical direction. For that reason we introduce the following decomposition of the analytic image, in which we make a distinction between positive and negative frequencies. The components of the analytic image are defined as

$$\mathcal{A}^\pm \{u(\mathbf{x}_D)\} = u_\pm^A(\mathbf{x}_D) = \mathcal{F}_D^{-2} \{ \chi_{R^\pm}(k_1) \chi_{R^\pm}(k_3) \mathcal{F}_D^2 \{u(\mathbf{x}_D)\} \}, \quad (4.17)$$

in which we employ \mathcal{A}^+ to indicate the part of the analytic image containing mostly of positive, and \mathcal{A}^- of mostly negative horizontal spatial frequencies. The operator \mathcal{F}_D^2 indicates 2-D spatial Fourier transformation over the variables in \mathbf{x}_D , and the characteristic functions χ_{R^+} and χ_{R^-} are given by

$$\chi_{R^+}(x) = \left\{ 0, \frac{1}{2}, 1 \right\} \quad \text{for } \{x < 0, x = 0, x > 0\}, \quad (4.18)$$

and

$$\chi_{R^-}(x) = \left\{ 1, \frac{1}{2}, 0 \right\} \quad \text{for } \{x < 0, x = 0, x > 0\}. \quad (4.19)$$

Equation (4.17) can be interpreted as a decomposition of the analytic image in Eq. (4.12) into positive and negative horizontal spatial frequencies. We can rewrite the analytic images of Eq. (4.17) into the envelope and phase,

$$u_\pm^A(\mathbf{x}_D) = |A_\pm(\mathbf{x}_D)| \exp(i\varphi_\pm(\mathbf{x}_D)). \quad (4.20)$$

When we rewrite Eq (4.12) in terms of the positive and negative components of the analytic image in Eq. (4.17) we obtain the following relation

$$\begin{aligned} u_3^A(\mathbf{x}_D) &= u_+^A(\mathbf{x}_D) + u_-^A(\mathbf{x}_D), \\ &= |A_+(\mathbf{x}_D)| \exp(i\varphi_+(\mathbf{x}_D)) + |A_-(\mathbf{x}_D)| \exp(i\varphi_-(\mathbf{x}_D)). \end{aligned} \quad (4.21)$$

Now, the instantaneous frequencies $\langle f_1^\pm \rangle$ along x_1 , containing positive or negative horizontal spatial frequencies, can be calculated with the following relation

$$\langle f_1^\pm(\mathbf{x}_D) \rangle = \frac{1}{2\pi} \frac{d\varphi_\pm(\mathbf{x}_D)}{dx_1}. \quad (4.22)$$

and the instantaneous frequency in the vertical x_3 direction can be calculated according to

$$\langle f_3^\pm(\mathbf{x}_D) \rangle = \frac{1}{2\pi} \frac{d\varphi_\pm(\mathbf{x}_D)}{dx_3}. \quad (4.23)$$

where the \pm -symbol indicates the frequency sector. From Eqs. (4.22) and (4.23), we can calculate the local polar frequency $|\langle f(\mathbf{x}_D) \rangle|$ according to

$$|f^i(\mathbf{x}_D)| = \sqrt{(f_1^i(\mathbf{x}_D))^2 + (f_3^i(\mathbf{x}_D))^2}, \quad (4.24)$$

in which

$$\langle f_1(\mathbf{x}_D) \rangle = \begin{cases} \langle f_1^+(\mathbf{x}_D) \rangle & \text{for } |A_+(\mathbf{x}_D)| \geq |A_-(\mathbf{x}_D)|, \\ \langle f_1^-(\mathbf{x}_D) \rangle & \text{for } |A_+(\mathbf{x}_D)| < |A_-(\mathbf{x}_D)|. \end{cases} \quad (4.25)$$

and

$$\langle f_3(\mathbf{x}_D) \rangle = \begin{cases} \langle f_3^+(\mathbf{x}_D) \rangle & \text{for } |A_+(\mathbf{x}_D)| \geq |A_-(\mathbf{x}_D)|, \\ \langle f_3^-(\mathbf{x}_D) \rangle & \text{for } |A_+(\mathbf{x}_D)| < |A_-(\mathbf{x}_D)|. \end{cases} \quad (4.26)$$

In the Eqs. (4.25) and (4.26) above, we use the envelopes of the positive and negative frequencies to decide which area of the image contains positive or negative horizontal spatial frequency information.

For the numerical implementation of the characteristic functions $\chi_{R^+}(\mathbf{x})$ and $\chi_{R^-}(\mathbf{x})$ in Eqs. (4.18) and (4.19), we use the maxflat projection filter P^+ in Eq. (4.5) and its complex conjugate P^- , respectively.

Again we have used the 128×128 zoneplate to illustrate the effectiveness of the representation. In Fig. 4.13, we show the resulting local polar frequency representation. For the characteristic functions we use the complex maxflat Daubechies-16 filters. The aliasing, still visible in the low and high frequency zone of Fig. 4.11 (b), has disappeared due to the inclusion of the second dimension for the calculation; This effect can be explained by the idea that the zone of instability for one filter is a stable zone for the other and vice versa. The frequencies range from near zero to almost $\pi\sqrt{2}$ along the diagonals. The cone shape is the shape one could expect from the shape of the image; low frequencies show-up in the center of the figure, gradually increasing concentrically towards the periphery.

Due to the quadratic sum in Eq. (4.24), no negative frequencies are present in the figure. The smoothness of the local frequency has improved tremendously in comparison to the instantaneous frequency in Fig. 4.11 (b). Note that we can vary the length of the projection filters in each direction. In some cases a local operator is preferable over an accurate frequency representation,

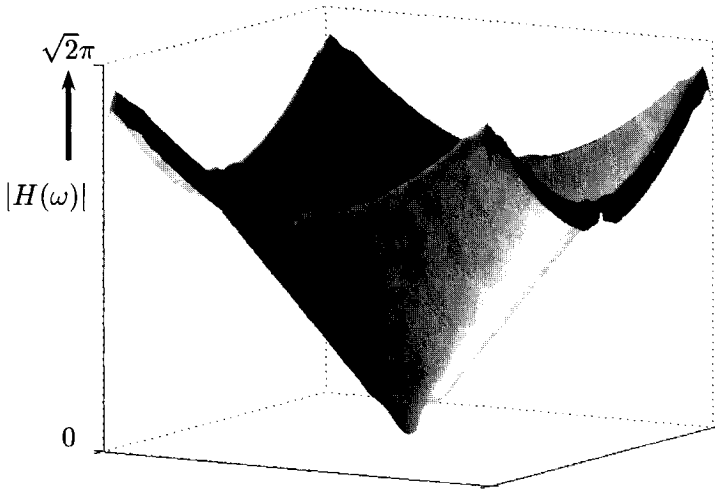
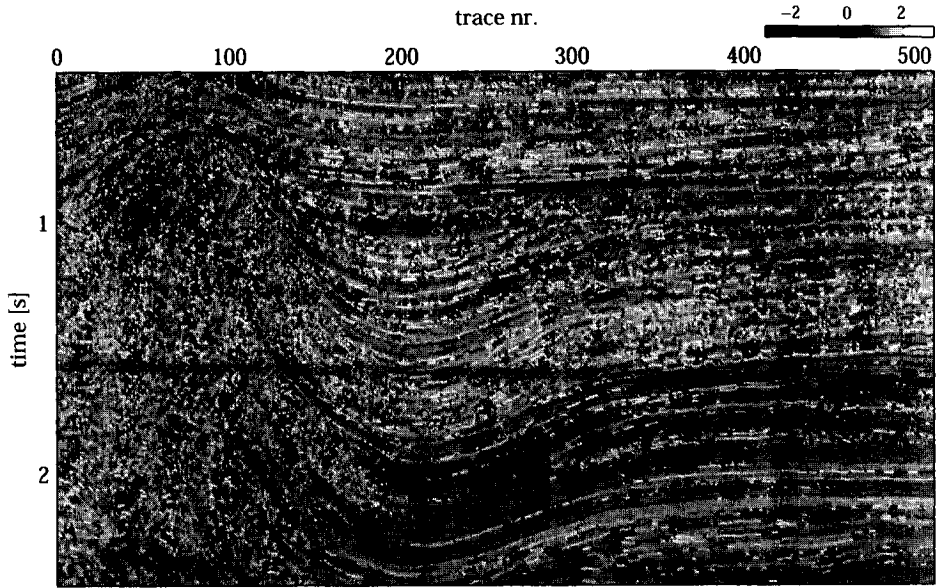


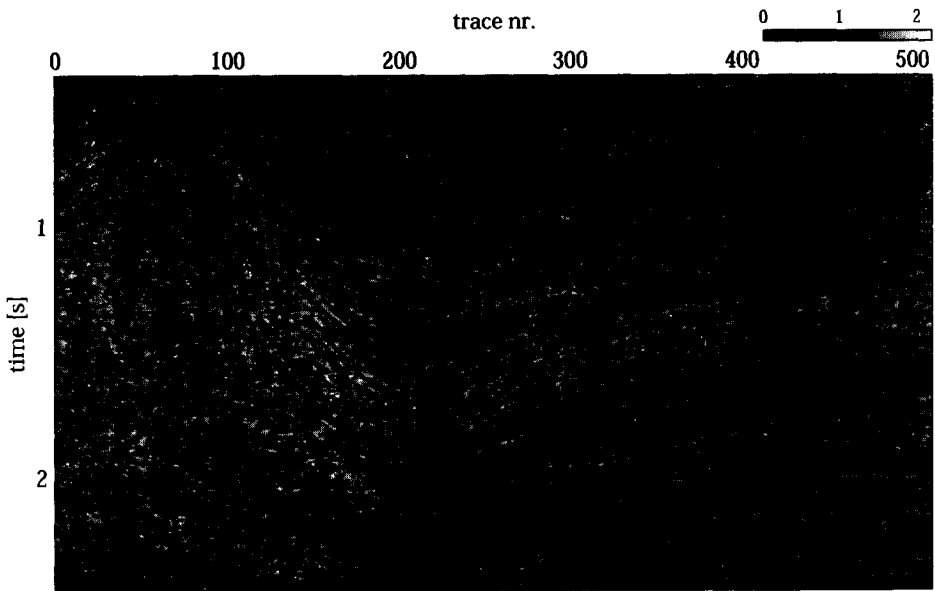
Figure 4.13: *Daubechies-16 maxflat local polar frequency of the zoneplate in Fig. 4.7 (a).*

for instance when we want to detect and localize small-scale features such as step functions. For the detection of channels and faults it might be useful to use a short filter in the lateral direction.

Let us consider the seismic example from Fig. 4.9 (a) again to illustrate the attribute; The high frequencies on the slopes of the salt-dome are hardly detected as such by the instantaneous frequency attributes in Fig. 4.12. The frequency content along the slopes in the vertical direction does not change as much as it does in the horizontal direction. Combining of the instantaneous frequencies in both directions yields the instantaneous polar frequency as shown in Fig. 4.14 (b). For comparison we also show the conventional instantaneous frequency from Fig. 4.12 (a) again in Fig. 4.14 (a). From the results we see an improvement of the contrast. The values in Fig. 4.14 (b) vary between 0 and π , revealing much more pronounced frequency differentiation, whereas the frequency in (a), varies between $-\pi$ and π . The higher frequencies on the slope of the salt dome clearly appear with higher values.



(a)



(b)

Figure 4.14: (a) *FFT-based instantaneous frequency of seismic section in Fig. 4.9;*
 (b) *its Daubechies-16 maxflat local polar frequency.*

Local angle The second geometric attribute is the angle of the reflector. After computing the local frequency in each direction, we can use the relations in Section 2.3.3, Eq. (2.19), which relate the angle in a spatio-temporal domain to the angle in the 2-D Fourier domain. From the information we extract we can compute the *local averaged angle* of a reflector. Since the angle in a spatio-temporal or spatial domain is linked by the following relation to an angle in the Fourier domain,

$$\tan(\alpha) = dx_3/dx_1 = dk_1/dk_3, \quad (4.27)$$

the local angles are related in the same way and we can extract the *local angle* $\langle \alpha(\mathbf{x}_D) \rangle$ according to

$$\langle \alpha(\mathbf{x}_D) \rangle = \tan^{-1} \left(\frac{\langle f_1(\mathbf{x}_D) \rangle}{\langle f_3(\mathbf{x}_D) \rangle} \right), \quad (4.28)$$

in which $\langle f_1(\mathbf{x}) \rangle$ and $\langle f_3(\mathbf{x}) \rangle$ are given by Eqs. (4.25) and (4.26).

We have used the zoneplate in Fig. 4.7 (a) for the illustration of the local angle, since the circles consist of the widest spectrum of local angles. For the computation of the angles we have used a complex Daubechies-16 maxflat filter. The result is shown in Fig. 4.15. The angles that are present in the zoneplate shown in the left figure (a) are displayed accurately without any

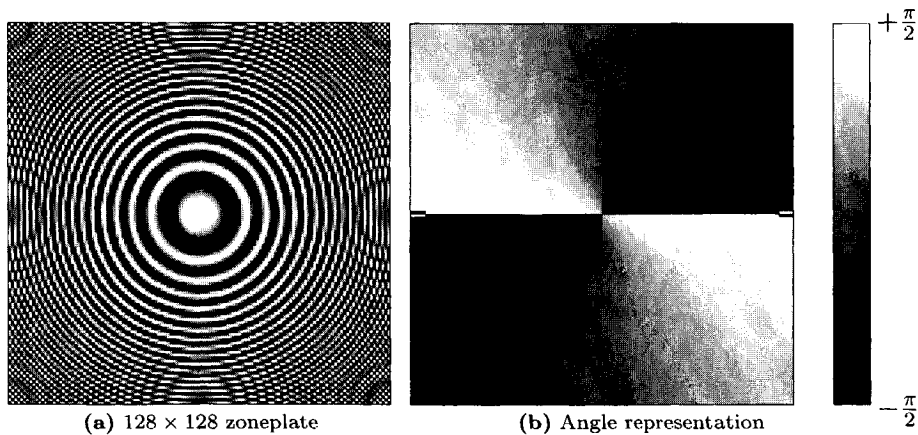


Figure 4.15: (a) 128×128 Zoneplate, (b) Angle representation of (a), using complex Daubechies-16 maxflat Hilbert operators.

aliasing in the figure on the right, (b). An important asset of the angular representation is its sensitivity for positive and negative angles.

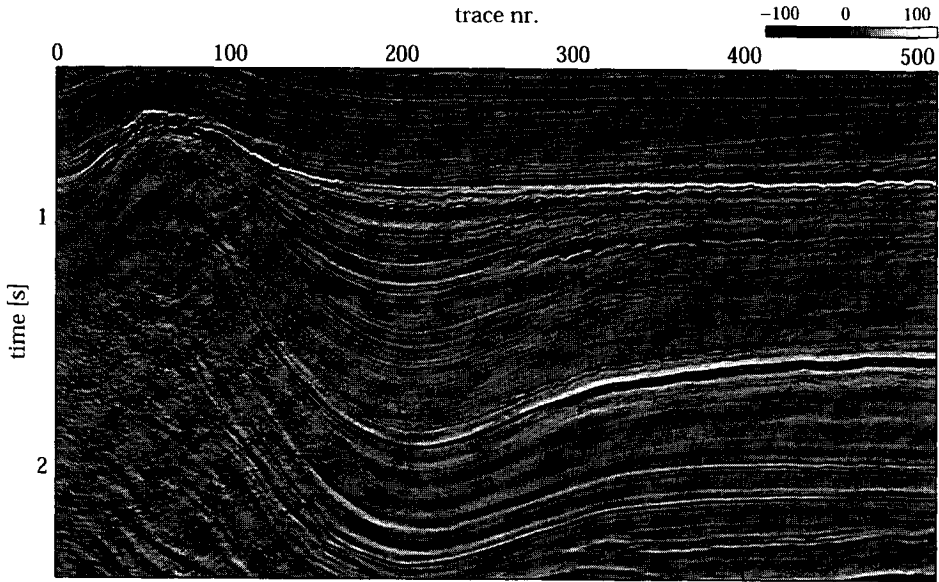
The algorithm is stable under all possible angles, and under the wide range of frequencies present in the zoneplate. The next step is to evaluate its performance on seismic data. Again we consider the seismic section in Fig. 4.9 (a), for convenience we have magnified the section in Fig. 4.16 (a) for reference. Below the section in Fig. 4.16 (b) we show the correspondent angle representation. The slope of the salt dome shows up in the figure as steep negatively dipping angles. The salt dome itself shows a chaotic distribution of angles, which is confirmed in the seismic section by the lack of any consistently correlating information. In between some of the reflections, thin lines show which seem to display inaccurate angle information. These thin lines are caused either by the aliasing of the instantaneous frequency in either of the directions or by the denominator in the right term of Eq. (4.28), which shows a pole at $\langle f_3 \rangle = 0$.

When we combine the information from our local polar frequency with the information of the local angle and the instantaneous reflection strength we come to a complete local characterization of the image. We can decompose an image into a geometric component, a polar Fourier component and an energy component. Although the extra information may not seem to add extra clarity for two-dimensional data, an enormous amount of extra information can be extracted using these techniques for three-dimensional volumes. This will be the topic of the next section.

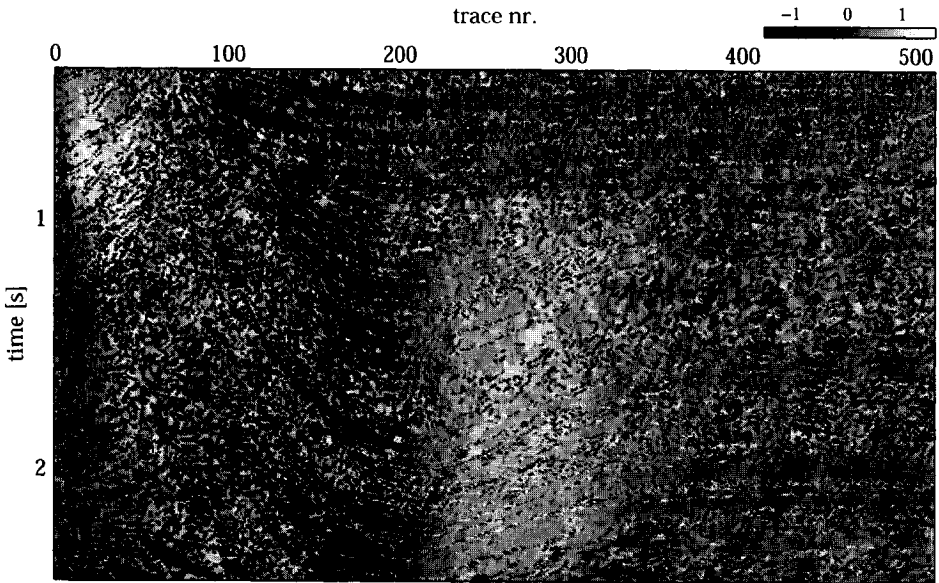
■ 4.4.3 Seismic volume attributes

The two-dimensional attributes that are introduced in the previous section can be extended to three dimensions. The local polar descriptions that are obtained then change into spherical descriptions and the geometry extends to the geometry in a volume. We will show some preliminary results of time-slices with 3-D attributes, local radial frequency, local dip and local azimuth.

Local radial frequency As we have seen in the previous section, the quality of the frequency attributes improves with the inclusion of an extra dimension. The reason for this behavior is that the additional dimension enhances the numerical stability of the algorithm. The polar frequency is per definition positively valued, and has a much smoother response than the instantaneous frequency in a single dimension (compare Fig. 4.11 and Fig. 4.13). In the case we are dealing with a seismic volume instead of a 2-D image, the additional



(a)



(b)

Figure 4.16: (a) Part of seismic section (512×512 samples, $dt = 0.004ms$) from L5-block in the North Sea, (b) angle representation of section in (a).

dimension has to be accounted for in a similar way as for the 2-D case. First we compute the analytic volume by performing a local Hilbert transformation in the vertical x_3 -direction. Subsequently this volume is divided into four quadrants. With the information on the phase in each of the quadrants we can calculate the local spherical or *radial* frequency in a volume. We first introduce the definition of the four quadrants of the analytic volume,

$$\begin{aligned} \mathcal{A}^{\pm\pm} \{u(\mathbf{x})\} &= u_{\pm\pm}^A(\mathbf{x}) \\ &= \mathcal{F}^{-3} \{ \chi_{R\pm}(k_1) \chi_{R\pm}(k_2) \chi_{R+}(k_3) \mathcal{F}^3 \{u(\mathbf{x})\} \} \end{aligned} \quad (4.29)$$

in which we employ \mathcal{A}^{++} , \mathcal{A}^{+-} , \mathcal{A}^{-+} and \mathcal{A}^{--} to indicate the four quadrants of the analytic volume, in which the plus and minus indicate the wavenumber sectors in k_1 and k_2 , respectively. The operator \mathcal{F}^3 indicates 3-D spatial Fourier transformation over the variables in \mathbf{x} , and the characteristic functions χ_{R+} and χ_{R-} are given by the Eqs. (4.18) and (4.19), respectively. Each of the quadrants on their turn can be rewritten in terms of an envelope and a phase

$$u_{\pm\pm}^A(\mathbf{x}) = |A_{\pm\pm}(\mathbf{x})| \exp(i\varphi_{\pm\pm}(\mathbf{x})), \quad (4.30)$$

which together add to the analytic volume

$$u_3^A(\mathbf{x}) = u_{++}^A(\mathbf{x}) + u_{+-}^A(\mathbf{x}) + u_{-+}^A(\mathbf{x}) + u_{--}^A(\mathbf{x}), \quad (4.31)$$

the instantaneous frequencies $\langle f_s^{\pm\pm}(\mathbf{x}) \rangle$ along the components of the vector $\mathbf{x} \in \mathbf{R}^3$, containing positive or negative horizontal spatial frequencies, can be calculated through the following relation

$$\langle f_s^{\pm\pm}(\mathbf{x}) \rangle = \frac{1}{2\pi} \frac{d\varphi_{\pm\pm}(\mathbf{x})}{dx_s}. \quad (4.32)$$

Upon combining the information from each of the components, we can calculate the local radial frequency $|\langle f(\mathbf{x}) \rangle|$, according to

$$|\langle f(\mathbf{x}) \rangle| = \sqrt{(\langle f_1(\mathbf{x}) \rangle)^2 + (\langle f_2(\mathbf{x}) \rangle)^2 + (\langle f_3(\mathbf{x}) \rangle)^2}, \quad (4.33)$$

in which

$$\langle f_s(\mathbf{x}) \rangle = \begin{cases} \langle f_s^{++}(\mathbf{x}) \rangle & \text{for } |A_{++}(\mathbf{x})| \geq |A_{+-}(\mathbf{x})| \cup |A_{-+}(\mathbf{x})| \cup |A_{--}(\mathbf{x})|, \\ \langle f_s^{+-}(\mathbf{x}) \rangle & \text{for } |A_{+-}(\mathbf{x})| > |A_{++}(\mathbf{x})| \cup |A_{-+}(\mathbf{x})| \cup |A_{--}(\mathbf{x})|, \\ \langle f_s^{-+}(\mathbf{x}) \rangle & \text{for } |A_{-+}(\mathbf{x})| > |A_{++}(\mathbf{x})| \cup |A_{+-}(\mathbf{x})| \cup |A_{--}(\mathbf{x})|, \\ \langle f_s^{--}(\mathbf{x}) \rangle & \text{for } |A_{--}(\mathbf{x})| > |A_{++}(\mathbf{x})| \cup |A_{-+}(\mathbf{x})| \cup |A_{+-}(\mathbf{x})|. \end{cases} \quad (4.34)$$

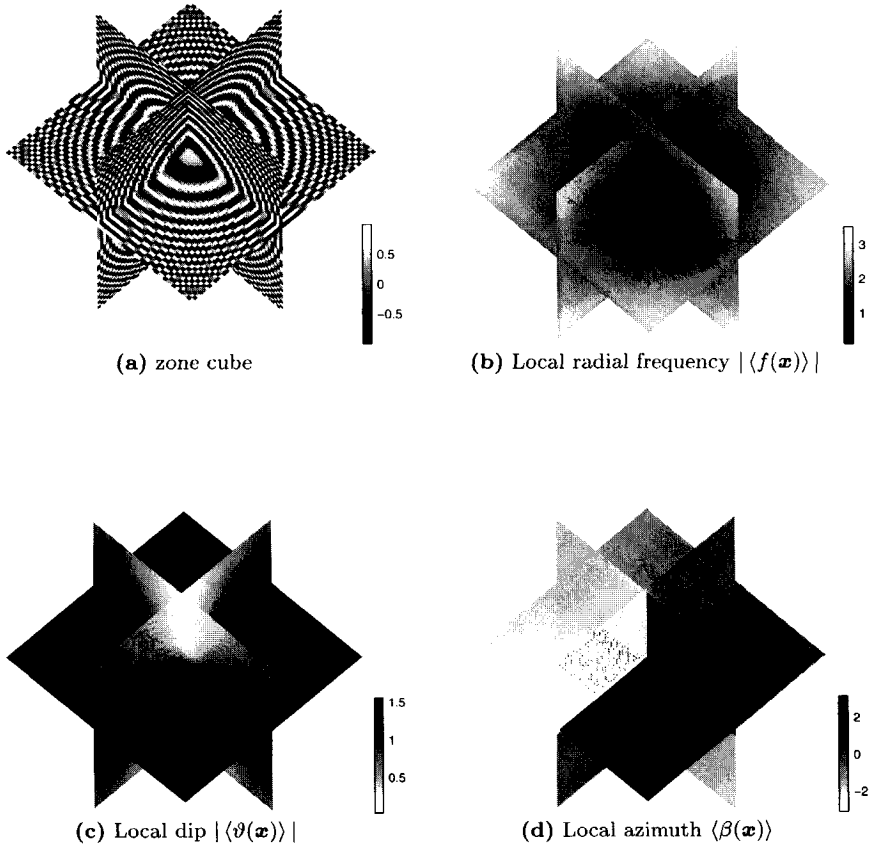


Figure 4.17: (a) Zonesphere, and its Maxflat Daubechies-16 volume attributes: (b) local radial frequency, (c) absolute local dip, (d) local azimuth.

For the numerical implementation of the characteristic functions $\chi_{R^+}(x)$ and $\chi_{R^-}(x)$ in Eq. (4.29), we use the maxflat projection filter P^+ in Eq. (4.5) and its complex conjugate P^- , respectively.

For the numerical evaluation of the attributes we introduce the zonecube as the 3-D equivalent of the zoneplate. We use the 64×64 zonecube as shown in Fig. 4.17 (a) to test the performance of the attributes. The cube consists of concentric spheres that have a chirp-like behaviour in the radial direction.

The cube contains all possible local geometries of correlating amplitudes, and shows a high range of radial frequencies, ranging from very low radial frequencies in the center towards very high frequencies at the periphery. In Fig. 4.17 (b), we show the slices through the three axes of the local radial frequency. For the determination of the spatial frequencies we used the complex Daubechies-8 maxflat filter. The trends in the resulting radial frequency representation agree with the description of the zonecube. It shows a very low radial frequency response in the center, represented by the dark-gray values. Towards the edges, the radial frequency gradually increases with radius, showing the highest frequencies at the boundaries of the cube. There is no sign of aliasing or other artifacts in the volume.

local dip and azimuth Similarly to the 2-D case, we can extract local geometric information of a reflector in the volume. To describe the geometry in a volume, we introduce the concepts *dip* and *azimuth*. The dip of a plane surface is defined as the angle of inclination of this surface with the horizontal plane. The azimuth is defined as its orientation. In a mathematical formulation, the dip ϑ is related to the derivatives in each direction of the spatial vector $\mathbf{x} \in \mathbf{R}^3$

$$\tan(\vartheta) = \frac{dx_3}{\sqrt{(dx_1)^2 + (dx_2)^2}}, \quad \text{with } 0 \leq |\vartheta| < \pi/2, \quad (4.35)$$

and the azimuth β as

$$\tan(\beta) = \frac{dx_1}{dx_2}, \quad \text{with } 0 \leq \beta < 2\pi. \quad (4.36)$$

As we have seen in Eq. (4.27), the angle can also be described in terms of ratios of spatial frequencies instead of spatial derivatives. In that case the dip ϑ is defined as

$$\tan(\vartheta) = \frac{\sqrt{(dk_1)^2 + (dk_2)^2}}{dk_3}, \quad \text{with } 0 \leq |\vartheta| < \pi/2, \quad (4.37)$$

and the azimuth as

$$\tan(\beta) = \frac{dk_2}{dk_1}. \quad (4.38)$$

When we want to describe the geometry *locally*, we can do that in terms of the local spatial frequencies $\langle f_s(\mathbf{x}) \rangle$ as given in Eq. (4.34). The *local* dip

$\langle\vartheta(\mathbf{x})\rangle$ is then defined as

$$\langle\vartheta(\mathbf{x})\rangle = \tan^{-1} \left(\frac{\sqrt{\langle f_1(\mathbf{x}) \rangle^2 + \langle f_2(\mathbf{x}) \rangle^2}}{\langle f_3(\mathbf{x}) \rangle} \right), \quad (4.39)$$

and the *local* azimuth $\langle\beta(\mathbf{x})\rangle$ is defined in terms of the ratio of the local horizontal frequency components according to

$$\langle\beta(\mathbf{x})\rangle = \tan^{-1} \left(\frac{\langle f_2(\mathbf{x}) \rangle}{\langle f_1(\mathbf{x}) \rangle} \right). \quad (4.40)$$

For the numerical evaluation of the accuracy and stability of local dip and azimuth, we refer to the zonecube in Fig. 4.17 (a) again. The spheres have the largest possible variety of local geometries containing all dips and azimuths. In Fig. 4.17 (c), we show the local dip representation as computed with the complex Daubechies-8 maxflat filter for the decomposition of the analytic volume into its quadrants (Eq. (4.29)). The dark gray-values indicate near vertical dips, the white gray-values indicate near-horizontal dips. The dip response confirms exactly what we see in the zonecube in Fig. 4.17 (a), containing horizontally oriented amplitudes around the vertical axis and vertical oriented amplitudes on the sides of the spheres.

In Fig. 4.17 (b) the local azimuth of the zonecube is shown. the azimuth shows the orientation or the direction in which the local dip is oriented. The local azimuth response looks smooth, gradually increasing clockwise from $\langle\beta\rangle = 0$ to $\langle\beta\rangle = 2\pi$ on the plane of the horizontal axes.

For seismic interpretation the local dip and azimuth are very informative, especially for interpretation of lateral slices such as time or depth slices. Looking at the orientation of the reflector reveals much more geometric information than the amplitude slice. The dip and the azimuth are vectors with a direction, whereas the amplitude is a scalar value, which hardly contains geometric information except for a blurred contourline. We will elaborate on the geometric attributes and their seismic implications later on in Chapter 7. In that chapter we also introduce a novel platform to represent the geometric attributes in the form of a virtual topography. This topography, which goes by the name of *pseudo-horizon*, provides us with an excellent platform to project multiple attributes in a single representation.

To get an idea of what the attributes look like for seismic data, we show a preview of a seismic example in this chapter. For this purpose we have selected a time-migrated seismic dataset from the F09-block in the North Sea near the Netherlands. The results are shown in Figs. 4.18 and 4.19. The

seismic amplitude slice is shown in Fig. 4.18 (a). In Fig 4.18 (b), the local radial frequency is shown. The strong amplitudes in the top of the timeslice show as a smooth constant low frequency band. The local dip and azimuth are represented in Fig. 4.19 (a) and (b). The strong amplitudes in the amplitude slice appear to be flat. It is logical that near horizontal reflectors show low frequent information. Steeply dipping reflectors tend to show high frequencies as we can observe from the seismic sections in Figs. 4.14 and 4.16. The azimuth shows the direction of the inclination revealing structural information. For horizontally oriented layering, the azimuth is hard to determine and the azimuth is often unstable.

The attributes we have discussed in this chapter reveal additional infor-

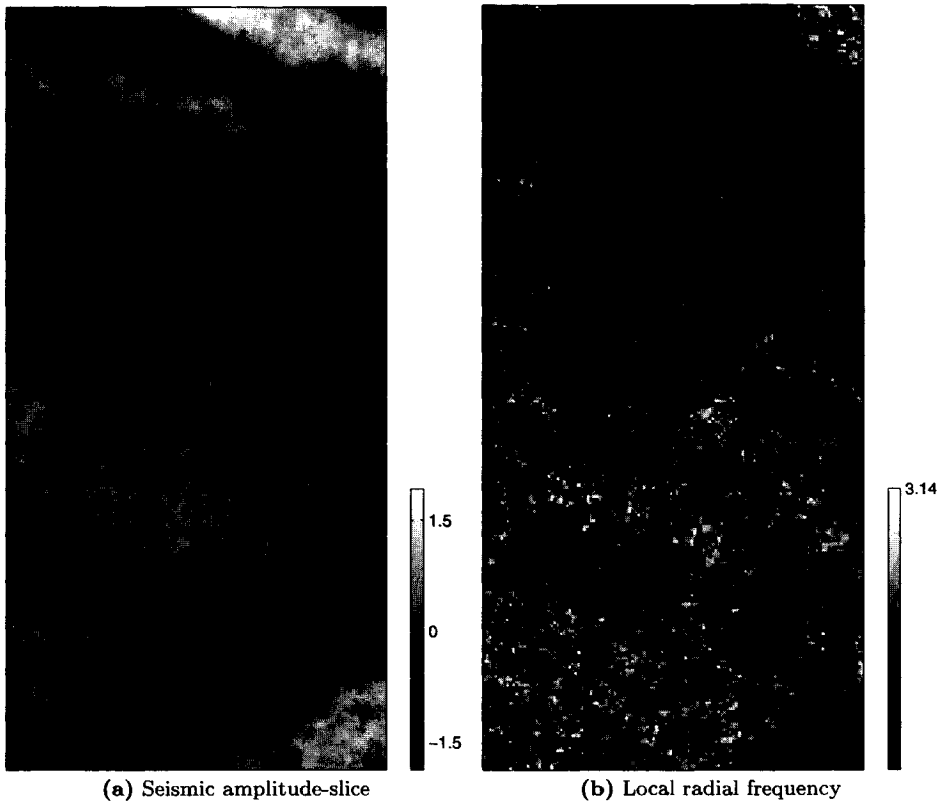


Figure 4.18: (a) seismic amplitude slice (256×128 , $dx = 12.5m$, $dy = 25m$) from F09-block, and its *Maxflat Daubechies-16* volume attributes: (b) local radial frequency

mation for the interpretation. Especially the timeslice interpretation is enhanced, because of the vectorial representation of the data. We have only shown some preliminary results for the evaluation of the method. Later on in Chapter 7 we will elaborate on all different attributes discussed in this thesis and various ways to combine them in a single representation. Because there is a high coherency between the various attributes, the right combinations of attributes enhance the information present.

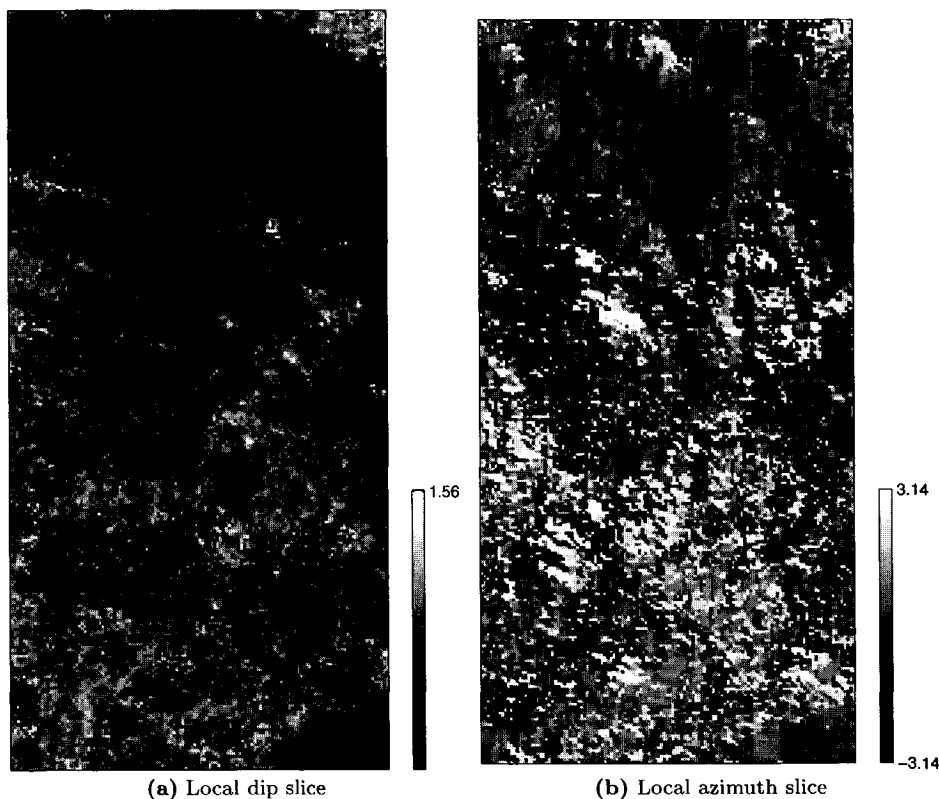


Figure 4.19: (a) Absolute local dip slice at same depth as time-slice in Fig 4.18 (a); (b) local azimuth slice.

Pre-projection complex wavelet transform

The added value of the phase in the wavelet transformation opens perspectives in directional information extraction, improvement of shift-invariance of wavelet transforms and potential for novel processing techniques. For understanding the drive behind the development of complex wavelet transforms, we refer to the *cosine transform*. The cosine transform builds up the signal with infinite cosine functions of varying frequency. The discrete cosine transform has been successfully applied in image and signal processing, for instance in compression techniques such as JPEG. There is a strong analogy between the wavelet transform and the cosine transform. The discrete cosine transform can be interpreted as a wavelet transform that uses the infinite cosine as its basis function. This analogy between these two transforms leads to a question. Although the cosine transform is very useful for certain signal manipulation operations, its brother the Fourier transform has proven to be useful for a much wider range of applications. The Fourier transform needs two basis functions to span a function, the cosine and the sine functions. These functions are in exact quadrature and form a Hilbert transform pair. Although the second set of functions increases the redundancy of the transform (which is a setback for data compression), the phase, described by

the imaginary sine function in the Fourier transform, opens gates in signal processing that could have never been opened with cosine functions alone. The advantages of non-redundancy in the cosine transform pales before the numerous benefits of the Fourier transform.

The question that comes to mind considering all this is, does there exist a wavelet equivalent of the Fourier transform? Yes, however, there is not one obvious solution. Due to the nature of wavelets there exist many complex equivalents. In this and the following chapter we will discuss two different types of complex wavelet transforms. Both have their own advantages and disadvantages. We have called the first implementation, the pre-projection complex wavelet transform, since it uses a projection of the function before wavelet transformation. For the second algorithm, we employ an iterated algorithm, so we call that the iterated complex wavelet transform. Just like the Fourier transform, both transforms can be described in terms of an amplitude and a phase.

In this chapter we will discuss the pre-projection complex wavelet transform, in the next chapter we will deal with the iterated complex wavelet transform. Both transforms use local Hilbert transforms for the calculation of the complex equivalents. It turns out that the local Hilbert transform is scale dependent. We will discuss the choices that lead to the different transforms and the advantages of each of the complex wavelet transforms. General advantages of complex wavelet transforms include shift-invariance of the transform and improved directional discrimination. After the introduction of the transforms, we will show how we can extend each of them to higher dimensionality which makes them suitable for computation of seismic attributes.

5.1 Complex wavelet transforms: How and why?

All roads lead to Rome in the world of complex wavelets (Abry, 1994; Kingsbury, 1998; Bernard, 1999; van Spaendonck *et al.*, 2000; Selesnick, 2001). First we have to get consensus of the desired properties that the transform should have. In this section we will illustrate the idea of complex wavelet transforms with the use of *ideal* filters. This section is a first theoretical step towards the complex wavelet transforms that are discussed in this and the next chapter. This approach is the key for choices that we have made.

The starting point in our deliberation is the conventional wavelet transform using ideal filters. An ideal filter is the continuous time rectangular

shaped filter in frequency, that gives us the exact right frequency information. The example of ideal filters is frequently used for the illustration of subband coding. We often design ideal filters passing through exactly the desired frequency information, and later on we compute an FIR approximation. Using ideal filters in the fast discrete wavelet transform would result in *no* aliasing in the subbands. This important observation should be kept in mind during the following deliberation.

In practice for a discretized signal, we are always condemned to use an approximation of such an ideal filter, since the information in such a filter is of infinite length in time. The continuous Hilbert transform is an example of an ideal filter. In practice we use either the discrete Fourier transform to approximate the ideal filter, or the local Hilbert transform as we have seen in the preceding chapter. Ideal filters will be indicated with the square cap symbol $\hat{\square}$.

When we look at multiresolution of real-valued functions in terms of ideal filters, the nesting spaces $\mathcal{V}_{\pi_0} - \mathcal{V}_{\pi_\infty}$ in Fig. 3.1 are spanned by rectangularly shaped scaling functions $\hat{\varphi}_{\pi_0}(\omega) - \hat{\varphi}_{\pi_\infty}(\omega)$. These functions are illustrated in Fig. 5.1 (a). The rectangular functions are completely nested in the finer resolution space. The property of multiresolution is one of the cornerstones of the discrete wavelet transform. The question is however, in how far we want to hold on to this property when we design *complex* wavelets. We will see that the discrete implementation sometimes rids of the multiresolution spaces.

Let us first consider the ideal real-valued scaling function $\varphi_\pi(t)$ which is

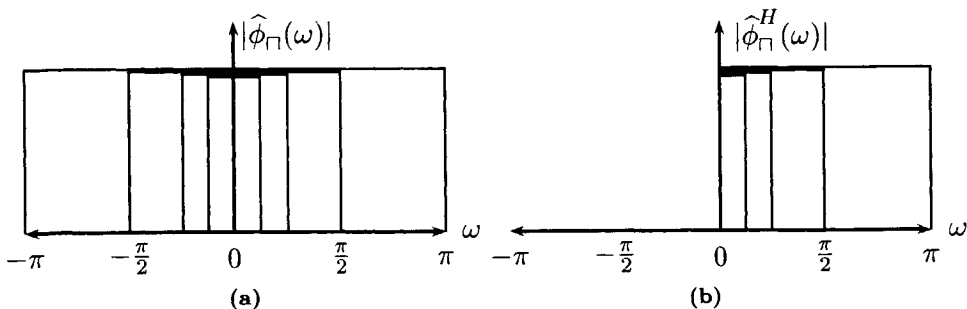


Figure 5.1: (a) Ideal scaling functions in the discrete wavelet transform, (b) Desired ideal analytic scaling functions of the analytic discrete wavelet transform.

defined to be real and given in frequency by

$$\hat{\varphi}_\Pi(\omega) = \begin{cases} 1, & \text{for } |\omega| < \omega_0 \\ 0, & \text{for } |\omega| \geq \omega_0 \end{cases}. \quad (5.1)$$

From the dilation equation Eq. (3.22) we know that the scaling function at the next coarser scale is given in terms of the scaling function at the current resolution, through a smoothing filter $H(\omega)$, so

$$\hat{\varphi}_\Pi(\omega) = H_\Pi\left(\frac{\omega}{2}\right) \hat{\varphi}_\Pi\left(\frac{\omega}{2}\right). \quad (5.2)$$

Owing to the simple shape of the scaling functions, we can easily show that $H(\omega)$ needs to satisfy

$$H_\Pi\left(\frac{\omega}{2}\right) = \begin{cases} 1, & \text{for } |\omega| < \omega_0 \\ 0, & \text{for } |\omega| \geq \omega_0 \end{cases}. \quad (5.3)$$

We can rewrite Eq. (5.2) in this special case as

$$\hat{\varphi}_\Pi(\omega) = H_\Pi\left(\frac{\omega}{2}\right). \quad (5.4)$$

The ideal scaling function $\hat{\varphi}_\Pi(\omega)$ at any resolution can now be written in terms of the cumulative product of filter coefficients

$$\hat{\varphi}_\Pi(\omega) = \prod_{k=1}^K H_\Pi\left(\frac{\omega}{2^k}\right). \quad (5.5)$$

The ideal *wavelets* $\hat{\psi}_\Pi(\omega)$ can be written in terms of the ideal scaling functions through the filter $G_\Pi(\omega)$, according to Eq. (3.45)

$$\hat{\psi}_\Pi\left(\frac{\omega}{2}\right) = G_\Pi\left(\frac{\omega}{2}\right) \hat{\varphi}_\Pi\left(\frac{\omega}{2}\right). \quad (5.6)$$

The highpass filter $G_\Pi(\omega)$ is given by

$$G_\Pi\left(\frac{\omega}{2}\right) = \begin{cases} 1, & \text{for } |\omega| > \omega_0 \\ 0, & \text{for } |\omega| \leq \omega_0 \end{cases}. \quad (5.7)$$

We can write the total signal as a summation of the coarsest scaling function with additional wavelets as discussed in Chapter 3. In the following two sections we will discuss the two different paths leading to the ideal complex analytic wavelet transform.

■ 5.1.1 Ideal analytic scaling functions and wavelets

What does the ideal *analytic* wavelet transformation look like? Ideally we want the same mathematical description as we use for the conventional wavelet transformation. We will show that the most straightforward approach does not provide us the desirable structure: we cannot iterate on complex scaling functions using complex filter coefficients. However, with a slight modification we can get the ideal analytic wavelet transform subbands in two different ways; One leads to the pre-projection algorithm, the other leads to the iterated complex wavelet transform.

When we consider ideal filters, the analytic function in the Fourier domain as defined in Section 4.1.1 is the summation of the real-valued function with its Hilbert transform. In the Fourier domain the analytic equivalent $\hat{u}^H(\omega)$ of the function $\hat{u}(\omega)$ is described by

$$\hat{u}^H(\omega) = \chi^+(\omega)\hat{u}(\omega), \quad (5.8)$$

in which the characteristic function $\chi^+(\omega)$ is given by

$$\chi^+(\omega) = \begin{cases} 0, & \text{for } \omega < 0 \\ 1, & \text{for } \omega = 0 \\ 2, & \text{for } \omega > 0 \end{cases}. \quad (5.9)$$

Due to their symmetry, analytic functions show several interesting properties. In the Fourier domain these are given by

$$\hat{u}^H(0) = \hat{u}(0), \quad (5.10)$$

and

$$\hat{u}(\omega) = \frac{1}{2} \left[\hat{u}^H(\omega) + \left(\hat{u}^H(-\omega) \right)^* \right]. \quad (5.11)$$

When we want to extend the wavelet transform straightforwardly to a complex analytic equivalent, we simply choose to use the analytic equivalents of the wavelets. Since we first consider the ideal filter implementation, we can justify to use the analytic implementation as discussed above. The ideal complex scaling function $\hat{\varphi}_\Pi(\omega)$ in Eq. (5.1), then becomes its analytic equivalent

$$\hat{\varphi}_\Pi^H(\omega) = \chi^+(\omega)\hat{\varphi}_\Pi(\omega). \quad (5.12)$$

Hence the *analytic scaling function* is exactly given by

$$\widehat{\varphi}_{\square}^H(\omega) = \begin{cases} 0, & \text{for } \omega < 0 \\ 1, & \text{for } \omega = 0 \\ 2, & \text{for } 0 < \omega < \omega_0 \\ 0, & \text{for } \omega \geq \omega_0 \end{cases} \quad (5.13)$$

In the same way as for the real-valued scaling function, we can write the enclosing scaling function at a finer scale $\omega/2$ as

$$\widehat{\varphi}_{\square}^H\left(\frac{\omega}{2}\right) = \begin{cases} 0, & \text{for } \omega < 0 \\ 1, & \text{for } \omega = 0 \\ 2, & \text{for } 0 < \omega < 2\omega_0 \\ 0, & \text{for } \omega \geq 2\omega_0 \end{cases} \quad (5.14)$$

The essential question is now if can we relate the two complex scaling functions in Eqs. (5.13) and (5.14) in the same way as we can relate the real scaling functions. Apparently there are two different ways to relate the analytic scaling functions. The first one, which leads to the pre-projection algorithm uses an ideal real-valued lowpass filter, which guarantees that the step at DC does not change. The other solution leads to the iterated complex wavelet transform and uses a complex filter to relate the analytic scaling function in Eq. (5.14) to the real-valued equivalent of the analytic scaling function in Eq. (5.13). The latter can be easily obtained due to the symmetry conditions for analytic signals.

For the ideal filters we consider here, there is no difference between the two methods. Both end up with the same result. However with the numerical implementation of the filters, the results are going to diverge with every next stage, because the local Hardy projection filter is dependent of the scale.

Hardy projection at the finest resolution. Let us have a closer look at the first implementation that leads to the pre-projection algorithm. We consider the finest ideal scaling function $\widehat{\varphi}_{\square}(\omega/2^K)$ (at the maximum signal resolution), and project this scaling function onto Hardy space H^2 . The analytic scaling functions at coarser scales can be calculated from the first by the formerly mentioned real-valued filter coefficients $H_{\square}(\omega)$ in Eq. (5.4). This is illustrated in Fig. 5.2 (a). Since the filter equals unity at DC (where the step is located in the analytic scaling function), the step function will persist over

each coarser scale of multi-resolution analysis. This idea is the basis for the pre-projection algorithm.

In a mathematical formulation, the above can be written as

$$\widehat{\varphi}_{\square}^H(\omega) = H_{\square}\left(\frac{\omega}{2}\right) \widehat{\varphi}_{\square}^H\left(\frac{\omega}{2}\right). \tag{5.15}$$

The ideal analytic scaling function $\widehat{\varphi}_{\square}^H(\omega)$ at any resolution can now be written in terms of the cumulative product of the real-valued filter coefficients with the analytic scaling function spanning the finest resolution, or

$$\widehat{\varphi}_{\square}^H(\omega) = \prod_{k=1}^K H_{\square}\left(\frac{\omega}{2^k}\right) \chi^+\left(\frac{\omega}{2^K}\right) \varphi_{\square}\left(\frac{\omega}{2^K}\right). \tag{5.16}$$

Although the scale of the characteristic function has no relevance in the context of continuous time, it is taken into account for the discrete implementation. In the same way as for the real wavelet transformation, we can derive the *analytic wavelets* according to

$$\widehat{\psi}_{\square}^H(\omega) = G_{\square}\left(\frac{\omega}{2}\right) \widehat{\varphi}_{\square}^H\left(\frac{\omega}{2}\right). \tag{5.17}$$

We will elaborate on this *pre-projection* algorithm in the Section 5.7, where we will see that in a practical implementation, the Hardy space projection is *not* insensitive for scale. As a consequence, we are condemned by the choice of our Hardy projection filter that is initially used to project the signal onto Hardy space. We will also see in Section 5.7 that this effect is articulated in the coarser scales.

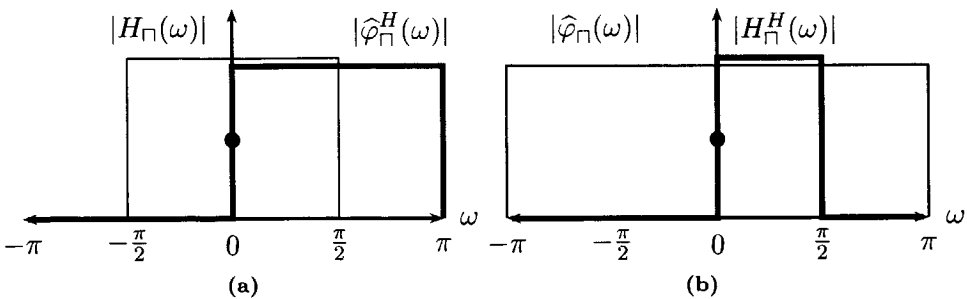


Figure 5.2: The relation between analytic scaling functions within the multi-resolution context: (a) filtering of the analytic scaling function with the real-valued filter $H_{\square}(\omega)$, (b) filtering the real-valued ideal scaling function with the analytic lowpass filter $H_{\square}^H(\omega)$.

Hardy projection of the filter coefficients. The second algorithm is based on the fact that the real part of the analytic signal is equal to the original input, due to the symmetry properties given by Eqs. (5.10) and (5.11). Again we want to calculate the analytic scaling function at any scale. This time, we do not use the analytic scaling function at a higher resolution, but we employ analytic *filter* coefficients to obtain the Hardy projections of the scaling functions. This algorithm is illustrated in Fig. 5.2 (b): The real-valued scaling function is filtered with the analytic filter coefficients. In the ideal analytic situation, this method and the previous show exactly the same results, the practical implementation will not.

Again we refer to Eqs. (5.13) and (5.14). We can calculate the analytic scaling function $\hat{\varphi}_{\Pi}^H(\omega)$ in Eq. (5.13) from its finer scale *real-valued* scaling function by

$$\hat{\varphi}_{\Pi}^H(\omega) = H_{\Pi}^H\left(\frac{\omega}{2}\right) \hat{\varphi}_{\Pi}\left(\frac{\omega}{2}\right), \quad (5.18)$$

with

$$H_{\Pi}^H(\omega) = \chi^+(\omega) H_{\Pi}(\omega). \quad (5.19)$$

We know that due to the symmetry properties of the Hardy-space projection (Eqs. (5.10) and (5.11)), by definition

$$\hat{\varphi}_{\Pi}(\omega) = \frac{1}{2} \left[\hat{\varphi}_{\Pi}^H(\omega) + \left(\hat{\varphi}_{\Pi}^H(-\omega) \right)^* \right]. \quad (5.20)$$

This implies that we can easily continue the iteration for the next step! The cumulative product for the calculation of the analytic scaling function at any coarser scale is now given by

$$\hat{\varphi}_{\Pi}^H(\omega) = \chi^+\left(\frac{\omega}{2}\right) \prod_{k=1}^K H_{\Pi}^H\left(\frac{\omega}{2^k}\right) \hat{\varphi}_{\Pi}\left(\frac{\omega}{2^K}\right). \quad (5.21)$$

In the same way as for the analytic scaling function, we can derive the analytic wavelets with the use of the analytic filter coefficients $G_{\Pi}^H(\omega)$

$$\hat{\psi}_{\Pi}^H(\omega) = G_{\Pi}^H\left(\frac{\omega}{2}\right) \hat{\varphi}_{\Pi}\left(\frac{\omega}{2}\right). \quad (5.22)$$

with

$$G_{\Pi}^H(\omega) = \chi^+(\omega) G_{\Pi}(\omega). \quad (5.23)$$

The implementation of the latter method is extensively discussed in Chapter 6. The FIR implementation of the algorithm leads to an *iterated* wavelet

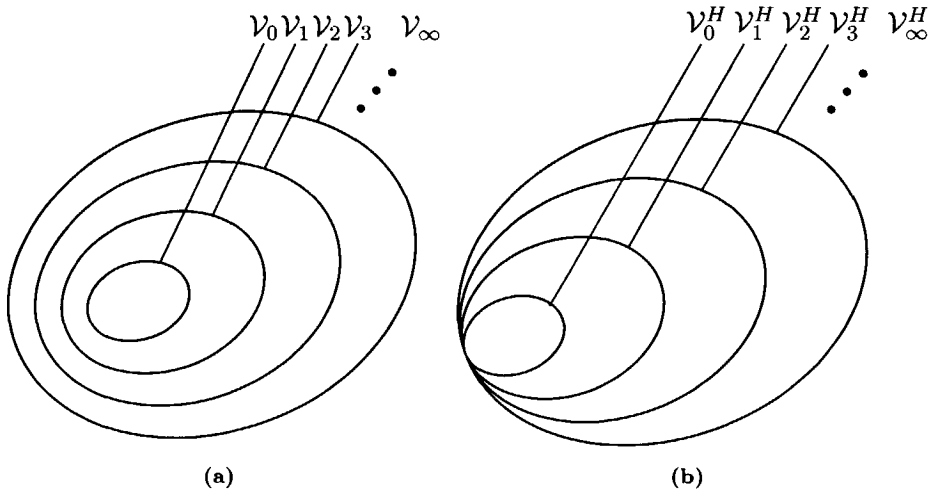


Figure 5.3: Comparison of nesting spaces for the DWT and the complex wavelet transform with ideal filters; (a) Spaces $\mathcal{V}_0 - \mathcal{V}_\infty$ are the spaces of the DWT, (b) Spaces $\mathcal{V}_0^H - \mathcal{V}_\infty^H$ are spaces of the ideal complex wavelet transform.

transform, which renews the Hardy projection at every consecutive stage in the wavelet transform, which makes the algorithm adaptive to scale.

One remark about the implementations is that either the scaling function is complex or the filter coefficients. We are not allowed to use both the analytic scaling function *and* analytic filter coefficients, because in that case the scaling functions are going to blow up with every next step relative to the DC-component. In other words, when we consider the real-valued cumulative product for calculation of the scaling function in Eq (3.34), we are allowed to introduce only one single characteristic function $\chi^+(\omega)$ on the right side of the equation.

■ 5.1.2 Spanning the spaces: Multiresolution or Hardy space?

The scaling functions in the conventional wavelet transform span different resolution approximations of a function. This property is called the *nesting* property and the idea is shown in Fig. 5.3 (a). When we take a closer look at the ideal analytic scaling functions, we understand that these functions also span nesting spaces. However, the spaces are compressed at one side where they all overlap at DC. The nesting spaces of the ideal analytic scaling functions are shown in Fig. 5.3 (b). The spaces \mathcal{V}_j^H are spanned by the

analytic scaling functions $\varphi_{\Pi}^H(t)$.

From the ideal scaling functions discussed in the preceding section, we can proceed to the scaling functions discussed in Chapter 3. As we have mentioned before, ideal filters are not implementable, because these functions have infinite duration. In the wavelet transformation we use FIR approximations of the ideal filters with certain beneficial properties. One of the crucial properties of scaling functions is their nesting property. The functions span multi-resolution approximations of a signal. Furthermore we can impose other constraints such as orthonormality on the system.

In Fig. 5.4 (a) we show the local scaling functions for the DWT. The functions are nested. The spaces spanned by the real-valued scaling functions are shown in Fig. 5.3 (a). These functions now are *locally* operating, and they are FIR. It is important to realize that the choice for these smooth types of filters as an approximation of the ideal scaling functions, is based on the fact that we want the transform to be locally operating. For the fast discrete wavelet transformation the approximation also means that we introduce some aliasing in the transform. From Fig. 3.7, we know that the aliasing becomes less when the filters that are used better approximate the rectangular filters.

The concepts for the complex transforms discussed in the context of ideal filters, can be extended to these type of scaling functions as well. The Fourier responses of the scaling functions obtained by either of the methods are then given by Fig. 5.4 (b). The nesting spaces of these analytic scaling functions are identical to those we obtained for the ideal analytic scaling functions and are given by Fig. 5.3 (b). Since each of the scaling functions contains the same step at DC, all the spaces coincide there. We see that the spaces spanning the analytic scaling functions tend to move to one side and are not concentric spaces. Since we are limited to use discrete functions in the implementation, the question is now, how do we implement the discrete Hilbert transformation? And what happens to the multi-resolution property?

The two approaches discussed in the previous paragraphs can be implemented using local Hilbert transformations. Due to its local form though, the Hilbert transform is not independent of scale anymore! Therefore, the methods will diverge and show different results. Later we will see that we can implement both methods using FIR filters. The first will retain the nesting property of the scaling spaces, but does not separately project each of the scaling functions, the second will not retain the nesting property, but will separately project each scaling function onto the approximate Hardy space.

In summary, in the discussion of complex wavelets we want to emphasize

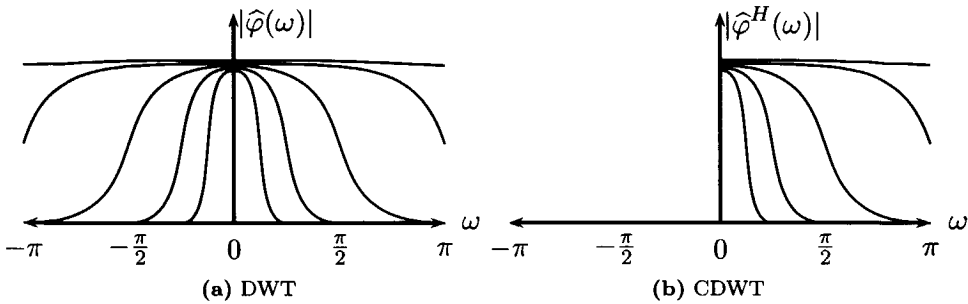


Figure 5.4: The difference in nesting between the DWT and the ideal CDWT. (a) Nesting scaling functions of the conventional discrete wavelet transform; (b) nesting scaling functions of the ideal analytic wavelet transform.

three properties that are important to keep in mind. These properties are

- Hardy symmetry. Does the complex transform satisfy the symmetry properties in Eq. (5.10) and (5.11)?
- Nested function spaces. How do the spaces spanned by the complex scaling function nest?
- Convergence to Hardy space. Does the transform span Hardy space with the complex wavelet transform in the limit?

5.2 Pre-projection complex wavelet transform

In this section we will show how we can use the local Hilbert transformation for the computation of the analytic scaling function. Previously, we have seen that we approximate the ideal scaling functions in the wavelet transform with FIR filters. However, we still have to deal with the Hardy operation to obtain an implementable analytic scaling function.

The Fourier responses of the type of complex scaling functions that we discuss in this section is shown in Fig. 5.5 (b) as opposed to the responses of the analytic scaling functions in Fig. 5.4 (b). In fact we project the scaling functions of the DWT onto local Hardy space \mathcal{H}^+ . This idea is illustrated in Fig. 5.5 (a). The spaces spanned by these scaling functions nest in the same way as those of the analytic scaling functions (Fig. 5.3 (b)).

For the pre-projection complex wavelet transform discussed in this section, we use a smoothed projection operator for the projection of the scaling

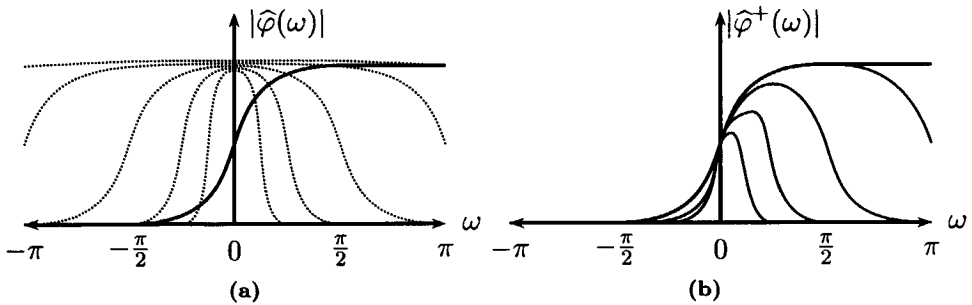


Figure 5.5: Wavelet transformation in *Softy* space: (a) iteration with real-valued scaling functions on *Softy*-space projected complex scaling function. The dotted lines represent the DWT scaling functions (b) The Fourier responses of the resulting scaling functions.

function onto a space containing locally positive frequencies only. In fact we will show that instead of using the local Hardy-space projection operator, we use its spectral factors. In that way we can separate analysis and reconstruction filters. The space in between L^2 and H^2 we call the *Softy* space, as opposed to the *Hardy* space. The *Softy* space is the space of functions that suppresses negative frequencies, but does not satisfy the Hardy symmetry criteria. In this section we will show that when we a real-valued function is spanned by a scaling function, both the real and imaginary part of the *Softy*-space projection of this function can be spanned by the same scaling function. This implies that we can use the real and imaginary component of this function as an input for the discrete wavelet transformation.

We will show how we can implement this algorithm in a fast filter bank decomposition and what the amplitude and phase response look like. The variance to shifting of the input signal is discussed in the last paragraph.

■ 5.2.1 Wavelet transformation in *Softy* space

The pre-projection complex wavelet transform involves two steps: the projection onto *Softy* space, and the subsequent wavelet transformation of the obtained complex signal (van Spaendonck *et al.*, 2000; Fernandes *et al.*, 2000). Since we are interested in performing a wavelet transformation, we first need to consider the function space.

A theoretical background on Softy spaces, is given in Fernandes (2001) and Fernandes *et al.* (2002c). In this thesis we only address the Softy space conceptually. The Softy space needs to meet three criteria. As an approximate Hardy space projection, the negative frequencies in Softy space S^+ are suppressed. Second, there has to be a linear mapping of L^2 onto Softy space. This guarantees that the wavelet transform is valid for functions in Softy space. The third criterion is the perfect reconstruction criterion; a function in Softy space needs to have an inverse mapping onto L^2 .

In the pre-projection algorithm, we perform a Hardy projection before the wavelet transformation. This is consistent with Eq. (5.16) where we perform a projection of the scaling function at the finest scale. We want to replace we the characteristic function $\chi^+(\omega)$ in this equation with the Softy-space projection. We first consider the definition of this space.

For $u(t) \in L^2$, the Softy-space projection is given by

$$\mathcal{S}^+\{u(t)\} = u^+(t) \in S^+. \quad (5.24)$$

The function space S^+ is the Softy space of complex functions of which the negative frequencies are suppressed. The projection $\mathcal{S}^+\{u(t)\}$ is a linear mapping of any real-valued signal $u(t) \in L^2$ onto the real and imaginary parts of $u^+(t)$. In a mathematical formulation this means for $u_0^+(t)$, the projection of $u_0(t) \in \mathcal{V}_0$ with $\mathcal{V}_0 \subset L^2$, that

$$\text{when } u_0(t) \in \mathcal{V}_0 \implies \begin{cases} \Re\{u_0^+(t)\} \in \mathcal{V}_0 \\ \Im\{u_0^+(t)\} \in \mathcal{V}_0 \end{cases} \quad (5.25)$$

and the function $u_0^+(t) \in \mathcal{V}_0^+$. In fact this property has the following implication; the real and the imaginary part of the Softy-space projection $\mathcal{S}^+\{u_0(t)\}$ of a signal $u_0(t) \in \mathcal{V}_0$ are each spanned by the same scaling function $\varphi_0(t)$.

At this point we reach the second stage, the wavelet transformation in Softy space. Since real and imaginary components of the projected signal both live in the same function space they can each be written as an expansion according to Eq. (3.1) and subsequently summed,

$$u_0^+(t) = \sum_{k=-\infty}^{\infty} a_k^R \varphi_{0,k}(t) + i \sum_{k=-\infty}^{\infty} a_k^I \varphi_{0,k}(t), \quad (5.26)$$

The expansion above can be rewritten when we join the two sums into a single expansion,

$$u_0^+(t) = \sum_{k=-\infty}^{\infty} (a_k^R + ia_k^I) \varphi_{0,k}(t). \quad (5.27)$$

Uniting the imaginary part a_k^I and the real part a_k^R into combined complex coefficients a_k^+ leads to the following representation for the expansion in of $u_0^+(t)$

$$u_0^+(t) = \sum_{k=-\infty}^{\infty} a_k^+ \varphi_{0,k}(t), \quad (5.28)$$

in which

$$a_k^+ = a_k^R + ia_k^I. \quad (5.29)$$

The structure of Eq. (5.26) resembles the structure that we have seen in Eq. (3.1). The exact same reasoning for the theory of scaling functions of real-valued functions applies for the complex signal $u_0^+(t)$, since the scaling functions remain real. This implies that the dilation equation Eq. (3.20) and the cumulative product of the filter coefficients in Eq. (3.35) still apply.

When we follow the same reasoning as above for the Softy-space projection of a function $S^+\{f_0(t)\} = f_0^+(t) \in \mathcal{W}_0^+$, for which $\Re\{f_0^+(t)\}, \Im\{f_0^+(t)\} \in \mathcal{W}_0$, we can write an expansion in terms of the wavelets $\psi(t)$, the complex equivalent of Eq. (3.38),

$$f_0^+(t) = \sum_{k=-\infty}^{\infty} b_k^+ \psi_k(t), \quad (5.30)$$

with

$$b_k^+ = b_k^r + ib_k^i. \quad (5.31)$$

Since the wavelet $\psi(t)$ is real-valued, just like the scaling functions, the relation between the wavelet and the scaling function in Eq. (3.41) still applies. Since we know that the theory in Section 3.1 applies for the complex projection of the real-valued signal $u(t)$, we are able to formulate the discrete wavelet transformation of the projected signal $u^+(t)$ as

$$u^+(t) = \sum_k a_k^+ \varphi(t-k) + \sum_{j=0}^{\infty} \sum_k b_{j,k}^+ 2^{j/2} \psi(2^j t - k), \quad (5.32)$$

which can be interpreted as two separate wavelet transforms, one of the imaginary part of $u^+(t)$ and one of the real part of $u^+(t)$. We know that we are able to reconstruct the wavelet transform of $u^+(t)$. However, we still have to perform the inverse projection to obtain $u(t)$ from $u^+(t)$.

The inverse projection preferably is a linear mapping of the Softy space S^+ back to L^2 . Fernandes (2001) showed in his dissertation that the inverse

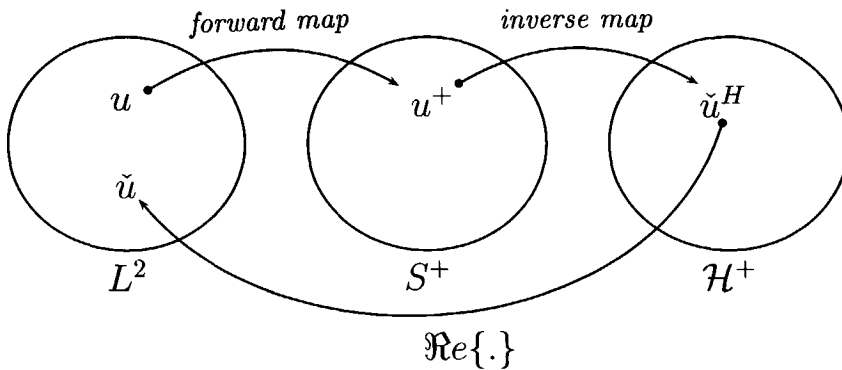


Figure 5.6: Projection onto Softy space and reconstruction via local Hardy space.

mapping is not feasible in general, unless the filters satisfy certain criteria. The problem is that the projection onto Softy space suppresses negative frequencies. This means that we throw away half of the frequencies present in the signal, and retain the other half. The following reasoning illustrates that we *can* perform an inverse mapping, because of the symmetry of real-valued signals in the Fourier transform.

As we have seen in the preceding chapter, for real-valued signals, half of the frequency information is sufficient, because of the symmetry in frequency. This means that if we are able to project a function in Softy space linearly onto the local Hardy space \mathcal{H}^+ , we can reconstruct the input signal. Both, Softy and Hardy space suppress negative frequencies. The difference is that the Hardy space has the additional constraint that the real part of a function in Hardy space is equal to the original real-valued signal. In this way we are able to isolate the signal from its Hardy projection. The idea of forward and inverse projection is illustrated in Fig. 5.6. We project signal $u(t) \in L^2$ by a linear projection onto S^+ . In this operation the negative frequencies in the signal are suppressed. Here we can perform any kind of processing on the complex signal, e.g. wavelet transformation. The inverse projection consists of a linear mapping of $u^+(t)$ onto the local Hardy projection $u^H(t)$ of $u(t)$.

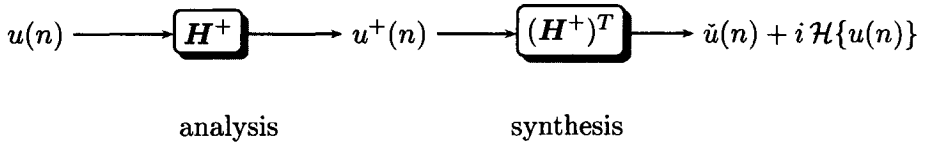


Figure 5.7: Reconstruction of real-valued input after projection without downsampling.

By subsequent segregation of the real part from this $u^H(t)$, the signal $u(t)$ is reconstructed.

In the next section we will discuss the design of the projection filters more extensively and show how we can easily implement the fast pre-projection wavelet transform using filter banks.

■ 5.2.2 Discrete filter bank implementation

We have shown that we can perform a wavelet decomposition after Softy-space projection. Perfect reconstruction can be obtained by the inverse wavelet transform and subsequent mapping from Softy space onto local Hardy space. But what do these projection filters look like and how can we implement them without losing the computational efficiency of the fast wavelet transform?

In the preceding chapter we have shown that we can use FIR filters for a local Hardy space projection. The filters we have used are family of the filters that we use in the wavelet decomposition. For the discrete Softy projection, we can simply use the spectral factors of the local Hardy projection filter, since we know that these yield perfect reconstruction of the real part. This is in perfect accordance with Fig. 5.6, where we show that the reconstruction can be obtained by a projection of the Softy onto the local Hardy space.

Let us revisit the discrete local Hardy projection filter $P^+(\omega)$ that projects a real-valued signal onto a local Hardy space,

$$P^+(z) = I(z) + i\mathcal{H}_N, \quad (5.33)$$

in which $I(z)$ is unity response and \mathcal{H}_N represents the order- N Hilbert transformation (see Chapter 4 for explanation). For the projections, we want to

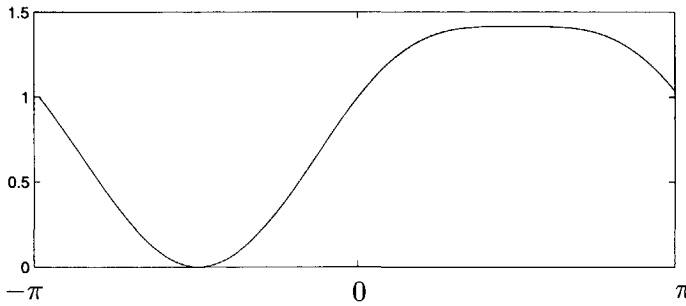


Figure 5.8: Magnitude response of Daubechies-4 pre-projection filter.

use the spectral factors $H^+(z)$ and $H^+(z^{-1})$ of the local Hardy projection operator $P^+(z)$, which can be obtained according to Eq. (4.9)

$$P^+(z) = H^+(z)H^+(z^{-1}). \quad (5.34)$$

Consider a discrete real-valued signal $u(n)$. We define the discrete Softy-space projection $\mathcal{S}^+\{u(n)\}$ to be the linear operation

$$\mathcal{S}^+\{u(n)\} = h^+(n) * u(n). \quad (5.35)$$

In Fig. 5.7 we show schematically the projection analysis and reconstruction operations. Since the analysis filter \mathbf{H}^+ has a complex character, the projected signal $u^+(n)$ is complex. The coefficients after transformation are used as input for the discrete wavelet transform. The synthesis filter $(\mathbf{H}^+)^T$ returns $\check{u}(n)$, a reconstructed version of the signal and its Hilbert transform $\mathcal{H}\{u(n)\}$. Note that the real as well as the imaginary part of $\mathcal{S}^+\{u(n)\}$ are needed for the reconstruction, which means that processing on the complex transform influences the total result.

In Fig. 5.8 we show an example of the magnitude response of the Daubechies-4 projection filter. The vanishing moments of this filter are located at $\pi/2$ and $-\pi/2$.

The coefficients of the discrete pre-projection complex wavelet transform can be found by cascading filter banks. The cumulative inner products for the coefficients in Eqs. (3.86) and (3.87) still apply for the wavelet transform part, and can be rewritten including the pre-projection according to the following two equations. For the consecutive averaging operations we can write

$$U_K^+(\Omega) = \prod_{j=1}^K H\left(\frac{\Omega}{2^j}\right) H^+\left(\frac{\Omega}{2^K}\right) U\left(\frac{\Omega}{2^K}\right) + \text{folding terms}, \quad (5.36)$$

in which $H(\Omega)$ is given by Eq.(3.70). For the detail operation, we can write the cumulative product as

$$U_{\Delta K}^+(\Omega) = G\left(\frac{\Omega}{2}\right) \prod_{j=2}^{\infty} H\left(\frac{\Omega}{2^j}\right) H^+\left(\frac{\Omega}{2^K}\right) U\left(\frac{\Omega}{2^K}\right) + \text{folding terms.} \quad (5.37)$$

with $G(\Omega)$ given by Eq. (3.71). In order to compare the outcome of the cumulative product and see in how far the folding terms interfere in the negative frequencies, we have computed the products $H^+(\Omega)H(\Omega)H(2\Omega)H(4\Omega)$ and $H^+(\Omega)H(\Omega)H(2\Omega)G(4\Omega)$ for Daubechies-4 and -16 filters. The frequency responses are shown in Fig. 5.9. We see that the negative frequencies are suppressed. Although the averaging filter seems to have a better suppression of the negative frequencies than the detail filter, the impression is deceptive. The hump in the averaging filter betrays that also this filter has substantial energy content in the negative frequency range. The more levels are included in the cumulative products in Eqs. (5.36) and (5.37), the worse the suppression of negative frequencies becomes, because the projection is not integrated with the iteration of the transform. This is a major disadvantage of the pre-projection complex transform. Improved results can be obtained by varying the length of projection filters as can be observed when we compare Fig. 5.9 (b), where we have used a Daubechies-16 projection filter with Fig. 5.9 (a). Longer filters have the drawback though, that they are operating less locally and deteriorate the computational efficiency.

The scheme for the analysis tree is given in Fig 5.10. We do not include the optional down-sampling operation after the projection with H^+ in order to reduce the aliasing terms.

The inverse complex wavelet transform works identically to the conventional wavelet transform followed by an inverse projection filter, the adjoint of the pre-projection filter $h^+(n)$. Just like the DWT, the pre-projection DWT can be easily reconstructed by using the inverse filter $(H^+)^T$ in Fig. 5.7. The reconstructed signal $\check{u}(n)$ will consist of a reconstructed real signal $\check{u}_R(n)$ and j times its local Hilbert transform $\mathcal{H}_N\{u(n)\}$.

The practical filter bank implementation of the reconstruction tree is shown in Fig. 5.11. The reconstruction tree reconstructs the signal and destroys the aliasing due to the down sampling operations in the analysis tree.

Because the scaling functions span a complex domain or the Softy space approximation of the Hardy space, the projection will not change with scale.

That is a drawback, because it means that the Softy-space projection is performed only at the highest resolution. An alternative algorithm is treated in the next section, which addresses an iterative complex wavelet transform. The pre-projection algorithm can be implemented in a critically sampled framework when we introduce downsamplers after projection filter \mathbf{H}^+ in Fig. 5.10 and up sampling operators before the reconstruction filter $(\mathbf{H}^+)^T$, in Fig. 5.11. In van Spaendonck *et al.* (2000) we prove that this is possible. Fernandes *et al.* (2002b) discusses the general framework for projection complex wavelet transforms with flexible redundancy. The pre-projection algorithm and its mathematical formulation are more extensively discussed by Fernandes *et al.* (2000, 2002a,c).

■ 5.2.3 Amplitude and phase

One of the main objectives of a complex analytic wavelet transform is the capacity to segregate the wavelet transform into an amplitude and a phase component. Doing so opens up new opportunities for signal processing and analysis with wavelet transforms. In this section we show how the amplitude and phase behavior of the pre-projection complex wavelet transform performs.

Since the pre-projection complex wavelet transform employs the spectral factors of the local Hardy projection in Chapter 4, the accuracy of the al-

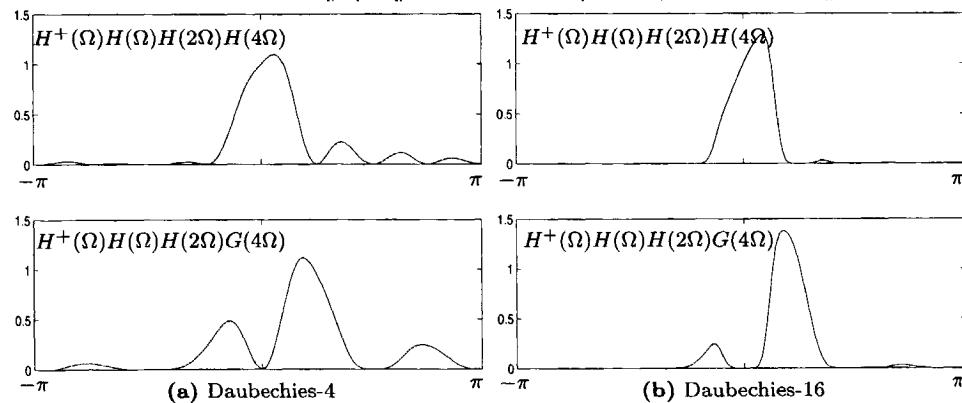


Figure 5.9: The Fourier magnitude responses of consecutive filtering including Softy-space projection for averaging and detail operation with (a) Daubechies-4 and (b) Daubechies-16 filters.

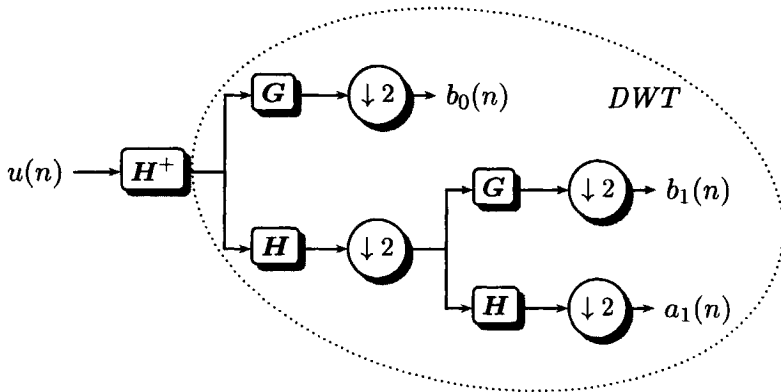


Figure 5.10: Pre-projection complex wavelet transform, a wavelet transform of the projected signal.

gorithm for the coarser scale subbands, i.e. the subbands located in the far branches of the wavelet tree operating at the lower resolution area, are influenced by the order of the local Hilbert transform that is used. The higher the order, the more accurate the quadrature between real and imaginary parts in the lower subbands will be. The drawback though of using longer filters for the projection is that the computational efficiency reduces and that information is more widely spread over the entire signal.

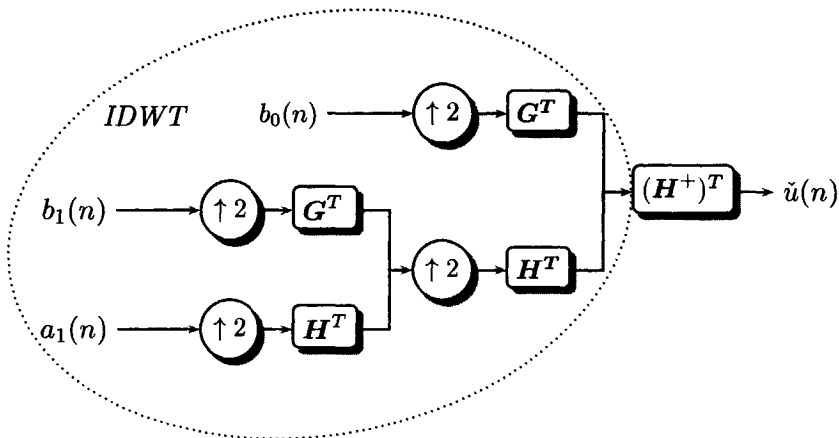


Figure 5.11: Reconstruction of the pre-projection wavelet transform; Inverse wavelet transform followed by inverse projection.

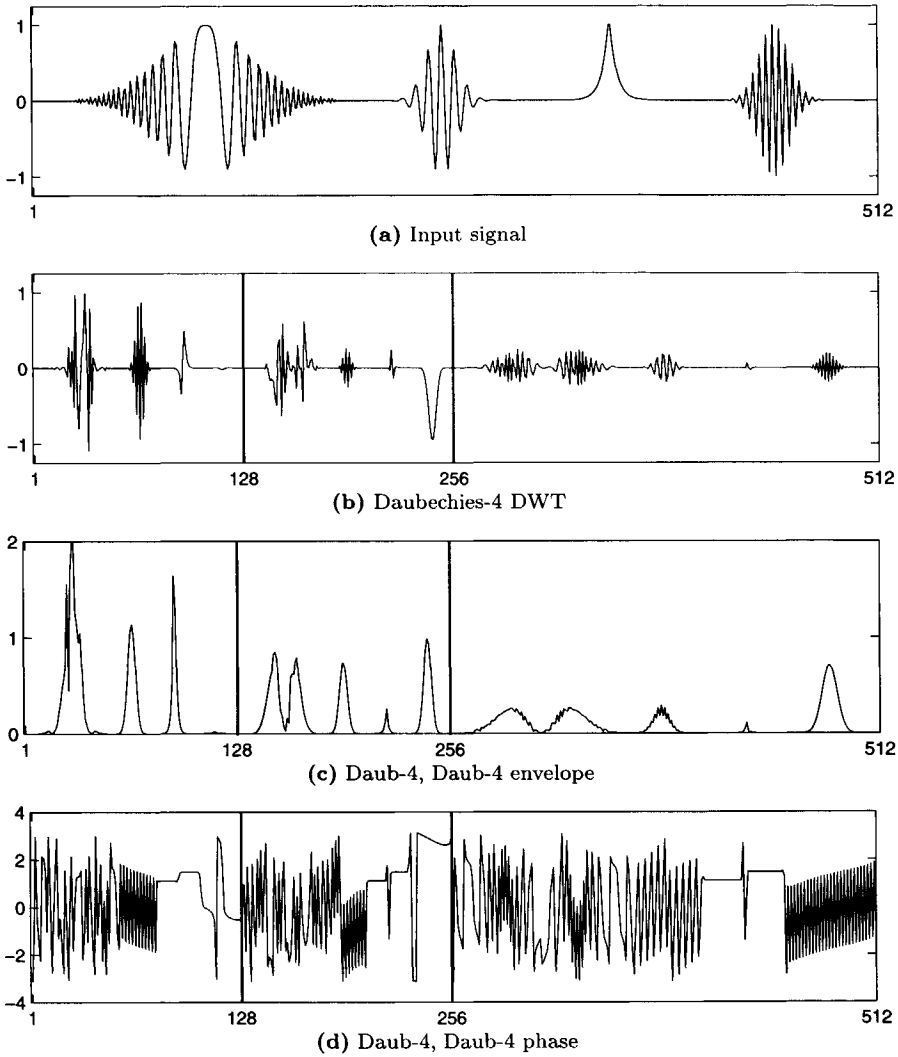


Figure 5.12: The complex wavelet transform of a signal. (a) The original signal, (b) its real-valued Daubechies-4 wavelet decomposition, (c) the amplitude spectrum of the Daubechies-4 pre-projection CDWT, (d) its phase. The scale subbands of the wavelet transform are depicted on the horizontal axes and are separated by vertical lines.

An important aspect is the consistency over scale of both quantities. In Fig. 5.12 (a) we show the signal employed for the illustration. Over its $N = 512$ samples, the signal consists of a wide range of frequencies and scales. A more distinct description of the signal can be found in Section 4.2.1. Fig 5.12 (b) shows the conventional two-stage discrete wavelet transform of the signal: The transform consists of three subbands, the lowpass information (samples $n = 1 - 128$), the middle bandpass information ($n = 129 - 256$) and the highpass information ($n = 257 - 512$). Figs. 5.12 (c) and (d) respectively show the amplitude and the phase component of the two-stage complex pre-projection wavelet transform. The transform has the same subband structure as the DWT in (b). When we compare the amplitude responses of the DWT in Fig. 5.12 (b) with the responses in (c) of the pre-projection CDWT, the latter of the two shows a smoother and more reliable representation in terms of energy than the DWT does. Apart from the fact that the imaginary part stabilizes the envelope, the phase, described by this imaginary part contains a treasure of information for signal processing applications. The instantaneous frequency in each subband for instance can be computed from the phase.

Because we know that larger length projection filters do a better job for Hardy-space projections, we vary the filter length and observe the effects. Since the algorithm is a simple concatenation of a projection filter followed by the conventional DWT, and the signal is not highly non-stationary, the projection does not necessarily need to be short. In Fig. 5.13 we show the same complex pre-projection wavelet transforms with different length projection filters. The wavelet tree in both cases uses length-4 Daubechies filters. In Fig. 5.13 (a) and (c) the amplitude and phase spectra are shown of the Daubechies-4 pre-projection CDWT. The Figs. 5.13 (b) and (d) show the amplitude and phase spectra of the Daubechies-20 pre-projection CDWT. The amplitude responses look very similar, although certain events tend to be smoother in Fig. 5.13 (b) than in (a). This feature is noticeable in wrinkling of the path of the leftmost two events in the highpass band in (a). Furthermore we notice a slight difference in shape of the intermediate pass band between the two bumps at 128th and 160th sample. The differences in phase are visible, but do not provide us as much information. For that reason we also have shown the instantaneous frequencies of each of the transforms in Fig. 5.13 (e) and (f). The instantaneous frequency is computed according to Eq. (2.17). The same remarks for the instantaneous frequency representations of the Hardy-space projections in Section 4.2.2 apply for instantaneous frequencies of the pre-projection wavelet transforms: The instan-

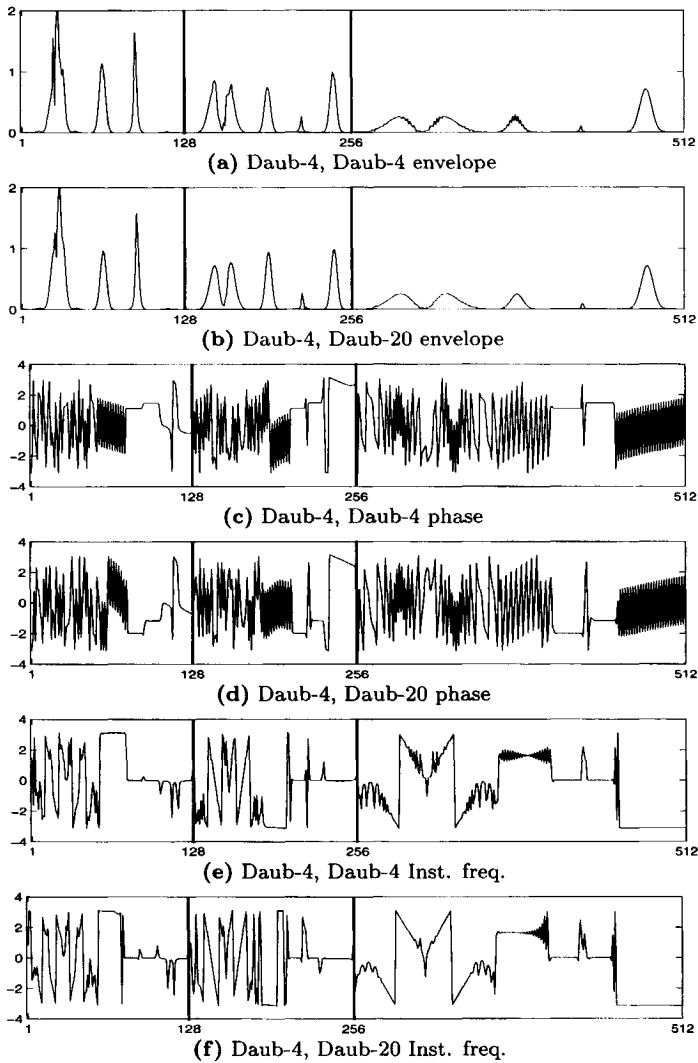


Figure 5.13: Comparison between transforms with different filters; wavelet transform of all figures is performed with a Daubechies-4 filter; subbands are separated by vertical bars (a) amplitude spectrum using Daubechies-4 projection filter, (b) same with Daubechies-20 projection filter, (c) phase spectrum with Daubechies-4 projection filter, (d) phase with Daubechies-20 (e) instantaneous frequency with Daubechies-4 projection filter, (d) instantaneous frequency with Daubechies-20.

taneous frequency of the Daubechies-20 projection CDWT is resolved better and smoother than the Daubechies-4 representation.

■ 5.2.4 Shift-invariance

Another important aspect of the discrete wavelet transform which has gained interest lately, is the shift-variance of the transform. Shift-variance means that the energy distribution in the transform changes due to shifting of the input signal. In some cases this property can be used to ones own benefit, for instance in data compression. When we want to compress data, we fancy the transform that contains the least energy, so we are able to suppress a substantial amount of the coefficients with small contributions. However in general it is beneficial to use transforms that are invariant or close to invariant to shifts in the input signal. Wavelet transforms that are completely shift-invariant do exist. The redundant discrete wavelet transform, for instance, is a transform that belongs to that category, but the tradeoff is a tremendous increase of data due to the absence of the sampling operators. Complex wavelet transforms compromise between shift-invariance and data explosion. They have proven to be moderately shift-invariant with only a data increase of twice the amount of data in the signal, which is the same as in the Fourier transform.

In this section we show the performance in shift-invariance of the Daubechies-4 discrete wavelet transform versus the Daubechies-4 pre-projection complex wavelet transform. The difference between the performance of the two transforms is illustrated using the same signal as above (Fig. 5.12 (a)). We have computed the transforms for the original signal, the signal shifted by $N = +19$ samples to the right and shifted by $N = -18$ samples to the left. The transforms are shown in Fig. 5.14. On the left we show the results of the traditional wavelet transform, on the right the results of the novel pre-projection transform. The difference in performance is clearly visible. Figs. 5.14 (a), (c), and (e) show severe exchange of energy between the subbands. Fig. 5.14 (b), (d), and (f) show a relatively constant shape in each subband, with hardly any energy exchanging between the subbands due to shifting of the signal.

For this particular example we have computed the energy within each of the three subbands of the two-stage wavelet transforms. The results are shown in Table 5.1. The energy-values of the subbands of the traditional wavelet transform are shown in the left table, those of the pre-projection complex wavelet transform are shown in the right table. The subbands are

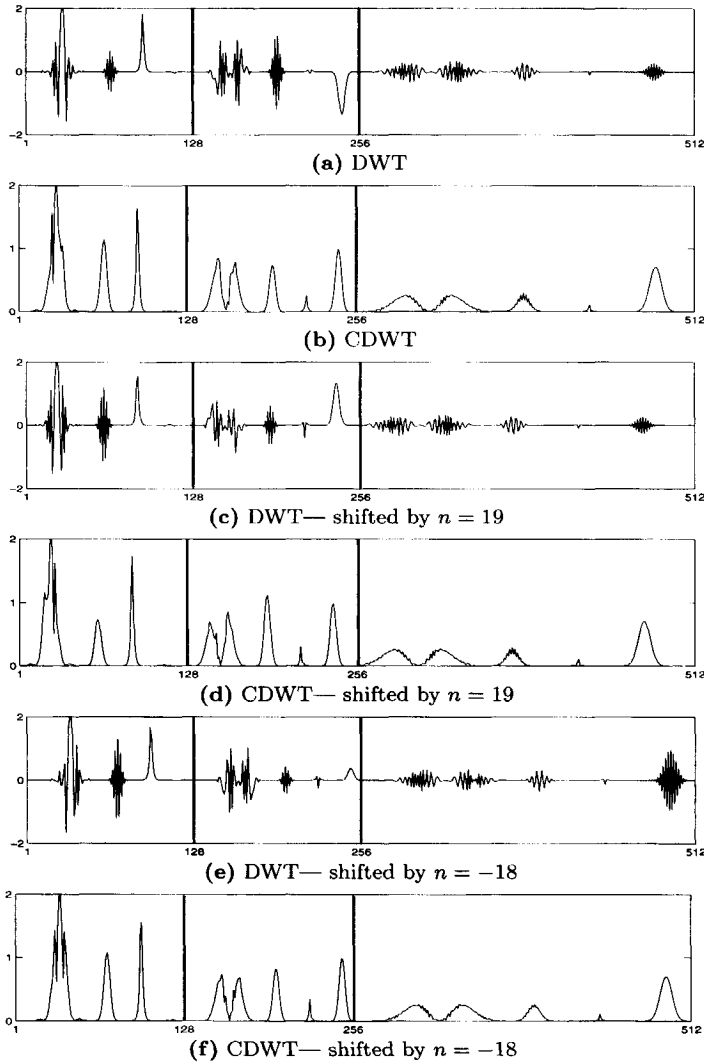


Figure 5.14: Shift-variance of the DWT compared with CDWT; the conventional DWT is shown on the left, pre-projection CDWT is shown on the right. (a)-(b) amplitude spectra of respective transforms, (c)-(d) under a positive shift of the input signal by 19 samples, (e)-(f) under a negative shift of the input signal by -18 samples.

indicated by the respective filter operations they have gone through Fig. 3.6 for the discrete wavelet transform and the tree in Fig. 5.10 for the complex

| <i>Energy content DWT</i> | | | <i>Energy content CDWT</i> | | | | |
|---------------------------|-----------|-----------|----------------------------|-----|-----------|-----------|----------|
| | <i>HH</i> | <i>GH</i> | <i>G</i> | | <i>HH</i> | <i>GH</i> | <i>G</i> |
| (a) | 25.8748 | 21.1500 | 3.0887 | (b) | 30.5968 | 13.0587 | 6.4580 |
| (c) | 33.2669 | 13.7580 | 3.0887 | (d) | 28.5400 | 15.1155 | 6.4580 |
| (e) | 31.4632 | 8.8480 | 9.8022 | (f) | 31.2412 | 12.4394 | 6.4330 |

Table 5.1: Computed cumulative energy in subbands of the transforms in Fig. 5.14.

wavelet transform. *HH* indicates the lowpass information ($n = 1 - 128$), *HG* represents the intermediate bandpass information ($n = 129 - 256$), and *G* is deployed for the highpass information in the transforms ($n = 257 - 512$). The general tendency in the values shows that the CDWT has overall less variance due to shifting of the input signal. Due to the imaginary part that is supposed to be in quadrature with the real part in the signal, the envelopes are relatively stable in each subband. The values do not fluctuate to excessive values, whereas the traditional DWT can fluctuate up to three times the mean value. The total sum of all the energies in each transform adds to 50.1135 and does not change under shifting by definition of the wavelet transform.

5.3 Geometric multi-dimensional complex wavelet transforms

Seismic images have a multi-dimensional nature, requiring a multi-dimensional approach. When we study a seismic image, the reflection amplitudes change along a reflector which often shows a complex geometry. Not only amplitudes vary along reflectors, but also the frequency or scale at which they show up. When we are able to separate all of this information, and subsequently quantify these parameters, we are able to extract considerably more information from our data than we can do by the eye or conventional techniques. The multi-dimensional wavelet transform is useful for the analysis of the scale at which reflections appear, however, due to the real nature of the transform, information in the subbands is difficult to compare.

Therefore we will extend the complex transform discussed in the previous sections to more dimensions. We will see that due the complex character of the transform, it has improved directional selectivity compared to the conventional wavelet transform, and the shift-invariance translates in more dimensions to better energy estimations in the subbands. In short, the complex

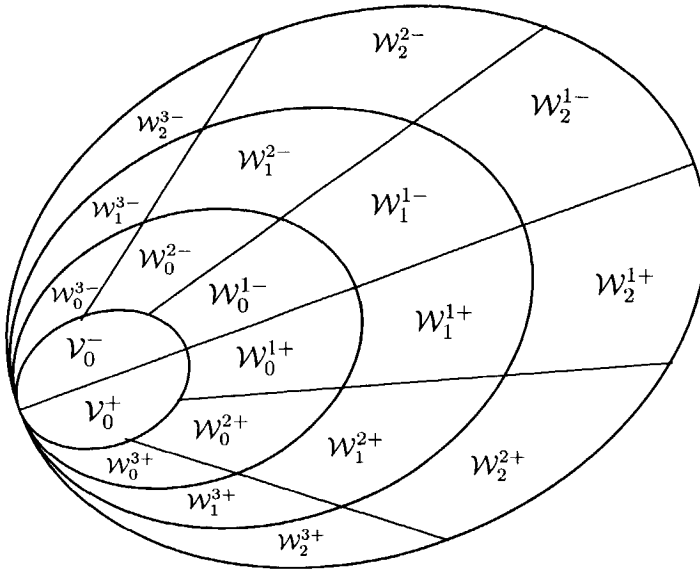


Figure 5.15: The resolution spaces spanned in the 2D pre-projection CDWT. The subbands spanned by the complex wavelets are divided into six regions.

wavelet transform has the ability to decompose seismic images into energy, scale and angle.

As we know from Chapter 4, we have to choose a *direction of preference*; the Fourier transform of an image is given in terms of the frequency along the horizontal axis and the frequency along the vertical axis. The Hardy projection operator suppresses negative frequencies. When we consider an image, we have to make a decision in which direction to suppress the negative frequencies; we call this direction the direction of preference. The only way to circumvent this problem is to switch to Clifford algebra (Blümich and Spiess, 1985; Mitrea, 1994), but that goes beyond the scope of this thesis.

The same problem arises in the multi-dimensional complex wavelet transform. As a spin-off of the extension of the algorithms to more dimensions, we will see how the directional information in an image is differentiated amongst the six subbands of the two-dimensional transforms. The two-dimensional transform easily extends to an arbitrary number of dimensions. Unless specified otherwise, we choose the direction of preference to be the vertical direction.

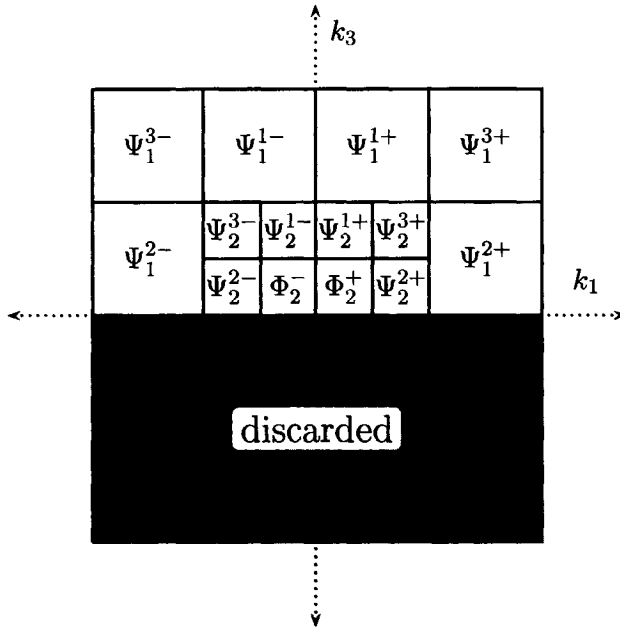


Figure 5.16: Frequency-domain energy localization of tensor wavelets in a two-level 2-D DWT.

■ 5.3.1 Two-dimensional pre-projection complex wavelet transform

The pre-projection complex wavelet transform can be easily extended to more dimensions. Since the projection resembles a local Hardy projection, we can use a similar multi-dimensional extension of the projection in the transform as we have seen in Eq. (4.17). After the projection we can subsequently perform the two-dimensional separable wavelet transform as discussed in Section 3.5 of each of the complex images that we obtain from the projection. The implementation gets more attention in the first paragraph. In the subsequent paragraphs we will discuss several properties of the two-dimensional transform, followed by the last paragraph of this section in which the extension of the transform to an arbitrary number of dimensions is discussed.

Two-dimensional filters As we mentioned before, the pre-projection transform can be split into two parts, the projection and the subsequent wavelet transformation (see Fig. 5.10). The multi-dimensional transformation employs the same scheme; first we project the image onto a two-dimensional Softy space, splitting the frequency information. Subsequently, we perform the conventional two-dimensional discrete wavelet transformation of the projected images. Just as the two-dimensional discrete wavelet transform filters, the two-dimensional projection filters are also separable filters.

In Fig. 5.15, the multi-resolution spaces are shown that are spanned by the two-dimensional complex wavelets and scaling functions. The spaces \mathcal{V}_0^\pm are the spaces spanned by the two-dimensional separable scaling functions, the space $\mathcal{W}_j^{m\pm}$ are the spaces spanned by the wavelets. From the figure we can see that the spaces spanned by the wavelets are split into six subspaces at each scale ($m\pm = 1-, 2-, 3-, 1+, 2+, 3+$). Owing to the same reasons as for the one-dimensional pre-projection transform, we find that although the spaces nest, they all coincide on one edge. The residual coarsest approximation of $U^+(x_1, x_2)$, spanned by the scaling functions is divided into two subspaces \mathcal{V}^- and \mathcal{V}^+ . The two-dimensional complex discrete wavelet transform of an image $U(x_1, x_2)$ is given by

$$\begin{aligned}
 U^+(x_1, x_2) &= \sum_l \sum_k [e^+(k, l)\Phi^+(x_1, x_2, k, l) + e^-(k, l)\Phi^-(x_1, x_2, k, l)] \\
 &+ \sum_{j=0}^{\infty} \sum_l \sum_k [f_j^+(k, l)\Psi_j^{1+}(x_1, x_2, k, l) + f_j^-(k, l)\Psi_j^{1-}(x_1, x_2, k, l)] \\
 &+ \sum_{j=0}^{\infty} \sum_l \sum_k [g_j^+(k, l)\Psi_j^{2+}(x_1, x_2, k, l) + g_j^-(k, l)\Psi_j^{2-}(x_1, x_2, k, l)] \\
 &+ \sum_{j=0}^{\infty} \sum_l \sum_k [h_j^+(k, l)\Psi_j^{3+}(x_1, x_2, k, l) + h_j^-(k, l)\Psi_j^{3-}(x_1, x_2, k, l)],
 \end{aligned} \tag{5.38}$$

in which $U^+(x_1, x_2)$ is the two-dimensional Softy representation of $U(x_1, x_2)$. The separable functions Φ^\pm and $\Psi_j^{m\pm}$ span the spaces \mathcal{V}_0^\pm and $\mathcal{W}_j^{m\pm}$, respectively in Fig. 5.15. They are given by the inner products of their one-dimensional equivalents

$$\begin{aligned}
\Phi^\pm(x_1, x_2, k, l) &= \varphi^+(x_1, k)\varphi^\pm(x_2, l), \\
\Psi_j^{1\pm}(x_1, x_2, k, l) &= \psi_j^+(x_1, k)\varphi_{j+1}^\pm(x_2, l), \\
\Psi_j^{2\pm}(x_1, x_2, k, l) &= \varphi_{j+1}^+(x_1, k)\psi_j^\pm(x_2, l), \\
\Psi_j^{3\pm}(x_1, x_2, k, l) &= \psi_j^+(x_1, k)\psi_j^\pm(x_2, l).
\end{aligned}
\tag{5.39}$$

In the same way as for the 2-D DWT, the first two summations in the expansion in Eq. (5.38) are a low resolution or smoothed version of $U^+(x_1, x_2)$; Each increasing index k in the following summations, adds a finer resolution with increasing detail. The Fourier responses of the tensor wavelets are shown in Fig. 5.16. The figure demonstrates that the coefficients show directional support. The pre-projection complex wavelet transform is *directional selective* for six angles. Where the 2D DWT only separates information into horizontal, vertical and diagonal information, the complex wavelet transforms separate the same information into six directional subbands, with the angles centered around $15^\circ, 45^\circ, 75^\circ$, and their negative equivalents.

For the pre-projection CDWT, the coefficients related to the different quadrants in Fig. 5.16 can be organized in an efficient way just like in the DWT. The two-dimensional tiling that we use for that purpose is shown in Fig. 5.17.

The basis functions contributing to the different angles are shown in Fig. 5.18 for Daubechies-4 filters in each direction. We have only shown the real part of the basis functions, because those better articulate the directional information. The directional shape of the basis functions is clearly visible. The basis functions have a local character.

Filter bank implementation As mentioned before, the pre-projection CDWT is a simple extension from the 1-D case. The filter bank implementation of the 2-D CDWT involves a two-dimensional separable projection, followed by a conventional 2-D discrete wavelet transform. Fig. 5.19 shows a schematic representation of the 2-D pre-projection CDWT. Since the transform is completely separable, and we know that both, the wavelet transform as well as the pre-projection segment, are invertable, we do not pay further attention to the inverse transform.

Amplitude and phase The amplitude and phase are the key properties for a complete description of the signal. The amplitude tells us something about the energy in the signal, the phase about its localization. These properties

| | | | | | | | |
|---------|---------|---------|---------|---------|---------|---------|---------|
| g_2^- | g_1^- | g_0^- | e_0^- | e_0^+ | g_0^+ | g_1^+ | g_2^+ |
| | | h_0^- | f_0^- | f_0^+ | h_0^+ | | |
| | h_1^- | f_1^- | | f_1^+ | | h_1^+ | |
| h_2^- | f_2^- | | f_2^+ | | h_2^+ | | |

Figure 5.17: Tiling of the transform coefficients of the two-dimensional pre-projection complex .

are extremely useful for images. Apart from the fact that these quantities are crucial for the description of wave-propagation, we can use them also for static image description. When we have both, the amplitude and the phase, we can compare these quantities with neighboring traces to obtain structural and reflectivity information.

We have seen that the complex wavelet transform results in a wavelet transform consisting of amplitude and phase. In more than one dimension we retain this property. We will show the amplitude and phase responses of the complex pre-projection transform. An important observation for future use of complex transforms is the consistency over scale of both parameters. This particular parameter is important for the statistical description of the transform, which can be used for segmentation of the image in future applications.

In Fig. 5.20 the pre-projection complex wavelet transform is shown of the 256×256 zoneplate in Fig. 4.7 (a) to illustrate the transform. The magnitude response in Fig. 5.20 (a) clearly shows the directional information in the subbands. The phase is shown in Fig. 5.20 (b).

In Fig. 5.21 we show the magnitude response of the pre-projection complex wavelet transform of the seismic image in Fig. 3.15 (a). Due to the

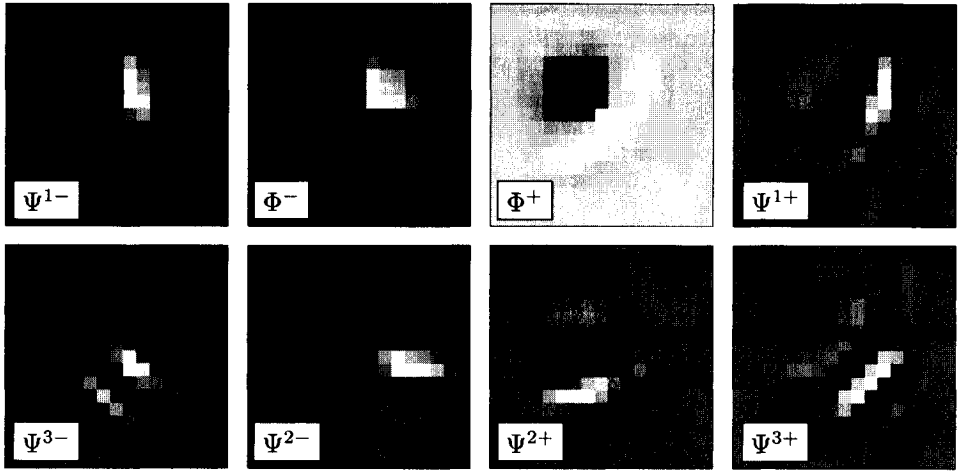


Figure 5.18: The eight directional basis functions of the pre-projection CDWT (real parts). Φ^+ and Φ^- indicate the scaling functions, Ψ^{1-} and Ψ^{1+} indicate the $\pm 75^\circ$ oriented wavelet subbands, Ψ^{3-} and Ψ^{3+} , the $\pm 45^\circ$ oriented wavelet subbands, and Ψ^{2-} and Ψ^{2+} , the $\pm 15^\circ$ oriented wavelet subbands.

directional discrimination, the faults are separated from the reflections. Vertical offsets in horizontal reflections (faults) are detected by the wavelets as

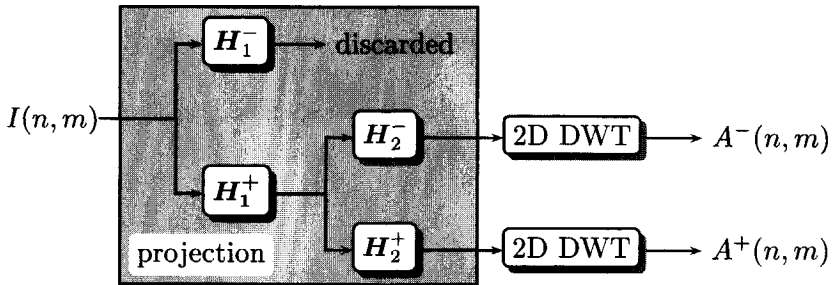
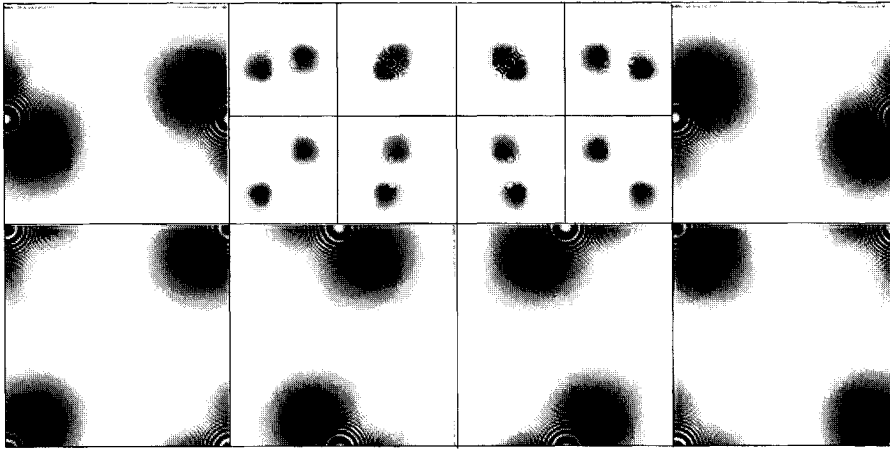
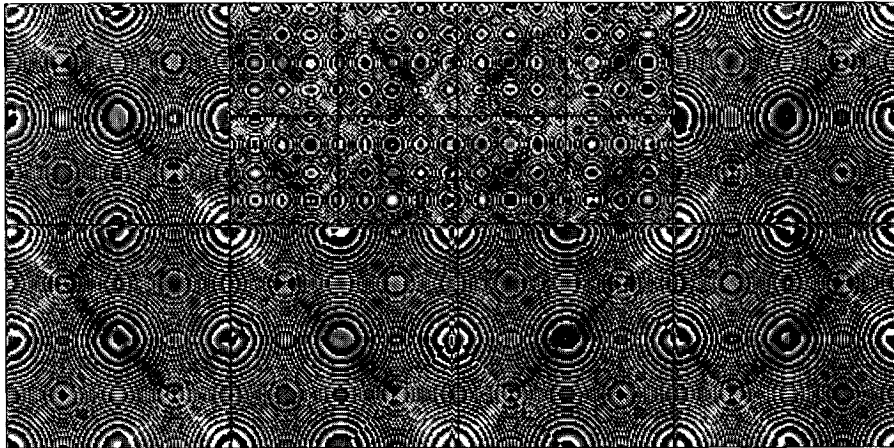


Figure 5.19: Analysis filter bank tree of $u(n)$ obtained by cascading complex low- and highpass filters. The outputs $b_0 - b_2$ are the complex wavelet- and a_2 the complex scaling coefficients. H indicates that the real part of the complex filter $H^+ (= H)$ is used for iteration.



(a)



(b)

Figure 5.20: (a) *The magnitude response of the Daubechies-4 complex pre-projection CDWT.* (b) *The phase responses of the same transform.*

horizontal discontinuities and thus show up in the subbands containing the vertical information. The reflection amplitudes are depicted in the horizontal subbands. The amplitudes consist over different scales, an important criterion for statistical decomposition of an image. Certain faults show up only at coarser scales. This indicates that these faults do not show a very pronounced step, but a smoothed step. At the next coarser scale these smooth steps can become more pronounced. At first sight the phase does not contain very

valuable information. By depicting the derivative of the phase we usually get a better impression of the information contained by the scale. Figure 5.22 shows the phase response of the transform. In this case the added value is not substantially, although we can distinguish the same directional features in the different subbands as with the magnitude response. Against our expectations the faults do not clearly show up on the phase representation, although the phase is often employed for visual fault detection.

Directional information According to the frequency information in the complex wavelet transform, the subbands contain directional information in the space domain (Fig. 5.16). The directional shapes of the basis functions affirm that (Fig. 5.18).

Let us verify if this is true using the wavelet transform of the synthetic zoneplate image (see Fig. 4.7 (a)) in Fig. 5.20. This image is especially useful for the illustration of the directional information and the polar frequency information. The zoneplate contains a wide variety of polar frequencies and has the widest possible variety in angles (after all, a circle contains all angles).

In the magnitude response of Fig. 5.20 (b), we clearly distinguish the directional information in the different subbands. Each subband extracts its characteristic angle range. The rectangular shape of the filters is not in harmony with directional selectivity. Wedge-shaped filters are specifically well-equipped for extraction of directional information. However, in the past we have been working with different types of wedge-shaped filters. The drawback of these types of filters is that they involve difficult design problems, and are hard to implement with local basis functions. Besides those reasons, they tend to cause an enormous data explosion due to oversampling (van Spaendonck and Baraniuk (1999); Hindriks *et al.* (2000); van Spaendonck *et al.* (2000)). Due to the local character of the basis functions of the complex wavelet transform, the angular selectivity performs quite well, as we will see later in the discussion about attributes.

■ 5.3.2 Three- or more dimensional pre-projection transform

As previously mentioned, the extension from two to three- or more dimensions is quite straightforward for separable wavelet transforms. For that reason we will only discuss the subject in short. The most important issue is the frequency response of the filters.

The three-dimensional pre-projection complex wavelet transform is again split into two operations: the three-dimensional projection, followed by a

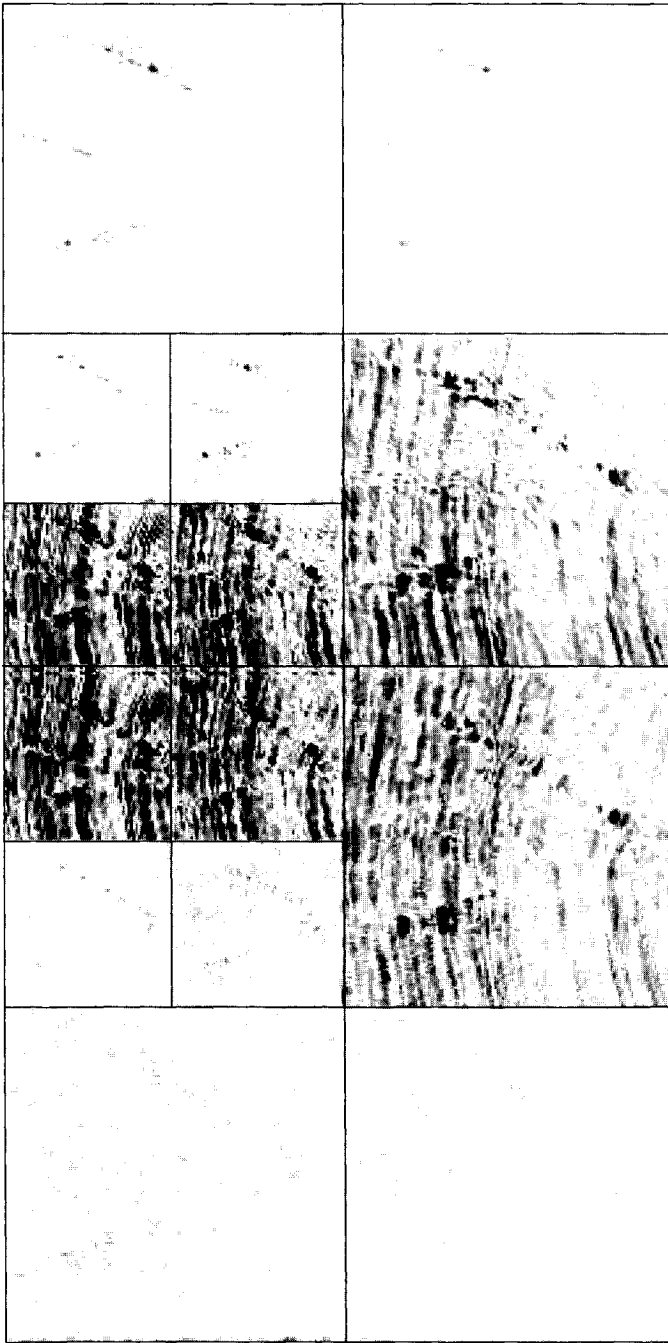


Figure 5.21: The magnitude response of the Daubechies-4 complex pre-projection CDWT of the seismic image in Fig. 3.15.

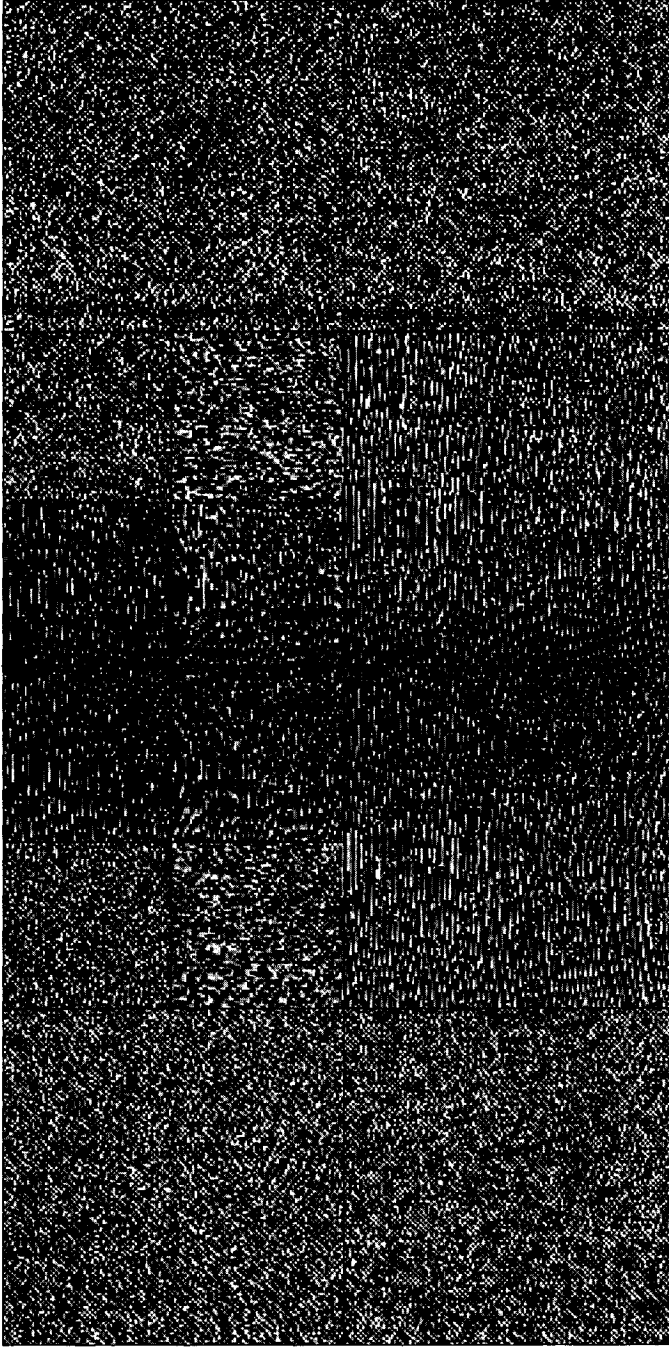


Figure 5.22: The phase response of the Daubechies-4 complex pre-projection CDWT of the seismic image in Fig. 3.15.

three-dimensional discrete wavelet transform. It is especially important to know how the three-dimensional Fourier domain is split by the filters, because it tells us something about the sensitivity to directional information.

In three dimensions, the conventional separable wavelet transform divides the outer frequency, spanned by the wavelets, into seven subspaces as shown in Fig. 3.16 (opposed to three in the two-dimensional case). This implies that only very little directional information is kept in each of the subbands.

The Fourier partitioning of the volume pre-projection complex wavelet transform is shown in Fig. 5.23. The pre-projection complex wavelet transform increases the number of wavelet subbands to 28 according to this figure! This means a dramatic improvement of directional discriminating abilities compared to the conventional three-dimensional wavelet transform. Pre-projection of the data cube divides the Fourier volume into four separate volumes, each located in the positive or negative lateral frequency zone. The subbands created by the conventional volume wavelet transform are divided into four separate subbands. This means that the volume pre-projection

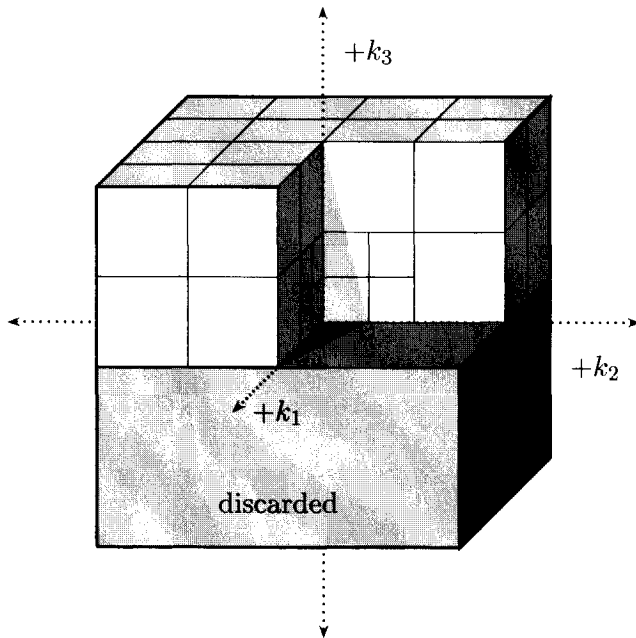


Figure 5.23: *Fourier-domain energy localization of tensor wavelets in a two-level complex 3-D DWT.*

complex wavelet transform has four times the number of subbands of its real-valued equivalent. In the next section, we will show that we can use the directional information for the estimation of the local geometry of a reflector in a volume based on a synthetic signal example.

Because of the equivalence between the two-dimensional pre-projection complex wavelet transform and the three-dimensional pre-projection transform we will show no additional examples of the transform. In the following chapter we will discuss the iterated complex wavelet transform which shows the same directional subbands but has a different scale structure.

■ 5.3.3 Volume attributes of the complex wavelet transform

With the three-dimensional complex wavelet transform, we are able to describe local quantities for the characterization in a three-dimensional volume (van Spaendonck *et al.*, 2001,?). In the previous section we have seen the Fourier partitioning that we obtain with the pre-projection complex wavelet transform (Fig. 5.23). From the subbands we can compute the different quantities by choosing the appropriate set of subbands in isolation and subsequent inverse transformation.

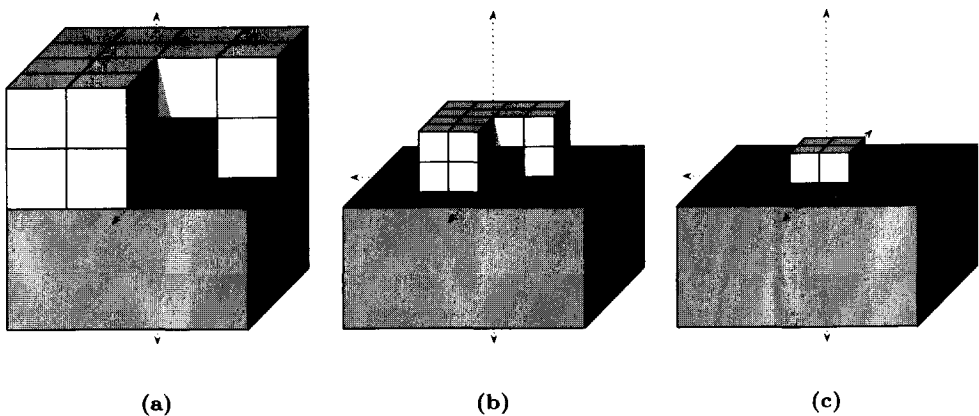


Figure 5.24: Isolated scale responses; (a) subbands contributing to the finest scale; (b) subbands contributing to the middle coarse scale; (c) subbands contributing to the coarsest scale (scaling function)

Scale The first attribute we describe is the local cubic scale. In Fig. 5.24 we show three sets of subbands that we use to compute the information at different scales for a two-stage wavelet transform. To sustain a local scale value to a certain position in a volume, we use the first moment to compute the average scale at the position, *viz.*

$$\langle \sigma \rangle = \frac{\sum_{\sigma=0}^N \sigma E(\sigma)}{\sum_{\sigma=0}^N E(\sigma)}. \quad (5.40)$$

in which $\langle \sigma \rangle$ denotes the average scale, σ , the discrete scale parameter ranging over the number of subbands N and $E(\sigma)$, the energy in each set of subbands of the transform. The scale attribute refers to a discrete scale parameter. Due to the separable character of the transform, the discrete scale filters have a rectangular shape in frequency.

The zonecube is used as an example for the synthetic validation of the algorithm. For this purpose we use the same $64 \times 64 \times 64$ zonecube as in the previous chapter. An orthogonal slice representation is depicted in Fig. 5.26 (a). The scale representation of the example is portrayed in Fig. 5.26 (b). From the figure we can observe that although each scale has a short transition zone, the resulting scale bands hardly suffer from the rectangular shapes of the filters. It is noteworthy that the outer band covers a large area with hardly any detailed information. This lack of detail in the finest scale band does not seriously affect our seismic applications, since the frequency information of seismic data in this area is limited to predominantly noise, since seismic images are band-limited signals (although we have to keep in mind that this does not apply for the spatial frequencies in lateral direction after seismic migration and stacking).

Dip and azimuth For the computation of dip and azimuth once more we combine sets of subbands. This time the subbands are combined in such a way that they collectively approximate a three-dimensional wedge shape, comprising a range of angles. We ultimately desire local filters with a wedge shape in the Fourier domain. Bamberger and Smith (1992) designed this type of filters. The reverse side of these filters is that they are difficult to design, and they lack the desirable benefits of the interscale relationship of the wavelet transform. In Chapter 7 we will expand upon this relationship

and how it could become useful in the future. When we want to compute the local geometry, we have to choose different combinations of subbands with coherent geometric information. An example of such a set of subbands can be found in Fig. 5.25. Each of the filter blocks in this particular set, carries similar information on the geometry of the signal, but at different scales. Each filter has a center azimuth of $\beta = 5\pi/8$. The center angle for the dip is $+1/4\pi$. In the same way, we can make other combinations of filter blocks that indicate different angles. When we are simply interested in either dip or azimuth, we can seek subbands with the same dip- or azimuth content, and combine these together in sets. For dip we can use the first moment over the angle which means for each position

$$\langle \alpha \rangle = \frac{\sum_{\alpha=\alpha_1}^{\alpha_6} \alpha E(\alpha)}{\sum_{\alpha=\alpha_0}^{\alpha_N} E(\alpha)} \quad (5.41)$$

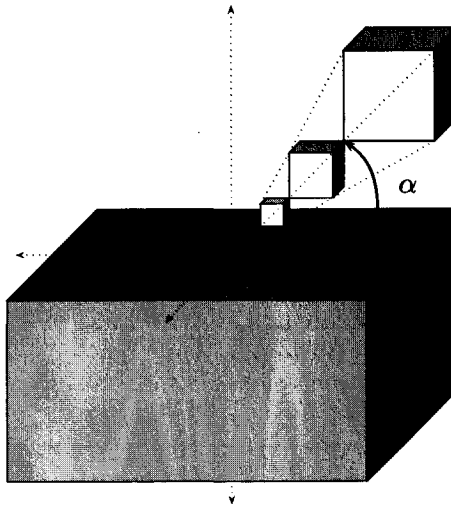


Figure 5.25: Isolated angle response; a set of subbands can be chosen with a consistent dip α and azimuth β .

in which $\langle \alpha \rangle$ denotes the average dip, and $E(\alpha)$, the energy in a set of sub-bands with the same dip information. The computation of the first moment is not particularly stable when we consider the azimuth. Seismic data contains a large amount of close to horizontal information. For this type of information it is hard to estimate an azimuth. Besides that, we would need a periodic moment, instead of the linear first moment we use for the dip. We have found the solution for this problem by the computation of the dip in the in-line and cross-line direction separately. We can use that information to compute the azimuth in a stable way.

In Fig. 5.26 we have shown the dip in (c) and azimuth in (d) of the zonecube. For the computation of the attributes we have used a three level Daubechies-8 projection Daubechies-8 DWT. Though not as sharp as in Fig. 4.17 (c) and (d), dip and azimuth are computed accurately. Later on we will show that the pre-projection complex wavelet transform attributes are generally more robust to noise. In Chapter 7 we will show the attributes applied on seismic field data.

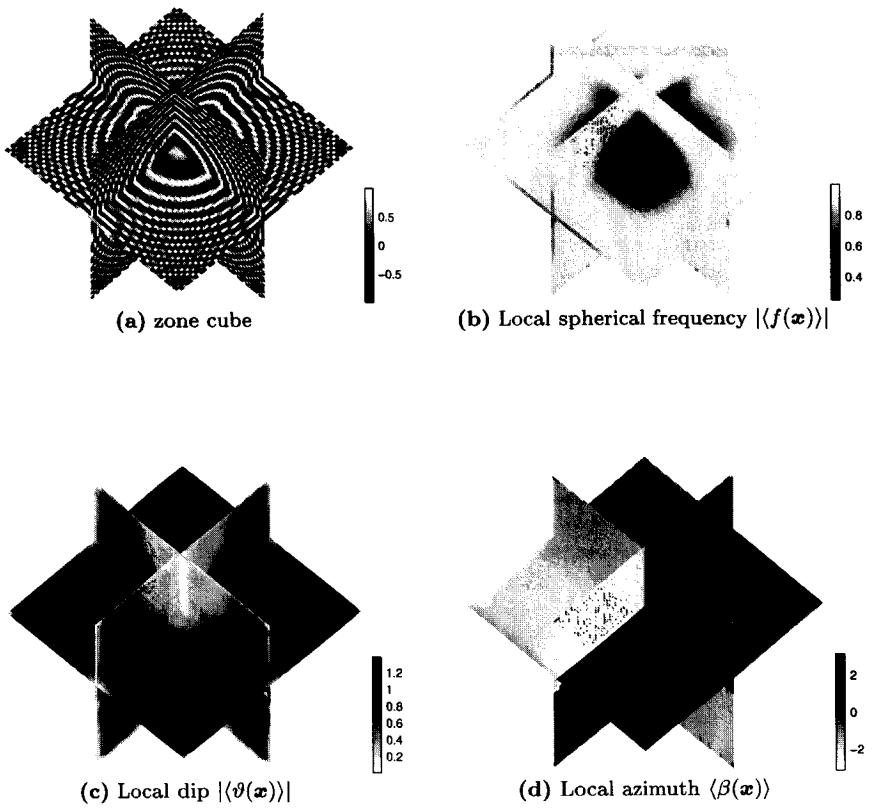


Figure 5.26: (a) Zonesphere, and its Maxflat Daubechies-16 volume attributes: (b) local radial frequency, (c) absolute local dip, (d) local azimuth.

Iterated complex wavelet transform

In this chapter we will introduce a novel complex wavelet transformation that embeds a local Hardy projection in the wavelet-tree.

The pre-projection complex wavelet transform is very effective for obtaining a wavelet transform with an amplitude and a phase and has a great amount of flexibility in the choice of filters and redundancy. The drawback of this complex transform is that, because the discrete Hardy projection is dependent on scale, we do not impose renewed quadrature at each consecutive step in the wavelet transformation. If we are able to include the projection filter at each step, then we can induce quadrature at different resolutions.

In the first section we will introduce a novel type of complex wavelet transformation that performs a local Hardy projection at each stage of the transformation and still retains perfect reconstruction. We call this transform the *iterated complex wavelet transform*. The algorithm is a concatenation of projection and wavelet filters and operates as a single tree transform with the same redundancy as the pre-projection complex transform. The advantage of the iterated over the pre-projection transform is that the renewed quadrature at each level provides improved shift-invariance and improved phase behavior of the transform. As a consequence of the integrated projection, the spaces in this complex wavelet transform do not nest. Due to the scale dependent projection, the spaces drift apart.

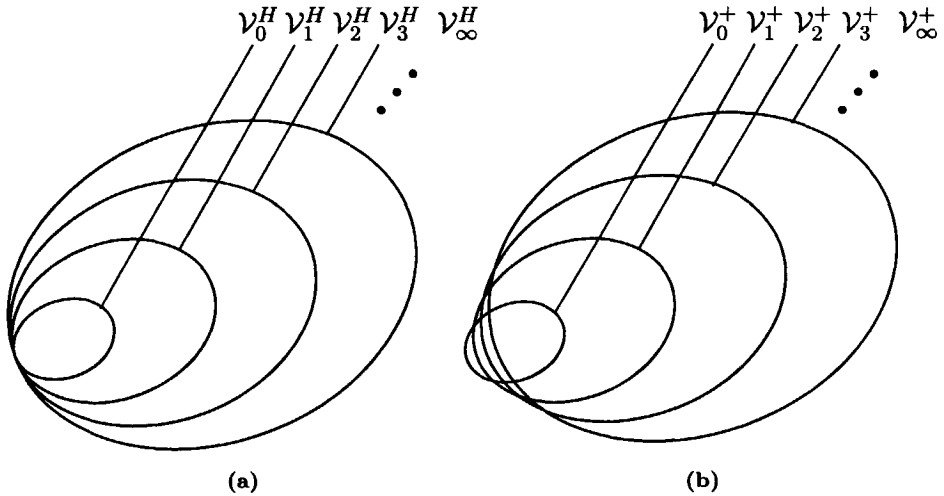


Figure 6.1: Drifting of the nested spaces; (a) ideal Hardy multiresolution spaces $\mathcal{V}_0^H - \mathcal{V}_\infty^H$, (b) approximate or local Hardy multiresolution spaces $\mathcal{V}_0^+ - \mathcal{V}_\infty^+$.

When we think about nested spaces, we presume that the signal that is subjected to multi-resolution, operates at the finest resolution, and that the spaces together span the signal. In the case we consider the complex wavelet transform, this formalism changes. With the complex wavelet transform we do not want to span the signal alone, but also its Hilbert transform! We want to compute the Hilbert transform on the basis of locally operating scaling functions and wavelets, using singly the real-valued input. This is the argumentation for the fact that we want to omit the conventional idea of multi-resolution in this chapter and introduce a new concept of complex multi-resolution. The complex form of multiresolution cannot be described in the context of nesting spaces, since the space we want to span is outside the range of any of the scaling functions alone. We will show that the span of the transform in the limits converges to Hardy space. The phenomenon of drifting spaces is illustrated in Fig. 6.1 and will be discussed more thoroughly in the next section.

6.1 Construction of complex scaling functions and wavelets

In Section 5.1.1, we have introduced two different ways to arrive at ideal analytic scaling functions. We have extensively discussed the first in the remainder of Chapter 5. Here we showed that we could substitute a local

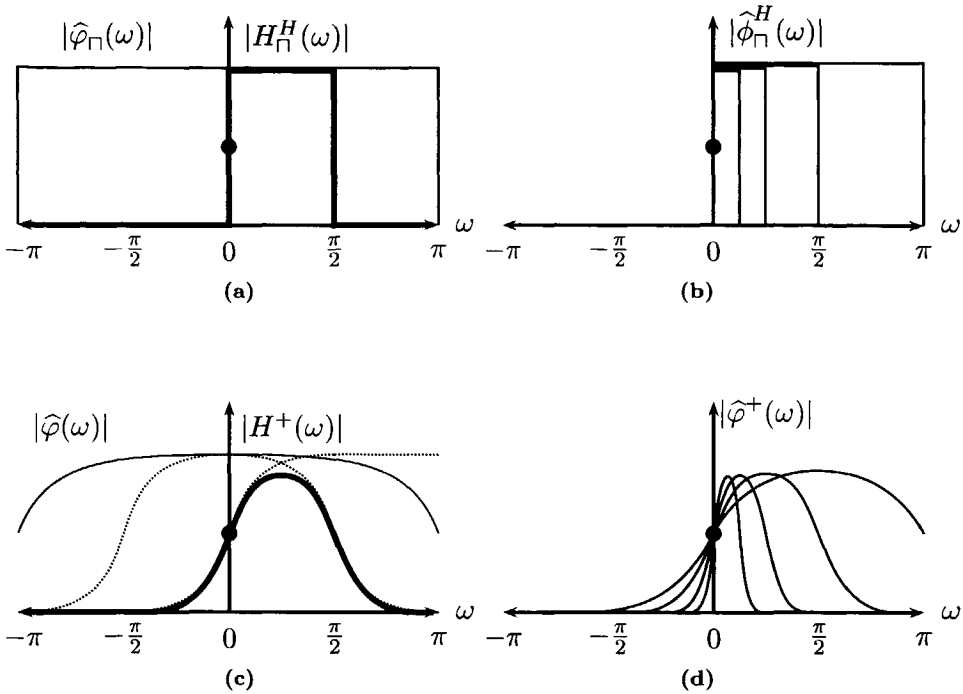


Figure 6.2: Fourier responses of scaling functions in the iterated complex wavelet transform. (a) The analytic ideal dilation filter H_0^H , (b) the resulting analytic ideal scaling functions $\hat{\varphi}_0^H(\omega)$. (c) The local analytic dilation filter $H^+(\omega)$, and (d) the resulting local Hardy projected scaling functions $\hat{\varphi}^+(\omega)$.

projection onto Softy space instead of the unrealizable ideal Hardy projection, without losing the multiresolution or perfect reconstruction property of the wavelet transform.

The second approach in Section 5.1.1 we have seen, uses the analytic dilation filter coefficients to relate the complex scaling functions. For this approach we cannot use the Softy-space projection to replace the Hardy-space projection, because we need the Hardy symmetry property. By replacing the Hardy-projection operator with the smoothed or *local* Hardy operator as discussed in Chapter 4, we are able to approximate the analytic scaling functions locally. However, because we use a local approximation, the spaces spanned by the scaling functions will drift apart, and the conventional multiresolution property of the wavelet transform is not valid anymore. The question remains, if we mind or desire this phenomenon.

■ 6.1.1 Revisiting the ideal analytic scaling functions

In Fig. 6.2 (b) we show the Fourier responses of the ideal analytic scaling functions again. Each ideal analytic scaling function can be obtained from its finer resolution parental scaling function, by taking the time-domain convolution of its real part with the analytic ideal dilation filter $h_{\Gamma}^H(n)$ as illustrated in Fig. 6.2 (a). Or, in frequency, the complex dilation equation is given by (Eq. (5.18))

$$\hat{\varphi}_{\Gamma}^H(\omega) = H_{\Gamma}^H\left(\frac{\omega}{2}\right) \hat{\varphi}_{\Gamma}\left(\frac{\omega}{2}\right), \quad (6.1)$$

with $H_{\Gamma}^H(\omega)$ defined in Eq. (5.19). In the ideal analytic case this iteration obviously works out. When we want to approximate the square analytic and ideal scaling functions as shown in Fig. 6.2 (d), we first have to know what are the constraints that lay at the foundation of the algorithm. The first constraint is that to be able to go from one scale to the next coarser scale, we need the real-valued equivalent of the analytic scaling function (following Eq. (6.1)) as is illustrated in Fig 6.2 (c). In the Section 5.1.1, we saw that in the ideal analytic case due to the symmetry conditions Eqs. (5.10) and (5.11), the real part of the analytic scaling function is equal to its real-valued equivalent. These are two essential constraints for the iterated complex wavelet transformation. They affect the local characteristic function used in the complex wavelet transform. The other constraints are related to the multi-resolution formulation. These address the functions used to approximate the ideal scaling function (excluding the Hardy projection) without losing the property of multiresolution and perfect reconstruction. These issues are extensively discussed in Chapter 3 and lead to the general wavelet solutions.

■ 6.1.2 Wavelets and scaling functions of the complex wavelet transform

First we have to realize that we do not necessarily want the nesting property as we have seen with the pre-projection in the preceding chapter. As soon as we leave this pattern, we obtain much more freedom in how to design the complex wavelets and scaling functions. For the derivation of the complex scaling function and the complex wavelets, we will follow the same reasoning as we did for the ideal analytic iterated complex analytic wavelet transform. Later on we will show that the complex wavelet transform spans Hardy space in the limits.

We can calculate the analytic scaling function $\widehat{\varphi}^+(\omega)$ from its finer scale *real-valued* equivalent by (compare Eq.(6.1))

$$\widehat{\varphi}^+(\omega) = H^+\left(\frac{\omega}{2}\right) \widehat{\varphi}\left(\frac{\omega}{2}\right), \quad (6.2)$$

with

$$H^+(\omega) = P^+(\omega)H(\omega), \quad (6.3)$$

in which $P^+(\omega)$ is defined to be a smooth Hardy-space projection operator. $P^+(\omega)$ can be interpreted as a smoothed version of the characteristic function. This operator is scale dependent, since it is finite in length.

Let the Hardy symmetry properties apply to the local Hardy-space projection (Eqs. (5.10) and (5.11)), which means that we constrain $\widehat{\varphi}^+(\omega)$ by

$$\widehat{\varphi}(\omega) = \frac{1}{2} \left[\widehat{\varphi}^+(\omega) + (\widehat{\varphi}^+(-\omega))^* \right] \quad (6.4)$$

This implies that we can continue the iteration for the next step, even for the local projections. The cumulative product now changes into

$$\widehat{\varphi}^+(\omega) = P^+\left(\frac{\omega}{2}\right) \prod_{k=1}^K H\left(\frac{\omega}{2^k}\right) \varphi\left(\frac{\omega}{2^K}\right). \quad (6.5)$$

The so-obtained complex scaling functions will show similar shapes as we have shown in Fig. 6.2 (d). In the same way as for the analytic scaling function, we can derive the analytic wavelets with the use of the analytic filter coefficients $G^+(\omega)$

$$\widehat{\psi}^+(\omega) = G^+\left(\frac{\omega}{2}\right) \widehat{\varphi}\left(\frac{\omega}{2}\right). \quad (6.6)$$

with

$$G^+(\omega) = P^+(\omega)G(\omega). \quad (6.7)$$

We have to note that there are other solutions that can be used for the calculation of the complex wavelet $\widehat{\psi}^+(\omega)$. For continuous time implementations we can also insert the complex equivalent of the scaling function in Eq. (6.6)

$$\widehat{\psi}^+(\omega) = G^+\left(\frac{\omega}{2}\right) \widehat{\varphi}^+\left(\frac{\omega}{2}\right). \quad (6.8)$$

However, after discretization, the Hilbert transform filter becomes periodic, which induces undesirable interference between $G^+(\omega/2)$ and $\phi^+(\omega/2)$.

Bernard (1999) suggested in his thesis an alternative method for calculation of the wavelets from the scaling function, by choosing the inner product between a real-valued $G(\omega)$ with the complex scaling function,

$$\tilde{\psi}^+(\omega) = G\left(\frac{\omega}{2}\right) \hat{\varphi}^+\left(\frac{\omega}{2}\right). \quad (6.9)$$

This is a good alternative for the wavelet solution as proposed in Eq. (6.6), and it is based on the same principles of inclusion of a local Hardy projection in each iteration. The drawback of this implementation is the absence of quadrature for the wavelets at the finest scale, since the algorithm requires a complex scaling function at a finer resolution and initially we use a real-valued signal as input. A solution to this problem can be found in the combination of Eqs. (6.6) and (6.9) in which we use the first for the computation of the initial complex analytic highpass band.

Since we now know the complex scaling functions and wavelets, we are able to write different local scale approximations of the Hardy projection of the signal. The analytic signal $u_j^+(t)$ in the space \mathcal{V}_j at scale j can then be written according to

$$u_j^+(t) = \sum_k a_k \varphi_j^+(t - k). \quad (6.10)$$

The complex space spanned by the complex wavelets can be written as

$$f_j^+(t) = \sum_k b_k \psi_j^+(t - k). \quad (6.11)$$

The subbands spanned by the wavelets is the space spanning the difference between the complex scaling functions. In the iterated complex wavelet transform, the subbands spanned by the wavelets and the scaling functions together yield an approximate Hardy projection of the real-valued input signal. The filter responses of the scaling functions and wavelets are shown in Fig. 6.3 (b). We will show in the next section that this projection converges to Hardy space in the limits going from infinite coarse scale to infinite fine scale.

Based on the Eqs. (6.10) and (6.11), we can write the iterated complex wavelet transform as

$$u^+(t) = \sum_k a_k \varphi^+(t - k) + \sum_{j=0}^{\infty} \sum_k b_{j,k} 2^{j/2} \psi^+(2^j t - k), \quad (6.12)$$

in which a_k and $b_{j,k}$ are the complex wavelet coefficients. We know that the real part of this complex wavelet transform spans L^2 . After Fourier transformation of Eq. (6.12), we obtain the following relation

$$\begin{aligned}\hat{u}^+(\omega) &= \hat{\varphi}^+(\omega) \sum_k a_k \exp(-j\omega k) \\ &+ \sum_{j=0}^K 2^{j/2} \hat{\psi}^+ \left(\frac{\omega}{2^j} \right) \sum_k b_{j,k} \exp(-j\omega k).\end{aligned}\quad (6.13)$$

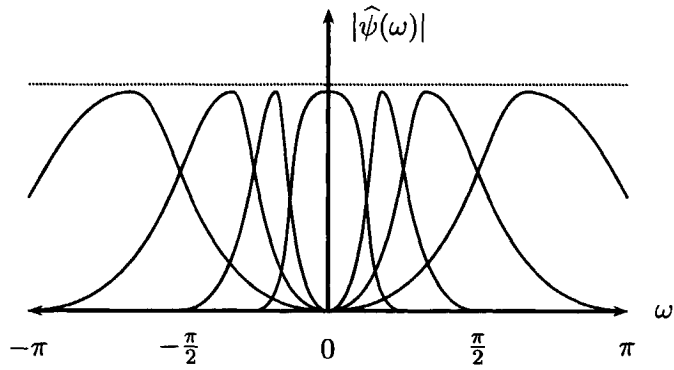
This means that the iterated complex wavelet transform spans the signal $\hat{u}^+(\omega)$, which suppresses negative frequencies. In the next section we will show that this wavelet transform in the limits spans the Hardy projection of $\hat{u}(\omega)$.

■ 6.1.3 Convergence to Hardy space

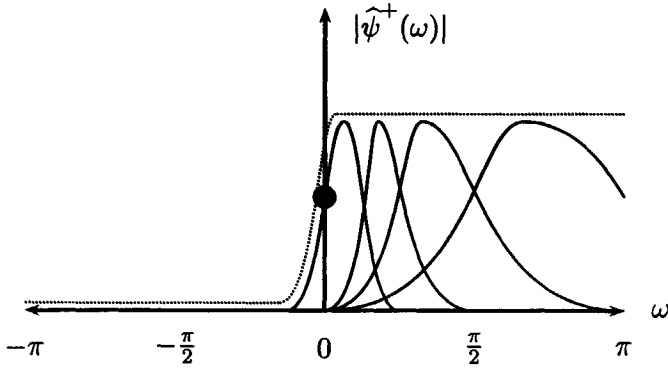
First we have to realize what we ultimately want to achieve with a complex wavelet transform. Consider the real DWT. The Fourier response of the real-valued wavelets and scaling functions is shown in Fig. 6.3 (a). In the real DWT we try to span spaces of resolution with short-duration functions. The signal is equal to the space with the finest resolution. In the limit the DWT spans L^2 , which is illustrated by the dotted line in Fig. 6.3 (a). We have to keep this in mind when we consider the complex wavelet transform.

With a complex wavelet transform we do not try to span L^2 , since this is a space of real-valued functions. Ultimately we want the complex wavelet transform to span the complex equivalent of L^2 , the Hardy space H^2 . A clear illustration of the Fourier responses of the basis functions in the complex wavelet transform can be found in Fig. 6.3 (b). The dotted line shows the envelope of the exact information covered by the filters. We see that the coarser we choose the lowpass averaging filter (or scaling function), the closer we approach Hardy space.

Is it realizable to span Hardy space with finite functions? We have seen in Chapter 4 that the local Hardy projection operator needs to be of infinite length to project on the Hardy-space. The filter length of the local Hardy projection operator limits its capacity. The repeated application at different scales in the iterated complex wavelet transformation is the solution for this problem. We are now able to adjust the local Hardy projection to the scale at which a scaling function or the wavelet operates. In that way we can



(a) DWT



(b) Iterated CDWT

Figure 6.3: Filters of the wavelet transforms: (a) The usual DWT filters and their combined magnitude (dotted line) converging to L^2 in the limits, (b) The filters in iterated complex wavelet transform and their combined magnitude (dotted line) converging to H^2 in the limits

implement the local Hardy projection for each separate scale. In the limits this approximation spans Hardy space as we will show hereafter.

Let us consider the function $\widehat{u}_\infty^+(\omega)$ in which we let the complex scaling function go to the coarsest possible hypothetical scale \mathcal{V}_0^+ and the complex wavelets span the complex spaces up to infinity $\mathcal{W}_{0-K \rightarrow \infty}^+$. The real part is spanned by real-valued wavelets (as we have seen in Chapter 3), the imaginary parts by their local Hilbert transforms. Equation (6.13) is now given by

$$\begin{aligned} \widehat{u}_\infty^+(\omega) &= \widehat{\varphi}^+(\omega) \sum_k a_k \exp(-j\omega k) \\ &+ \sum_{j=0}^{\infty} 2^{j/2} \widehat{\psi}^+ \left(\frac{\omega}{2^j} \right) \sum_k b_{j,k} \exp(-j\omega k). \end{aligned} \quad (6.14)$$

We want to show that $\widehat{u}_\infty^+(\omega)$ converges to its Hardy projection,

$$\widehat{u}_\infty^+(\omega) = \widehat{u}^H(\omega). \quad (6.15)$$

What are the key properties of the Hardy projection operator? Consider the analytic signal $g^H(t)$ of $g(t) \in L^2$,

$$g^H(t) \in H^2, \quad \text{iff } \widehat{g}^H(\omega) = \begin{cases} 2\widehat{g}(\omega), & \text{for } \omega > 0 \\ \widehat{g}(\omega), & \text{for } \omega = 0 \\ 0, & \text{for } \omega < 0 \end{cases}. \quad (6.16)$$

Two of those properties came up several times before. These are the symmetry properties that are given in Eqs. (5.10) and (5.11). Because we have used local Hardy projection operators for the calculation of the scaling function and wavelets, we can say that

$$\widehat{\varphi}_0(\omega) = \frac{1}{2} \left[\widehat{\varphi}_0^+(\omega) + (\widehat{\varphi}_0^+(-\omega))^* \right], \quad (6.17)$$

and

$$\widehat{\psi}_j(\omega) = \frac{1}{2} \left[\widehat{\psi}_j^+(\omega) + (\widehat{\psi}_j^+(-\omega))^* \right]. \quad (6.18)$$

Both, the wavelet and the scaling function are obtained through local Hardy projections and hence satisfy the symmetry conditions. Automatically this implies that $\widehat{u}_\infty^+(\omega)$ satisfies

$$\widehat{u}_\infty(\omega) = \frac{1}{2} \left[\widehat{u}_\infty^+(\omega) + (\widehat{u}_\infty^+(-\omega))^* \right], \quad (6.19)$$

which is one of the basic symmetry properties of the Hardy projection.

The DC-components of the scaling function and wavelets are per definition given by

$$\widehat{\varphi}_0^+(0) = \widehat{\varphi}_0(0) = 1, \quad (6.20)$$

and

$$\widehat{\psi}_j^+(0) = \widehat{\psi}_j(0) = 0. \quad (6.21)$$

This shows that the DC component is determined solely by the DC of the scaling function, and is given by

$$\widehat{u}_\infty^+(0) = \widehat{u}(0). \quad (6.22)$$

This is the second crucial property of the Hardy projection filter. Since we want to know how good of an approximation the iterated complex wavelet transform would give us of the Hardy projection, we will need to study the limits of the transform. In the case of the real discrete wavelet transform, the determination of the scaling function in the limits is sufficient, since the wavelets reside in the spaces spanned by the scaling functions. In the case we consider the iterated *complex* wavelet transform, we need to consider the entire transform, because scaling functions and wavelets span different spaces. Let us first consider the limits at DC, then the limit for $\omega \rightarrow \infty$,

$$\lim_{\omega \downarrow 0} \widehat{u}_\infty^+(\omega) = 2\widehat{u}(\omega), \quad (6.23)$$

and

$$\lim_{\omega \uparrow 0} \widehat{u}_\infty^+(\omega) = 0. \quad (6.24)$$

At infinite coarse scale, the complex scaling function shows the step function of the Hardy projection operator. The next question is how the wavelets behave at the infinite boundaries.

$$\lim_{\omega \rightarrow \infty} \widehat{u}_\infty^+(\omega) = 2\widehat{u}(\omega), \quad (6.25)$$

and

$$\lim_{\omega \rightarrow -\infty} \widehat{u}_\infty^+(\omega) = 0. \quad (6.26)$$

Since we know that $u(t) \in L^2$, and the real parts of the scaling function and wavelets span L^2 , the definition of Hardy space projection in Eq. (6.16) is satisfied. Due to the fact that the symmetry relation in Eq. (6.19) applies for the entire transform, we immediately see that perfect reconstruction is satisfied when we use the conventional *real* inverse wavelet transform using the adjoints of the real parts of the wavelets and scaling functions.

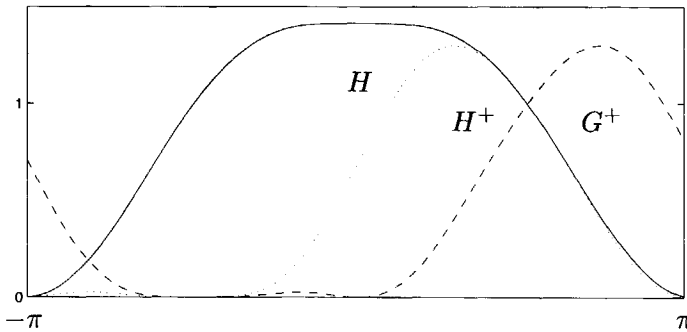


Figure 6.4: The filter responses of the iterated complex wavelet tree. Iteration on the real lowpass filter H , the tip of each branch uses the projection highpass filter G^+ or lowpass filter H^+ .

6.2 Discrete filter bank implementation

We have shown how we can use a smooth Hardy projection for the creation of complex wavelets and scaling functions that in the limit span Hardy space. In this section we will show how we implement the iterated complex wavelet transform by cascading of FIR filter banks.

For the discretization of the iterated complex wavelet transformation, we choose to use an FIR filter to replace the characteristic function $\chi^+(\omega)$. For the iterated complex wavelet transform we do not use the spectral factors of the local Hardy projection filter $P^+(z)$, as we did with the pre-projection. Instead we use the local Hardy projection filter $P^+(z)$ itself (Eq. (4.5)). This filter consists of a real-valued impulse and an imaginary local Hilbert transform (see Chapter 4).

In Chapter 4, we have seen that we can use the local Hardy projection filter as an approximation of the characteristic function. With the discretization of the operators in the transformation, we introduce periodicity. Instead of the smooth Hardy projection operator with a smoothed step function at DC, we are condemned to introduce a second step function in the local Hardy projection filter. This step is introduced due to the periodicity of the filter. The second cross-over will be localized at π and $-\pi$.

We can design two FIR filters as discretized equivalents of the filters in Eq. (6.3) and (6.7) according to

$$H^+(z) = P^+(z)H(z), \quad (6.27)$$

and

$$G^+(z) = P^+(z)G(z), \quad (6.28)$$

in which $H(z)$ and $G(z)$ are given in Eqs. (3.70) and (3.71), and $P^+(z)$ by Eq. (4.5). The real parts of $h^+(n)$ and $g^+(n)$ are equal to the input lowpass $h(n)$ and highpass $g(n)$ filters, respectively. The imaginary parts are their order- N discrete Hilbert transforms. The filters H, G^+ and H^+ mentioned above that link the different scales in the discrete iterative complex wavelet transform are shown in Fig. 6.4.

The cumulative product in Eq. (6.5) for a signal $u_K(t)$ at a certain resolution K changes into the discrete cumulative product

$$U_K^+(\Omega) = H^+ \left(\frac{\Omega}{2} \right) \prod_{j=2}^K H \left(\frac{\Omega}{2^j} \right) U_0 \left(\frac{\Omega}{2^K} \right) + \text{folding terms}. \quad (6.29)$$

The cumulative product for the detail in a signal $u_{\Delta K}(t)$ at a certain resolution K changes into the discrete cumulative product

$$U_{\Delta K}^+(\Omega) = G^+ \left(\frac{\Omega}{2} \right) \prod_{j=2}^{\infty} H \left(\frac{\Omega}{2^j} \right) U_0 \left(\frac{\Omega}{2^K} \right) + \text{folding terms}. \quad (6.30)$$

The structure of the filter bank implementation of the iterated complex wavelet transform is illustrated in Fig. 6.5. The real signal $u(n)$ enters an analytic highpass branch and a real lowpass branch. The real-valued lowpass branch is subsequently used as an input for the next stage. For the inverse transform we can use the inverse of the conventional real wavelet transform. For a three stage transform, the inverse scheme is shown in Fig. 3.9.

The Daubechies-4 complex high- and lowpass filters we use in the iterated complex wavelet transform are depicted in Fig. 6.6 in discrete time. Figure 6.6 (a) portrays the real part, (b) imaginary and (c) modulus of the lowpass filter $h^+(n)$. Figure 6.6 (d) depicts real part, (e) imaginary and (f) modulus of the highpass filter $g^+(n)$. When we take a closer look at the moduli in (c) and (f), we notice that the modulus of $g^+(n)$ is a flipped version of the modulus of $h^+(n)$!

Symmetry in wavelets and filters is not uncommon, for instance when we use spline wavelets in the biorthogonal wavelet transform (Unser, 1999). However, these wavelets show internal symmetry, whereas the shapes of these complex high- and lowpass filters differs. That the shape of these filters is not identical, is easily explained by the fact that the real-valued low- and highpass filters per definition have different shapes.

Just like the pre-projection transform, the iterated complex wavelet transform can be written in terms of its amplitude and phase. The variance to shifting of the input of both quantities is dependent of the length of the filter and its corresponding number of vanishing moments. We will discuss the amplitude and phase response and the shift-variance in the next paragraphs.

■ 6.2.1 Amplitude and phase

In accordance with the pre-projection transform, the iterated complex wavelet transform can be written in terms of an amplitude and phase. In the previous paragraph we showed how to design the iterated transform, in this paragraph we will show what it looks like and in what way the algorithm is different from the pre-projection transform.

Again we refer to Fig. 5.12 (a) as the signal we use for the illustration of the transform. We perform a two-stage transformation of the signal according to the diagram in Fig. 6.5. This means that we use the real-valued equivalent of the lowpass filter for the iteration. The ends of the branches contain the projection filters. The complete iterated discrete wavelet transform is shown in Fig. 6.7.

Figure 6.7 (a) shows the amplitude spectrum of the iterated transform, and (b) its modulus and (c) the phase. The figure represents a two-stage wavelet transform, which constituted of three subbands, a lowpass (samples $n=1-128$), an intermediate band-pass ($n=129-256$) and a highpass ($n=257-512$). The filters used are the Daubechies-4 filters, for the real part, as

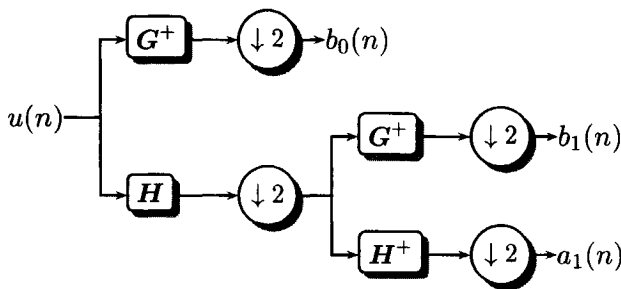


Figure 6.5: Analysis filter bank tree of $u(n)$ obtained by cascading complex low- and highpass filters. The outputs $b_0 - b_2$ are the complex wavelet- and a_2 the complex scaling coefficients. H indicates that the real part of the complex filter $H^+ (= H)$ is used for iteration.

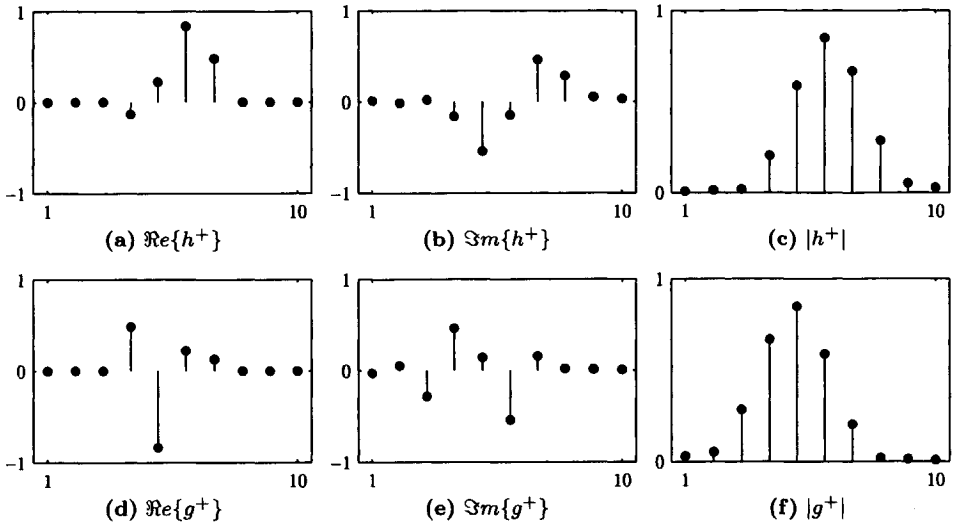


Figure 6.6: The time responses of the complex Daubechies-4 filters of the iterated complex wavelet tree. (a) Real part, (b) imaginary part, and (c) modulus of lowpass filter $h^+(n)$. (d) real part, (e) imaginary part, and (f) modulus of highpass filter $g^+(n)$.

well as for the projection. The modulus in (b) looks similar to the results that we have seen from the pre-projection transform in Fig. 5.12 (c). The results of the iterated transform however seem to be less susceptible to noise in the highpass region and are less disturbed in the lowpass region. The amplitude seems to be very consistent through scale. This is a very favorable property which is especially useful for the statistical modeling and description of images and signals (Magrin-Chagnolleau *et al.*, 1999; Choi *et al.*, 2000). Note that the relatively short Daubechies-4 filter seems to be of sufficient length to induce quadrature over the entire range of subbands in the complex transform. For the pre-projection transform we needed larger length filter to resolve quadrature completely. In this iterated transform, the down-sampling operator and the repeated application of the projection takes care of lower frequencies. This is a very important advantage over pre-projection, where the number of levels chosen for the transform affects the accuracy of the quadrature between imaginary and real part. As a side-effect for increasing number of scale levels, the length of the Softy-space projection operator needs to be increased.

The phase response in Fig. 6.7 (c) resembles the phase of the pre-projection

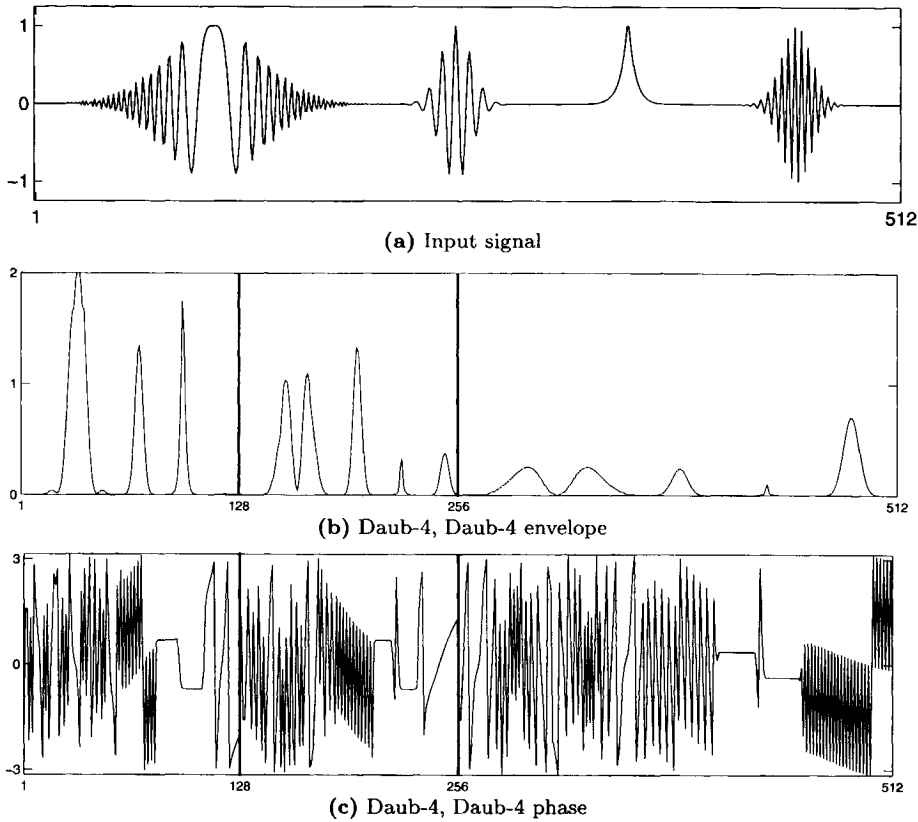


Figure 6.7: The iterated complex wavelet transform of a signal: (a) The original signal, (b) the modulus of the Daubechies-4 iterated CDWT, (c) its phase. Subbands are separated by the vertical bars.

transform in Fig. 5.12 (d) and also shows a trend through scale. Again we remark that the phase will be consistent no matter how many levels are included in the transform in contrast with the phase of the pre-projection algorithm which is established first and consequently put through the transform.

For the illustration of the consistency of amplitude and phase over scale, we refer to Fig. 6.8. for this figure we have computed a three stage transform of the test signal. We show the amplitude and phase response separately on the left and the right respectively. From top to bottom we expose the coarsest scale to the finest scale. The number of samples increases downwardly

according to fining scale. When we have the signal in mind we can clearly see the differentiation of the amplitudes according to the frequencies in the chirp and the sinusoids. The scaling delta pulse is present in all scales as one would expect.

The phase shows a similar trend although harder to discern. The phase signature of each of the sinusoids and the delta-pulse can be distinguished clearly in the different scales. In the next paragraph we will address the shift-variance of the transform to explore the stability of the transform under shifting of the signal.

■ 6.2.2 Shift-invariance

The amplitude and phase are important parameters for signal processing and modeling. However to be confident that we have the stable amplitude and a consistent phase, we fancy a transform that is shift-invariant. As we have

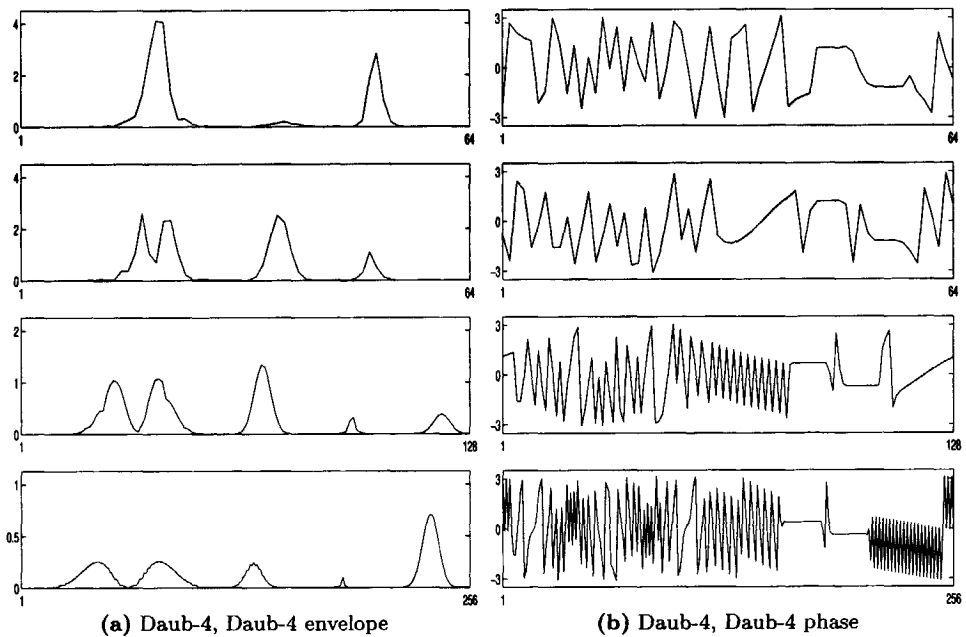


Figure 6.8: The four subbands of the three stage iterated complex wavelet transform; (a) the envelopes from the lowpass scaling function (top) to the finest wavelet approximation of the signal (bottom). (b) The respective phases.

seen in preceding sections, the pre-projection algorithm does a reasonable good job. However the algorithm has a weak spot in the low frequency zone, which can only be resolved by choosing larger length projection filters. Since we fancy a local transform we need to circumvent the use of long filters.

We will show with an example that the iterated complex wavelet transform is close to shift-invariant. There is hardly any energy exchange between the subbands under shifting of the input signal.

In Fig. 6.9 we have computed the two-stage complex wavelet transform according to the scheme in Fig. 6.5. We have used the signal in Fig. 4.5 (a) to illustrate the invariance to shifting of the input signal. The figures can be compared to Fig. 5.14, where we compare the shift-variance of the pre-projection algorithm with the shift-variance of the traditional wavelet transform. Figure 6.9 (a) shows the amplitude spectrum of the original signal. In (b) we have shifted the input signal by 20 samples to the left and in (c) by 12 samples to the right. From the three figures we immediately notice a strong consistency of the transform under shifting. Hardly any difference can be noticed when the signal is shifted. In order to quantify the interchanging of energies between the subbands, we have computed the cumulative energy in each subband. The results can be found in Table 6.1. The variance between the values is considerably lower than the values that we saw in Table 5.1 of the pre-projection complex wavelet transform and the traditional wavelet transform. Even with the short-length wavelet that we have used for this purpose.

We have to note that under further shifting of the signal to the right (> 12) we noticed a distinct change in the amplitude response of the intermediate band of the transform. For these shifts, the transform is disturbed by edge effects, which influence certain transform coefficients. The total energy in each of the amplitude spectra sums to 70.9965. As a preliminary conclusion we can remark that the iterated complex wavelet transform establishes a quadrature relationship in all subbands of the wavelet transform, even in the lowest frequency zone. The transform is insensitive for shifting of the input signal, even given its low redundancy.

6.3 Wavelet-based discrete Hardy-space projection

In this section we propose a novel complex wavelet-packet approach for Hardy projection of discrete-time signals. We will show that we can span the boxcar filter that we know from the discrete Hardy projection in the Fourier domain

with finite-length wavelets coupled with sampling operators. In doing so we are flexible to vary the range of influence of the Hardy projection. As a consequence we can suppress ringing phenomena, without application of tapering operations.

■ 6.3.1 Discrete Hardy-space projection with complex wavelet packets

With the iterated complex wavelet transformation we can span Hardy space in the limit as we have proven in Section 6.1.3. With each iteration, the scal-

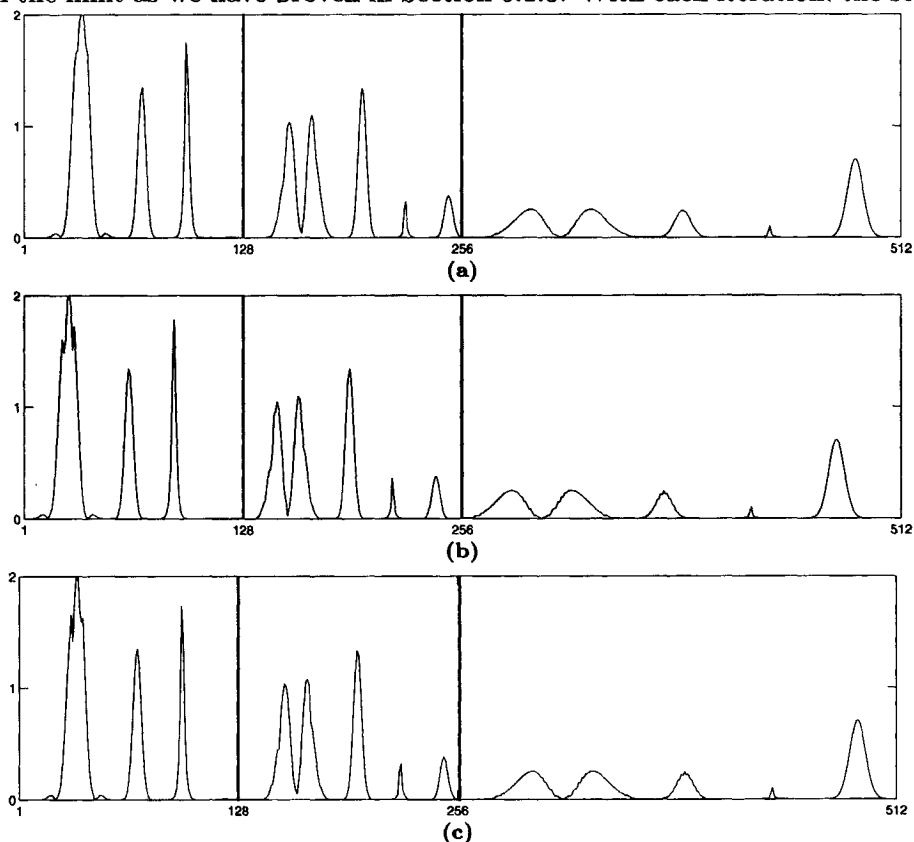


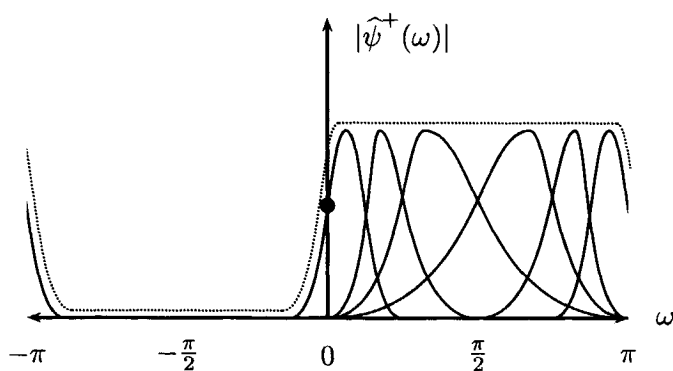
Figure 6.9: Shift-invariance of the Daubechies-4 iterated complex wavelet transform of the signal depicted in Fig. 6.7 (a). (a) The envelope of the iterated complex wavelet transform of the signal, (b) its 20-sample shifted version, (c) its 12-sample shifted equivalent.

Energy content ICDWT

| | <i>HH</i> | <i>GH</i> | <i>G</i> |
|-----|-----------|-----------|----------|
| (b) | 44.9248 | 19.7474 | 6.3243 |
| (d) | 44.8768 | 19.7953 | 6.3243 |
| (f) | 44.9248 | 19.7474 | 6.3243 |

Table 6.1: *Computed cumulative energy in subbands of the transforms in Fig. 6.9.*

ing function widens in time, but becomes more localized in frequency. In the limits the wavelets together with the coarsest complex scaling function span the characteristic function that is typical for Hardy space. What happens to this projection when we consider a discrete input signal? For discrete signals, the frequency coordinate ω becomes the periodic frequency coordinate Ω , which is periodic by 2π . Besides the periodicity, the number of iterations is limited. The Hardy projection of a discrete signal $f(n)$ is defined in the

**Figure 6.10:** *Discrete Hardy space spanned with complex wavelet packets: The combined magnitude of the filters in the transform converges to discrete a boxcar filter in the limit*

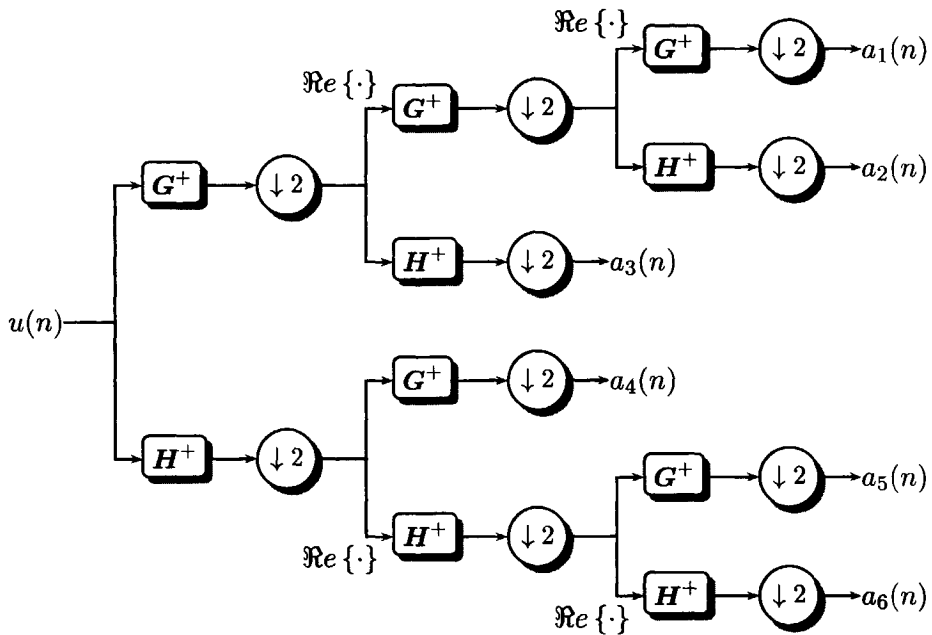


Figure 6.11: Analysis filter bank tree of $u(n)$ obtained by cascading low- and highpass filters. The outputs $a_0 - a_5$ are the wavelet- and scaling coefficients.

discrete-time Fourier domain as

$$\hat{f}^H(\Omega) = \begin{cases} 0, & \text{for } -\pi < \Omega < 0 \\ \hat{f}(\Omega), & \text{for } \Omega = 0 \\ 2\hat{f}(\Omega), & \text{for } 0 < \Omega \leq \pi \end{cases} \quad (6.31)$$

Periodicity implies that besides the characteristic step function at $\Omega = 0$, there is a step from $\Omega = \pi$ to its next period $\Omega = -\pi$. The Hardy projection we introduced in Section 6.1.3 does not take periodicity into account. The wavelets span the space of positive frequencies going to infinity. We can use the same approach for discrete signals, but this means that some of the highpass information will be wrapped around and contain negative frequency information.

The novel approach we propose, uses complex-wavelet packets to suppress the negative frequencies not only leaking through at $\Omega = 0$ but also at $\Omega = \pi$. In Section 6.1.3, we have seen that we can approximate the step-function at DC with a concatenation of complex wavelets and sampling operators. In

this section we use the same concatenation to approximate the step-function between $\Omega = \pi$ and $\Omega = -\pi$. The filters contributing to the discrete Hardy projection are shown in Fig. 6.10.

We have designed the filters using the scheme that is given in Fig. 6.11. The lowpass branch of the scheme is similar to the filtering scheme for the complex wavelet transformation proposed by Bernard (1999). His scheme does not account for the first stage highpass information. Alternatively we have proposed to substitute the highpass filtering operation of the iterated complex wavelet transformation. In this section we propose a totally different approach for the highpass branch. Both filters, the initial complex lowpass filter as well as the initial complex highpass filter are subject to iteration. As a result the wavelets and the scaling functions together form a boxcar function in the limit. This boxcar function $B(\Omega)$ is given by

$$\widehat{B}(\omega) = \begin{cases} 0, & \text{for } -\pi < \Omega < 0 \\ 1, & \text{for } \Omega = 0 \\ 2, & \text{for } 0 < \Omega \leq \pi \end{cases} . \quad (6.32)$$

The discrete-time convolution with this particular boxcar function is equal to the discrete-time Hardy projection. The FFT-implementation of this operation is the generally used operation for the computation of the discrete analytic signal.

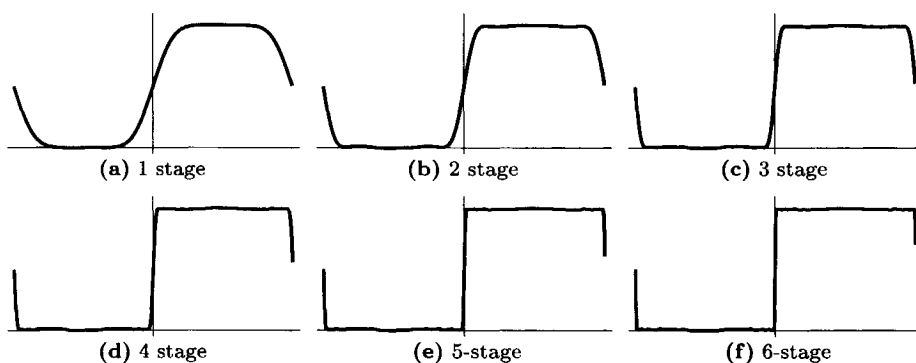


Figure 6.12: The Fourier responses of Daubechies-8 combined discrete Hardy projection filters.

■ 6.3.2 Building the boxcar filter with finite functions

We argue that we approximate a discrete Hardy projection with finite filters. In order to demonstrate how close we can approximate the boxcar function we will show several examples and compare the approximation with the Fourier results. The benefits of using local instead of global filters for the approximation of a Hardy projection filter are the flexibility in the number of stages included in the transform and the computational efficiency. We can choose the range of influence of each filter and hence the extent of interference of signal events. A local Dirac function in a signal has a global effect in its Hilbert transform. In order to reduce the effect of these types of functions on the transform we can limit the number of subbands we include. For our examples we have used the concept of the wavelet-packet tree depicted in Fig. 6.11. We have joined the synthesis and analysis filters in a single filter and used up-sampling operators instead of down-sampling operators to obtain the desired frequency range. These measures had to be taken, because the reconstruction of the analysis tree does not yet provide us the desired properties of the imaginary part. The measures affect the computational efficiency rather than the results.

For the illustration of the idea we refer to Fig. 6.12. In this figure we show the filters that correspond to the total sum of the filters in the tree in Fig. 6.11. We have used the Daubechies-8 filter for the projection as well as for the wavelet filters. The number of stages in the tree is indicated in the caption of each figure. Figure 6.12 (a) is the result after the first stage, which equals the original shifted Daubechies-8 halfband projection filter. In (b)-(f) we show the results of the consecutive stages. Figure 6.12 (f) closely approximates the square shape of a boxcar function. The difference between this figure and the figure depicted in (d) is however almost negligible. We stress once more that all of the filters shown in Fig. 6.12 are accomplished using *local support* filters.

For the illustration of the performance of this discrete Hardy projection we consider the non-stationary signal shown in Fig. 6.13 (a) once more. We have computed the envelope of this signal with the wavelet-packet Hardy projection for different number of stages. As a references we have shown the envelope of the FFT-based Hardy projected signal in Fig. 6.13 (b), and the envelope of the local Daubechies-4 Hardy projected signal in (c) (compare Fig. 4.5 (c)-(e)). The latter is identical to the envelope of the single-stage Daubechies-4 wavelet-packet discrete Hardy projected signal. In Figs. 6.13 (d) and (e) we have shown the 3 stage and the 6 stage envelopes of

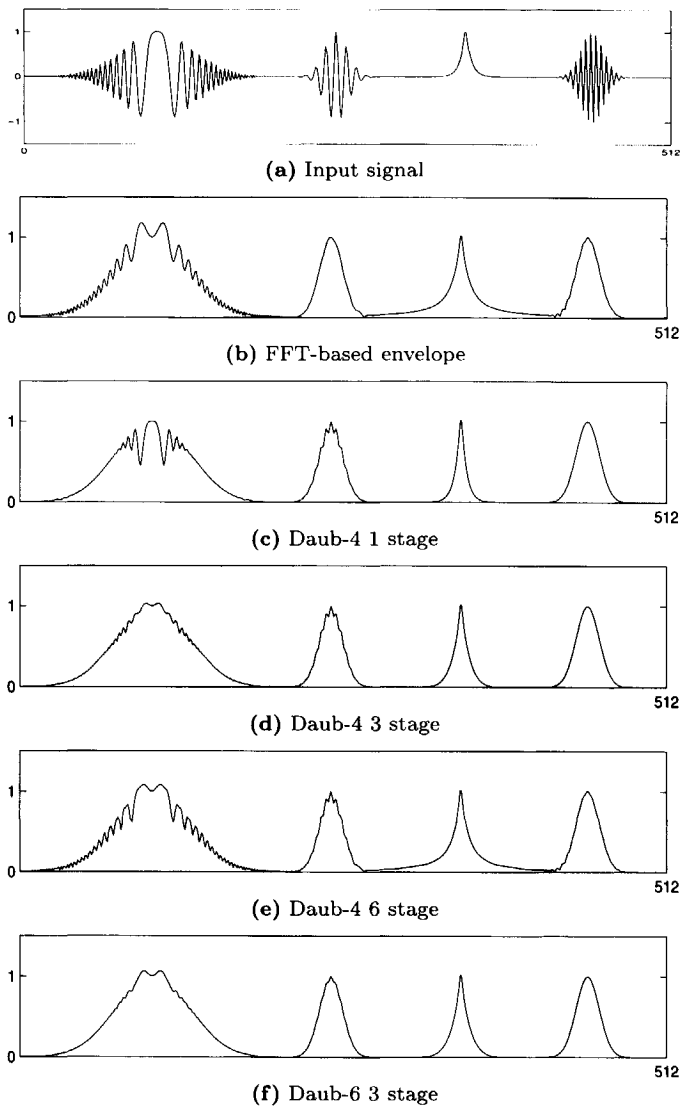


Figure 6.13: The envelopes of a non-stationary signal; (a) the input signal; (b) envelope of the FFT-based analytic signal; (c)-(e) envelopes of analytic signals using Daub-4 basis functions in one, three, and six stages; (f) envelope with a three-stage Daub-6 discrete Hardy projection.

the Daubechies-4 wavelet-packet discrete Hardy projection of the signal. The figure confirms what we expected to see; each additional stage in the wavelet-based discrete Hardy projection resolves a wider frequency range. This effect can be observed typically in the chirplets at the beginning of the signal. When we compare the 3-stage projection with the single stage projection, we see that the lower frequencies in the middle between two mirrored chirplets are better resolved in the 3-stage projection. Figure 6.13 (e), illustrates another effect. The envelope is becoming much more similar to the envelope shown in Fig 6.13 (b), the envelope of the FFT-based projection of the signal. Due to the sampling operators, the local filters of the wavelet-based discrete Hardy projection have influence in a wider range. This effect is shown in the scaling Delta function (third peak from the left). At the base, the envelope extends much further than in (c) and (d). Another effect of these wide-range filters is the introduction of effects that are comparable to the Gibbs phenomena visible in the chirplets. The global effect of the additional filters in the last couple of stages causes this irregularity of the envelope. In summary we can state that we can compute a wavelet-based discrete Hardy projection with short-duration filters. The local Hardy projection in (c) does not cover a range of frequencies that is wide enough to resolve the proper envelope at all frequencies. On the other hand the envelope of the 6-stage wavelet-based discrete Hardy projection seems to be over-resolved at some frequencies, which results in a less smooth envelope and the introduction of interference effects. As an extra example we have included the envelope of the Daubechies-6 three-stage wavelet-based discrete Hardy projection. With the variation of the number of stages and the order of vanishing moments, we can optimize the envelope. However, the number of stages and hence the slope of the boxcar is limited by the length of the projection filters. With shorter filters the slopes are better approximated, whereas with longer filters, the flatness at the top of the boxcar is emphasized.

■ 6.3.3 Instantaneous frequency by wavelet-packet Hardy projection

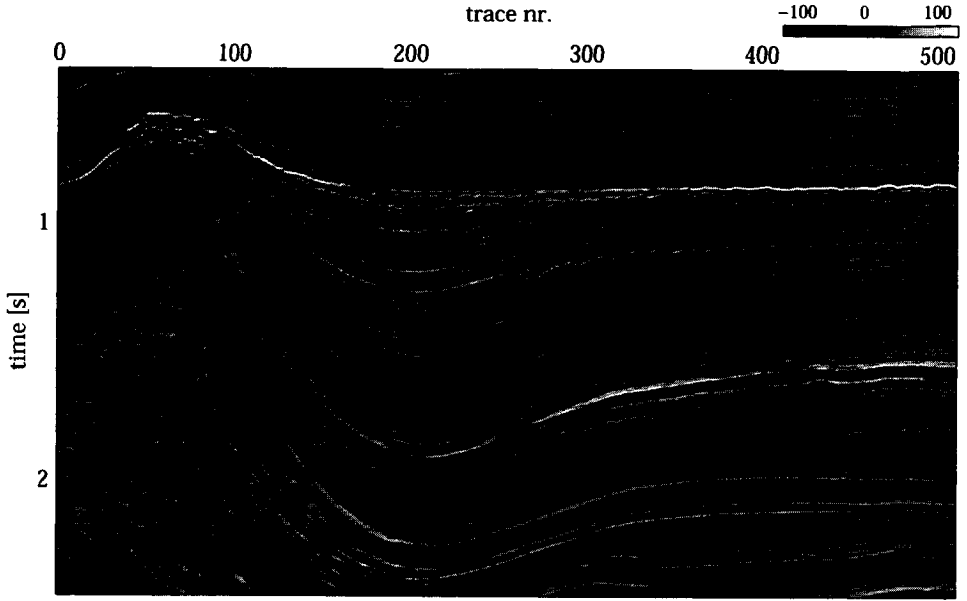
A variety of attributes can be extracted from the wavelet-packet Hardy projection. We are not going to much into detail on the different attributes. Because the instantaneous frequency plays an important role, also in the discussion of other attributes, we have decided to use it as an illustration of the algorithm. For the computation of attributes with the discrete Hardy projection, we make use of the redundant subband representation. Each subband corresponds with the original signal convolved with one of the filters

in Fig. 6.10. We have computed the instantaneous frequencies of each of the subbands, and subsequently computed the first moment weighed by the envelopes in each subband. By doing so, we obtain a smooth representation that lacks negative frequencies; Those sections of each subband with high energy show accurate instantaneous frequencies. The same method can be employed for the computation of other attributes, too. The resulting instantaneous frequency representation is shown in Fig. 6.14 (b). Compared to the instantaneous frequencies computed through the FFT-based Hardy projection in Fig. 4.12 (a) and the local Hardy projection in (b), this representation is hardly contaminated with noise or spikes. Although less computationally efficient than the previously mentioned techniques, the method is still much faster than other time-frequency transform based techniques, such as the spectrogram.

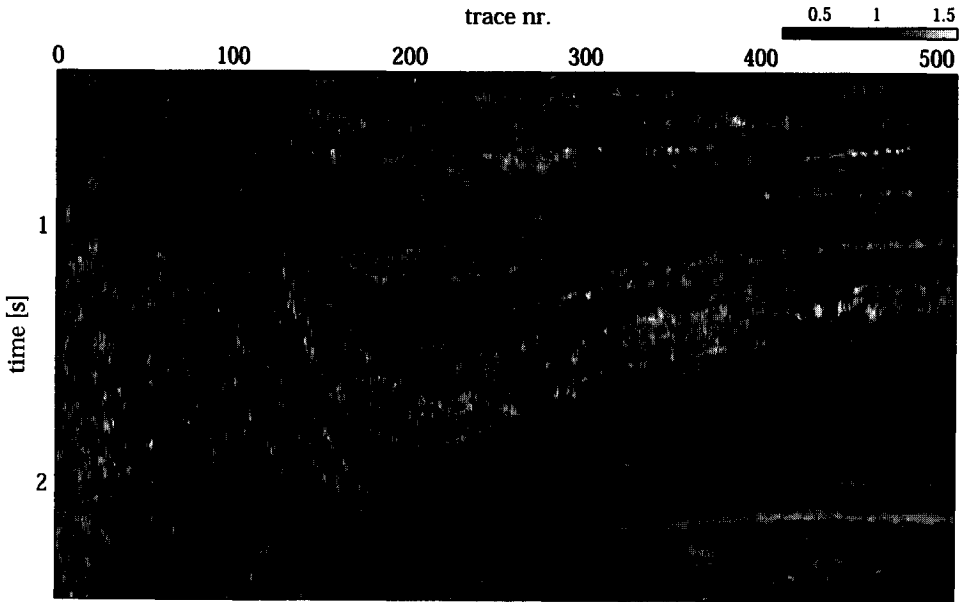
In this section we have illustrated some of the properties and implications of the iterated complex wavelet transform. Next we will extend the transform to higher dimensions.

6.4 Multi-dimensional iterated complex wavelet transforms

We will extend the complex transform discussed in the previous sections to more dimensions. We will see in accordance with the observations we did in Chapter 5, that due the complex character of the transform, the transform improves the directional selectivity compared to the conventional wavelet transform. Due to the improved filter design and the integrated scale dependent local Hardy projection, the iterated complex wavelet transform shows an even better angle distribution in the same six subbands as the multi-dimensional pre-projection algorithm. The flexibility of the multi-dimensional iterated complex wavelet transform not only encompasses the broad range of wavelets that we can use in the transform, but also the choice between a real-valued or a complex geometric wavelet transform. This simply means that besides the regular complex extension of the iterated complex wavelet transform with its accessory redundancy, we can also obtain a real-valued equivalent of this transform *with* directional selectivity! This might be useful in certain types of applications. Consistent with the pre-projection complex wavelet transform, the iterated geometric wavelet transform decomposes seismic images into energy, scale and angle. The improved shift-invariance of the iterated complex wavelet transform translates in more dimensions to even better energy estimations in the subbands than for the



(a)



(b)

Figure 6.14: (a) Seismic data (L5-block); (b) wavelet-packet instantaneous frequency.

geometric pre-projection transform.

Although the iterated complex wavelet transform is more complicated to extend to more dimensions than the pre-projection transform is, the multi-dimensional iterated complex wavelet transform is a straightforward extension of its one-dimensional equivalent. We will address the discrete filterbank implementation of the multi-dimensional complex wavelet transform, since the continuous principles can be easily extrapolated from the one-dimensional complex wavelet transform and the wavelets and scaling functions are of the same form as those discussed in pre-projection. We make extensive use of the fact that the projection filters operating in negative frequency space are the complex conjugates of those operating in the positive frequency space. The implementation is discussed in the first paragraph. In the subsequent paragraphs we will discuss several properties of the two-dimensional transform, followed by the last paragraph of this section in which the extension of the transform to an arbitrary number of dimensions is discussed.

■ 6.4.1 Two dimensional iterated complex wavelet transform

As we have mentioned before, the two-dimensional wavelets and scaling functions have very similar shapes as those discussed in the pre-projection transform. The two-dimensional wavelets and scaling functions are separable and can be obtained according to Eq. (5.39).

In Fig. 6.15, the multi-resolution spaces are shown that are spanned by the two-dimensional iterated complex wavelets and scaling functions. The spaces \mathcal{V}_0^\pm are the spaces spanned by the two-dimensional separable scaling functions, the space $\mathcal{W}_j^{m\pm}$ are the spaces spanned by the wavelets. From the Figure we can see that the spaces spanned by the wavelets are split in the same way as for pre-projection. There are six subspaces at each scale ($m\pm = 1-, 2-, 3-, 1+, 2+, 3+$). In conformity with the one-dimensional equivalent, the spaces are not nested.

The two-dimensional complex discrete wavelet transform of an image $U(x_1, x_2)$ is given by the same representation as in Eq. (5.38). The wavelets and the scaling functions themselves are different of course, because they are obtained in a different way; the resulting complex image as well. These differences are related to the different approaches in the previous section. The tensor wavelets in both cases support the same directional and scale information. The Fourier responses of the tensor wavelets are shown in Fig. 5.16. In accordance with the pre-projection complex wavelet transform and most of the other complex wavelet transforms, the iterated transform senses a differ-

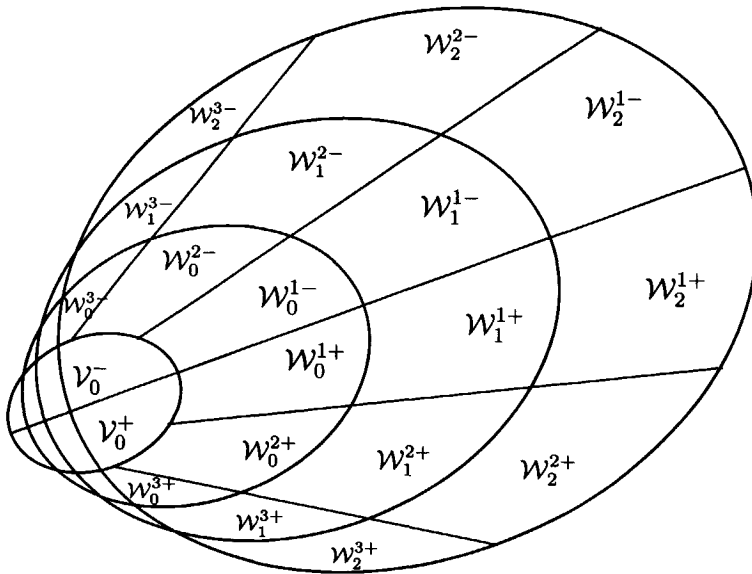


Figure 6.15: The resolution spaces spanned in the 2D iterated CDWT. The subbands spanned by the complex wavelets are divided into six regions.

ence between positive and negative angles, which leads to six instead of the usual three directional highpass subbands, with the angles centered around 15° , 45° , 75° , and their negative equivalents. Since the redundancy of the iterated complex transform is equal to the redundancy of the pre-projection transform, the same tiling can be used, which is shown in Fig. 5.17.

An important remark about the multi-dimensional iterated complex wavelet transform is that we can also calculate its real-valued angular selective equivalent. Each subset in the transform satisfies the symmetry conditions of Eqs. (6.17) and (6.18). When we select the real values of $U^+(x_1, x_2)$, the transform given in Eq. (5.38), we obtain a real-valued transform that still shows directional selectivity and satisfies the perfect reconstruction property. We will dwell upon this later on in this section.

The basis functions contributing to the different angles are shown in Fig. 6.16 for Daubechies-4 filters in each direction. When we compare these functions with the basis functions spanning the pre-projection complex wavelet transform, we observe that the functions have a much more pronounced sense of directionality. We have only shown the real part of the

basis functions, because those better illustrate the directional information. The local character of the basis functions is clearly visible in the limited number of samples.

Filter bank implementation In contrast to the pre-projection CDWT, the 2-D iterated CDWT is less easily implemented. The diagram for the filter bank implementation is shown in Fig. 6.17. The discrete image $I(n, m)$ is used as an input for the 2-D transform. First, the image is put through the two filters G_1^+ and H_1^+ . These represent matrix multiplication to replace the linear convolutions with the matrix components. The direction 1 is the direction of preference, which means that we can discard the negative counterpart in the transform. After downsampling each of the branches is subjected to four filters in the second direction. The matrices G_2^+ and H_2^+ contain the complex high- and lowpass filters in the lateral direction. Their negative equivalents are the complex conjugates of their positive counterparts. The output is shown on the right and can be compared with the coefficients (single stage) shown in the tiling of the transform in Fig. 5.17 (two stage). The

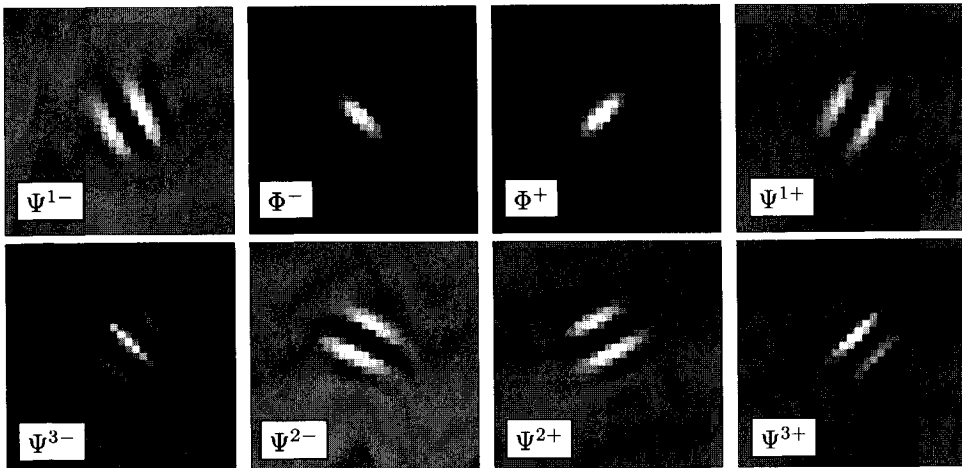


Figure 6.16: The eight directional basis functions of the iterated CDWT (real parts). Φ^+ and Φ^- indicate the scaling functions, Ψ^{1-} and Ψ^{1+} indicate the $\pm 75^\circ$ oriented wavelet subbands, Ψ^{3-} and Ψ^{3+} , the $\pm 45^\circ$ oriented wavelet subbands, and Ψ^{2-} and Ψ^{2+} , the $\pm 15^\circ$ oriented wavelet subbands.

transform can be easily reconstructed from its coefficients by simply adding the negative and positive coefficients and subsequently performing a conventional 2-D inverse DWT.

Amplitude and phase The iterated complex wavelet transform is the second new type of complex wavelet transform introduced in this thesis. We compare the transform with the pre-projection complex wavelet transform. First we discuss the amplitude and phase representations. These are key properties for a complete description of a seismic image. A high performance

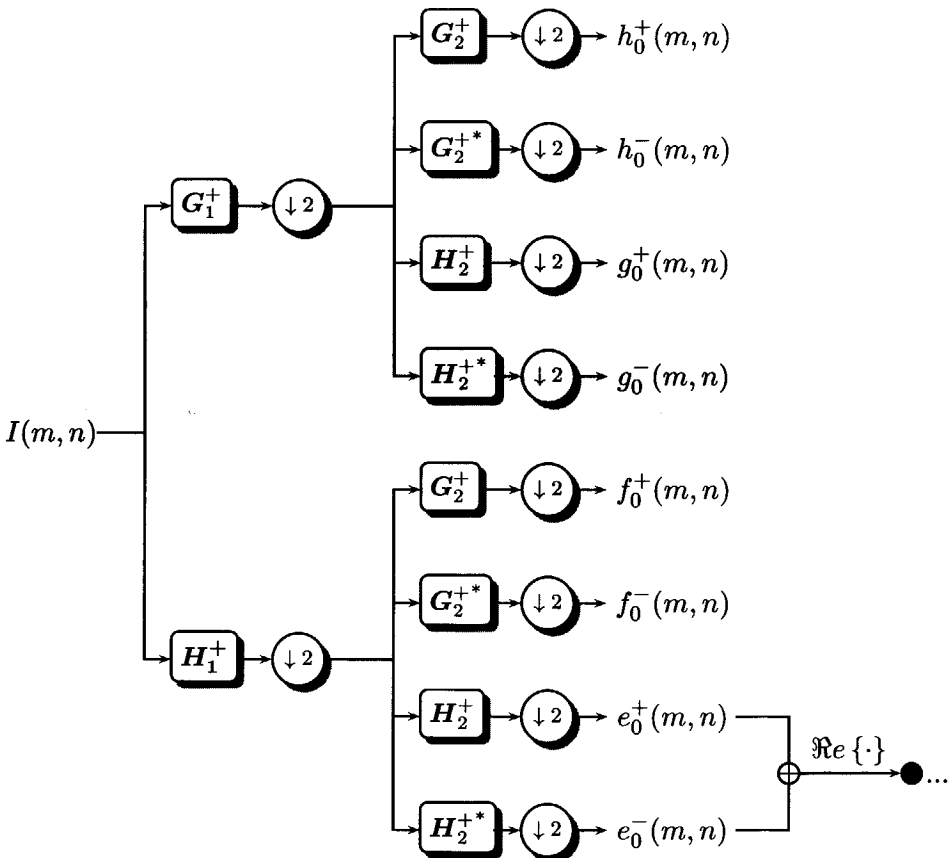


Figure 6.17: Two-dimensional iterated complex wavelet transform filter bank tree. The real part of the sum of the lowpass filters is used as an input for the next iteration.

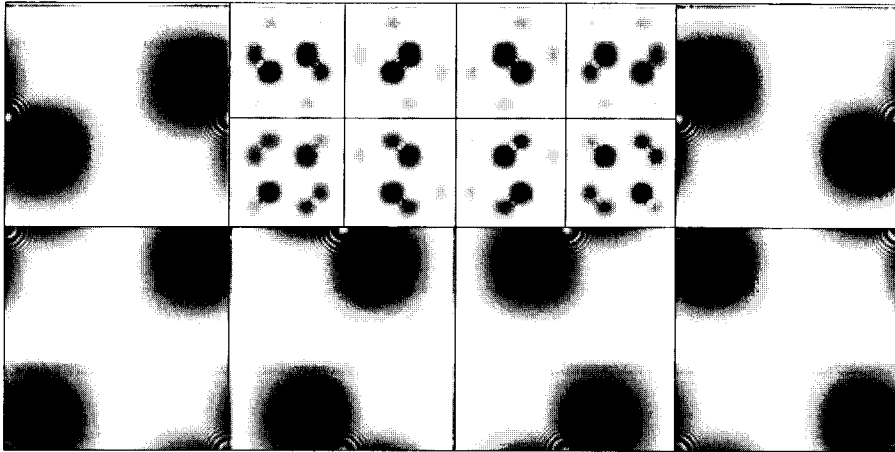
with regard to these properties will lead to more accurate attributes.

We have seen that the complex wavelet transform results in an amplitude and phase representation. In more than one dimension we retain this property. We will show the amplitude and phase responses of the iterated complex wavelet transform. An important observation for future use of complex transforms is the consistency over scale of both parameters. This particular parameter is important for the statistical description of the transform, which can be used for segmentation of the image in future applications. This topic is discussed in the next chapter.

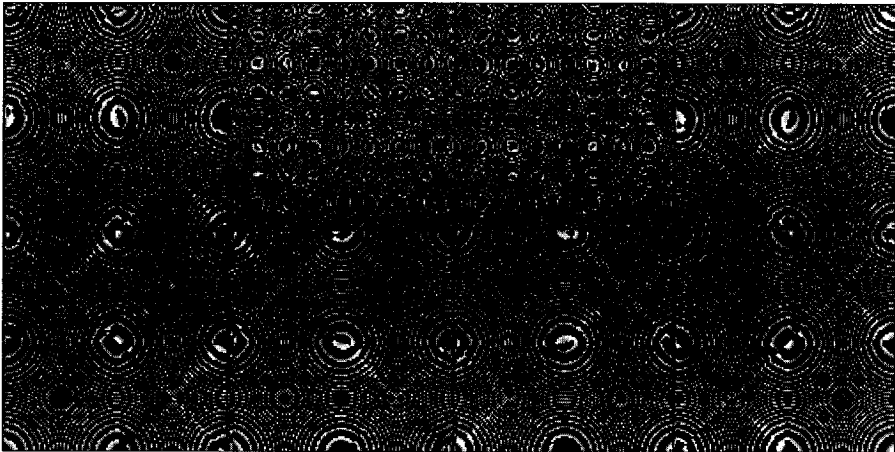
In Fig. 6.18 the iterated complex wavelet transform is shown of the 256×256 zoneplate to illustrate the transform. The magnitude response in Fig. 6.18 (a) clearly shows the directional information in the subbands. The phase is shown in Fig. 6.18 (b). The boundaries of the angular information in each subband of the amplitude response (b) are much more clearly defined than we have seen in the same representation of the pre-projection transform (Fig. 5.20 (b)). The envelopes of the response have a smooth character and hardly show any aliasing. They give a much sharper representation than the pre-projection complex wavelet transform. There is some local interference in the subbands of the regions in the second stage. These mainly result from inter angle information exchange, because of the narrow filter length (Daubechies-4). In contrast to the phase of the pre-projection transform of the zoneplate in Fig. 5.20 (b), the phase response of the iterated complex wavelet transform has a distinguishable directional sensitivity. This phenomenon is expressed most clearly in the center of each of the finest resolution subbands. As we have mentioned in the former chapter, the consistency over scale of information is important for the statistical analysis of images. The iterated complex decomposition is very much consistent through scale.

Figure 6.19 shows the magnitude response of the iterated complex wavelet transform of the image in Fig. 3.15 (a). The same can be observed as previously for the pre-projection complex wavelet transform: the faults are separated from the stratification due to their vertical nature, whereas the horizontal stratification is localized in the appropriate near horizontal subbands.

The reflection amplitudes are depicted in the horizontal subbands. The amplitudes consist over different scales, an important criterion for statistical decomposition of an image. Certain faults only show up at coarser scales. Those faults consist of a smoothed step, rather than a sharp step. At the next coarser scale these smooth steps can become more pronounced. The phase of



(a)



(b)

Figure 6.18: (a) The magnitude response of the Daubechies-4 complex iterated CDWT. (b) The phase responses of the same transform.

the transform of the signal is depicted in Fig. 6.20. The phase shows similar concentric circles in each subband. An interesting observation is that the phase tend to show the direction of the filter.

Directional information The filters of the iterated complex wavelet transform show the same frequency partitioning as the pre-projection transform. According to the frequency information in the complex wavelet transform,

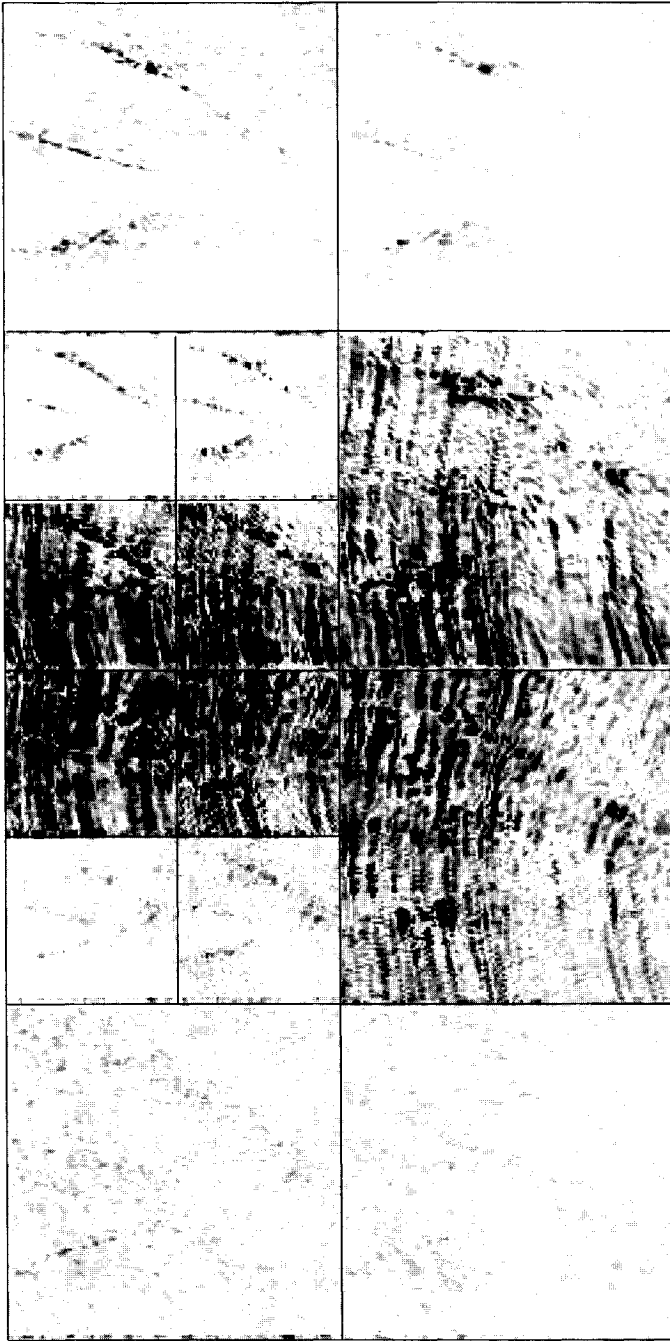


Figure 6.19: The magnitude response of the Daubechies-4 complex iterated CDWT of the seismic image in Fig. 3.15.

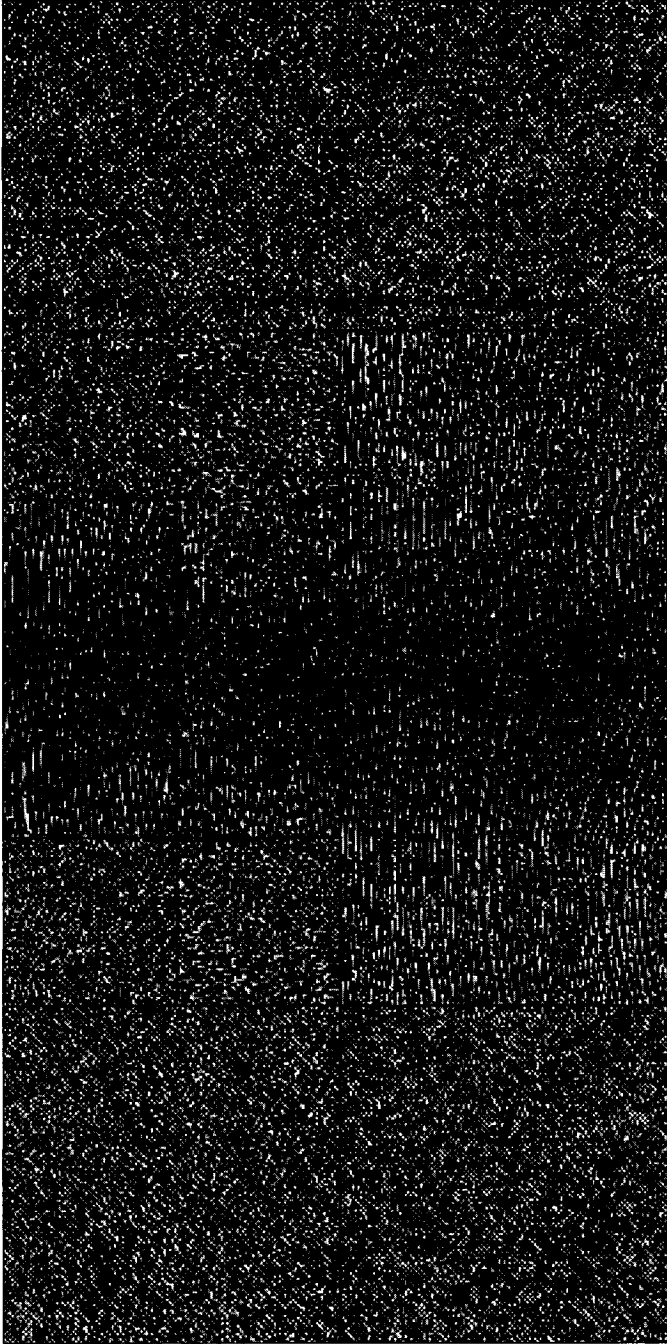


Figure 6.20: *The phase response of response of the Daubechies-4 complex iterated CDWT of the seismic image in Fig. 3.15.*

the subbands contain directional information in the space domain (Fig. 5.16). The directional shapes of the basis functions affirm that (Fig. 6.16).

Let us evaluate the directional information present in the subbands of the iterated complex wavelet transform using the synthetic zoneplate image in Fig. 6.18. We have seen this image several times before, because it is especially useful for the illustration of the directional information and the polar frequency information. The zoneplate contains a wide variety of polar frequencies and has the widest possible variety in angles (after all, a circle contains all angles).

In the magnitude response of Fig. 6.18 (b), we clearly distinguish the directional information in the different subbands. Each subband extracts its characteristic angle range. Of course the same comments hold for the filter shapes as we have discussed in Section 5.3 that the rectangular shape of the filters is not in harmony with directional selectivity. Due to the local character of the basis functions of the complex wavelet transform as can be seen in Fig. 6.16, the angular selectivity performs well. In comparison with the direction performance of the pre-projection complex wavelet transform, we can say that the directions are more sharply bounded.

An issue that has come up a couple of times is that the iterated complex wavelet transform can be used for a real-valued direction wavelet decomposition. The redundancy is reduced in that way, but the directional information is maintained. In Fig. 6.21 we show an example of the *real* iterated two-dimensional transform. The data in the low pass subbands and in the close to horizontal subbands is slightly clipped to emphasize the information in the other subbands. This figure shows a more distinct directional discrimination between the subbands (compare Fig. 3.15). We do not employ this particular transform for attribute extraction, because for that purpose the quadrature relation between real and imaginary decomposition is indispensable.

■ 6.4.2 Three and higher dimensional iterated complex wavelet transform

We will not address the extension to three dimensions in this thesis, because it is a straightforward extension of the two-dimensional approach. The Fourier partitioning of the three-dimensional iterated complex wavelet transform is identical to that of the pre-projection transform and is illustrated in Fig. 5.23.

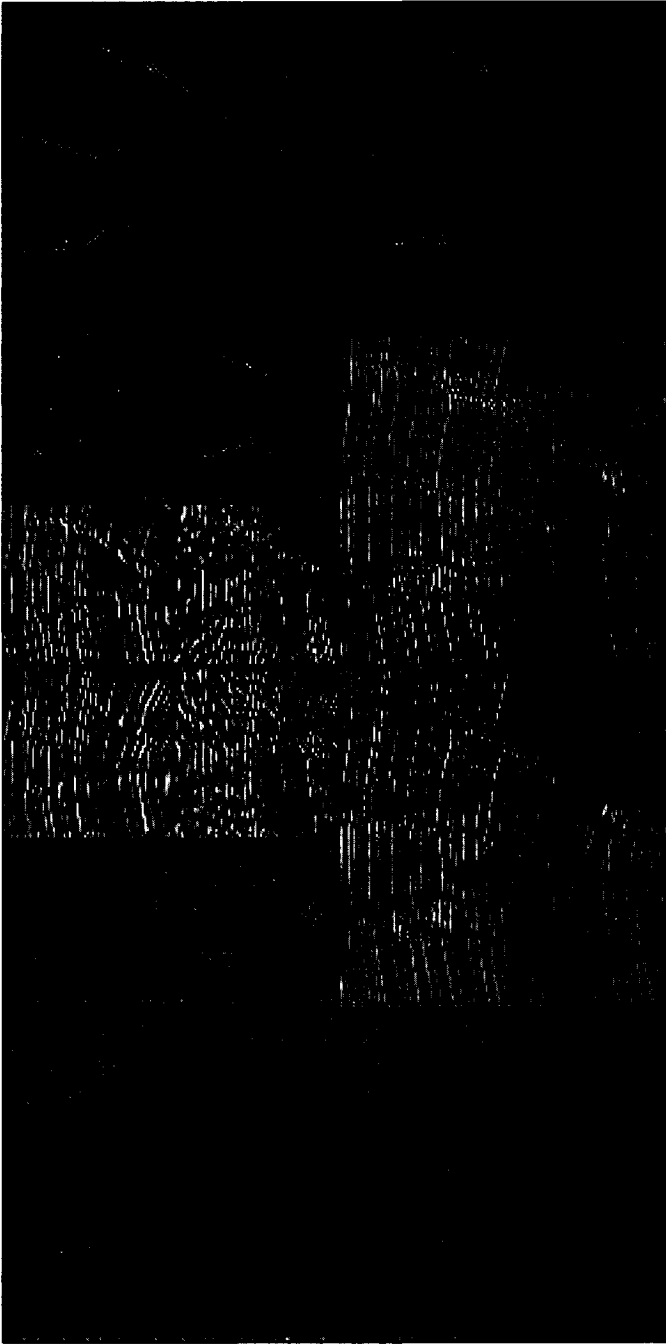


Figure 6.21: A real-valued directional selective transform: perfect reconstruction can be obtained from this real-valued iterated CDWT representation.

Quantitative seismic volume attributes

The decomposition of three-dimensional seismic data into the local components geometry, frequency and reflection strength, leads to a better understanding of the seismic reflector and thus of the subsurface properties. Migrated seismic reflection data are opaque volumes containing reflection information from contrasts in the subsurface. Seismic interpreters scrutinize the seismic volume at all scales, varying from large scale structures to detailed reservoirs. The conventional techniques used for this purpose encompass the auto-tracking of prominent reflection surfaces and derivatives of this surface, and section-by-section analysis of data with the help of conventional complex-trace attributes. Although it is a very time-consuming effort, the interpreter obtains a clear idea of structures. The keen eye of the interpreter often sees the differences in sedimentary architecture, not on basis of the single reflection amplitudes, but based on patterns of reflection amplitudes. With our novel mathematical techniques, we want to categorize this type of information in an efficient way.

The conventional trace-by-trace visualization and interpretation of reflection data with wiggle plots, is not doable with the vast amounts of data we are handling nowadays. Moreover, trace-by-trace analysis indicates a

one-dimensional analysis of the volumetric data, which does not take the geometric extent of the reflector into account. Time-slices are underutilized, because the often blurred contourlines of the reflection amplitudes hardly add any value to the seismic sections. In these modern times, in which the computer plays such a prominent role and the digital signal plays a key role in society, we have to use the computational power to characterize the signal and visualize the details that we overlook with our eyes. The computer has the ability to see in a multi-dimensional space with its digital sensors. With the computer we can link, correlate and combine the information in the volume. This gives the opportunity to study the reflector *environment*.

The type of data we consider is migrated seismic data. With migration we have removed the wave-propagation effects from our data. The measured waves have been roughly de-propagated to where they originated, the contrast between the rock parameters. The image or volume after migration can thus be interpreted as a one-to-one mapping of the contrasts in the Earth's subsurface. The migrated seismic data contains a treasure of information. With the existing techniques we are able to follow reflections along the reflector to get an idea of the structures in that reflection surface. The amplitude of reflections is related to the contrasts in the Earth, the phase to the timing of the reflections. In seismic data, small amplitudes with high-frequencies are often dominated by larger amplitudes with lower frequencies. Generally data is visualized such that a good impression of structures is obtained. This means that excessive amplitudes are clipped by a maximum value, whereas small often high-frequency events often lose their relevance, because they are overshadowed by the larger amplitudes. What is it in fact that we are looking for? The rough layering in seismic sections merely gives an impression of the structures of the subsurface. But what about the fine-scale information? Can we extract detailed information from a seismic image, which is limited by resolution criteria? Yes, we can. Channels and small-scale information are well-localized and often laterally oriented. The information on these events is in the phase rather than the amplitude. Although migration operates on the phase, the channels tend to be located in a single macro-layer, and thus undergo the same operations. This means that the small scale events are not damaged by migration, but rather improved. It is the fine scale information on top of the rough structural information that we want to visualize. The quest in this chapter is to extract meaningful physical and structural parameters with data driven quantitative interpretation techniques. We will show that these help us in the understanding and interpretation of the geology. In

this way we want to enhance the transparency of the seismic volume data.

For this purpose we use the attributes developed in Chapters 4 and 5. We do not employ the transform discussed in Chapter 6. In order to obtain a better understanding of the sensitivity and the meaning of the attributes, we will discuss each of them using a simple synthetic seismic model. The example that we consider is a synthetic seismic data volume, containing a single reflector with a wavelet imprint. Subsequently we will show two seismic field-data sets for the illustration of the attributes. The first field data set is the Amoco South Marsh Island data set which is frequently used as an example for the illustration of seismic attributes. The second data set concerns a data set from the L05 block in the North Sea near the Netherlands.

7.1 Synthetic reflection model

The attributes that we derived in Chapter 4 and 5 were only tested on the zonecube, a synthetic signal representation that contains a wide variety of frequencies and all possible angles. In a seismic volume, the geometry and frequencies are not so uniformly distributed as in the zonecube. In order to evaluate volume attributes for seismic images, we have generated a simple synthetic seismic model. This model is used in the subsequent two sections to get a better understanding of the attributes. The model is a much simplified representation of seismic data, in which we know the structure, the history and the shape of the signal. The model consists of a single reflector with a simple sedimentary structure, and a moderately varying geometry. The reflection coefficients of the reflector vary depending on its geological character. For the example we have chosen to use a submarine fan, containing a feeder channel, a debris fan or slump and a slope structure. In addition to imitate tectonic activity the debris fan is intersected by a normal fault. We will encounter all of these events when we consider the field data in the subsequent sections

■ 7.1.1 Shape of single reflector

We have used some simple mathematical functions to model a three-dimensional reflection interface. The shape of the reflector is shown in Fig. 7.1. The model represents a reflector in a submarine fan: a feeder channel cuts through the sediments on the continental slope and builds submarine fans at its bottom. After sedimentation, tectonic activity formed a normal fault with a certain orientation with respect to the structure. We have appointed various

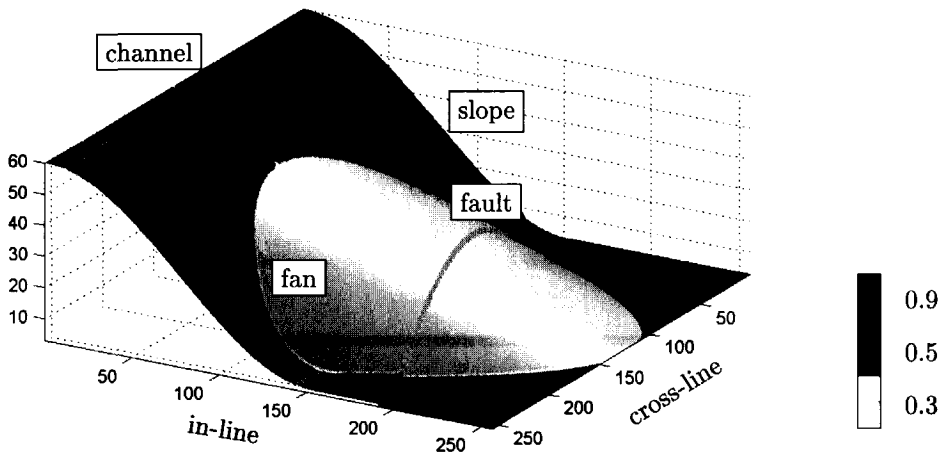


Figure 7.1: A simple reflector model for the validation of attributes, consisting of a feeder channel and a submarine fan cut by a fault.

reflection coefficients to each of the sedimentological units. The grayvalues of the segments are indicative for the respective reflection coefficients of which the values are given in the scale on the right. The slope, which is modeled to have a sinusoidal shape, has a reflection coefficient of $R = 0.5$, the feeder-channel bed has a reflection coefficient of $R = 0.3$, the debris fan or slump of $R = 0.3$ and the base of $R = 0.9$. The reflection coefficients are strictly positive, and between 0 and 1.

■ 7.1.2 Synthetic migrated seismic data

The size of our data set measures 256×128 samples at a sampling density of 25×50 [m] in the in-line and cross-line direction, respectively. For the synthesis of migrated seismic data, we have performed vertical convolution with a zero-phase length-50 Ricker wavelet in order to simulate migrated zero-offset data. Subsequently we have down-sampled the volume by 4 samples along the vertical component, in order to obtain a delta structure that is comparable with the information we have from field data with a time-sampling interval of 4 [ms]. The total time-span for the seismic data is set to 352 [ms]. The structure shows merely moderate angle variations and hardly any

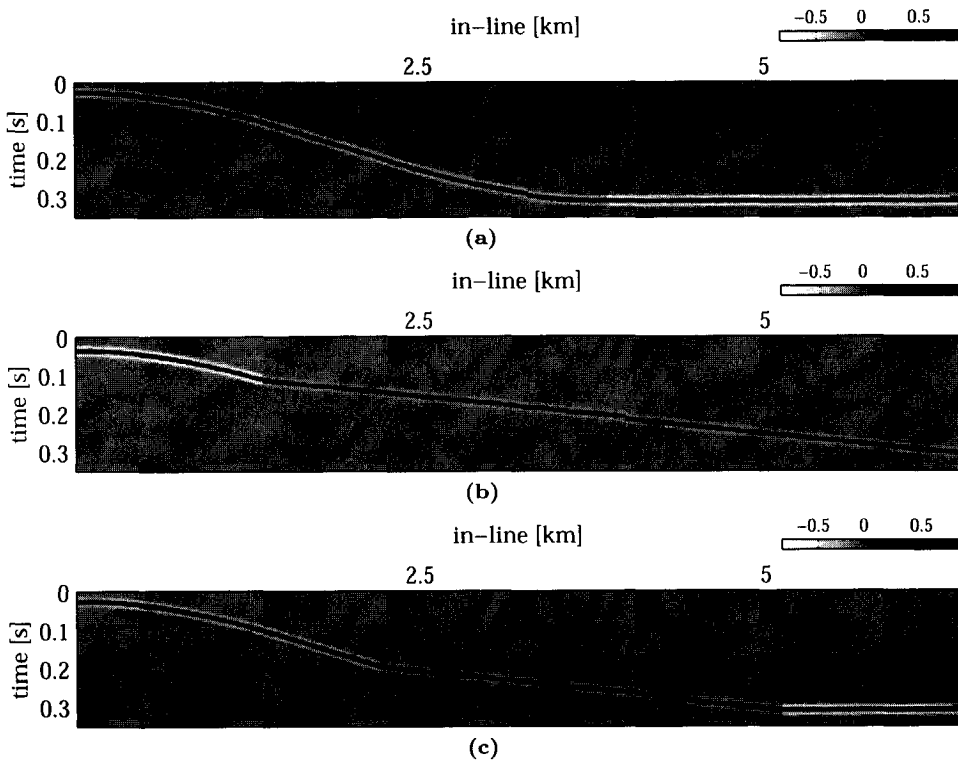


Figure 7.2: *In-lines of the modeled seismic data; (a) at cross-line position 500 [m]; (b) 3250 [m]; (c) at 5000 [m].*

vertical frequency variations. We have depicted several sections in Fig. 7.2 and Fig. 7.3 along in-line and cross-line direction, respectively.

In the next two sections we discuss the different attributes on the basis of the synthetic seismic data.

7.2 Attributes based on local Hardy projection

First we will elaborate on the attributes that were introduced in Section 4.4.3 and in particular their seismic meaning. By computing the attributes of the synthetic model, we can get a better idea of the similarities and differences between the two different attribute approaches, those based on the local Hilbert transform and those based on the pre-projection complex wavelet transform, from now on simply referred to as complex wavelet transform.

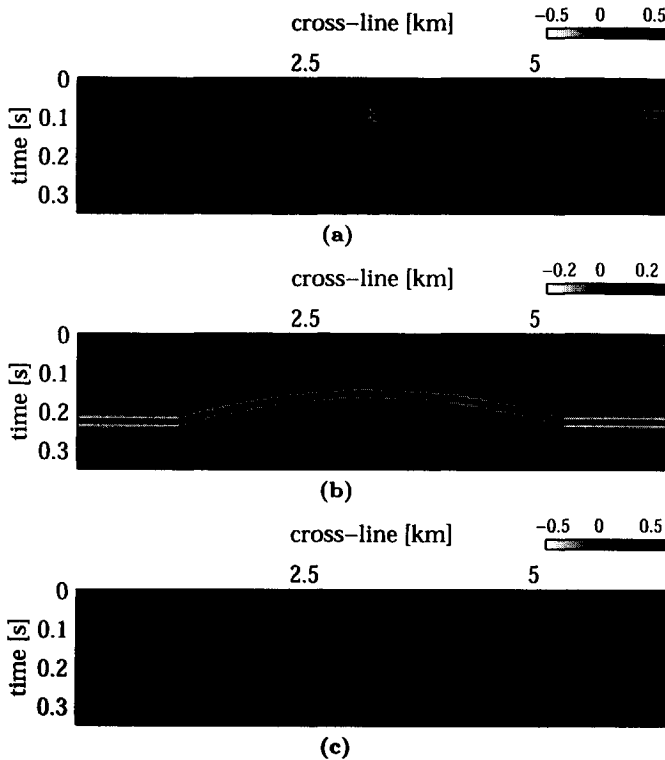


Figure 7.3: *Cross-line sections of the modeled seismic data; (a) at in-line position of 1250 [m]; (b) at 2500 [m] and c at 4000 [m]*

■ 7.2.1 Radial frequency

Instantaneous frequency is a standard attribute provided in all of the seismic interpretation software packages and is often used as a lithology indicator. Each characteristic stratigraphy or sequence of reflections, shows up in frequency as such. The instantaneous frequency tells us locally which characteristic frequency belongs to which part of the seismic section. The word instantaneous frequency already reveals its one-dimensionality. Not surprisingly, none of the interpretation packages provides the opportunity to study the instantaneous frequency on a time-slice representation. We have introduced a new type of local frequency in Section 4.4.3 that fits within our scope, the multi-dimensional characterization of seismic reflections. The fact that we are working with multi-dimensional data, requires a multi-dimensional approach. On the basis of our synthetic seismic data, we show that the

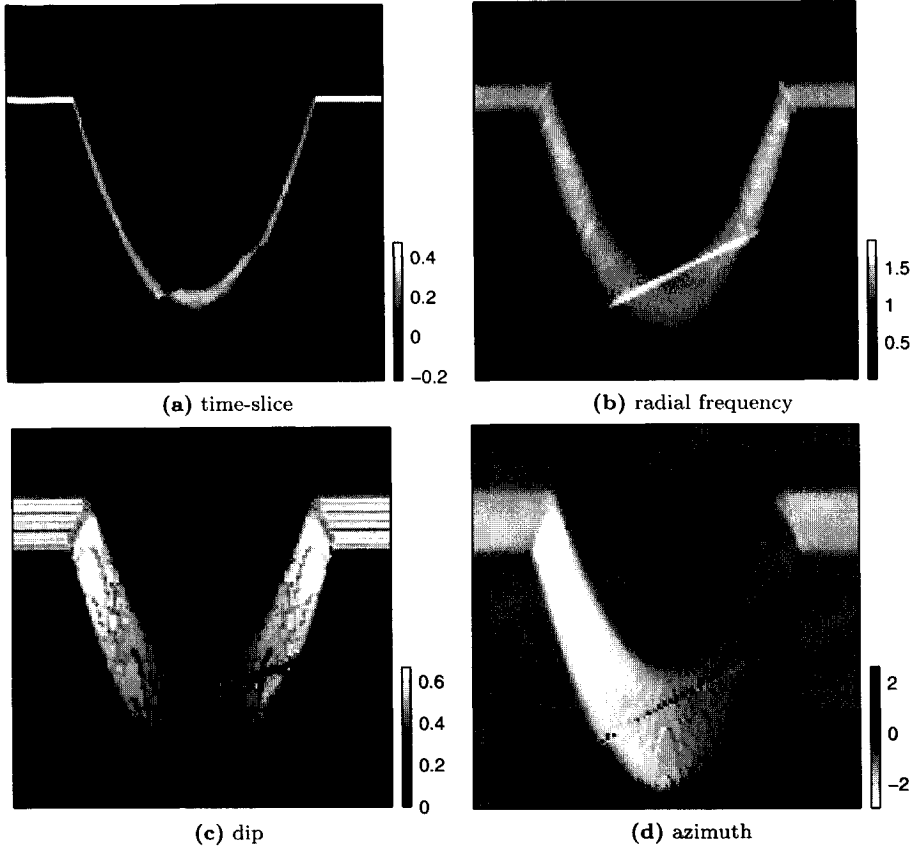


Figure 7.4: Local Hardy projection-based attributes of synthetic model; (a) Amplitude slice at $t=224$ [ms]; (b) radial frequency representation; (c) dip representation; (d) azimuth.

multi-dimensional radial frequency is very useful for structural and stratigraphic interpretation of time-slices.

Figure 7.4 (a), shows a horizontal time-slice taken from the modeled seismic data at $t=224$ [ms]. For convenience we selected a window reaching from 1650 [m] to 4825 [m] in-line. The slice intersects with the normal fault. In Fig. 7.4 (b), we show the local radial frequency slice. The frequency looks very pure without much noise interference. The frequency increases along the slopes of the fan compared to the ridge of the fan, where the frequency decreases. The edge of the fault becomes visible as a continuous event and appears as high frequency information. The frequency character of the Ricker

wavelet shows up as the imprint of the frequency response, with the maximum frequency in the center and decaying towards the edges. Overall we state that the radial frequency computed through the local analytic signal is reliable for the 3-D synthetic seismic model.

■ 7.2.2 Dip and azimuth

Local geometry has played a central role in the development of our algorithms. The extraction of geometric information has had an enormous impact on the use of time-slices for structural interpretation. In this section we will show how the dip and azimuth attributes introduced in Section 4.4.3 perform on the synthetic data set. In Fig. 7.4 (c) the local dip is shown and in (d) the local azimuth. On the ridge of the fan the local dip appears to be less than towards the edges. This is in conformance with the structure in Fig. 7.1. The fault can be clearly distinguished in the figure as an anomaly in dip. Although we obtain a sharp impression of the direction of inclination, even the finest steps appear to be sensed by the algorithm, judging by the very fine arc-shaped alignments visible on the fan. Although it seems desirable to be able to operate at fine resolution, it turns out that this also affects the stability as we will see later on with the application of the algorithm on field data. The azimuth in (d) clearly distinguished both sides of the fan. The fault appears to have a slightly positive azimuth and is colored accordingly. The azimuth representation shows the same arc-shaped alignments on the fan as the dip-representation.

7.3 Pre-projection complex wavelet transform based attributes

The attributes discussed in Chapter 5 performed well on the synthetic zone-cube. The complex wavelet attributes do not have a high angular resolution. The number of angles is limited to 6 in each direction. Nevertheless the complex wavelet transform performs well on seismic data, as we will show later on. The attribute used to characterize the frequency of the signal is the local scale. This attribute is comparable to the radial frequency in the previous section. Since the wavelet transform is known for its edge detecting properties, we expect that the attributes show a clear response to faults and discontinuities in any direction (Dessing, 1997). In the first two paragraphs we will discuss the attributes on the basis of the synthetic seismic model. An important reason to use wavelet transforms for the computation of attributes, is their potential for signal segmentation on statistical basis. We will shortly

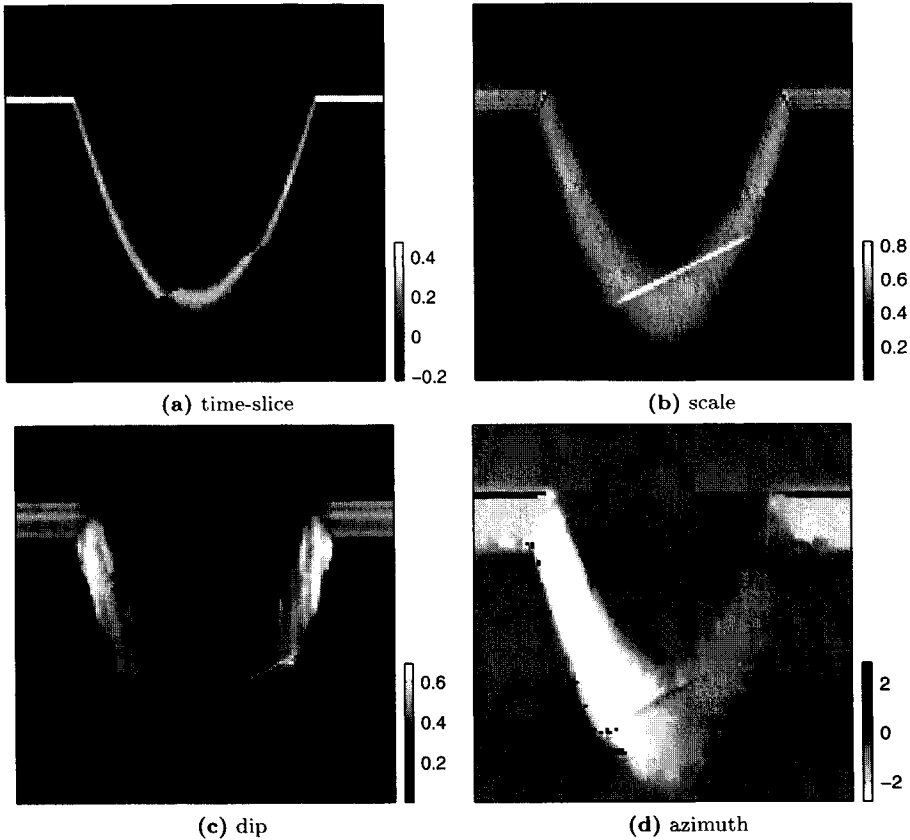


Figure 7.5: Pre-projection complex wavelet transform-based attributes of synthetic model; (a) Amplitude slice at $t=224$ [ms]; (b) scale representation; (c) dip representation; (d) azimuth.

speculate on this topic in the third paragraph of this section.

■ 7.3.1 Scale

In our deliberation of the complex wavelet transform attributes, we consider the same time-slice from our synthetic seismic model as in the previous section. Again the amplitude slice at is shown in Fig. 7.5 (a). The first attribute that we consider is the local scale. The algorithm for the computation is discussed in Section 5.3.3. The attribute slice is shown in Fig 7.5 (b). Not surprisingly, there is a large resemblance between the radial frequency discussed in the previous section (Fig. 7.4 (b)). Both attributes show ra-

dial frequency information. The radial frequency from the previous section shows a more detailed distribution of frequencies. Especially along the side lobes of the fan, where we see the increasing radial frequency, we hardly see any response to that in the scale. The normal fault, which is a lateral step function, has the same resolution and can be located accurately in the scale representation. In both representations, the fault shows up as an anomaly in the attribute, with higher values than the adjacent values. In the section on the seismic field data we will show that the scale is extremely valuable for geological interpretation and is more stable to noise.

■ 7.3.2 Dip and azimuth

The complex wavelet transform has a limited directional sensitivity. The two-dimensional transformation only possesses six directional subbands. However, when we include the scale, we can approximate the perfect angular selective wedge-shaped filter with a combination of square directional filters. This immediately implies that a range of frequencies is included in the directional analysis. This is different from other frequency-based techniques that are often dependent on window length.

In Fig. 7.5 (c) we show the dip representation. The distribution of the dips is comparable with the dip representation we saw in Fig. 7.4 (c); On the ridge of the fan the local dip appears to be less steep than towards the edges. This is in conformance with the structure and what we saw in Fig. 7.4 (c). The fault can be clearly distinguished in the figure as an anomaly in dip. When we compare both dip representations, we see that the complex wavelet transform based dip is not interfered by the arc-shaped alignments that we saw in Fig. 7.4 (c), but still shows the sharp line of the fault at a very fine resolution. The azimuth in Fig. 7.5 (d) clearly distinguishes both sides of the fan. The fault appears to have a positive azimuth and is colored accordingly. In the next paragraph the potential of the wavelet transform for seismic data segmentation is discussed.

■ 7.3.3 Towards volume segmentation of seismic data

The complex wavelet transform has shown its potential in attribute extraction in the previous paragraphs. In this paragraph we hypothesize about follow-up algorithms for attributes using complex wavelet transforms, and we motivate its potential compared to other statistical approaches.

The complex wavelet transformation decomposes an image according to

scale, magnitude and angle. With our attributes we compress the information in the transformation. We take an average along scale and along directions to be able to obtain a proper and interpretable representation of our data. However, we do not account for all the information in the transform. The transform has also combined information on the angles at a certain scale, and vice versa. In industry scientists have come up with numerous attributes that provide information on the signal. Nowadays, the providers of interpretation software are using statistical approaches to combine the attributes and characterize certain features on the basis of these combinations of attributes. Many of these software development companies use neural networks and other statistical algorithms for this purpose. The drawback of such a procedure is that incompatible pieces of a puzzle are matched.

In our approach, with the complex wavelet transform, we are in a different situation. We have a transform that contains a very complete representation of the signal in terms of scale, geometry, phase and reflection strength. In the previous sections, we have shown that we can compress the information in an attribute representation on the basis of averaging. One important property of the wavelet transform that we did not yet use is the interscale relationship. One of the reasons that the wavelet transform is par excellence suitable for compression is that the information is consistent over scale. This interscale relationship can be modeled with statistical algorithms. Crouse *et al.* (1998) showed that the statistical relationship between different scales can be modeled with hidden Markov models (HMT). Choi and Baraniuk (1999) on their turn showed that these HMT models can be used for the segmentation of images and signals. Segmentation of seismic images using wavelet domain-classification has been previously applied successfully on attribute slices (Magrin-Chagnolleau *et al.*, 1999). Due to the complex character of the complex wavelet transform, it has proven to perform even better than the conventional wavelet transform and that the statistical relationship is even considerably stronger (Choi *et al.*, 2000). Suppose that we can compress the transform on the basis of these statistical relationships that describe the complete transform and thus the complete signal character: We can segment the data according to its statistical relationship. In that way we put the pieces of the same puzzle together! 3-D HMT Segmentation of the complex wavelet transform could possibly lead to sophisticated data driven attributes, which segments on the basis of the complete signal description in terms of amplitude, phase and angle relationships over scale.

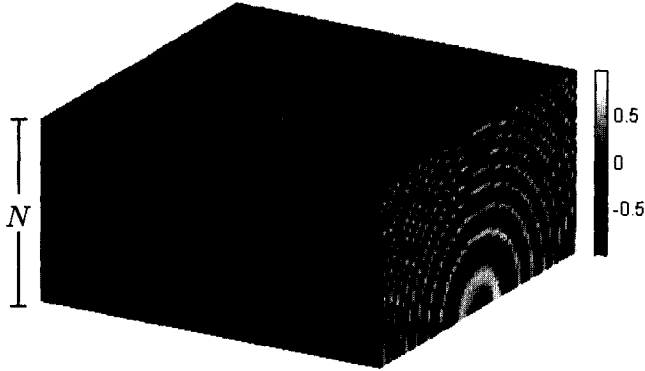


Figure 7.6: Upper half of the zonecube with $N=32$ samples thickness. The cube contains a wide variety of radial frequencies and all angles.

7.4 The Pseudo-horizon for visualization

The geometric attributes discussed in Chapter 4 and 5 can be united into a topographical representation of the local structures. The topography can be used as a platform for combined attribute representation.

Steeghs (2002) shows that when we have computed the dip in the in-line as well as the cross-line direction, we are able to compute a surface that represents the local structural variations by integrating over dips. The derivative of this surface in in-line and cross-line direction is then equal to the original input. The idea originated from the remote sensing field, where satellite information is conjoined to reconstruct the surface of the Earth. In this section we will illustrate how the technique works, with several examples. For this purpose we will revisit the zonecube and the synthetic seismic model. We will show the pseudo-horizon for both the local Hardy projection based attributes and the pre-projection complex wavelet transform based attributes. For the theoretical aspects concerning the algorithm we refer to Steeghs (2002).

■ 7.4.1 From amplitude to virtual topography

Let us reconsider the upper half of the $64 \times 64 \times 64$ zonecube as given in Fig. 7.6. We can compute the local variations in dip and azimuth using the algorithms discussed in Chapter 4 and 5. Alternatively we can rearrange the

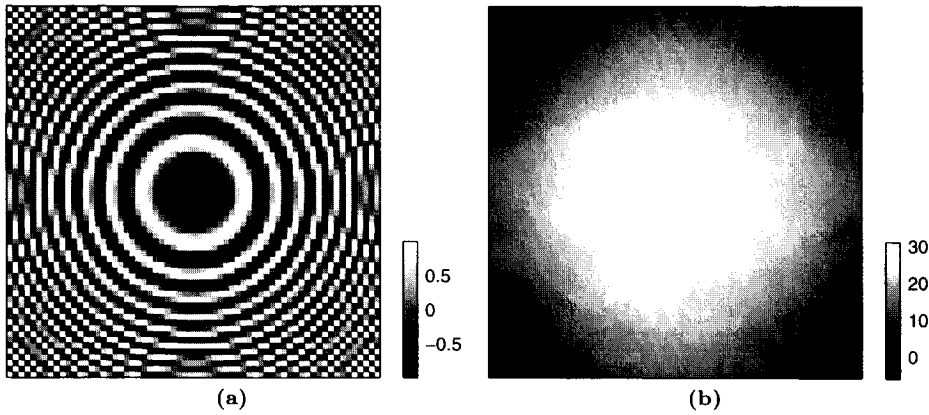


Figure 7.7: Illustration of a “pseudo-horizon”;(a) A single slice from the zonecube depicted in Fig. 7.6 at $n=18$ samples counted from the bottom; (b) altitude representation of the topography computed with the pseudo-horizon technique.

information in such a way that we obtain the cross-line angle of inclination and the in-line angle of inclination. Each of these separate representations can be subsequently integrated to a surface representation, and remapped to match each other. The latter involves a smoothing operation, which is not discussed into detail in this thesis.

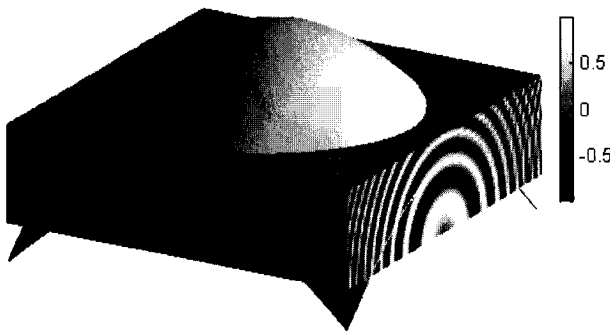


Figure 7.8: 3-D impression of the pseudo-horizon in Fig. 7.7 (b), combined with the original input slice with its underlying information.

To illustrate the pseudo-horizon algorithm we use the attributes as derived in Chapter 4, because the representation for the synthetic data is very accurate and sharp. In Fig. 7.7 (a), we show an arbitrary slice through the zonecube, that is located at sample $n = 18$ samples counted from the bottom. The slice looks similar to the zoneplate (see Fig. 4.5 (a)). In our perception each slice of the image contains the same frequency content, which is not the case for the entire, three-dimensional zone cube. The lowest radial frequency content is definitely found in the center of the zonecube, whereas the highest frequency content is found towards the periphery in the corners of the cube. The virtual topography or pseudo-horizon corresponding to this slice can be found in Fig. 7.7 (b). The values indicated in the bar on the right have been scaled to match the altitude in the zonecube. The horizon representation portrays an interface on the basis of the geometry information we have computed in the slice. The values give an indication of the structure locally at that particular plane interface. The information from above and from below are taken into account with the computation of the volume attributes. Since we have computed the virtual altitude at each position we can span a surface with these values. In Fig. 7.8 this surface is depicted together with the zonecube. The cube is sliced exactly at the reference altitude of $n = 18$ samples.

■ 7.4.2 Combined attribute representations

The pseudo-horizon provides us not only a unique representation of information on the local geometry of the data, but also a platform for combined attribute representation. In this paragraph we will show how we can depict the geometric information together with other attributes. For this purpose we use the pseudo-horizon depicted in Fig. 7.8 and the same slice from our radial frequency representation in Fig. 4.17 (b). The result is shown in Fig. 7.9. An interesting observation is that the low frequencies that were present in Fig. 4.17 (b) are no longer present. The frequency ranges from little bit less than $\pi/2$ to almost π . This confirms the fact that we are offset from the center of the zonecube with the lowest frequency content (close to $\omega = 0$). The horizon representation of our local geometry together with the local frequency information reveals information on the local structure and signal character that is invisible in the time-slice alone. It accommodates us with an excellent platform for the visualization of opaque seismic data.

To illustrate the attribute on synthetic data, we revisit the synthetic model discussed in Section 7.1. In these data we have modeled a mainly

sub-horizontally layered submarine fan. Although the model does not show the whimsical structures of seismic field data, still it helps us in understanding of the topography. We consider the same time-slice that we have used for the illustration of our attributes in Section 7.2. We have used the local Hardy projection for the computation of the in- and cross-line dip. The resulting pseudo-horizon is depicted in Fig. 7.10. The radial frequency —based on the local Hardy projection (Fig. 7.4)— is imprinted on the topography, the amplitude is indicated in the table on the right. The axes have the same sampling rate as used in Fig. 7.1. The combined attribute representation gives us an indication of the local structure and frequency content at the altitude of the time-slice. It is interesting to note that the normal fault that can be noticed on the ramp of the fan structure, is not directly recognizable as such. The front end of the fan structure that is cut off by the fault, has reduced in size. This effect is owed to the fact that we are still working with time-slice representations. The front end of the delta lobe moved downward. Hence, when the slice cuts through the delta lobe, including this front lobe, the part that has moved downwards appears smaller in size. This effect is clearly illustrated in the original time-slice in Fig. 7.4 (a). Again, we need to keep in mind that we are not looking at the actual horizon or structure but

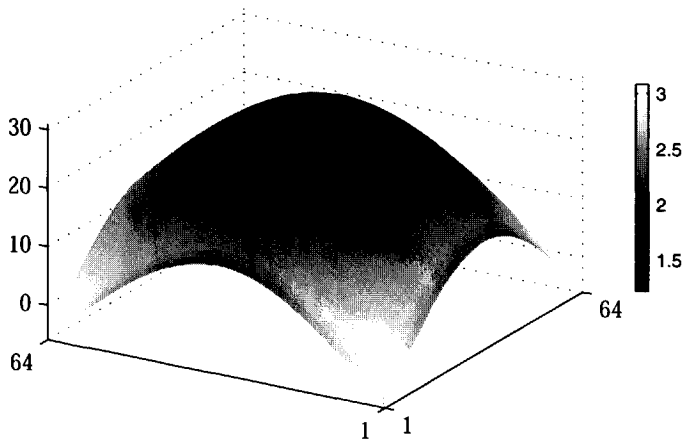


Figure 7.9: radial frequency imprinted on the pseudo-horizon in Fig. 4.17 (b): The topography is shaped with the pseudo-horizon algorithm, where the (gray-)values are an indication of local radial frequency content.

at a structure that is based on the local information on a time-slice.

The geological implications of the volume attributes and the pseudo-horizon technology for seismic interpretation are discussed in the next section.

7.5 Seismic Field data

For the validation of our attributes on seismic field data, we employ two seismic field data sets. The first data set considered is located in the Gulf of Mexico which is repeatedly used for the illustration and validation of volume attributes, such as the coherency cube (Bahorich and Farmer, 1995b) and the Wigner-Radon techniques (Steeghs, 1997). The second data set comes from the North Sea on the Dutch part of the continental shelf. The latter data are of extremely good quality, because they have rather recently been acquired. Both data sets contain interesting geological and stratigraphic phenomena. We have subjected the Gulf data to a more extensive study. We discuss two algorithms for attribute extraction and each attribute in isolation. For the data set from the Netherlands, we solely show the combined

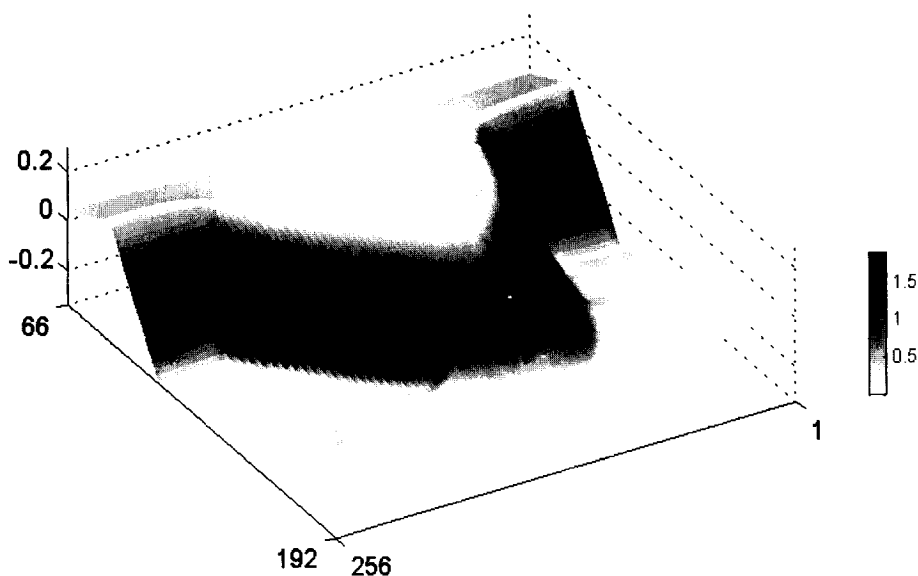


Figure 7.10: Imprint of radial frequency (Fig. 7.4 (b)) on pseudo-horizon corresponding with time-slice at $t=224$ [ms] in Fig. 7.4 (a).

attribute representation using the pseudo-horizon technique for the combined representation of dip and azimuth.

■ 7.5.1 Gulf of Mexico, South Marsh Island

For the illustration of the algorithms we have chosen two seismic data sets. The first data originates from the Gulf of Mexico. The data are recorded in the South Marsh Island area on the continental shelf, west and adjacent to the Mississippi delta. The data set is a part of a larger speculative survey of the area. It is frequently used for the illustration and validation of volume attributes, such as the coherency attribute (Haskell *et al.*, 1995; Nissen *et al.*, 1995; Steeghs, 1997).

The sampling interval of this dataset is 8 [msec], the in-line trace distances are 25 [m], the cross-line distances are 50 [m]. These data are down-sampled from a post-stack 2-D by 2-D migrated volume. The original sampling rate was 4 [ms] and the in- and cross-line trace distances were sampled at 12.5 [m] and 25 [m], respectively.

To give an impression of the structures and the quality of the data set we have provided a set of two in-lines and three cross lines at different locations in Figs. 7.11 and 7.12. The first in-line in Fig. 7.11 (a) is located at a cross-line position of 6.25 [km]. We clearly distinguish a salt dome with some pronounced dipping layers around 5 [km] and between 1.0 and 1.5 [s]. Some growth faults are associated with the dome. The chaotic pattern located at a depth of 1 [s] has been interpreted as the head of a submarine canyon, produced by mass wasting (Nissen *et al.*, 1995)

The second in-line in Fig. 7.11 (b) is a section at the cross-line position 12.5 [km]. The salt dome has disappeared in this section, although we can still discern some growth faults between 0 and 5 [km] that are indisputably related to the salt dome. The remainder of the section shows predominantly horizontal reflections with some distinct faulting.

In Fig. 7.12 a set of three cross-lines is shown through different areas of the data set. The upper cross-section is located at an in-line position of 8 [km], and cuts right through the salt dome. Figs. 7.12 (b) and (c) are located at the in-line positions of 12.5 [km] and 15 [km], respectively. Both section cut through a sort of basin and show the chaotic pattern of the submarine canyon fill.

We have subjected various time-slices for the geometric volume attribute study. For one time-slice, we will show the complete attribute-set computed with the local Hardy projection, as well as through the 3-D pre-projection

complex wavelet transformation. Although both methods have their advantages, we will only show an additional set of examples of different time-slices of the pre-projection transformation.

Local Hilbert transform-based attributes The South Marsh Island data set is particularly interesting for attribute validation, because of its stratigraphically and structurally interesting features. For the analysis of the geometric attributes we have chosen a time-slice at $t=1.292$ [s], that cuts right through the salt dome and its associated faults. At the same time it reveals some interesting channel remainders. The amplitude slice is shown in Fig. 7.13 (a). Negative amplitudes are indicated in red, positive in blue. In the slice we can discern the salt-dome at in-line position of 4 [km] and between cross-line position 6 and 10 [km]. The channels are located along the lower edge of the egg-shaped region a channel and perpendicular to the edge at the in-line position of 20 [km].

First we will consider the fastest approach for the computation of geometric attributes i.e. the algorithm based on the local Hardy projection (Chapter 4). The discrete analytic signal is obtained by a 3-D local Hilbert transformation using a Daubechies-10 maxflat filter. We have computed three different attributes of the volume; radial frequency, for the stratification quantification, and dip and azimuth, which together describe the structure. The radial frequency is shown in Fig. 7.13 (b). The salt dome and channels are clearly visible. The width of the channels is approximately 300-500 [m]. The present-day Mississippi River trunk channel varies in width between 1000 to 1300 [m], its smaller distributary channels have a width of the order we observe here (Haskell *et al.*, 1995). In subsequent time-slices, that refer to greater depth, we observed that the lateral migration of the channels is relatively small. In the present day delta we see the same tendency, where the channels are prevented from lateral migration, because they are entrenched into the underlying marine clays (Haskell *et al.*, 1995). The local frequency character of the reflection energy originating from the contrasts between the surrounding clays and the channel infill clearly differs from the character of the surrounding reflection energy.

The local time-dip is shown in Fig. 7.14 (a) and the azimuth in (b). The time-dip is contaminated with noise. The nature of the algorithm is extremely local, it has superior resolution and is very sensitive to even the tiniest variations in instantaneous frequency. For that reason the time-dip fluctuates greatly, resulting in a noisy representation. The azimuth in Fig. 7.14 (b)

suffers from the same oversensitivity. The channels are visible in each of the figures, but do not have such a distinct geometric character.

As we have discussed before, the pseudo-horizon is a valuable platform for the combined attribute representation. The geometric attributes dip and azimuth can be combined into a surface that can be interpreted as a virtual topography representative of that particular time-slice. On top of this topography we can imprint the character of the signal, for instance local frequency or scale. We show the pseudo-horizon with the local radial frequency imprint of the time-slice at $t=1.292$ in Fig. 7.17. The figure strongly resembles the representation in Fig. 7.13 (b), however, with the inclusion of the geometric aspects we can add perspective to the impression of the reflectivity character. In the concept of virtual topography, the intensity or brightness is used to indicate the geometry, the color the frequency characteristics. It is important to realize that the measure for topographic structure is solely given by the shadows and brightness due to a light source. The color is purely an indication for the signal characterization, frequency or scale.

The vertical lineations that show up predominantly in the upper right area of the figure are artifacts that have their origin in the *acquisition footprint* (Marfurt *et al.*, 1995). The footprint is visible in the original time-slice but is emphasized in the attribute representation, predominantly owing to the geometric attributes (see Fig. 7.14). This representation of attributes combines the complete three-dimensional reflection character in terms of radial frequency and geometry. We will compare the attributes discussed in this section with those computed with the complex wavelet transform in the next paragraph.

Pre-projection complex wavelet transform Although the pre-projection algorithm can be computationally efficiently implemented, it is slower for the computation of geometric attributes than the method discussed in the previous paragraph.

For this particular study we have used a three-stage complex wavelet transform that uses Daubechies-8 filters for the 3-D projection and Daubechies-4 filter for the wavelet decomposition. Again we have computed three attributes of the volume; radial scale, which is comparable to the previously discussed radial frequency, dip and azimuth.

The local cubic scale of the time-slice at $t=1.292$ [s] is shown in Fig. 7.15 (b). For convenience we have depicted the time-slice again in Fig. 7.15 (a). The salt dome and channels are clearly visible. Compared

to the radial frequency in Fig. 7.13 (b), we see a more stable, but less detailed representation. The acquisition footprint is clearly visible in the upper right corner and in the general horizontal lineation in the figure. For the pre-projection, the same reasoning applies as above: the local character of the transform emphasizes the detailed changes in reflections. The figure shows a variety of signal character. The channels tend to show a coarse scale character, whereas the layers that embed the channels show up as a dark green area with a fine scale character (see also Fig. 7.20).

When we compare the time-dip and the azimuth in Fig. 7.16, with those in Fig. 7.14, the attributes computed with the complex wavelet transform make a much smoother impression. The limited number of angles together with the contribution from different scales, have a smoothing effect on the geometric attributes. Nevertheless, the attributes still contain detailed information; for instance, the channels can be recognized in the time-dip as well as in the azimuth representation. In Fig. 7.18, the virtual topography of the time-slice is shown, from which we obtain a clear impression of structural as well as of stratigraphic information in a perspective view.

We discuss two more interesting time-slices of the South Marsh Island data set. The first slice is located at a lower time-level at $t=1.356$ [s] and is shown in Fig. 7.19. The channels in the lower region of the section have disappeared, whereas the channel crossing through the egg-shaped region in Fig. 7.18 continues and connects in the center. The channel is visible in the amplitude data and shows up in red at a position of about 5 [km] cross-line and 15 [km] in-line. In the topographical representation in Fig. 7.20, the strong contrast in frequency between the channel belt and the surrounding reflections is accentuated even more clearly. The sand colored channel is embedded in a dark green environment of fine scale reflection energy. The topography shows a true to life perception instead of the abstract time-slice. We have to keep in mind, however, that this is not a seismic horizon. One interesting feature we want to illuminate is the channel. Although the channel seems to be gully shaped, it is not. In Fig. 7.23, we show a bird's eye view of the attributes slice in Fig. 7.20. When we take a closer look at the channel, we see that instead of a gully, the channel has an arc shape. The channel is located on top of the surface! We can interpret this phenomenon in two different ways. The first explanation is due to differential compaction, because the shales compact more than the channel sand, resulting in a positive relief of a previously incised feature. Another explanation can be found in the fact that it is not the contrast of the channel bounds, but it is the contrast of the

channel infill that we observe.

With the last time-slice from the South Marsh Island data set, we want to illustrate some faults that show up as stratigraphic boundaries. The time-slice is located at $t=1.468$ [s]. In this part of the data set, there is no indication of channels. The amplitude response is shown in Fig. 7.21. The bowl is built up of nice concentric circles with constantly alternating positive and negative amplitudes. Figure 7.22 shows its topographical attribute representation. The green area in the upper part of the slice between 10 [km] and 15 [km] in-line has an interesting shape. The bounds of the area appear to be very abrupt. This effect is caused by faulting. Faulting has caused an uplift of the green area, that now adjoins a reflection pattern with a totally different stratigraphy. We can substantiate the effect with Fig. 7.11 (b). This section is located at a crossline position of 12.5 [km] close to the edge of the time-slice. The faults are located at 10 and 15 [km] in-line. The block in between the two faults is lifted.

■ 7.5.2 North Sea, Block L05

In this section we will validate the attributes on a seismic data set from the Netherlands. For this purpose we consider the pre-projection wavelet transform attributes, since these tend to be more informative than those based on the local Hilbert transform.

The data set is acquired at about 70 kilometers northwest of the Netherlands in 1991. The data is poststack migrated seismic data and cover an area of nearly 650 [km²] with 1241 in-line and 898 cross-line traces. The spatial sampling distances of the traces are 25 [m] in each direction. The data is sampled an interval of 4 [ms]. We consider a window of these data of 20×15 [km²] and approximately 1 [s]. The dataset contains interesting stratigraphic and structural features. The segments can be clearly distinguished on the in-line sections in Fig. 7.24 and the cross-line sections in Fig. 7.25. The segment for our study consists of three different areas of interest. A molar shaped *salt dome* is visible in the data. This dome was formed due to halokinesis which started in the pre-Zechstein and could possibly still be active. The dome prevails the shape of the data set due its deformation. In the Tertiary, during the Neogene, a thick bed of *deltaic sediments* formed that stretches over the whole area, and is pushed upwards in the area of the salt dome. In the data set, the delta is located around 400 [ms] just on top of the heavily faulted *mid-Miocene unconformity* at 600 [ms]. The faulting of the beds reaches from base-Tertiary up to the mid-Miocene unconformity. A theory for the

faulting is that these originated due to differential compaction of clays and shales that were dehydrated by the salt intrusions (Tigrek, 1998). This could also be a plausible explanation for the polygonal structures of the faults that is so typical for shrinkage.

In Fig. 7.26 a time-slice is shown at $t=564$ [ms]. The salt dome is located in the lower area of the slice between 15-20 [km] in-line. On the right of the salt dome we can already distinguish the polygonal faulting pattern, though not yet clearly. Furthermore we observe a vertically aligned pattern. The time-slice is located in the middle of the deltaic sediment beds. The vertical alignments are the intersected foresets of the delta. The topography representation of the time-slice is depicted in Fig. 7.27. The local scale is imprinted for the frequency characterization. The colorbar on the right indicates the scale content in the image. Dark green colors indicate finer scale reflection patterns, the lower values indicate coarser scale information. The

The alignments are visible in the color as well as the illumination, which means that their character is described in frequency as well as in structure. The salt dome consists of mainly fine scale information, but is bounded by some coarser reflection events.

The second time-slice we consider is located close to the mid-miocene unconformity at a depth of 640 [ms]. This part of the data set consists of polygonal fault structures covering the entire area apart from the salt dome. The slice makes a chaotic impression except for the polygonal shaped alternating amplitudes in the upper right corner. The combined reflection geometry and character attributes are portrayed in Fig. 7.29. The combination of geometry and scale provides us with a consistent pattern of polygonal faulting. The impression of a bedding with a persistent character, which reminds us of the dry red soil in southern Spain. In the deeper area of the data set at $t=880$ [ms], the faulting becomes less dense and changes shape to a more stretched out pattern as illustrated in Fig. 7.30. The attribute slice is depicted in the subsequent Fig. 7.31 which shows a moderate variation in geometry and scale.

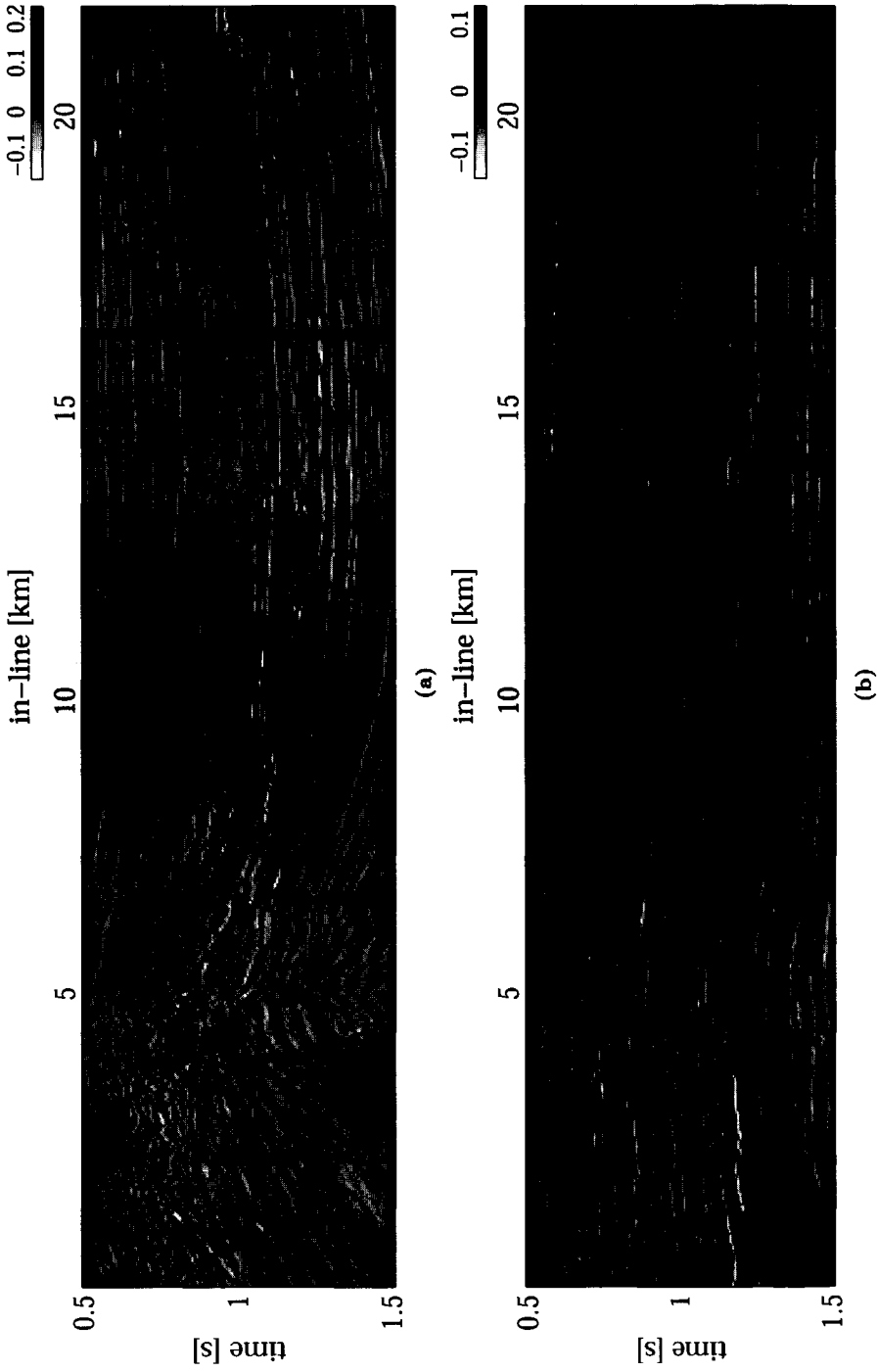


Figure 7.11: *In-lines of the South Marsh Island data; (a) at cross-line position 6.25 [km]; (b) at 12.5 [km]*

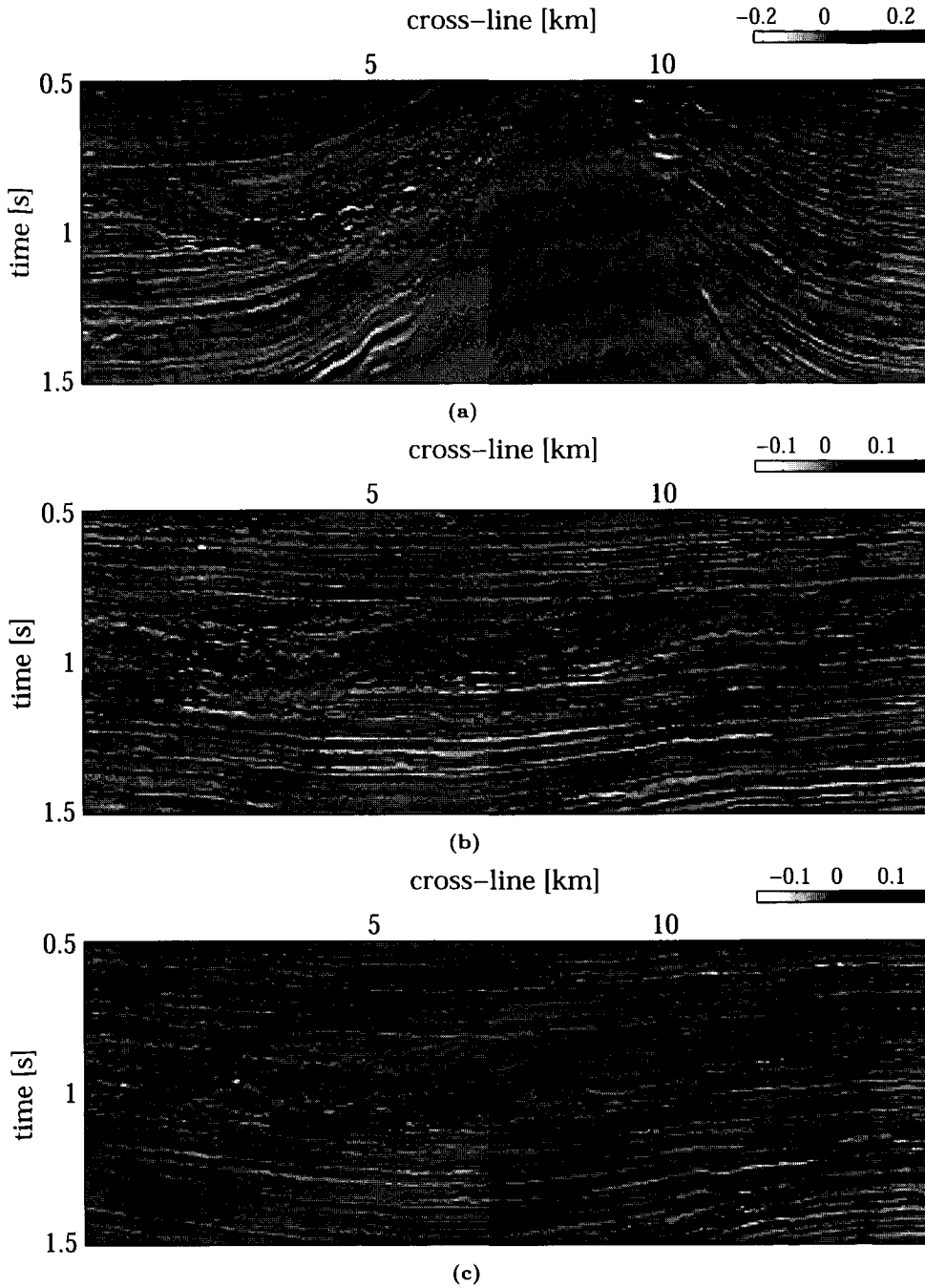


Figure 7.12: Cross-line sections of the South Marsh Island data; (a) at in-line position of 8 [km]; (b) at 12.5 [km] and c at 15 [km]

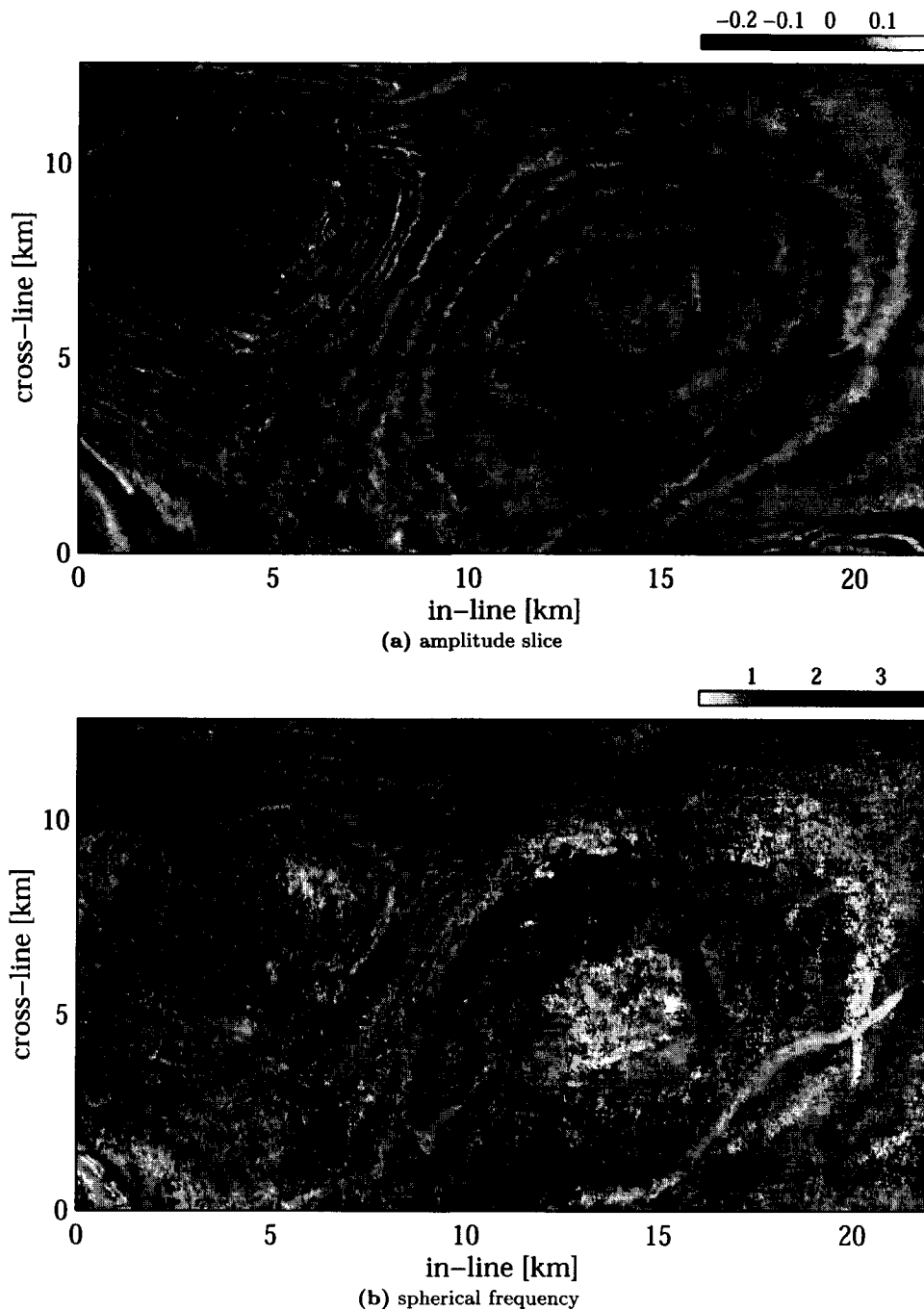


Figure 7.13: Time-slices of the South-Marsh Island Gulf of Mexico dataset at $t = 1.292$ [s]. (a) Amplitude slice; (b) spherical frequency slice computed with length-10 local Hilbert transformation.

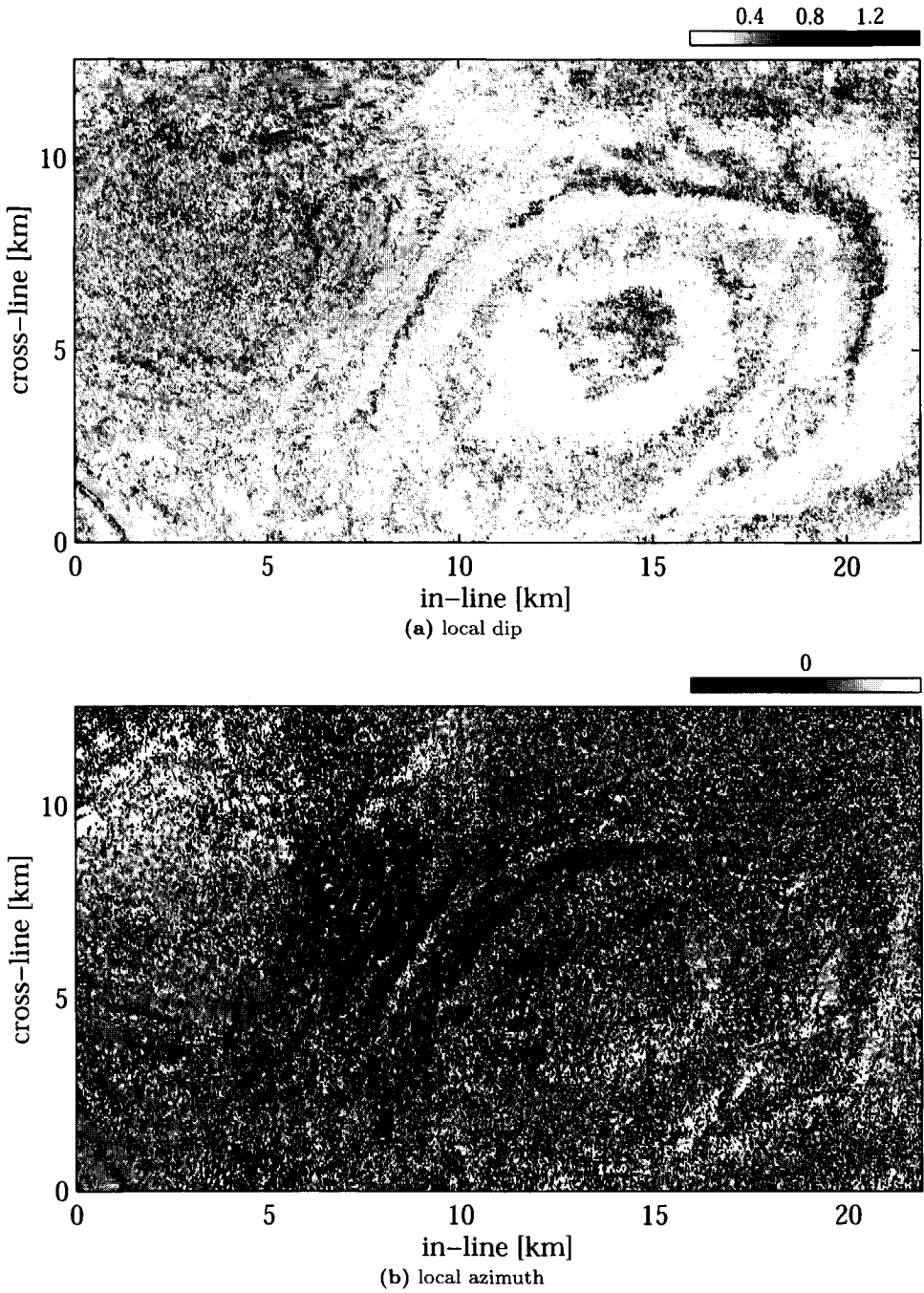


Figure 7.14: Geometric attributes at $t = 1.292$ [s] computed with length-10 local Hilbert transformation. (a) Local dip; (b) local azimuth.

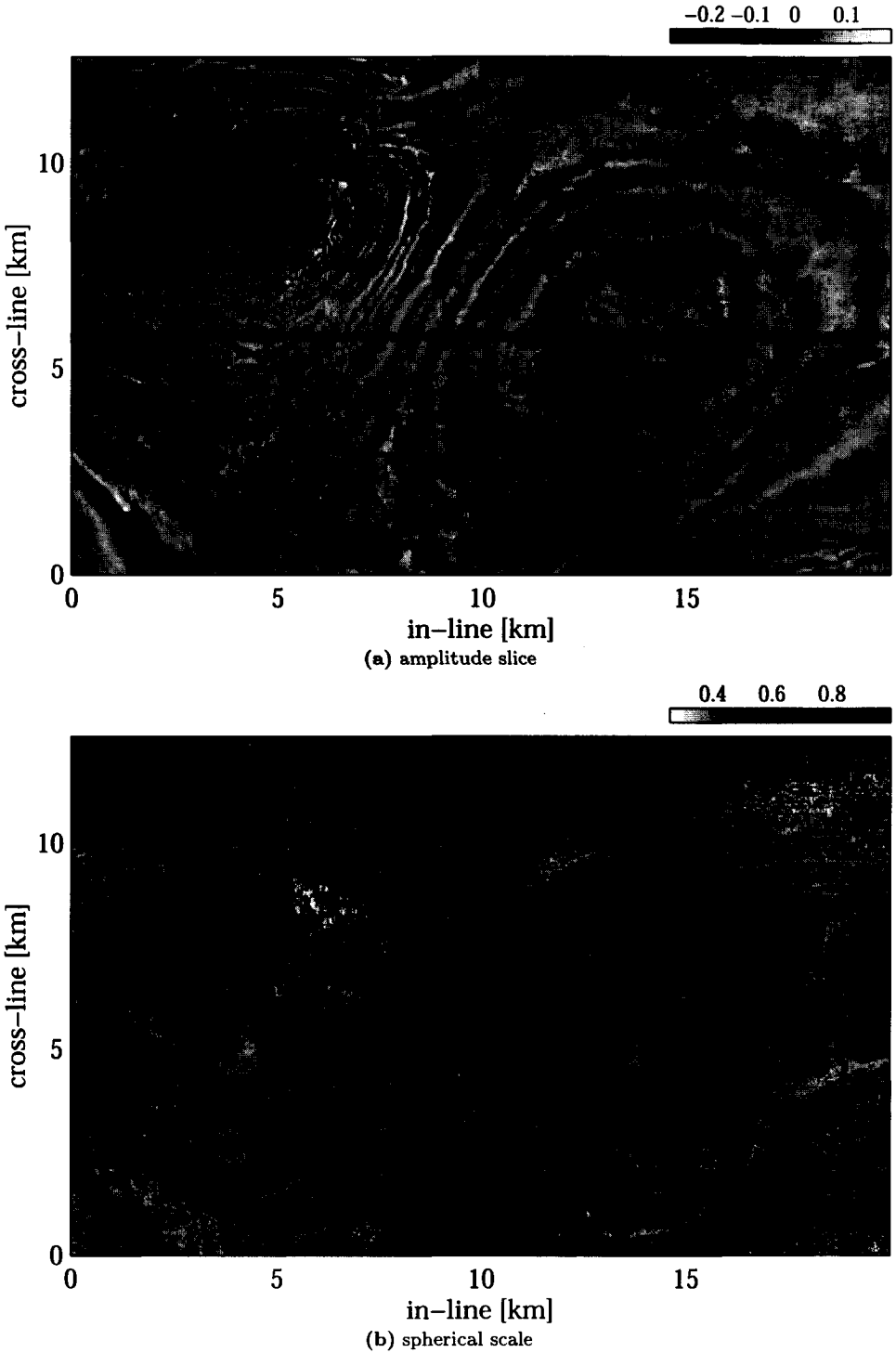


Figure 7.15: Time-slices at $t = 1.292$ [s]. (a) Amplitude slice; (b) spherical scale slice computed with Daubechies-8 pre-projection complex wavelet transformation.

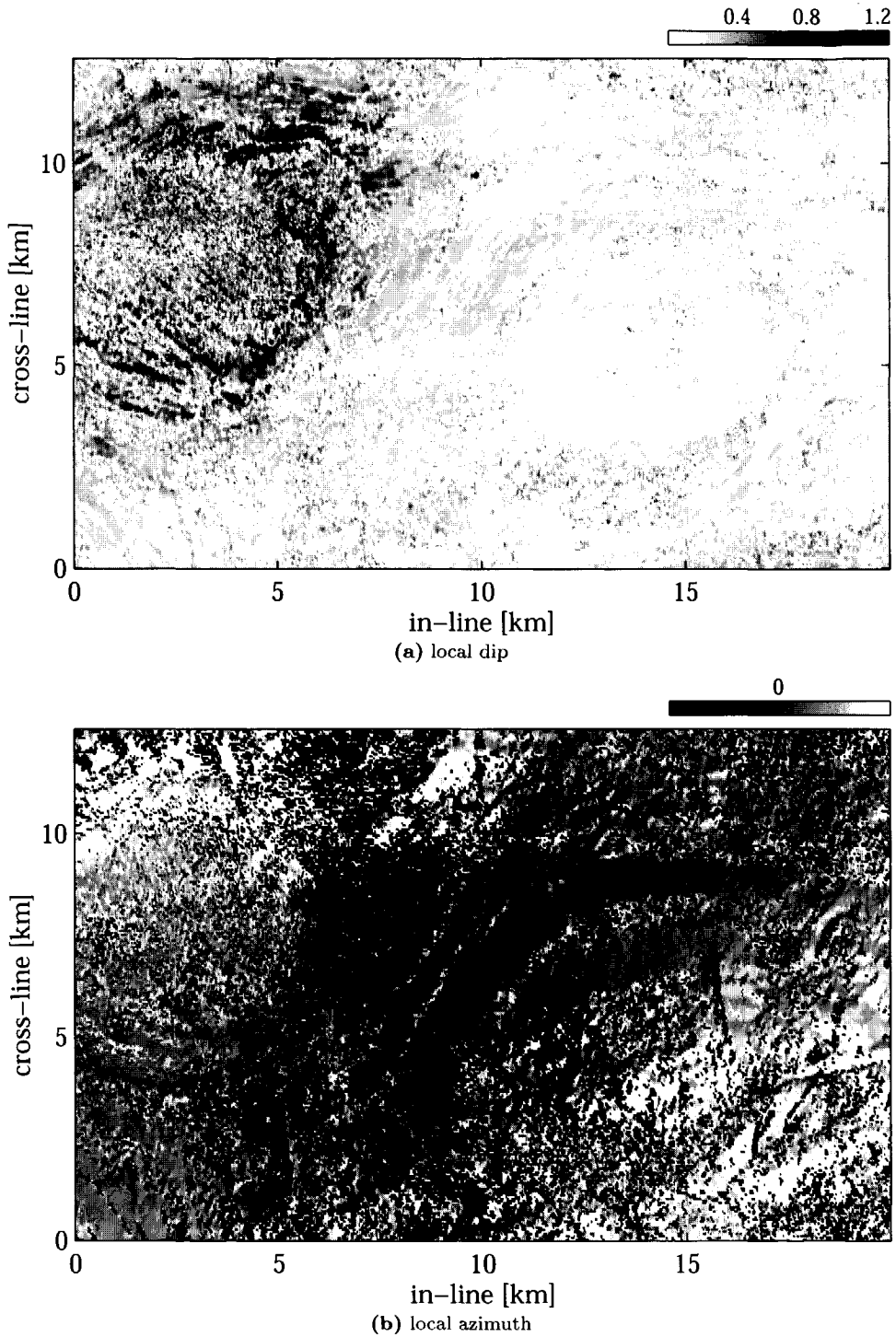


Figure 7.16: Geometric attributes at $t = 1.292$ [s] computed with Daubechies-8 pre-projection complex wavelet transformation. (a) Local dip; (b) local azimuth.

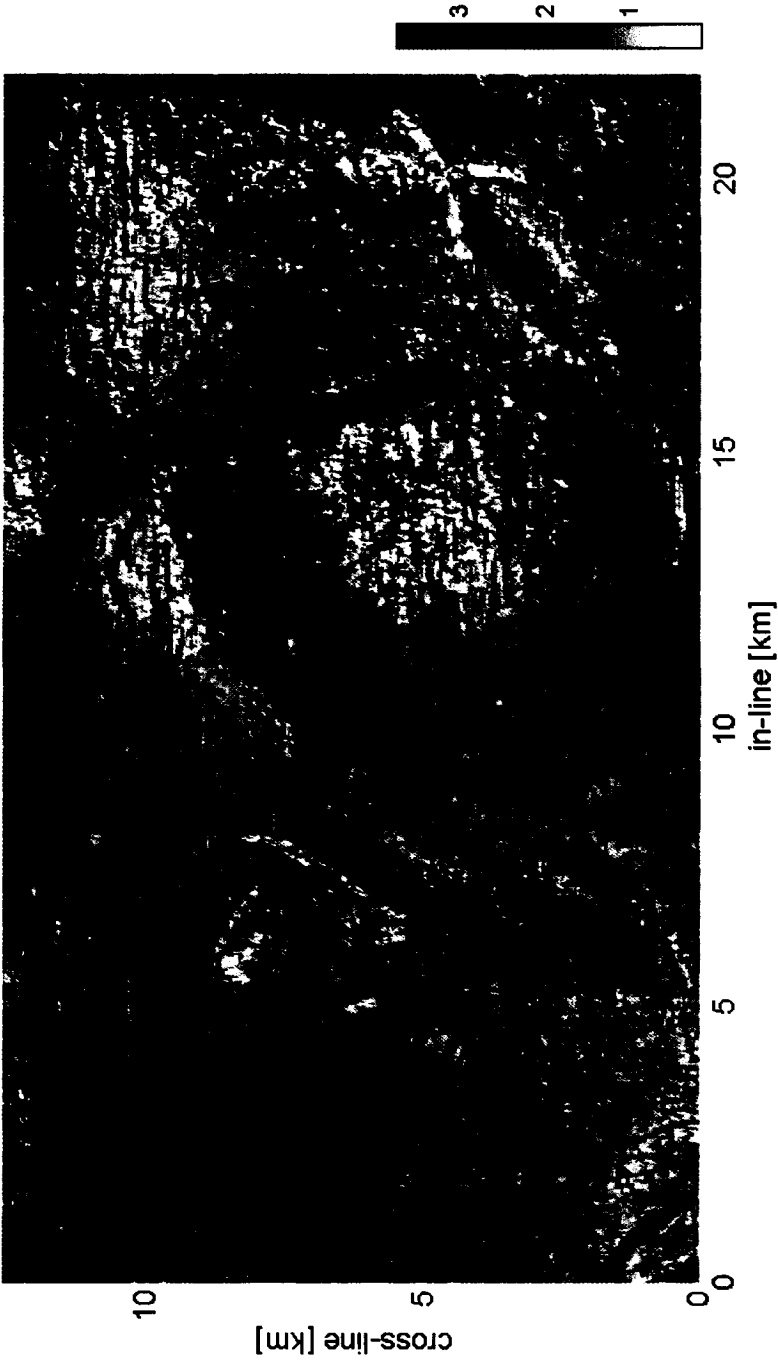


Figure 7.17: Local Hilbert transform attributes from Figs. 7.13 and 7.14 combined in a virtual topography of the time-slice in Fig. 7.13 (a)

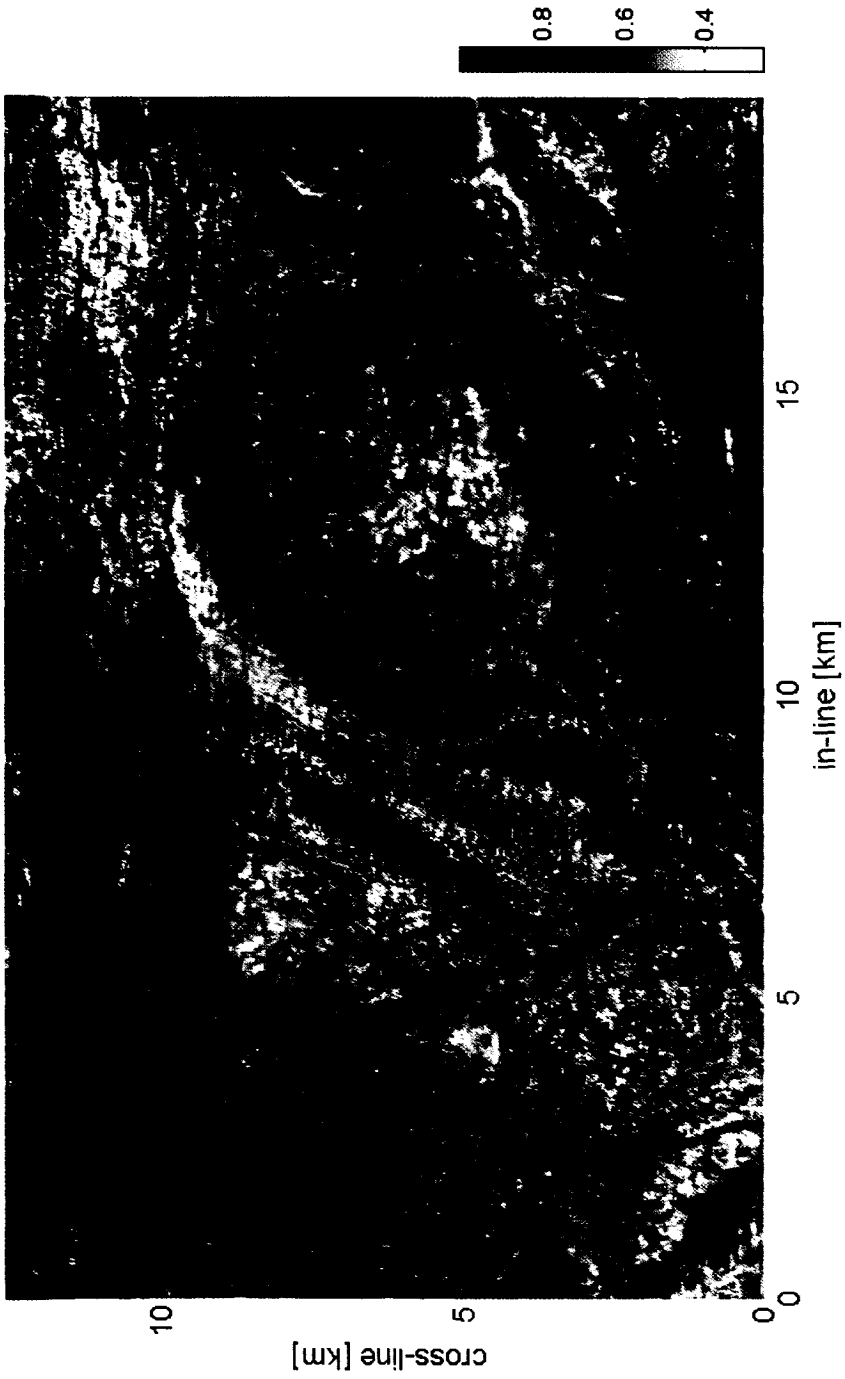


Figure 7.18: 3-D CDWT attributes from Figs. 7.15 and 7.16 combined in a virtual topography of the time-slice in Fig. 7.15 (a)

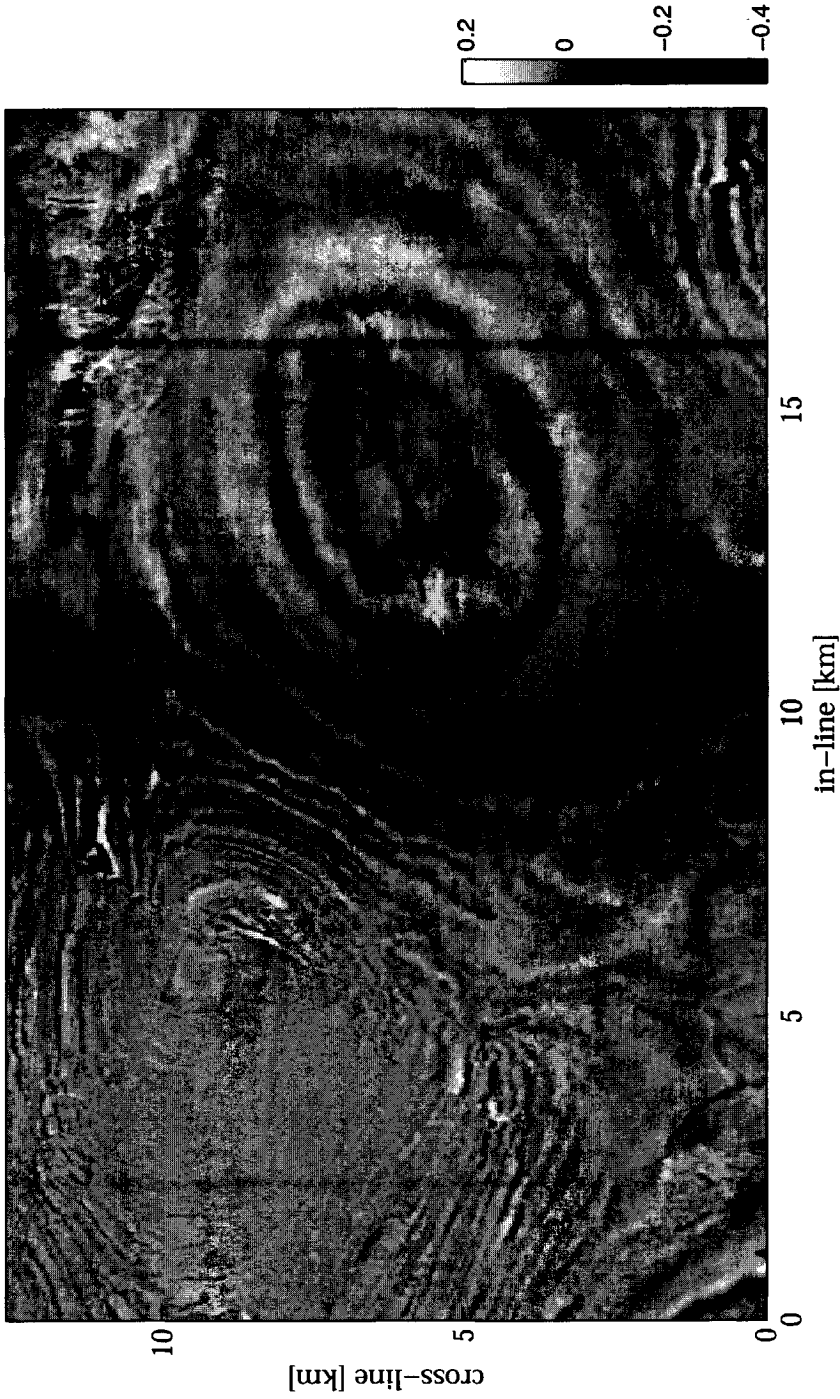


Figure 7.19: Amplitude time-slice from Gulf data at $t = 1.356$ [s].

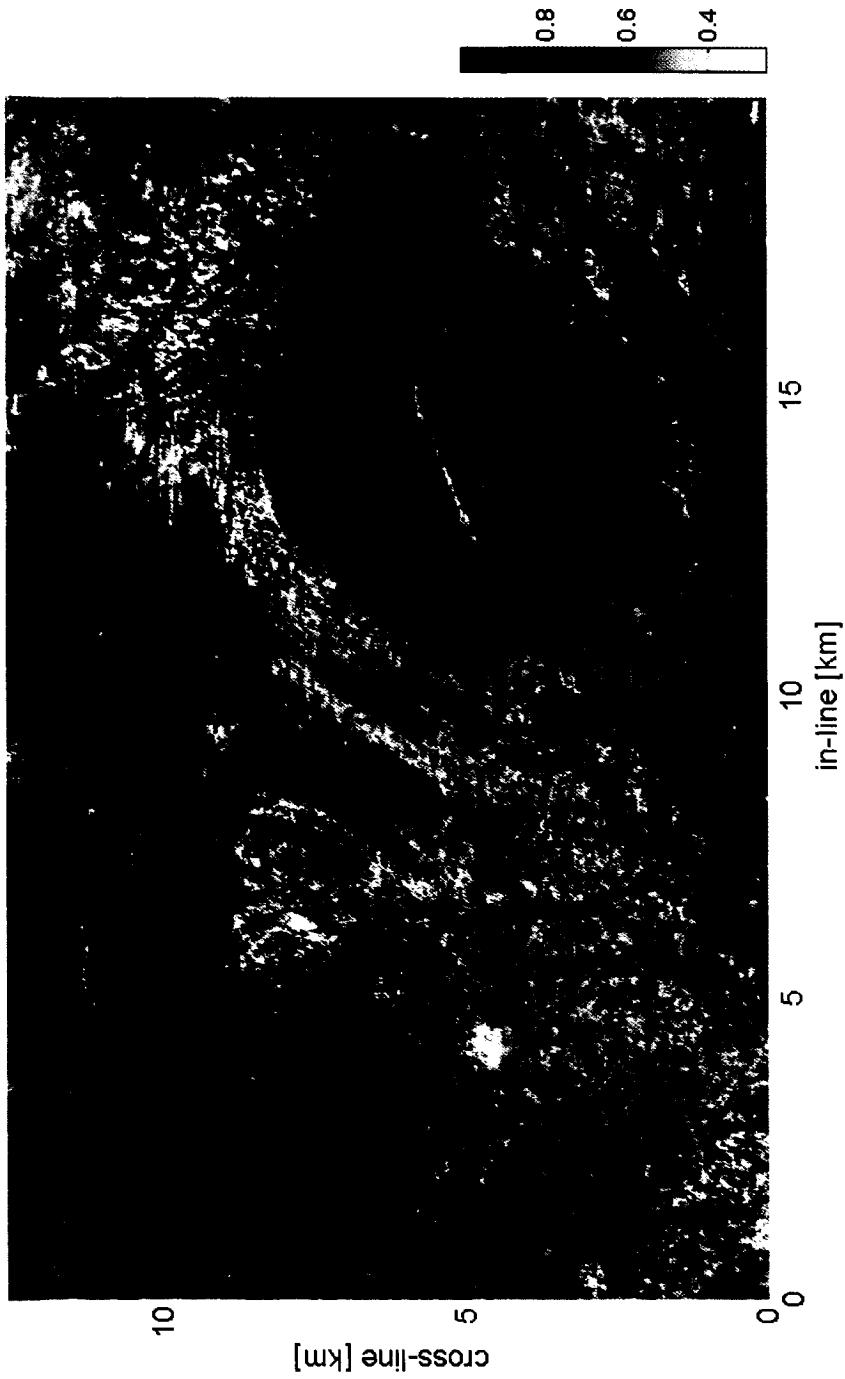


Figure 7.20: Virtual topography-scale representation of time-slice in Fig. 7.19 computed with Daubechies-8 3-D CDWT.

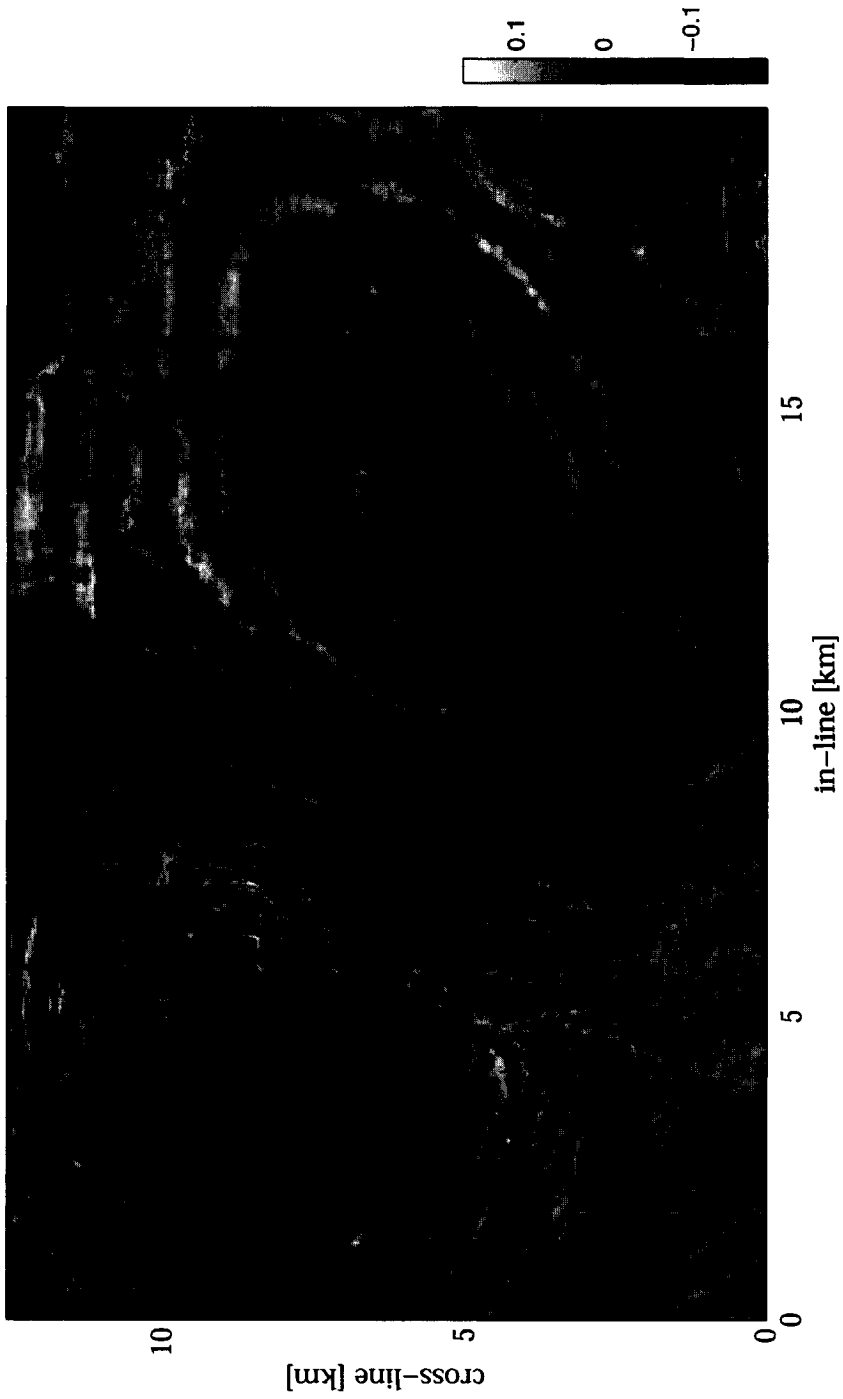


Figure 7.21: Amplitude time-slice from Gulf data at $t = 1.468$ [s].

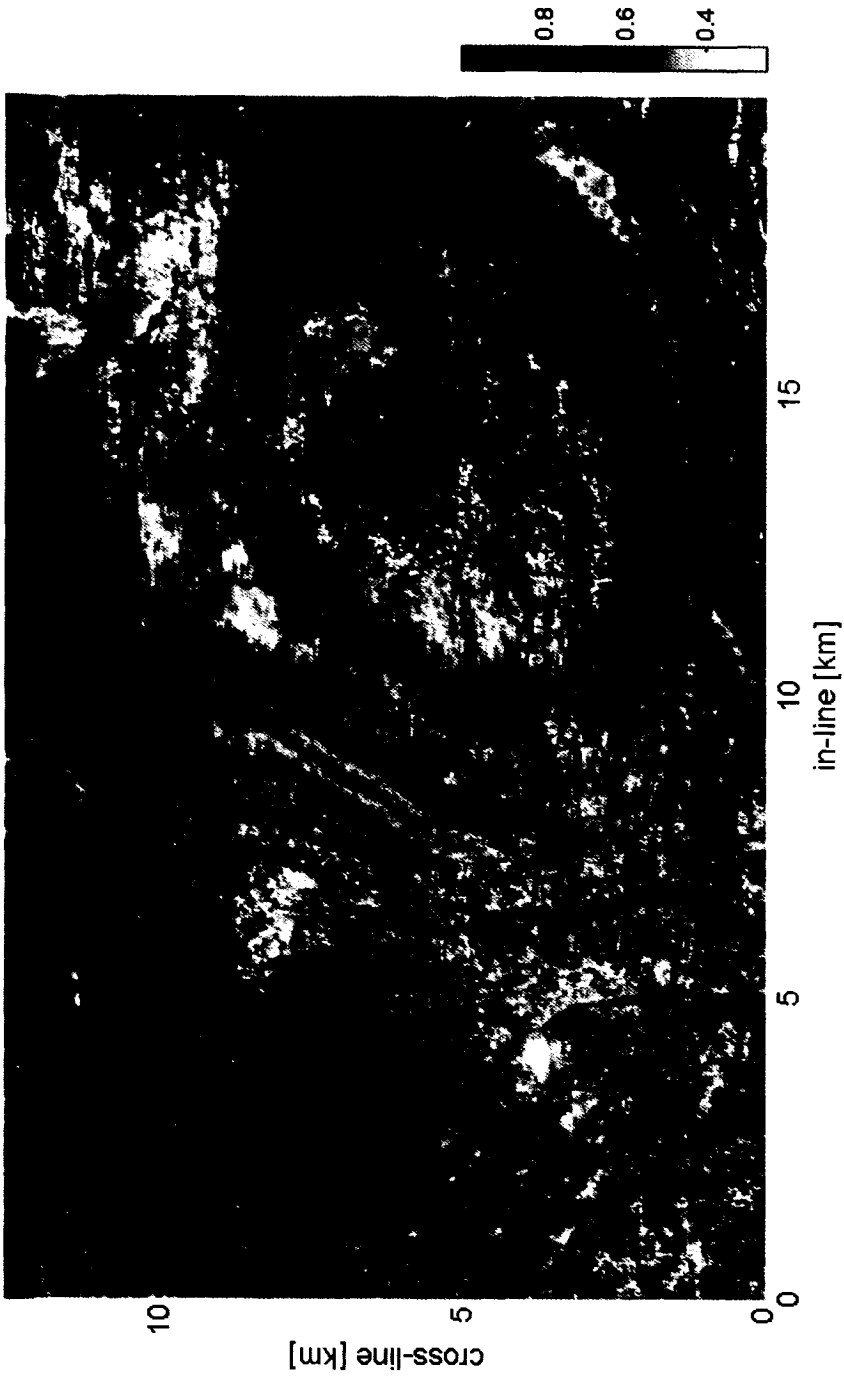


Figure 7.22: Virtual topography-scale representation of time-slice in Fig. 7.21 computed with Daubechies-8 3-D CDWT.

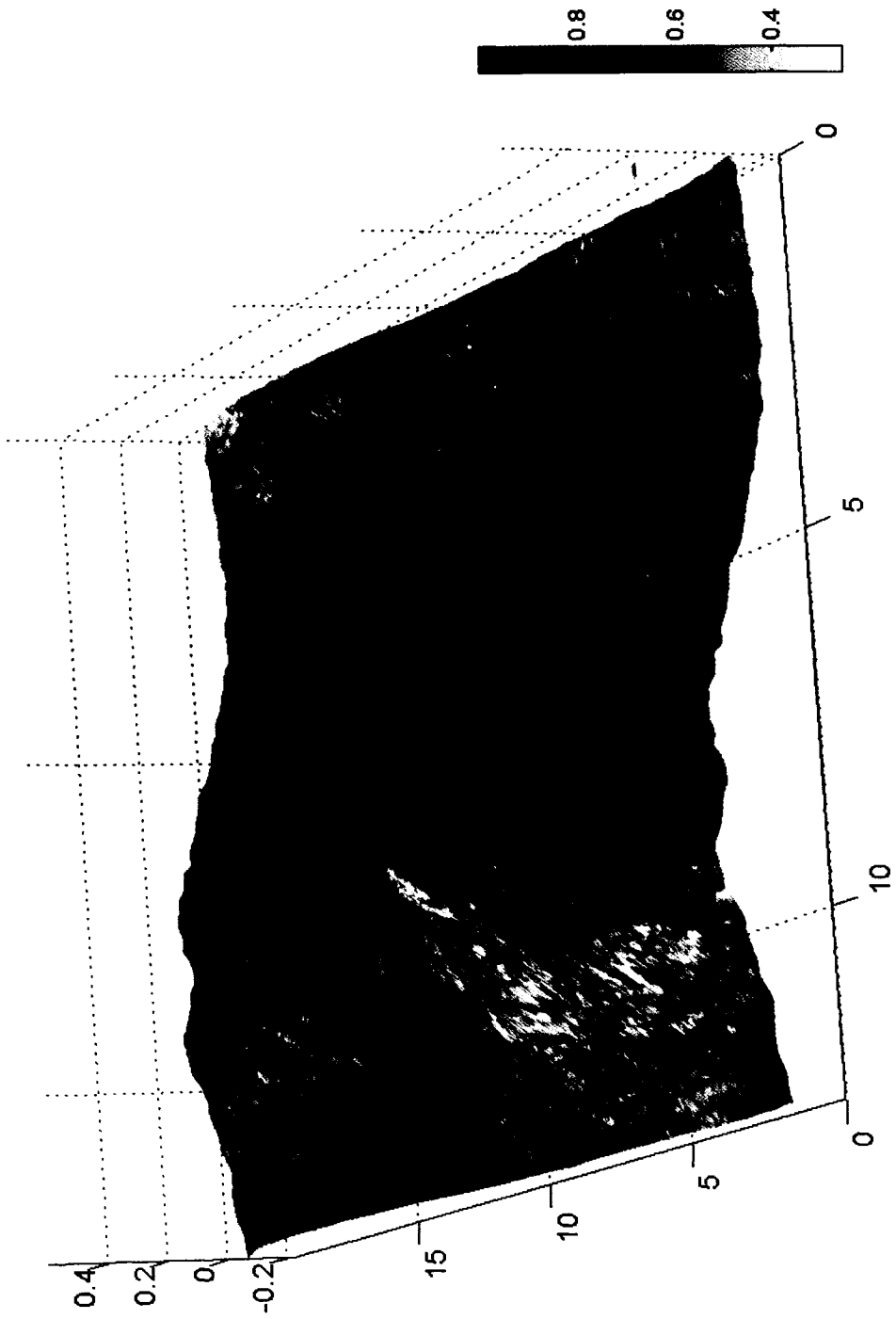


Figure 7.23: Topographic representation of Fig. 7.20

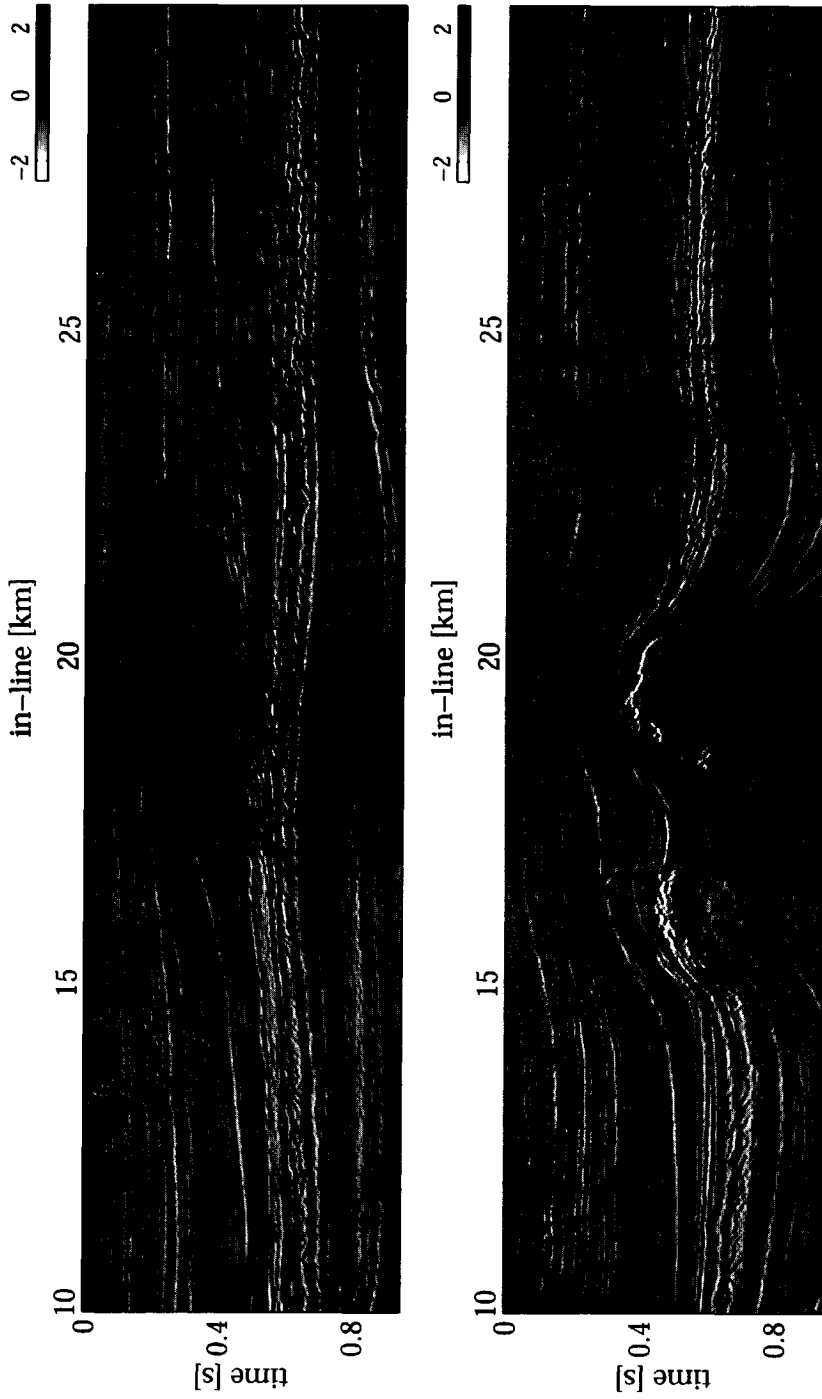


Figure 7.24: In-lines of the L5 data; (a) at cross-line position 7.5 [km]; (b) at 15 [km]

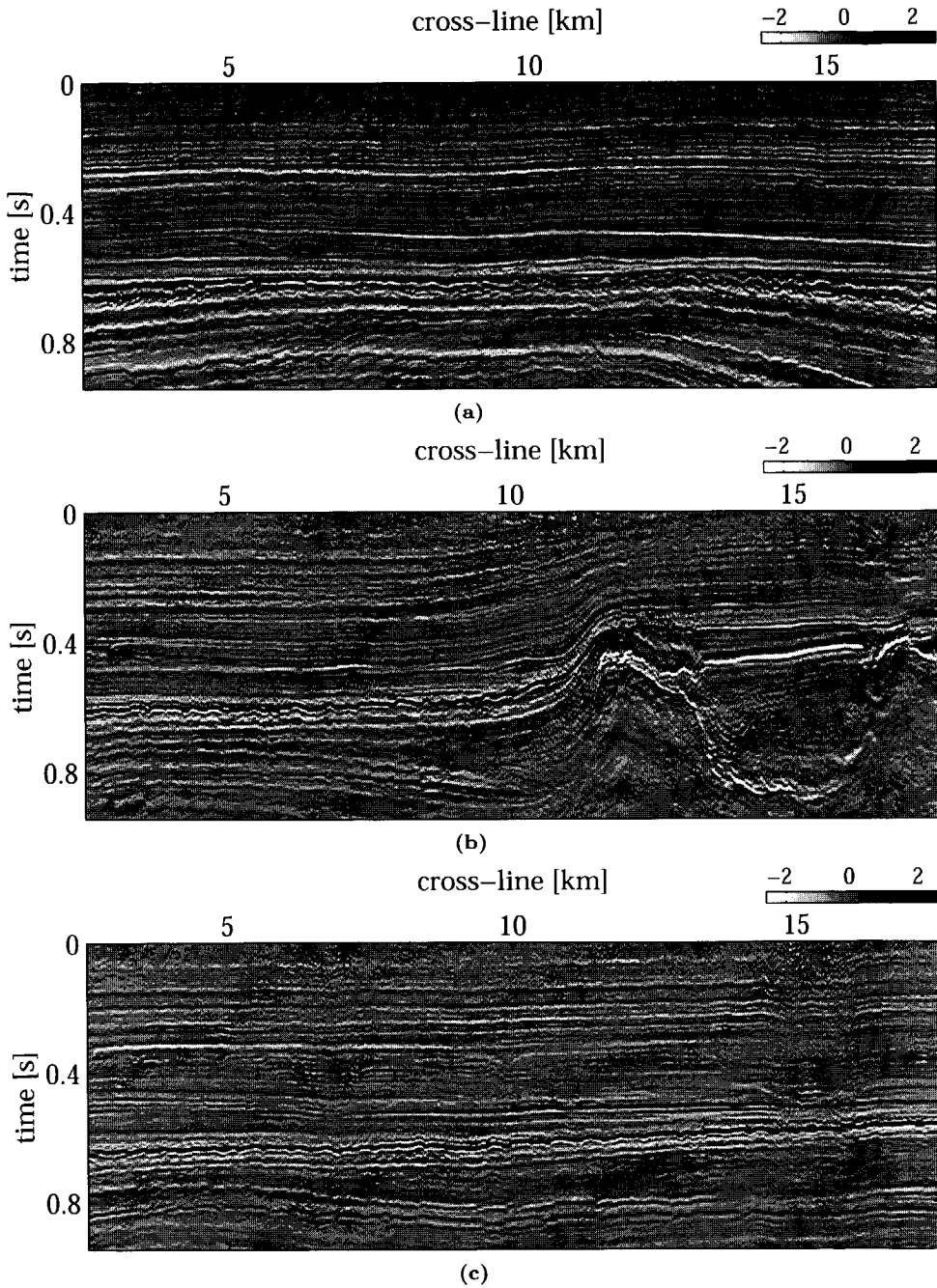


Figure 7.25: Cross-line sections of the L5 data; (a) at in-line position of 7.5 [km]; (b) at 13.75 [km] and c at 22.5 [km]

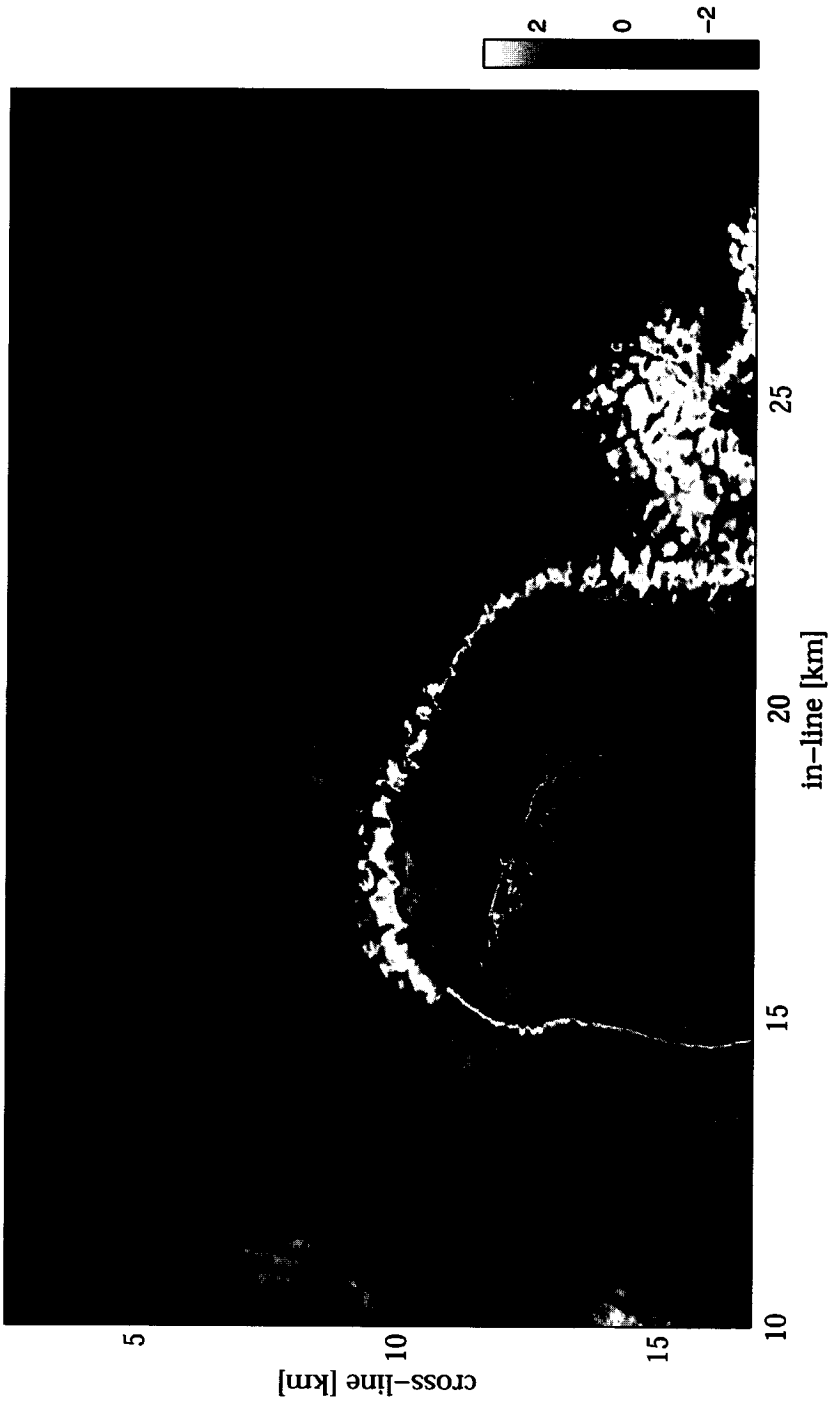


Figure 7.26: Amplitude time-slice of L5 data set at $t=564$ [ms].

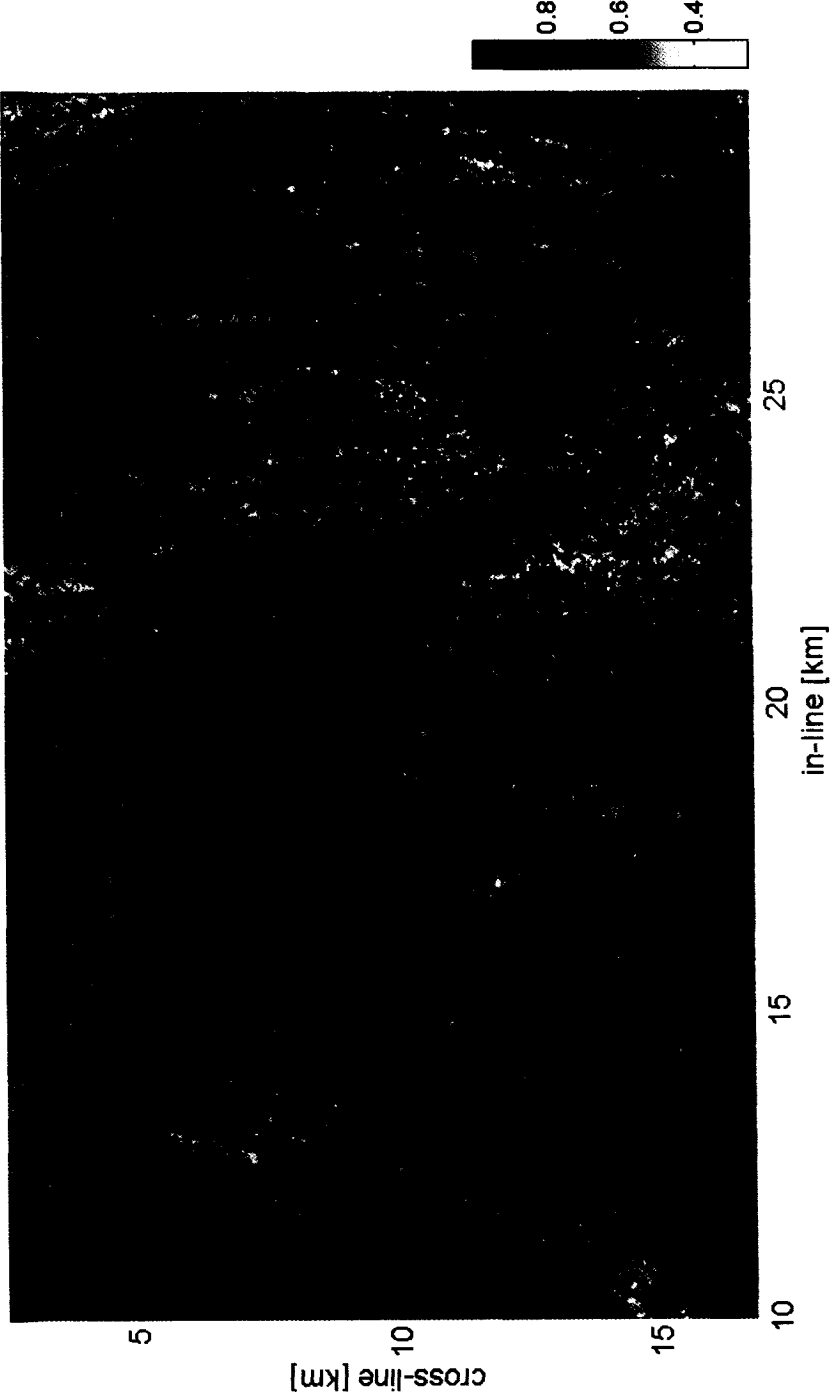


Figure 7.27: Topographic representation of Fig. 7.26

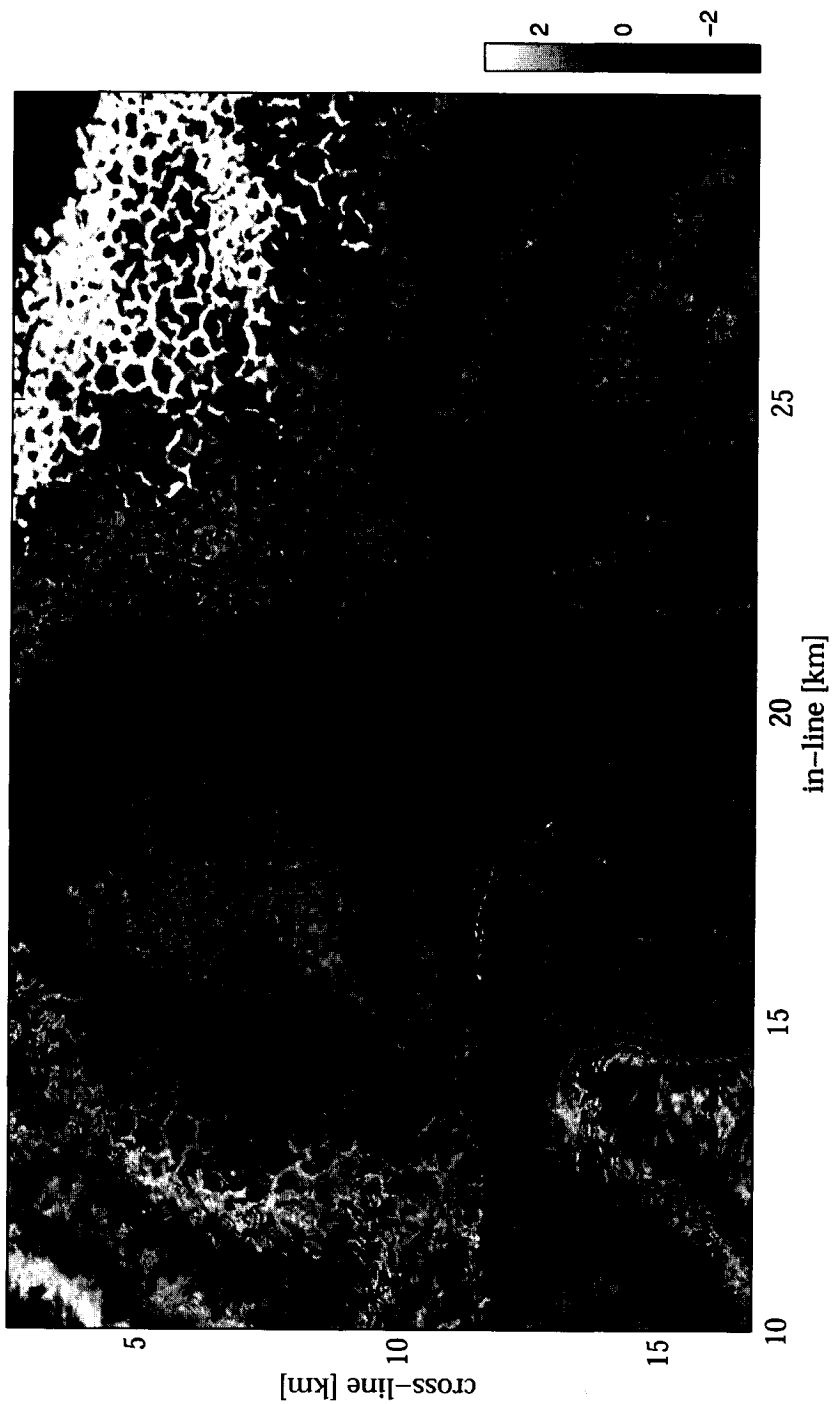


Figure 7.28: Amplitude time-slice of L5 data set at $t=640$ [ms].

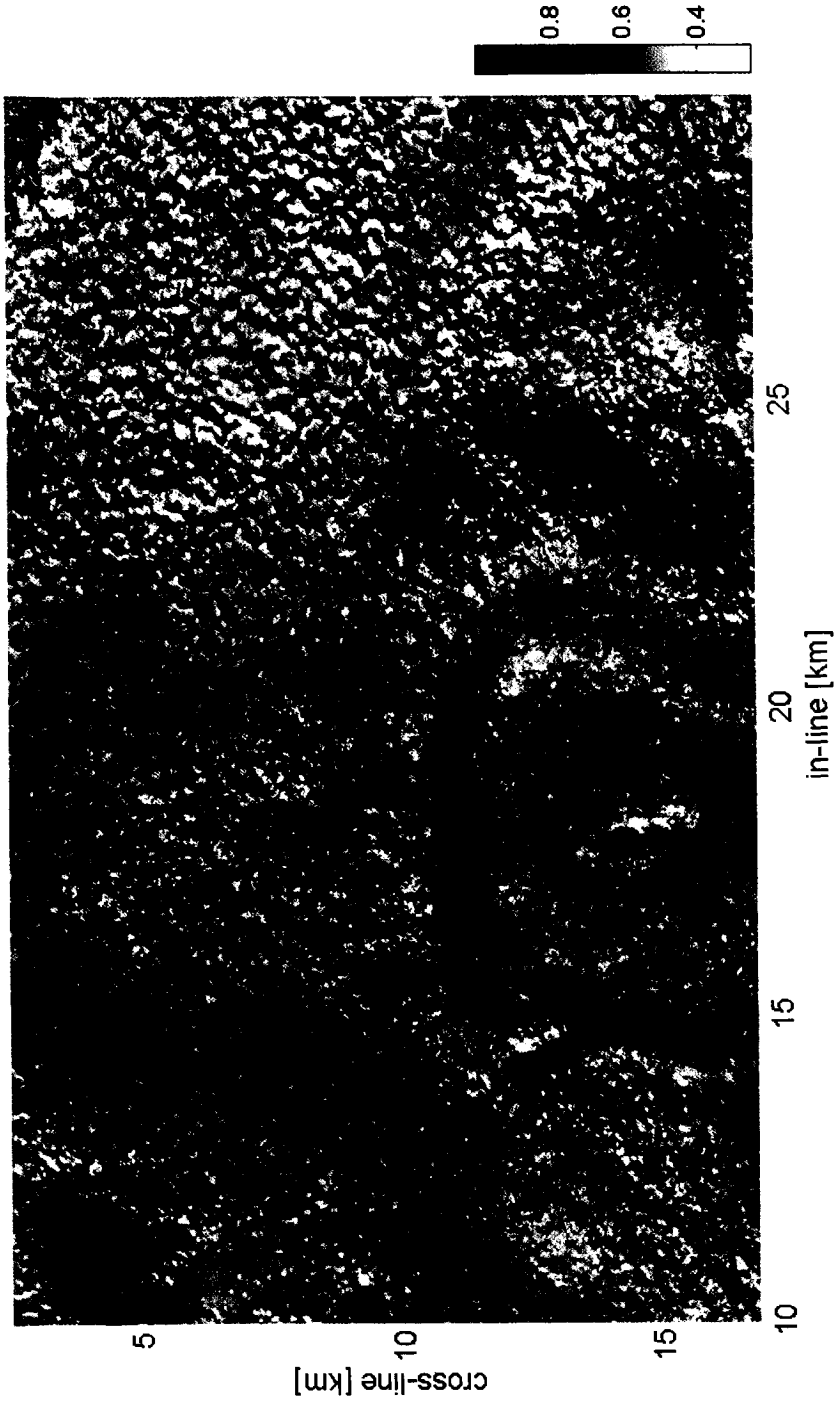


Figure 7.29: Topographic representation of Fig. 7.28

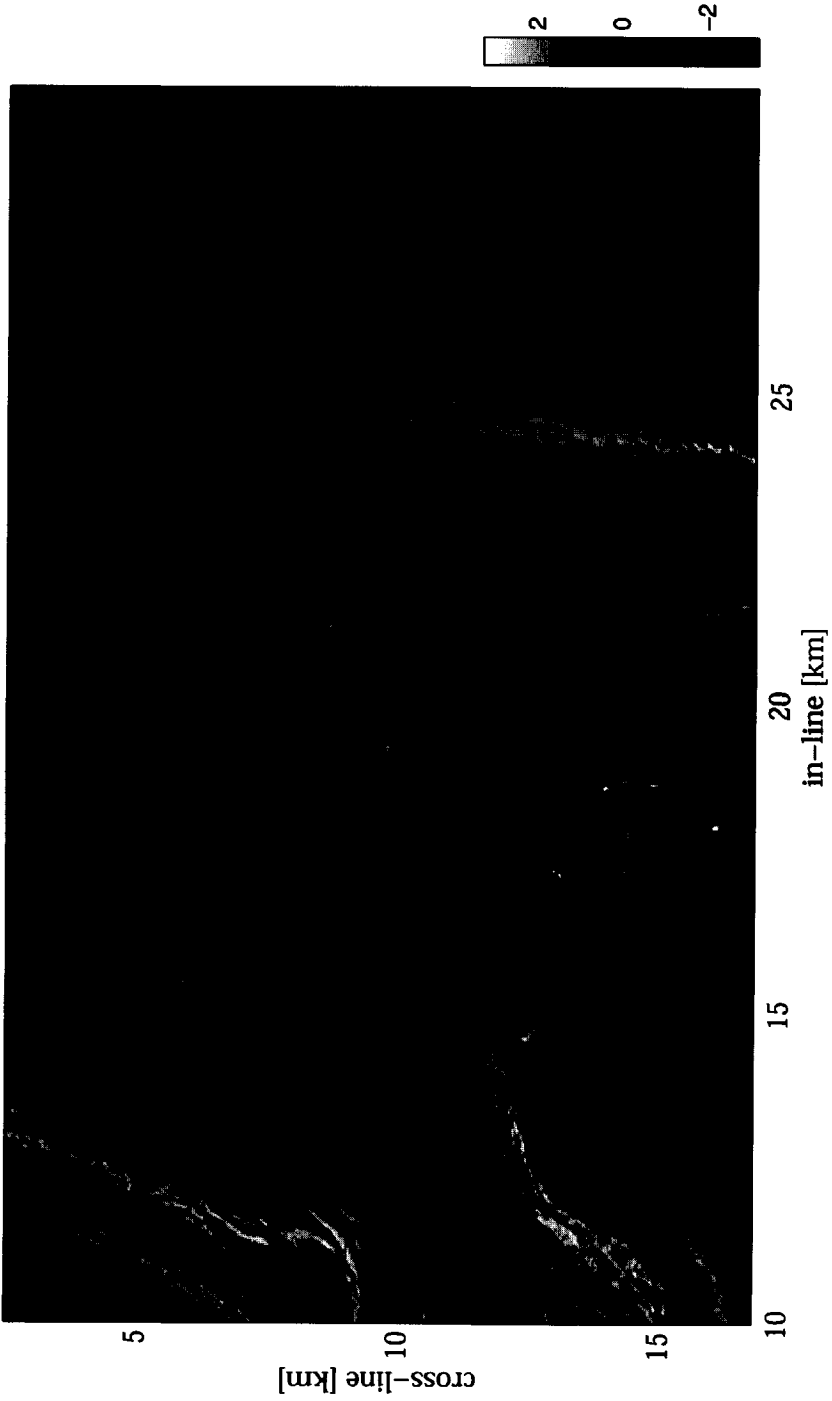


Figure 7.30: Amplitude time-slice of L5 data set at $t=880$ [ms].

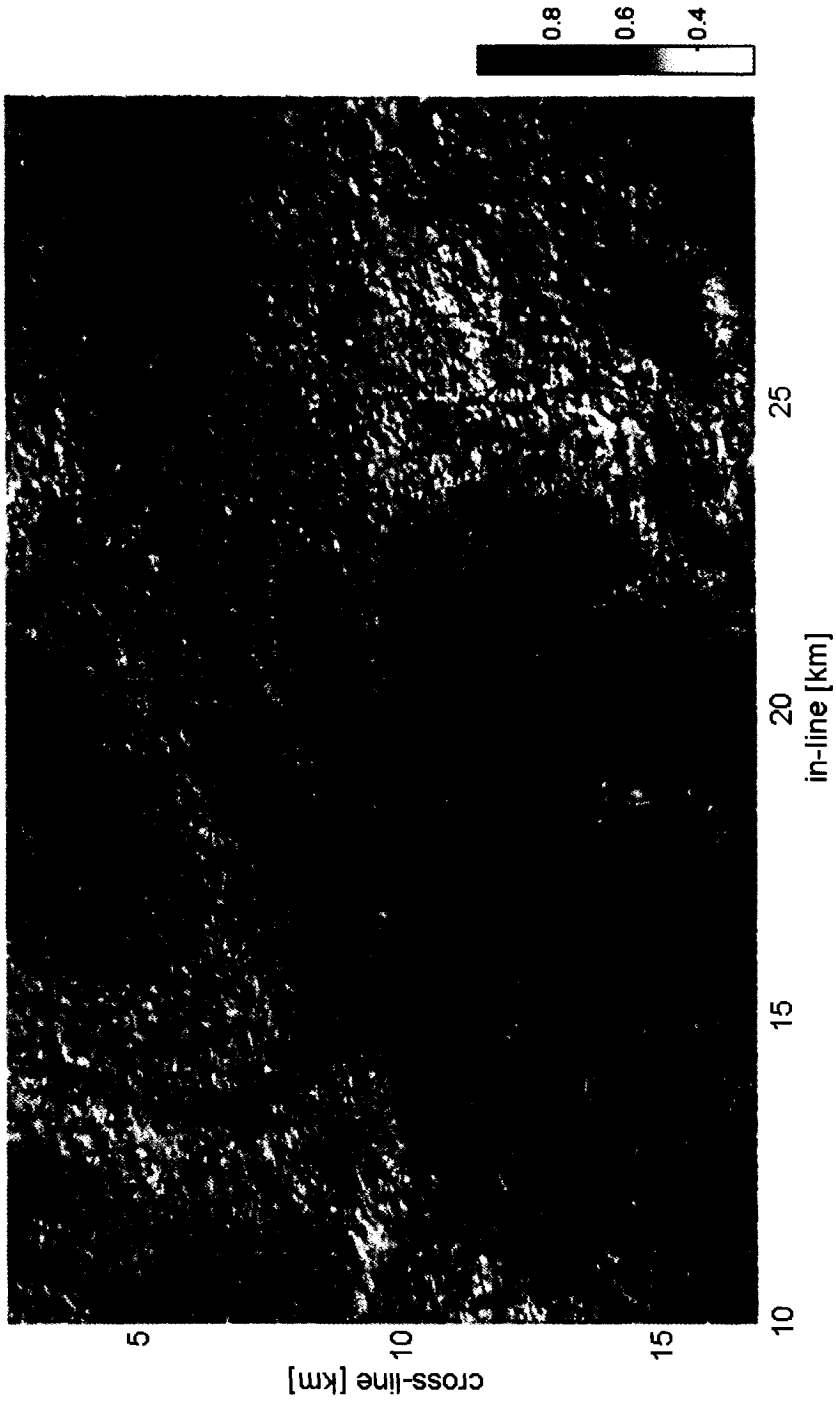


Figure 7.31: Topographic representation of Fig. 7.30

Conclusions

In this thesis we have introduced novel signal processing algorithms for the local volume analysis of the migrated seismic reflection data. The seismic attributes extracted from the transforms are focused on the reflection *environment*, rather than the event itself. The motivation for wavelet analysis can be found in the fact that in a seismic image, the seismic reflection events are localized features, and wavelet transforms are the ideal tool for analysis of the local signal behaviour.

Because the discrete wavelet transform lacks the capacity for directional discrimination, the transform needs modification to make it useful for directional analysis. Based on the ideal filter theory, we have created two different complex wavelet transforms; the first complex wavelet transform uses a local projection onto positive frequencies, and hence is called the *pre-projection complex wavelet transform*. The use of local projections preserves the character of the wavelet transform. The second transform we have introduced is a wavelet transform that integrates the projection onto positive frequencies with the wavelet projections at each level in the transformation. This transform is called *iterated complex wavelet transform*. Both transforms have their own advantages and drawbacks, which we have illustrated.

The filters we have used for the projection onto positive frequencies are both approximations of analytic filters. In combination with the wavelet

transforms, the filters can be used for projection onto the positive frequency-axis. However, they can also be used to compute local attributes directly from the signal. Because the filters are locally analytic they have many desirable mathematical properties. A crucial property in the context of seismic signal analysis is that the filter enables separation into the quantities amplitude and a phase, which are the two basic seismic attributes.

We have shown how the analytic filters as well as the complex wavelet transforms can be used for multi-dimensional analysis. The attributes, computed with the three-dimensional algorithms show that a treasure of information can be extracted from the environment of the reflector. We demonstrated that the multi-dimensional character of the attributes is of crucial importance for seismic interpretation. This is the key observation where structural interpretation of three-dimensional opaque seismic data is concerned. The three-dimensional nature of the algorithms makes it possible to reveal the smallest detail. The small three-dimensional variations in the data can be observed with mathematical accuracy and objectivity.

The geometric information we extract from the algorithms can be effectively used for the structural interpretation of lateral time or depth slices. This idea is demonstrated with virtual topography, computed from the geometric information in a lateral slice. This visualization technique provides us with a versatile platform for combined attribute representation. It enables the visualization of the coupled parameters dip and azimuth in a single representation.

In Chapter 4, the local Hilbert transformation is introduced. This is a local discrete implementation of the Hilbert transformation and can be used to compute the imaginary part of a local-analytic signal. The filter has finite support, and thus acts only locally on the signal. Due to its local character, these filters are very well-suited for the computation of attributes of non-stationary signals on the basis of the amplitude and phase. These are the so-called complex trace attributes —instantaneous phase, frequency and reflection strength.

A wide range of filters can be used, depending on signal length and frequency character of the signal. The algorithm is computationally more efficient than the Fourier-based Hilbert transformation due to the short filter length. When longer filters are considered, the computational efficiency is comparable to that of the Fourier transformation.

We can construct volume attributes by combining the horizontal and vertical instantaneous frequencies. The local radial frequency is used to measure

the volume-frequency content of the seismic reflections — a parameter that is impossible to assess from two-dimensional sections only. The other two volume attributes that we computed from the phase of the local analytic signal, were the two geometric attributes: the local dip and the local azimuth. The three attributes each show complementary information, and combined they describe the local three-dimensional character of reflections.

We have used the local-analytic filters for the design of a novel complex wavelet transformation in Chapter 5. The local-analytic filters are strongly conditioned. They are closely related to the family of Daubechies filters used in the wavelet transformation. The filters contain half the entire frequency range and can be subjected to spectral factorization. The resulting two filters form a perfect reconstruction filter pair. The perfect reconstruction finds its origin in the fact that the consecutive filtering with the analysis and synthesis filter results in the local-analytic filter. The real part of this filter is equal to a delta-pulse. We have used the spectral factors of the local-analytic filters for the design of the complex wavelet transformation. Before wavelet transformation, the signal is decomposed into a real and imaginary part, through projection with the analysis filter. With projection we are able to improve directional selectivity, and moreover, the invariance of the transform under shifting of the input signal. Both properties are crucial for the computation of volume attributes. Another beneficial aspect of the projection is the introduction of phase in the transform.

Due to the separation of negative and positive angular information, the complex wavelet transforms contains six directional highpass subbands in the two-dimensional transform that is used for images. The traditional discrete wavelet transform consists of three highpass subbands showing horizontal, vertical, and diagonal information. For the three-dimensional equivalent of the complex wavelet transforms, the directional subbands increase up to 28 highpass subbands as opposed to 7 in the conventional discrete wavelet transform. The fact that the complex wavelet transform reconstructs a local analytic equivalent of the signal or image, after reconstruction, contributes to its usefulness for attribute computation. By inverse transformation of each individual subband, in which shift-invariance of the transform plays a crucial part, a selection of angular information of the image can be reconstructed. The first moment with respect to energy in the angular subbands results in a local angle representation.

In the Fourier domain, the optimal directional information is described by wedge-shaped filter. With the inclusion of additional scale subbands, we can

approximate a wedge shape in frequency with the rectangular-shaped filters contributing to the complex wavelet transform. Additionally, we demonstrated that the transformation can be used for the extraction of the local scale. The local scale is extracted by the isolated reconstruction of a set of subbands contributing to each particular scale. The first moment with respect to these subbands results in the scale attribute.

The complex wavelet transformation's computational efficiency and limited redundancy make it suitable for three-dimensional application. In three dimensions, the angular information is represented in a dip- and azimuth representation. These extracted quantities are comparable to those extracted with the local-analytic filters. Although these attributes generally show a finer resolution, the fine resolution comes at the cost of increased sensitivity to noise in the data.

The local cubic scale attribute is a very powerful attribute. It enables the segmentation of the data into very distinct regions of characteristic three-dimensional scale. These regions are related to the geological stratification. As in the case with the geometry attributes, the scale representation is less sensitive to noise than the radial-frequency attribute.

Ultimately, the complex wavelet transform has more potential for the computation of attributes than the analytic filters. The transform contains a wealth of information. The information that is extracted from the complex wavelet transform can be used as input for statistical segmentation algorithms.

In Chapter 6 we have developed a wavelet transformation that integrates a local projection at each stage in the discrete wavelet transform. This iterated complex wavelet transform has some desirable extra properties. As a consequence of the integration of the projection filters, there is no nesting property of scaling function. However, we have proved that the transform in the limit spans Hardy space — the space of functions that contain strictly positive frequencies. The phase of the transform is much more pronounced and consistent over scale than in the pre-projection transform. The directional selectivity is improved by the symmetrical shape of the filters.

We also demonstrated the use of a complex wavelet-packet approach for the construction of discrete-time Hardy projection filters. With the use of short-duration smooth filters linked by sampling operators, we are able to approximate the brick-wall frequency response, typical for the discrete-time Hardy projection. The benefit of this algorithm is its flexibility in the number of stages of the approximation. This allows us to regulate the influence

of undesirable effects in the filtered signal, such as ringing. We compared the instantaneous frequencies of this approach to the conventional Fourier-based instantaneous frequency and observed that the novel algorithm is barely contaminated with noise and negative frequencies that tends to reduce the quality of these types of representations.

In Chapter 7 we discussed volume attributes. We deployed a simple seismic model and two seismic field-data sets. For the purpose of validation of the attributes, we employed a single reflector model for the construction of synthetic seismic data. The reflector consists of moderate geometry and radial frequency variations and a normal fault. The attributes computed for the synthetic data illustrate the character of each attribute adequately. The local radial frequency illustrates the character of the signal independent of the geometry. Dip and azimuth are useful attributes for the interpretation of the structures in the reflector. The fault appears in all of the attributes due to its singular character. The wavelet-based and analytic-filter based attributes show very similar results. The latter shows a sharper representation of the attributes for synthetic data.

The geometric attributes dip and azimuth can be effectively combined at lateral slice level for the construction of a virtual topography that represents the local structure at that particular interface. The topography combines the information from two attributes into a single representation. This visualization technique opens new perspectives for structural interpretation of lateral slices. It allows for combined attribute representation in which the radial frequency character and the structure, containing complementary information, are molded into one picture. These quantities summarize the frequency character of the reflector in a single representation, and open the gate for a "bird's-eye view" quantitative interpretation of lateral slices. The technique is demonstrated with the attributes computed from the synthetic seismic model for the conceptual understanding of the method.

We have selected two seismic field-data sets to show the practical feasibility of the algorithms and to illustrate their relevance for geological interpretation. The first data set is from South Marsh Island in the Gulf of Mexico. This data set is often used as a reference for the validation of volume attributes. The filter-based attributes turned out to be more sensitive to noise than the wavelet-based attributes. This is especially true in the case of the geometry attributes. However, there is no algorithm that is computationally more efficient, because the filters used in the convolution are of particular short length. The iterated complex wavelet transform was not incorporated in the

validation, but has high potential for the computation of volume attributes.

We demonstrated that the scale attribute contains useful information. In the scale representation, channels and other characteristic information related to the stratification can be seen. Due to their relative indifference to noise, the wavelet-based attributes are preferred above the filter-based attributes.

The second seismic field-data set we have considered is located in the L05-block in the North Sea on the Dutch part of the continental shelf. The structures in the data set are dominated by a large salt dome. In addition to the salt dome, the data set contains deltaic sediments overlaying a heavily faulted Dongen Clay Formation. The geological events show up clearly in the virtual topography representation. Above all, the faulted area illustrates the value of this representation over the conventional amplitude representation.

In summary we conclude that the analysis of the reflection environment rather than single reflection interfaces or single trace analysis merits seismic interpretation in multiple aspects. The geometry representation in terms of vectors is indispensable for structural interpretation based on lateral slices. The local radial frequency and scale representations reveal the three-dimensional signal character, which is hard to quantify on the basis of sections only. The local transforms that we have developed for the purpose of local analysis have the computational efficiency and the mathematical accuracy for the calculation of the attributes without extensive data increase.

Bibliography

- P. Abry. *Transformées en Ondelettes-Analyses multiresolution et signaux de pression en turbulence*. PhD thesis, l'Universite Claude Bernard de Lyon, 1994.
- M. S. Bahorich and S. L. Farmer. 3-d seismic discontinuity for faults and stratigraphic features: The coherence cube. *The Leading Edge*, 14(10): 1053–1058, 1995a.
- M. S. Bahorich and S. L. Farmer. 3-d seismic discontinuity for faults and stratigraphic features: The coherence cube. In *Annual Meeting Abstracts*, pages 93–96. Society Of Exploration Geophysicists, 1995b.
- M. S. Bahorich, J. Lopez, N. L. Haskell, S. E. Nissen, and A. Poole. Stratigraphic and structural interpretation with 3-d coherence. In *Annual Meeting Abstracts*, pages 97–100. Society Of Exploration Geophysicists, 1995.
- R. H. Bamberg and M. J. T. Smith. A filter bank for the directional decomposition of images: Theory and design. *IEEE Transactions on Signal Processing*, 40(4):882–893, 1992.
- R. G. Baraniuk and D. L. Jones. Signal dependent time-frequency representation: Optimal kernel design. In *IEEE transactions on Signal Processing*, volume 41, pages 1589–1602. IEEE, 1993.
- C. Bernard. *Wavelets and ill-posed problems: optic flow and scattered data interpolation*. PhD thesis, Ecole Polytechnique, France, 1999.

- B. Blümich and H. W. Spiess. Quaternions as a practical tool for the evaluation of composite rotations. *Journal of Magnetic Resonance*, 61:356–362, 1985.
- R. N. Bracewell. *The Fourier transform and its applications*. McGraw-Hill International Editions, 1978. Singapore.
- A. R. Brown. *Interpretation of Three-Dimensional Seismic Data*. SEG-AAPG, 1999.
- C. S. Burrus, R. A. Gopinath, and H. Guo. *Introduction to Wavelets and Wavelet Transforms, A Primer*. Prentice Hall, 1998.
- C. H. Chapman. Generalized radon transforms and slant stacks. *Geoph. Jour. Royal Astron. Soc.*, 66:455–460, 1981.
- H. Choi and R. G. Baraniuk. Image segmentation using wavelet-domain classification. In *Proc. SPIE Technical Conference on Math. Mod., Bayes. Est., and Inv. Probs.*, volume July, pages pp. 306–320, 1999.
- H. Choi, J. K. Romberg, R. G. Baraniuk, and N. G. Kingsbury. Hidden markov tree modeling of complex wavelet transforms. In *Proc. of IEEE Int. Conf. on Acoustics, Speech and Signal Proc. - ICASSP'00*, 2000.
- L. Cohen. *Time-Frequency Analysis*. Prentice-Hall, New Jersey, 1995.
- M. S. Crouse, R. D. Nowak, and R. G. Baraniuk. Wavelet-based signal processing using hidden markov models. *IEEE Trans. on Signal Proc.*, April, 1998. Special Issue on Wavelets and Filterbanks.
- I. Daubechies. Orthonormal bases of compactly supported wavelets. *Comm. on Pure and Appl. Math.*, 4:909–996, 1988.
- I. Daubechies. *Ten Lectures on Wavelets*. SIAM, 1992.
- S. R. Deans. *The Radon transform and some of its applications*. John Wiley & Sons, 1983. New York.
- F. Dessing. *A Wavelet transform Approach to Seismic Processing*. PhD thesis, Delft University of Technology, Delft, Netherlands, 1997.
- M. W. P. Dillen. *Processing of time-lapse seismic data*. PhD thesis, Delft University of Technology, Delft, Netherlands, 2001.

- F. C. A. Fernandes. *Directional, Shift-Insensitive, Complex Wavelet Transforms with Controllable Redundancy*. PhD thesis, Rice University, 2001.
- F. C. A. Fernandes, R. L. C van Spaendonck, and C. S. Burrus. Applications of complex wavelet transforms. *IEEE Trans. Image Proc.*, 2002a. (in preparation).
- F. C. A. Fernandes, R. L. C. van Spaendonck, and C. S. Burrus. A new framework for complex wavelet transforms. *IEEE Trans. Signal Proc.*, 2002b. submitted.
- F. C. A. Fernandes, R. L. C. van Spaendonck, and C. S. Burrus. Shiftable, projection-based complex wavelet transforms. In *IEEE Proc. Int. Conf. Acoustics, Speech and Signal Proc.* IEEE, 2002c.
- F. C. A. Fernandes, R. L. C. van Spaendonck, M. Coates, and C. S. Burrus. Directional complex-wavelet processing. In *Proceedings of SPIE 2000*, volume 4119, pages 61–61, 2000.
- J. T. Fokkema and P. M. van den Berg. *Seismic Applications of Acoustic Reciprocity*. Elsevier, 1993. Amsterdam.
- W. T. Freeman and E. H. Adelson. The design and use of steerable filters. *IEEE Pat. Anal. Mach. Intell.*, 13(9):891–906, 1991.
- A. Gersztenkorn and K. J. Marfurt. Eigenstructure based coherence computations. In *Annual Meeting Abstracts*, pages 328–331. Society Of Exploration Geophysicists, 1996.
- J. Goudswaard. *Multi-scale characterisation of seismic reflection data*. PhD thesis, Delft Univ. of Techn., 2001.
- A. Grossman and J. Morlet. Decomposition of hardy functions into square integrable wavelets of constant shape. *SIAM J. Math. Anal.*, 15(4):723–736, 1984.
- A. Haar. Zur theorie der orthogonalen funktionen-systeme. *Math. Ann.*, 69: 331–371, 1910.
- N. L. Haskell, S. E. Nissen, J. A. Lopez, and M. S. Bahorich. 3-d seismic coherency and the imaging of sedimentological features. In *Annual Meeting Abstracts, 65th Ann. Int. Meeting*, pages 1532–1534. Society Of Exploration Geophysicists, 1995.

- H. J. A. M. Heijmans. *Discrete wavelets and multiresolution analysis.*, pages 49–80. *Wavelets: An elementary treatment of theory and applications.* World Scientific, 1993.
- F. J. Herrmann and C. Stark. *Monoscale analysis of edges/reflectors using fractional differentiations/integrations*, pages 1837–1840. Soc. of Expl. Geophys., 1999.
- F. M. Hindriks, R. L. C. van Spaendonck, G. G. Drijkoningen, and J. T. Fokkema. Directional scale analysis for three-dimensional seismic data. In *62nd Mtg. EAGE., Extended Abstracts*, pages A–02. Eur. Assn. Geosci. Eng., 2000.
- A. Karasaridis and E. P. Simoncelli. A filter design technique for steerable pyramid image transforms. *ICASSP*, 1996.
- N. G. Kingsbury. The dual-tree complex wavelet transform: A new technique for shift-invariance and directional filters. In *IEEE DSP Workshop*, Bryce Canyon, 1998.
- I. Magrin-Chagnolleau, T. P. H. Steeghs, R. Baraniuk, H. Choi, and R. L. C. van Spaendonck. Multiscale texture segmentation of dip-cube slices using wavelet-domain hidden markov trees. In *Annual Meeting Abstracts*, pages 1512–1515. Society Of Exploration Geophysicists, 1999.
- S. Mallat. Multiresolution approximations and wavelet orthonormal bases of L^2 . *Trans. Amer. Mth. Soc.*, 315(8):69–87, 1989.
- S. Mallat. *A Wavelet Tour of Signal Processing*. Academic Press, 1998.
- K. J. Marfurt, R. L. Kirlin, S. L. Farmer, and M. S. Bahorich. 3-d seismic attributes using a semblance-based coherency algorithm. *Geophysics*, 63 (04):1150–1165, 1998.
- K. J. Marfurt, R. M. Scheet, J. A. Sharp, G. J. Cain, and M. G. Harper. Suppression of the acquisition footprint for seismic sequence attribute mapping. In *Annual Meeting Abstracts*, pages 949–952. Society Of Exploration Geophysicists, 1995.
- Y. Meyer. Principe d'incertitude, bases hilbertiennes et algebres d'operateurs. In *Seminaire Bourbaki*, number 662, 1985-1986.

- Y. Meyer. *Ondelettes et operateurs, I: Ondelettes, II Operateurs de Calderon-Zygmund, III: Operateurs multilineaires*. 1990.
- M. Mitrea. *Clifford wavelets, singular integrals and Hardy spaces*. Lecture notes in mathematics 1575. Springer-Verlag, 1994.
- J. Morlet. *Sampling theory and wave propagation*, volume 1 of *NATO ASI series*. Springer-Verlag, 1983.
- S. E. Nissen, N. L. Haskell, J. A. Lopez, T. J. Donlon, and M. S. Bahorich. 3-d seismic coherency techniques applied to the identification and delineation of slump features. In *Annual Meeting Abstracts, 65th Ann. Int. Meeting*, pages 1532–1534. Society Of Exploration Geophysicists, 1995.
- I. W. Selesnick. Hilbert transform pairs of wavelet bases. *IEEE Signal Processing Letters*, 8(6), 2001.
- E. P. Simoncelli. <http://www.cis.upenn.edu/~eero>. web, 2002.
- E. P. Simoncelli, W. T. Freeman, E. H. Adelson, and D. J. Heeger. Shiftable multi-scale transforms. *IEEE Transactions on Information Theory*, 38: 587–607, 1992.
- M. J. T. Smith and T. P. Barnwell. Exact reconstruction techniques for tree-structured subband coders. *IEEE Trans. on Acoustics, speech and Signal Proc.*, June:434–441, 1986.
- H. Steeghs, T. P and G. G. Drijkoningen. Seismic sequence analysis and attribute extraction using quadratic time-frequency representations. *Geophysics*, 66(6):1947–1959, 2002.
- T. P. H. Steeghs. *Local Power Spectra and Seismic Interpretation*. PhD thesis, Delft University of Technology, Delft, Netherlands, 1997.
- T. P. H. Steeghs. Pseudo-horizon for visualization of seismic time-slices. *First Break*, 3, 2002. To be submitted.
- T. P. H. Steeghs, I. Overeem, S. Tigrek, and J. T. Fokkema. Volume attributes for seismic interpretation. Not yet submitted, 2001.
- G. Strang and T. Nguyen. *Wavelets and Filter Banks*. Wellesley-Cambridge Press, Wellesley, MA, 1996.

- M. T. Taner, F. Koehler, and R. E. Sheriff. Complex seismic trace analysis. *Geophysics*, 44(06):1041–1063, 1979.
- M. T. Taner and R. E. Sheriff. Applications of amplitude, frequency and other attributes to stratigraphic and hydrocarbon determination. *AAPG Memoir*, 26, 1977.
- S. Tigrek. 3-d seismic interpretation and attribute analysis of the 108-block, southern north sea basin. Master's thesis, Delft University of Technology, Delft, Netherlands, 1998.
- M. Unser. Splines, a perfect fit for signal and image processing. *IEEE Signal Processing Magazine*, November:22–38, 1999.
- P. P. Vaidyanathan. Quadrature mirror filter banks, m-band extensions and perfect-reconstruction techniques. *IEEE ASSP Magazine*, 4:4–20, 1987.
- P. P. Vaidyanathan. *Multirate Systems and Subband Coding*. Prentice Hall, 1993.
- R. L. C. van Spaendonck and R. G. Baraniuk. Directional scale analysis for seismic interpretation. In *Annual Meeting Abstracts*, pages 1844–1847. Society Of Exploration Geophysicists, 1999.
- R. L. C. van Spaendonck, F. C. A. Fernandes, R. G. Baraniuk, and J. T. Fokkema. Local hilbert transformation for seismic interpretation. In *64rd Mtg.EAGE*. Eur. Assn. Geosci. Eng., 2002a. (accepted).
- R. L. C. van Spaendonck, F. C. A. Fernandes, R. G. Baraniuk, and J. T. Fokkema. Wavelet-based hilbert transformation for local operations. *IEEE Trans. Signal Proc.*, 2002b. in preparation.
- R. L. C. van Spaendonck, F. C. A. Fernandes, M. Coates, and C. S. Burrus. Non-redundant, directionally selective, complex wavelets. In *IEEE Proc. Int. Conf. Image Proc., Extended Abstracts II*, pages 379–382. IEEE, 2000.
- R. L. C. van Spaendonck, F. C. A. Fernandes, and J. T. Fokkema. Wavelet-based volume attributes. In *71st Annual meeting abstracts*, pages 1957–1960. Soc. of Expl. geophys., 2001.
- R. L. C. van Spaendonck, F. M. Hindriks, F. C. A. Fernandes, and G. G. Drijkoningen. Three-dimensional attributes for seismic interpretation. In

- Annual Meeting Abstracts*, pages 2059–2062. Society Of Exploration Geophysicists, 2000.
- R. L. C van Spaendonck, T. P. H. Steeghs, and J. T. Fokkema. 3-d seismic data information extraction with wavelet and time-frequency representations. In *EAGE wavelet workshop*. Eur. Assn. Geosci. Eng., 2001.
- F. Verhelst. *Integration of seismic data with well-log data*. PhD thesis, Delft Univ. of Techn., 2000.
- M. Vetterli. Filterbanks allowing perfect reconstruction. *Signal Processing*, 10(3):219–244, 1986.
- M. Vetterli. Wavelets and filterbanks. *IEEE Tran. Signal Proc.*, SP-40, 1992.
- M. Vetterli and J. Kovačević. *Wavelets and Subband Coding*. Prentice Hall, 1995.

Samenvatting

Dit proefschrift behandelt de ontwikkeling en toepassing van nieuwe multiresolutie signaalverwerkingstechnieken voor het analyseren van de seismische reflector en zijn omgeving.

Seismische attributen spelen een cruciale rol in de interpretatie van drie-dimensionale seismische data. Na migratie en stacking van de ruwe data, correspondeert het seismische beeld met een amplitude kaart van de stratificatie en structuren van de ondergrond. Om geologische structuren te kunnen identificeren aan de hand van het seismische beeld, moeten we de seismische signaalparameters kwantificeren aan de hand van attributen. In het ideale geval zijn deze direct te relateren aan de stratigrafie. Vooral voor de ondoorzichtige drie-dimensionale data zijn attributen onmisbaar voor visualisatie en karakterisering van de reflectie-eigenschappen. In de afgelopen jaren zijn er verfijnde multi-trace technieken ontwikkeld waarmee breuken en laterale variaties kunnen worden gedetecteerd. Onze filosofie met betrekking tot de analyse van seismische data is dat we, door de omgeving van de reflector uit te drukken in significante structurele en fysische grootheden, een beter begrip krijgen van de geologie in de ondergrond.

De omvangrijke hoeveelheid data waarmee we in de seismische beeldvorming te maken hebben, vergt een aanpak met efficiënte algoritmieken. Conventionele attributen worden dan ook veelal verkregen door karakterisering van geïsoleerde traces of aan de hand van simpele operaties op meerdere traces. Mede hierdoor zijn de huidige volume-attributen, zoals instantane frequentie, instantane fase en laterale coherentie niet noodzakelijkerwijze ontwikkeld om het signaal weer te geven in relevante geologische of fysische parameters,

maar meer vanwege de efficiëntie van bestaande algoritmen.

De efficiëntie van het algoritme gaat niet alleen ten koste van de geologische betekenis van enkele attributen, maar ook van de trefzekerheid. De complexe trace-attributen die afgeleid zijn van het analytische signaal zijn hiervan een duidelijk voorbeeld. De complexe trace-attributen worden berekend aan de hand van puntsgewijze operaties en Fourier transformaties. Hoewel de berekening relatief snel kan worden gedaan, illustreert het algoritme de contradictie tussen lokale en globale operaties, doordat de attributen over het algemeen door spikes en oscillatie-artefacten worden verstoord.

Onze methode voor volume-analyse maakt gebruik van de discrete wavelet transformatie (DWT). De motivatie hiervoor is dat de basisfuncties van deze transformatie zowel lokaal in tijd als in frequentie zijn. Hierdoor levert de transformatie een natuurlijk platform voor multiresolutie analyse. Dit wil zeggen dat we de frequentie van het signaal lokaal kunnen bestuderen in tijd, waarmee we een compleet beeld van het signaal verkrijgen. Een tweede motivatie voor het gebruik van de DWT is dat zij erg efficiënt is. De wavelet transformatie is een van de meest succesvolle mathematische technieken voor signaalverwerking van de laatste jaren. Zij is met succes toegepast in beeld compressie, ruisonderdrukking, segmentatie, data-modelering en vele andere toepassingen.

We gebruiken de multiresolutie-eigenschap van de DWT voor de berekening van volume attributen, zoals bijvoorbeeld schaal, hellingshoek en hellingsrichting. De DWT heeft echter een aantal belangrijke minpunten. Daar seismische beelden een meting van geluidsgolven betreffen, spelen de amplitude en fase een cruciale rol, zoals in elk golfpropagatiesysteem. In het seismische beeld geeft de amplitude de mate van contrast in gesteente-parameters weer en de fase bepaalt de aankomsttijd van de reflecties. Daarom is de fase onontbeerlijk voor een complete beschrijving van het seismische signaal. Helaas ontbreekt de fase in de DWT. Een ander nadeel van de DWT is dat deze niet invariant is onder translatie en dat de transformatie voor hogere dimensies nauwelijks informatie over richting laat zien.

Alhoewel er reeds wavelet transformaties bestaan met fase-informatie, hebben deze ofwel een gecompliceerd ontwerp, ofwel een imaginair deel en een reëel deel welke samen geen lokaal analytisch paar vormen. Zonder deze laatste eigenschap is de fase niet bruikbaar voor het doeleinde van attribuut bepaling.

Een van de nieuwe bijdragen van dit proefschrift is de uitbreiding van de DWT naar twee nieuwe complexe wavelet transformaties. Beide transfor-

maties kunnen gerealiseerd worden door gebruik te maken van een willekeurig reëel wavelet. De transformaties behouden de wenselijke eigenschappen van de DWT, maar bevatten tevens fase-informatie. Daarbij zijn beide transformaties aanzienlijk minder variabel onder translatie en bevatten zij meer richtingsgevoelige informatie. Het ontwerp van de beide algoritmen is relatief simpel en efficiënt te implementeren. De eerste transformatie maakt gebruik van projectie alvorens de wavelettransformatie toe te passen. De tweede transformatie integreert de projectie in de wavelet decompositie.

De projectie die we gebruiken om het imaginaire deel van de complexe transformaties te berekenen, is gebaseerd op een lokale vorm van de Hilberttransformatie. Deze nieuwe implementatie van de Hilberttransformatie is op zichzelf al toepasbaar voor attributenanalyse. Zij kan zowel gebruikt worden voor lokale signaalanalyse als voor de berekening van complexe trace volumeattributen.

In onze zoektocht naar de complete beschrijving van de reflectie-omgeving, berekenen we de lokale geometrie, schaal- en reflectiesterkte. Voor deze berekeningen maken we gebruik van de nieuwe complexe wavelettransformatie welke besproken wordt in dit proefschrift. De geometrie splitsen we in de hellingsrichting en de hellingshoek. De attributen zijn gevalideerd aan de hand van een simpel synthetisch model van een enkele reflector met licht variërende geometrie en constante frequentie. De resultaten van de attributen laten zien dat de complexe wavelet transformatie uitstekend toegerust is voor de kwantificering van de geometrische vorm van de reflector en haar drie-dimensionale schaaleigenschappen.

De attributen toegepast op praktijkdata, laten zien dat deze een aantal signaal eigenschappen zichtbaar maken die verborgen blijven in de amplitude-data. De attributen zijn stabiel onder lichte variaties en ruis in de praktijkdata. Voor afbeelding van de attributen introduceren we het concept van de virtuele topografie van een tijd- of dieptedoorsnede. Door de geometrische informatie in een laterale doorsnede op de juiste manier te combineren, kunnen we een oppervlak construeren dat representatief is voor de geometrie in de omgeving van die doorsnede. Op deze manier kunnen we de twee geometrie attributen in één enkel beeld vangen. Dit concept biedt nieuwe perspectieven voor visualisatie en structurele interpretatie van seismische data; we kunnen nu de complete lokale beschrijving van de toonaangevende reflectie-eigenschappen vatten in een enkele afbeelding.

Dankwoord

Dit proefschrift is het resultaat van multidisciplinair onderzoek waaraan velen hebben bijgedragen. Gaarne wil ik hen daarvoor danken, om te beginnen met mijn promotores.

Prof. dr. ir. J. T. Fokkema, beste Jacob, dankzij je kritische begeleiding-op-afstand kwam ik allengs tot het besef dat je er voldoende vertrouwen in had dat ik dit proefschrift op mijn eigen(wijze) wijze tot een goed einde zou brengen. Daarmee heb je niet alleen een essentiële bijdrage geleverd aan mijn wetenschappelijke, maar ook aan mijn persoonlijke ontwikkeling. Behalve over de aard van de vraag, heb je me tevens geleerd na te denken over de aard van het beestje. Ik ben je daarvoor veel dank verschuldigd.

Prof. dr. R. G. Baraniuk, dear Richard, during my first visit to Rice University, you have introduced me to the world of wavelets. Your clear and simple explanations of complicated math has majorly contributed to my understanding of wavelets. My visits to Houston, complemented by our workshops in Rochemaure have been fertile grounds not only for the research, but also for a precious friendship. I am honoured to have a brilliant scientist like you as my promotor and I am delighted to continue working with you in Lausanne and Houston.

Naast mijn twee promotoren, noem ik dr. Philippe Steeghs in het bijzonder. Beste Philippe, als een goede vriend en wijze mentor heb jij mij de juiste weg gewezen. Hartelijk dank voor jouw steun, bijdrage en grenzeloze inzet. Op moeilijke momenten, heb ik me altijd tot jou kunnen wenden voor excellente raad.

Dr. ir. Guy Drijkoningen als directe begeleider mag zeker niet ontbreken.

Beste Guy, jouw grondige kennis over de seismische meting en data verwerking zijn onmisbaar geweest voor een goed begrip van het seismisch beeld. Onvergetelijk is het weekend in West-Texas, dat gekruid was met discussies over geologie, geofysica en nóg aardse zaken, terwijl we getooid gingen met cowboy-hoeden.

Felix Fernandes, I very much enjoyed working with you. Thanks for a fruitful and delightful cooperation. I will never forget the fun we have had at Rice during the development of the Softy space and the "cough"-IR reconstruction filters.

Mijn naaste collega's dank ik voor een goede tijd. Jan-Willem Schoolmeesters, van keldervloer tot beursvloer hebben we ons mannetje gestaan, mijn dank voor deze memorabele tijd. Kees Hindriks, ik heb genoten van onze kelderraam escapades. Irina Overeem wil ik vermelden wegens haar fantastische geologische feedback. Als discussie partner wil ik tevens Evert Slob noemen, die altijd nieuwe inzichten had.

Richard Kaper en Folkert Hindriks, met jullie afstudeeronderzoeken hebben jullie elk wezenlijk bijgedragen aan mijn onderzoek. Bedankt hiervoor en voor de plezierige samenwerking.

Voorts gaat mijn dank uit naar de andere leden van de vakgroep Technische Geofysica, Kees, Rob, Michel, Menno, Jeroen, Jeroen, Jan, Lourens, Sevgi, Hedi, Gerdje, Martijn, Jesper, Antonio, Nicoletta en natuurlijk de studenten van DOGS.

My colleagues at Rice University, Benhaam, Doug, Rob, Jan, Rolf, Hyeokho, Justin, Neelsh, Vinay, and Mark, thanks for the pleasant times in Houston and the Gingerman.

Arthur en Jurjan dank ik voor de gedenkwaardige stroveer tijd, en voor de grootste kamer. Alhier het resultaat.

Mijn ouders, Jorrit en Femke, bedankt voor jullie nimmer aflatende steun en vertrouwen.

Lieve Karin, omdat je er was, ook als je er niet was.

Curriculum Vitae

Rutger van Spaendonck was born on april 28, 1971 in Nijmegen, the Netherlands. He went to the Stedelijk Gymnasium Nijmegen in 1983. After completing his secondary school in 1989, he joined the Mining and Petroleum Engineering Department of Delft University of Technology as a Masters student. He graduated for his Masters in Applied Geophysics in 1996 on the subject of time-lapse seismic data processing.

Rutger continued research as a doctorate student in Delft starting in 1997 in the Applied Geophysics group that had now become part of the Faculty of Applied Earth Sciences. His research focused on data driven seismic volume analysis for geological interpretation.

During this period he has frequently paid extended visits to the Digital Signal Processing (DSP) group at Rice University where he collaborated with leading scientists in the DSP community. In cooperation with this group he worked on the development of geometric multi-resolution techniques for the analysis of seismic images and volumes.

To broaden his academic horizons beyond geophysical interests, he joined the DSP group at Rice University in Houston as a postdoctoral fellow in February 2002. In this context, he spent several months as a visiting scholar at the Laboratoire Communication Audiovisuelle of the École Polytechnique Fédérale de Lausanne in Switzerland.



